UNIVERSIDAD NACIONAL AUTÓNOMA DE MÉXICO

PROGRAMA DE POSGRADO EN ASTROFÍSICA

INSITUTO DE ASTRONOMÍA

ESTUDIO DE LA DINÁMICA DE DISCOS ESTELARES EN HALOS TRIAXIALES COSMOLÓGICOS DE MATERIA OSCURA

TESIS

PARA OPTAR POR EL GRADO DE:
MAESTRO EN CIENCIAS (ASTROFÍSICA)

PRESENTA:

RODRIGO ADOLFO CAÑAS VÁZQUEZ

TUTOR
DR. HÉCTOR MANUEL VELÁZQUEZ, INSITUTO DE ASTRONOMÍA, UNAM

COMITE TUTOR
DR. HÉCTOR ACEVES CAMPOS, INSTITUTO DE ASTRONOMÍA, UNAM
DR. CARLOS ROMÁN ZÚÑIGA, INSTITUTO DE ASTRONOMÍA, UNAM

ENSENADA, BAJA CALIFORNIA, MÉXICO

NOVIEMBRE 2015

UNIVERSIDAD NACIONAL AUTÓNOMA DE MÉXICO

PROGRAMA DE POSGRADO EN ASTROFÍSICA

INSTITUTO DE ASTRONOMÍA

STUDY OF THE DYNAMICS OF STELLAR DISKS IN COSMOLOGICAL TRIAXIAL DARK MATTER HALOS

THESIS

SUBMITTED FOR THE DEGREE OF:
MASTER IN SCIENCE (ASTROPHYSICS)

PRESENTED BY:

RODRIGO ADOLFO CAÑAS VÁZQUEZ

SUPERVISOR
DR. HÉCTOR MANUEL VELÁZQUEZ, INSITUTO DE ASTRONOMÍA, UNAM

SUPERVISING COMMITEE
DR. HÉCTOR ACEVES CAMPOS, INSTITUTO DE ASTRONOMÍA, UNAM
DR. CARLOS ROMÁN ZÚÑIGA, INSTITUTO DE ASTRONOMÍA, UNAM

ENSENADA, BAJA CALIFORNIA, MÉXICO

NOVEMBER 2015

A mis padres,
que siempre me han apoyado en todas mis decisiones,
y siempre han estado presentes a pesar de la distancia.

Agradecimientos

No me alcanzan las palabras para describir lo agradecido que estoy con mi papá y mamá, que siempre me han apoyado en todos los aspectos y decisiones que he tomado, tanto académicas como personales, y que han dedicado su vida a asegurarse que nada me falte. Si he llegado tan lejos ha sido gracias a ustedes. Y a ti Cynthia gracias por siempre recibirme con una sonrisa, y que aunque lleguemos a pelear algunas veces, sé que estaremos el uno para el otro y que podemos contar con nosotros siempre.

Quiero agradecer también a mis asesores en estos años de maestría. Al Dr. Velázquez por su paciencia en la realización de este proyecto y por enseñarme a ver todo desde diferentes perspectivas. Al Dr. Aceves por el apoyo que me ha brindado desde la licenciatura, por mostrarme que aún siendo adulto Santa Claus no se olvida de uno, pero sobre todo por ser además de un buen asesor un gran amigo. Y al Dr. Carlos Román, que siempre ha tenido tiempo para mis visitas express y peticiones de última hora, pero sobre todo, gracias Carlos por el apoyo y las palabras de aliento que me brindas.

Quiero agradecer al Dr. Vladimir Ávila, Dr. Pedro Colín, Dr. Leonel Gutiérrez y al Dr. Ivânio Puerari por los comentarios, discussiones, sugerencias y correcciones que han servido para mejorar este trabajo.

Agradezco a todo el personal del Instituto de Astronomía, tanto con sede en CU como en Ensenda, por el apoyo que se me ha brindado en diversos asepectos durante la maestría.

A mis amigos de Ensenada, Monterrey, D.F. y Edomex, que de alguna u otra forma han estado presentes y me han apoyado tanto en las buenas como en las malas. A ustedes que me conocen contento, enojado, molesto, intenso, friki, mandón, que aunque no me reporte seguido saben que sigo aquí, y que, ya sea dentro o fuera del trabajo hacen que los momentos sean alegres y amenos.

A ti Adriana, que has sido tan paciente conmigo y esta tesis en este año, muchas, muchas gracias por haberme apoyado en este largo camino. Gracias por tu enorme cariño que todos los días nos das a Ami, a Mika y a mí. Gracias por esta bonita familia.

Por último quiero reconocer el apoyo de CONACyT por la beca de Posgrado de Excelencia No. 357679 que se me otorgó para poder realizar estos estudios, y a las becas de los proyectos CONACyT 179662 y PAPIIT IN108914 por el apoyo para terminar este proyecto. La mayoría de las simulaciones de este trabajo se realizaron con los servidores Erebus del proyecto CONACyT CB-2010 152160, con la supercomputadora Miztli de la DGTIC de la UNAM y el servidor Atocatl del Instituto de Astronomía de la UNAM.

Contents

List of Figures

List of Tables

Abstract

Numerical simulations are one of the most important tools to understand the universe and the phenomena that occur in it. Problems such as the hierarchical formation of large-scale structure of the universe, and, the formation and evolution of galaxies are treated mainly with N-body and hydrodynamic simulations due to the complexity and non-linear nature of these problems. This work presents a study of the morphology and dynamics of stellar disks in a cosmological context by means of N-body simulations.

A new and alternative method to grow a stellar disks in dark matter halos is implemented, stimulated by different works in the literature. Milky Way-mass dark matter halos in an isolated environment and with a quiet accretion history are identified in low-resolution simulations and re-simulated using the zoom-in technique. Inside these high-resolution halos, semi-analytic inferred exponential disks are adiabatically grown by increasing the mass fixed particle distribution. An extension of previous works is done here by growing the disks in several orientations with respect to the principal axes of the halo inertia tensor. Once the disks reach their total mass, they are taken to a nearly-equilibrium state using an iterative method, and then self-consistently evolved in a cosmological zoom-in simulation using the public version of GADGET-2.

The results show that the morphology of the disks at the end of the simulation at $z = 0$ is very similar, independently of the initial orientation. Grand design spirals are displayed by minor- and major-oriented models, while intermediate orientations show a transition from grand design towards flocculent spirals as the angle with respect to minor axis $\theta_{\rm ori}$ increases.

Several characteristic phases were noticed during the evolution of disk heating, bar strength, and the ratio $\mathcal{R}$ of the corotation radius to the bar length of the galaxies. It is shown that these phases are connected, and are explained by the interaction between the bar and resonance regions. These interactions are accompanied by the growth of vertical modes in a standing wave-like patterns observed when the bar termination crosses ultraharmonic resonance (UHR) regions. These modes, that are also well delimited by the inner Lindblad resonance (ILR) and the bar termination at UHRs, are important mechanisms of disk heating, and the development of deformations in the disk, such as prominent corrugations when the bar termination crosses

$\Omega - \kappa/8$, and the buckling instability of the bar when $\Omega - \kappa/4$ crossing occurs. This is the first time these phenomena are found in these kind of studies.

It is observed that all disks experience some degree of tilt during their evolution, although a tendency for large reorientation is seen only for high $\theta_{\rm ori}$ models. Additionally, all models with large $\theta_{\rm ori}$ present ring structures that separate from the rest of the disks, independently of the reorientation of the disk. These models show a strong resemblance to observed Polar Ring Galaxies (PRGs), hence are proposed here for the first time as a possible PRG formation scenario.

Finally, it is found that the disk angular momentum shows a strong tendency to align parallel to the minor axis of the halo from the inside to ever large radii. This suggests that there exists a strong coupling between the mass distribution of the halo and the angular momentum of the disk, confirming what has been found in other studies reported in the literature.

Resumen

Introduccción

La formación y evolución de galaxias es un tema que los astrónomos han tratado de entender durante muchos años. Desde las observaciones llevadas a cabo por Willian y Caroline Herschel, que situaban nuestro sol en el centro de la Vía Láctea (Herschel, 1785), pasando por los estudios hechos por Shapley, que localizaban el sol a dos tercios del tamaño de la galaxia de su centro, hasta la primer "simulación" de interacción de galaxias por Holmberg (1941), estos objetos han sido objeto de estudio entre la comunidad científica, y en general han sido una interminable fuente de fascinación para la humanidad.

Las galaxias son conjuntos de (miles de millones de) estrellas que estan ligadas gravitacionalmente y estan soportadas por rotación en el caso de galaxias de disco, or por la "presión" del movimiento aleatorio de las estrellas para las galaxias elípticas o esferoidales. Estos objetos presentan un rango amplio en masa y tamaño, desde galaxias enanas con masa de $\sim 10^8 M_\odot$ y diámetro de unos cuantos kpc (e.g. Pequeña y Gran Nubes de Magallanes), hasta masas de $\sim 10^{13} M_\odot$ y diámetros de decenas de kpc de las galaxias cD en el centro de cúmulos de galaxias (e.g. ESO 146-IG 005 en el cúmulo Abell 3827 Carrasco et al. 2010).

Estos objetos muestran diversas formas que surgen tanto de la formación secular de la galaxia o por interacción y/o fusión con otra. Las formas predominantes son esferoides y discos, que son comunmente conocidas como galaxias tempranas y tardías respectivamente en la secuencia de Hubble. Las galaxias de disco muestran características importantes que han sido objeto de interés y estudio por muchos años, como lo son los brazos espirales y la barra que domina la parte central. Las barras son importantes ya que el $\sim 67\%$ de las galaxias espirales presentan barras tanto fuertes como débiles (Barazza et al., 2008; Eskridge et al., 2000), y debido a que existe evidencia observacional que sugiere la presencia de una barra en la Vía Láctea (Weinberg, 1992). Adicionalmente, algunas galaxias de disco muestran características y configuraciones que no se encuentran normalmente en toda la población de galaxias, como lo son alabeos y componentes fuera del plano de la galaxia mostrados por las galaxias de anillo polar (PRG, por sus siglas

en inglés). Estudios de estas dos características han tratado de atribuir estas estructuras a la interacción de la galaxia principal con una galaxia o subhalo que lo orbita, sin embargo, es de interés explorar la posibilidad que estas configuraciones sean producto solamente de la evolución secular de la galaxia, que se ha llevado a cabo en simulaciones aisladas por Jeon et al. (2009), pero no se ha abordado en un contexto cosmológico.

El paradigma ΛCDM ha sido considerado en años recientes como el modelo cosmológico "estándar". Este modelo tiene sus bases en el principio cosmológico y en la teoría de la relatividad de Einstein, en la que la evolución del universo está determinada por la interacción de las diferentes contribuciones de energía, compuestas en un $\sim 72\%$ de energía oscura, que expande el espacio separando objetos, y $\sim 28\%$ de materia (Hinshaw et al., 2013), que trata de agruparlos.

Las simulaciones numéricas son una de las herramientas más importantes que nos ayudan a entender el universo y los fenómenos que ocurren en él. Problemas como la formación jerárquica de la estructura a gran escala del universo y la formación y evolución de galaxias, son abordados principalmente con simulaciones hidrodinámicas y de N-cuerpos (e.g. Boylan-Kolchin et al. 2009; Klypin et al. 2011; Vogelsberger et al. 2014a) debido a la complejidad y naturaleza no-lineal de estos problemas.

Las simulaciones hidrodinámicas que incluyen su física debería ser la principal herramienta para estudiar la formación y evolución de galaxias. Sin embargo, el espacio de parámetros en dichas simulaciones es enorme, lo que hace que diferentes tratamientos de retroalimentación y formación estelar afecta altamente el resultado de las simulaciones como ha sido mostrado recientemente en estudios de comparación de códigos como lo son el proyecto Aquila (Scannapieco et al., 2012). Esto hace aún más difícil separar los efectos producidos por cada uno de estos parámetros, por otro lado, el enfoque de N-cuerpos nos permite estudiar los efectos que surgen solamente de la interacción gravitacional, por lo que son todavía una herramienta bastante útil.

Este trabajo estudia la evolución de discos estelares galácticos embebidos en un halo de materia oscura con masa similar al de la Vía Láctea obtenido de una simulación cosmológica. Se seleccionaron halos que hayan tenido una historia de acreción "quieta" desde $z = 1$ y cumplieran con un criterio de aislamiento. Se corrieron simulaciones tipo *zoom-in* en las que se introdujo un disco estelar para estudiar la dinámica y propiedades no axisimétricas de estos discos.

Metodología

Halos Cosmológicos tipo Vía Láctea de Alta Resolución

Las simulaciones cosmológicas y las de evolución de galaxias difieren típicamente por varios órdenes de magnitud en tamaño y masa (e.g. Boylan-Kolchin et al. 2009; Dubinski et al. 2009;

Klypin et al. 2011), por lo que algunas veces es difícil o incluso imposible estudiar la dinámica de galaxias en un contexto cosmológico si no se tiene acceso a grandes recursos computacionales (e.g Vogelsberger et al. 2014a).

Existen varias aproximaciones que pueden ser usadas para abordar este problema. En una de ellas se simula una pequeña caja cosmológica periódica con una sobre-densidad o sub-densidad constante, de tal forma que se tomen en cuenta las perturbaciones a gran escala, el modo DC (e.g. Pen 1997; Sirko 2005). Otro método es el llamado *zoom-in*, el cual consiste en identificar una region de interés en una simulación de baja resolución para después agregar un número mayor de partículas a dicha región en la condición inicial para obtener una mayor resolución espacial y en masa (e.g. Avila-Reese et al. 2011; Colín et al. 2010; Springel et al. 2008). Este último enfoque se utiliza en este trabajo.

Todas las simulaciones se corrieron utilizando el model cosmológico ΛCDM caracterizado por los parámetros de densidad $\Omega_{\rm m} = 0.288$ y $\Omega_\Lambda = 0.712$, la fluctuación de masa en esferas de 8 h^{-1} Mpc de $\sigma_8 = 0.830$, un índice espectral de $n_s = 0.971$, y una constante de Hubble de $H_0 = 69.33$ km s^{-1}Mpc^{-1} a tiempo presente. Estos valores concuerdan con las restricciones impuestas por WMAP-9 (Hinshaw et al., 2013).

Para establecer las simulaciones de los discos, el primer paso fue correr una simulación cosmológica de N-cuerpos de 512^3 partículas en una caja de 100 h^{-1} Mpc de lado, para identificar halos de materia oscura cuyas propiedades se parecieran a las del halo de la Vía Láctea, lo que se logró utilizando la herramienta *Amiga Halo Finder* AHF, una herramienta pública para identifiar halos (Gill et al., 2004; Knollmann & Knebe, 2009). Los halos fueron seleccionados estableciendo restricciones en la masa del halo ($9 \times 10^{11} \leqslant M_{\rm halo}/h^{-1}\,M_\odot \leqslant 1.25 \times 10^{12}$), que tuvieran una historia de accreción tranquila (masa máxima accretada en un merger de $M_{\rm sub} < 1.2 \times 10^{10} M_\odot$) desde $z = 1$, y un criterio de aisalmiento, de tal forma que no hubiera un vecino con masa $M_{\rm neighbor} > 0.5 M_{\rm halo}$ dentro de una esfera de radio de 2 h^{-1} Mpc a $z = 0$, para poder estudiar la evolución secular de galaxias en halos con masa tipo Vía Láctea en un contexto cosmológico.

Inclusión de Discos Estelares en Halos Cosmológicos

La formación de galaxias no puede ser completamente estudiada sin incluir bariones y su física, por lo que deben ser simuladas hasta cierto punto. El enfoque utilizado en este estudio supone un crecimiento adiabático del potencial de un disco exponencial utilizando una distribución fija de partículas. De esta manera, la forma y dinámica del halo de materia oscura anfitrión responderá a la presencia del disco que crece lentamente, en lugar de insertar súbitamente varias $10^{10} M_\odot$ en el centro del halo oscuro, lo cual generaría efector artificiales no

deseados.

Por simplicidad se asumió un crecimiento lineal de la masa de disco $m_{\rm d}$ entre un redshift inicial de inserción $z_{\rm insert}$ y un redshift final $z_{\rm live}$, cuando el disco para de crecer y alcanza la masa total asumida para este componente. La distribución de densidad de masa del disco es simplemente una función dependiente de la masa total, para ser específicos

$$\rho(R, z, a) = \frac{m_{\rm d}(a)}{4\pi R_{\rm d}^2 z_{\rm d}}\, e^{-R/R_{\rm d}}\, {\rm sech}^2\left(\frac{z}{z_{\rm d}}\right) \tag{1}$$

donde R y z son las coordenadas cilíndricas, $R_{\rm d}$ y $z_{\rm d}$ son las escalas radial y vertical del disco respectivamente, a es el factor de escala, y $m_{\rm d}$ es la masa total del disco a un tiempo dado, con $m_{\rm d}(z_{\rm live}) = M_{\rm d}$. Los $M_{\rm d}$, $R_{\rm d}$ y $z_{\rm d}$ de todos los discos son estimados utilizando el método descrito por Mo et al. (1998) en el cual la escala radial de los discos depende en las propiedades del halo anfitrión, por lo que el tamaño de los discos cambiará de un halo a otro.

En este método todos los discos empiezan a crecer una masa inicial de $m_{\rm d} = 1\ M_\odot \times N_{\rm p}$ a $z_{\rm insert}$, esto se hace para evitar errores computacionales cuando se calcule la interacción gravitacional entre particulas masivas y sin masa con Gadget-2 (Springel, 2005; Springel et al., 2001). Para los parámetros utilizados en este trabajo esto significa una masa inicial del disco de $5 \times 10^5 M_\odot$ distribuida entre 500,000 partículas, que es aún menor que la masa de una sola partícula de materia oscura de alta resolucón. Este enfoque es similar al implementado por DeBuhr et al. (2012) y Yurin & Springel (2015), sin embargo, algunos procedimientos en la metodología de DeBuhr et al. (2012) no son explicados a fondo, además de que ambos DeBuhr et al. (2012) y Yurin & Springel (2015) utilizan un modelo de disco único para todos sus halos estudiados, a diferencia de nuestro procedimiento, como se indica arriba.

Para alcanzar nuestro objetivo se hicieron dos modicaciones a la versión pública del código Gadget-2. La primer modificación incrementa la masas de las partículas tipo Disco de acuerdo a la Ecuación (1), entre $z_{\rm insert}$ y $z_{\rm live}$. La segunda modificación consiste en insertar un partícula de prueba viva en el centro del halo, moviéndose con su velocidad instantánea a $z_{\rm insert}$, y seguirla a medida que se mueve con el centro del halo, las partículas del disco simplemente copian el movimiento de esta partícula.

A pesar de la simplicidad de este método, su precisión es altamente dependiente en el número de partículas en la vecindad del lugar deseado, y en la masa de la partícula de prueba. Como es una partícula viva, ésta interactúa gravitacionalmente con el resto del halo por lo que orbita al rededor del centro del halo. Para probar la precisión de este método se corrieron cinco simulaciones cambiando la masa de la parícula de prueba y añadiendo el disco inicialmente sin masa. Las masas utilizadas para la partícula de prueba fueron 1 $M_\odot$, 1, 8 and 64 veces la masa

de una partícula de materia oscura de alta resolución.

Como es de esperarse entre mayor es la masa de la partícula prueba, es menor el movimiento que ésta tiene con respecto al centro del halo, y mayor es el efecto sobre la distribución de partículas en el centro del halo oscuro. A pesar de que el centro del halo es seguido por la partícula prueba, existen altas desviaciones para las escalas de interés ya que la distancia entre le centro y la partícula es varias veces la escala vertical típica, $z_{\rm d}$, de discos galácticos. La alta variación es una consecuencia del bajo número de partículas de materia oscura en el centro del halo. Este problema se resolvió agregando las partículas del disco para poblar la región de interés, de esta forma el movimiento de la partícula prueba está restringido a un radio mucho menor que $R_{\rm d}$ y $z_{\rm d}$, y aún más importante por debajo de la escala de suavizamiento $h_{\rm soft} = 50\ h^{-1}\,{\rm pc}$, utilizada para las partículas del disco en todas las simulaciones.

Trabajo previo (e.g. Hayashi et al. 2007) ha mostrado que se espera que el momento angular del halo se alinee paralelo al eje menor del tensor de momento de inercia del halo. Sin embargo, los ejes principales y el momento angular de halos cosmológicos cambia entre las partes internas y externas (e.g. Bett & Frenk 2012). Por ello, un disco alineado paralelo a un eje principal del momento de inercia del halo no necesariamente está alineado paralelo a su momento angular. Motivados por esta razón se exploraron varias orientaciones del momento angular del disco $L_{\rm disk}$.

Las simulaciones se corrieron orientando el disco (a) con su momento angular $L_{\rm disk}$ paralelo al eje menor $C_{\rm halo}$ y el mayor $A_{\rm halo}$ del tensor de inercia, (b) con $L_{\rm disk}$ haciendo un ángulo $\theta_{\rm ori}$ con respecto a $C_{\rm halo}$, orientado sobre el plano descrito por los ejes menor y mayor, y (c) con el disco rotando en la dirección opuesta que la orientación original. Los ejes principales del momento de inercia se calcularon utilizando las partículas dentro de una esfera que contiene la mitad de la masa del halo a $z_{\rm insert}$.

La contribución de la masa del halo y del disco al sistema se visualiza en la Figura 1, donde se muestra la curva de rotación para todos los discos con orientación a lo largo del eje menor a $z_{\rm live}$. Por simplicidad la curva de rotación se calcula como la velocidad circular que corresponde a toda la masa dentro de una esfera a un radio dado r, es decir

$$V_c = \sqrt{\frac{GM(<r)}{r}} \tag{2}$$

donde G es la constante de gravitación universal, $M(<r)$ es la masa total dentro de un radio r. Para todos los discos excepto 3795, la contribución de la masa a radios pequeños es ligeramente dominada por el disco, mientras que a radios externos V_c es dominada por el halo, donde una curva de rotación plana es mostrada por todos los sistemas.

Se espera que los discos sean estables contra la formación de la barra si el criterio de Efstathiou et al. (1982) se debe de cumplir

$$Q_{\rm bar} \equiv \frac{v_{\rm max}}{(GM_{\rm d}/R_{\rm d})^{1/2}} > 1.1 \tag{3}$$

donde $v_{\rm max}$ es el máximo de la curva total de rotación, $R_{\rm d}$ es la escala radial del disco y $M_{\rm d}$ es la masa total del disco. $Q_{\rm bar}$ para todos los discos a $z_{\rm live}$ se muestra en la Tabla 1. Ninguno de los discos cumple con la condición expresada en la Equación 3, por lo que, en principio, se espera que todos los discos formen barras.

Tabla 1: Parámetros de las simulaciones de disco orientadas a lo largo del eje menor. $M_{\rm d}$ es la masa, $N_{\rm p}$ el número de partículasr, $R_{\rm d}$ y $z_{\rm d}$ son las escalas radial y vertical respectivamente. $Q_{\rm bar}$ es el criterio de estabilidad para formar barra de Efstathiou et al. (1982) calculado a $z = 1$.

Disk	$M_{\rm d}$ $[10^{10}\,h^{-1}\ M_\odot]$	N_p	$R_{\rm d}$ $[\ h^{-1}\,{\rm kpc}\ ]$	$z_{\rm d}$ $[\ h^{-1}\,{\rm kpc}\ ]$	$Q_{\rm bar}$
3180	4.348	500,000	1.493	0.149	0.776
3741	3.744	500,000	1.491	0.149	0.793
3748	3.189	500,000	1.337	0.133	0.805
3795	4.711	500,000	2.031	0.203	0.840

Después de que el halo de materia oscura ha respondido a la presencia gravitacional del disco que crece en masa, el único paso que falta para establecer las condiciones iniciales es asignar velocidades a las partículas rígidas del disco. Para este propósito se utilizó el método iterativo de propuesto por Rodionov et al. (2009). El método iterativo permite hacer esto estableciendo las partículas del halo como condición de frontera, i.e. como un potencial rígido. Se utiliza este método en lugar de ajustar potenciales (e.g. DeBuhr et al. 2012) o utilizar distribuciones simétricas de partículas que simulen el halo, ya que dichos procedimientos pueden introducir comportamientos espurios al momento que el disco se vuelve "vivo". Asimismo para evitar errores que pudiesen surgir del corte esferérico de los halos identificados con AHF, se utilizan como condición de frontera las partículas de lhalo dentro de una esfera de radio $R = 2\,R_{\rm vir}$.

Para checar la estabilidad de los discos construidos, se calculó el parámetro derivado por Toomre (1964)

$$Q_{\rm Toomre} \equiv \frac{\sigma_R\ \kappa}{3.36\,G\,\Sigma} \tag{4}$$

donde σ_R es la dispersión de velocidades en la dirección radial, κ es la frecuencia epicíclica, G es la constante de gravitación universal, y Σ es la densidad estelar superficial. Se muestra $Q_{\rm Toomre}$ como función del radio en la Figura 1 para todos los discos orientados paralelos al eje menor. De la Figura 1 se puede ver que todos los discos cumplen el criterio de estabilidad mayor a 1, y se espera que sean localmente estables contra la formación de inestabilidades axisimétricas a todos radios.

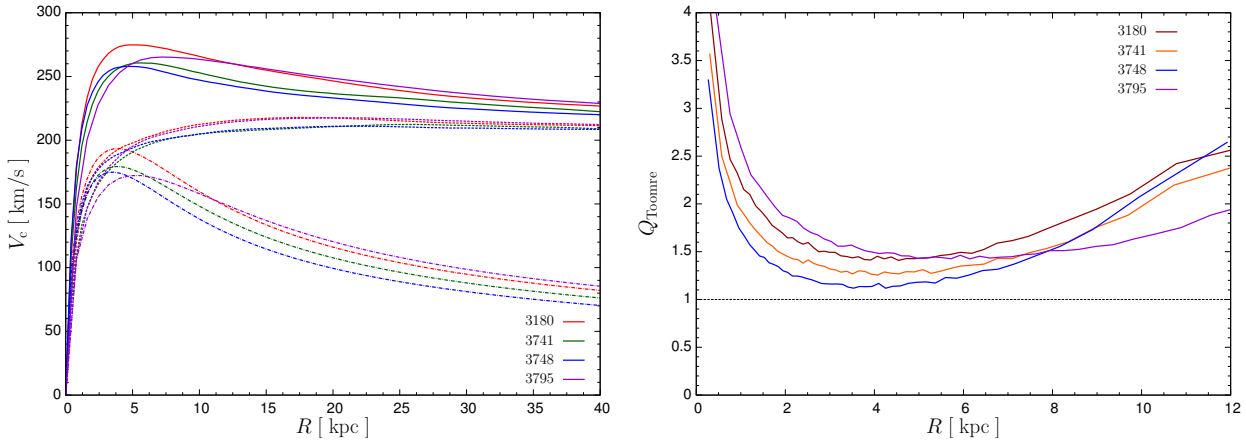

Figura 1: Velocidad circular (izquierdo) y parámetro de Toomre (derecha) Q a $z = 1$ de todos los discos orientados paralelos con el eje menor. *Izquierda* La línea sólida muestra la curva de velocidad circular total, la linea segmentada muestra la contribución del halo, yla línea punteada la contribución del disco. *Derecha* La línea punteada indica el límite para estabilidad local. Se muestra que todos los discos son localmente estables contra perturbaciones axisimétricas a todos los radios.

Resultados

En esta sección se presentan los resultados de las simulaciones descritas arriba. Se ilustra la evolución morfológica con vistas de cara y de canto. Se muestran también la densidad superficial, Σ, y densidad vertical, ρ, la dispersión de velocidades en la dirección σ_z, y la evolución de la media de la altura del disco, $z_{1/2}$. A pesar de que todos los discos presentan una evolución similar de $\Sigma(r)$, existe una diferencia clara en $z_{1/2}$, en las partes externas del disco para las orientaciones mayores y menores debido a la presencia de estructuras de anillo que no son coplanares al disco. Se presenta también la evolución del calentamiento vertical ζ y la fuerza de la barra A_2 de los discos, y se muestra cómo las diferentes fases evolucionarias de estas dos cantidades se relacionan a la interacción de la barra con resonancias. Por último, se presenta la evolución de la inclinación del disco y el desarrollo de de estructuras de anillo no coplanares en discos con un ángulo, $\theta_{\rm ori}$, grande con respecto al eje menor del momento de inercia del halo.

Por simplicidad se referirá al momento angular del disco y del halo como $L_{\rm disk}$ y $L_{\rm halo}$ respectivamente. Adicionalmente, los ejes principales del tensor de momento de inercia son siempre medidos al radio de masa media del halo, a menos que se especifique, y los ejes mayor, intermedio y menor serán referidos como $A_{\rm halo}$, $B_{\rm halo}$, y $C_{\rm halo}$respectivamente.

Evolución Morfológica

Los discos orientados a lo largo del eje mayor presentan una evolucin similar en dos etapas principales. La primer fase dura a aproximadamente los primeros dos Gigaños (Gyrs) de evolución y se caracteriza, primero, por el desarrollo de dos brazos spirales cerrados, que empiezan en la orilla de una barra larga para todos los discos, excepto por el modelo `3795`, que parece tener una barra más débil y corta. Después los discos parecen experimentar un debilitamiento de la barra y múltiples estructuras espirales. Estas características comienzan a borrarse al final de esta fase. Durante la segunda fase, aproximadamente los últimos 6 Gyrs de evolución, la estructura de cara para todos los discos presenta: una barra prominente, que se acorta y frena a medida que la amplitud crece; un anillo fuera de la barra; y estructuras difuminadas en las partes externas del disco, que en algunos casos parecen brazos espirales mientras que otros parecen tener segmentos de anillos.

Estas dos etapas se distinguen también en la evolución vista de canto. La primer etapa muestra una evolución vertical quieta, en la que los discos muestran un tipo de corrugación, alabeos débiles, picos verticales que son asimétricos con respecto al plano $x - y$, o una combinación de todos. La segunda etapa presenta una evolución gradual de la misma estructura general de todos los discos, que consiste en un pseudo-bulbo con forma de X/cacahuate, un disco grueso que sigue calentándose hasta $z = 0$.

Los discos orientados a lo largo del eje mayor presentan, en general, una comportamiento similar a La diferencia más notable entre las orientaciones mayor y menor se aprecia durante la segunda fase de evolución. En esta fase, estructuras anulares de la galaxia se separan completamente del plano descrito por los 7 kpc internos del disco. Esto significa que mientras la galaxia evoluciona y cambia su orientación, existe una sección que se separa completamente de este inclinamiento en bulto, formando un anillo coplanar que se mantiene rotando alrededor del centro de la galaxia, pero con una orientación de momento angular, $L_{\rm ring}$, diferente a $L_{\rm disk}$. A $z = 0$ esto es evidente para los modelos `3795` y `3748`, mientras que los modelos `3180` y `3741` muestran estructuras que aparentan ser una fase de transición del desacoplamiento.

Por último, la evolución de distintas orientaciones de los discos `3795` y `3180`, se observa un comportamiento similar al de los demás discos, mostrando las dos mismas etapas evolutivas. En la primer etapa se observa que el ángulo $\theta_{\rm ori}$ entre $L_{\rm disk}$ y $C_{\rm halo}$ incrementa, la estructura

espiral cambia de gran diseño hacia una galaxia foculante, mostrando la estructura de gran diseño cuando $L_{\rm disk}$ es paralelo a $A_{\rm halo}$. Esto parece indicar que la estructura espiral es más estable cuando $L_{\rm disk}$ está orientado paralelo a $A_{\rm halo}$y $C_{\rm halo}$.

Midiendo la Evolución de los Discos

Se presenta la evolución de la densidad supercial de los discos, Σ, y los perfiles de densidad vertical, ρ, muestran como el material se reacomoda radial y verticalmente, y cómo se relaciona con las propiedades observadas en la evolución morfológica. La dispersión vertical σ_z y la mediana de la altura, $z_{1/2}$, de las partículas de disco son usadas para medir cómo diferentes partes del disco se calientan en la simulación.

Densidad Superficial y Vertical

La evolución de los perfiles de densidad del disco `3180` orientado paralelo a $C_{\rm halo}$, se se muestra en la Figura 2. La evolución del perfil de densidad de todos los discos presenta un comportamiento similar, y se puede divir en tres regiones. La primera corresponde a la parte más interna de los discos, empezando en el centro del disco y terminando en el radio donde Σ a un redshift z dado cruza el perfil Σ inicial; la región intermedia corresponde a los radios que limitan el primer y segundo cruce del perfil inicial. Estas regiones son consistentes con la idea de que a medida que la simulación evoluciona, las partículas de disco se re-distribuyen debido a la formación de las estructuras observadas en la evolución morfológica.

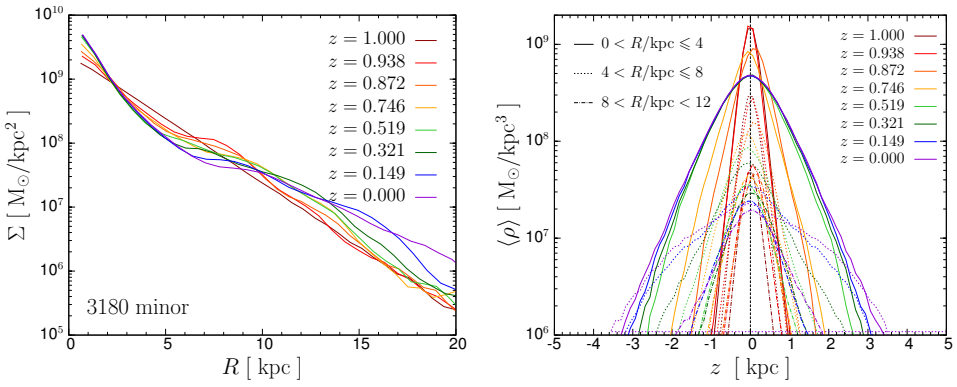

Figura 2: Densidad superficial Σ (panel izquierdo) y vertical $\langle\rho\rangle$ (panel derecho) del disco `3180` con $L_{\rm disk}$ orientado paralelo a $C_{\rm halo}$del halo anfitrión

La primer región presenta un imcremento en Σ durante todo el tiempo de simulación, y representa la estructura del pseudo-bulbo que se forma y crece en el centro de todas las galaxias. La presencia de este pseudo-bulbo explica parcialmente la reducción en Σ con respecto a la

condición inicial en la segunda región, dado que el material de la segunda región es añadido a la primera a medida que el pseudo-bulbo crece. La tercer región experimenta un incremento notable en Σ, casi un órden de magnitud, desde $z = 1$ a $z = 0$, a pesar de eso, este no es un incremento gradual, como el que se observa en la región interna, como puede observarse por los cruces múltiples durante los primeros ~ 2 Gyrs de evolución, y son consecuencia de los múltiples espirales que afectan las partes más externas de la galaxia durante la primer fase.

La dispersión vertical ρ se muestra en el panel derecho de la Figura 2. Para todos los discos se observa que la parte interna del disco presenta una disminución del pico y un ensanchamiento del perfil. Sin embargo, en cierto momento el pico converge a un vakirm nuentras que el ensanchamiento sigue creciendo. El primero se debe a la presencia de una estructura tipo caja en el centro de los discos, que se expande en radio pero se mantiene fijo en altura, mientras que el ensanchamiento es causado por el crecimiento de las alas del pseudo-bulbo con forma de X/cacahuate.

Los perfiles Σ y ρ para el resto de las simulaciones muestra un comportamiento similar al de los discos orientados paralelos a $C_{\rm halo}$. Esto indica que la distribución general de densidad para discos en aislamiento (sin fusiones) en un contexto cosmológico no dependen altamente en la orientación inicial de $L_{\rm disk}$, con la excepcion de las estructuras de anillo encontradas en orientaciones con $\theta_{\rm ori}$ alto, que esparcen material de los radios externos fuera del plano del disco.

Velocity Dispersion σ_z and Disk Height $z_{1/2}$

La evolución de estas cantidades se muestra en la Figura 3 para el disco `3180` con $L_{\rm disk}$ orientado paralelo a $C_{\rm halo}$. Es claro que σ_z crece a todos radios para todas las simulaciones. Hay también una evidente diferencia en la evolución de las regiones internas y externas en el perfil σ_z. A radios internos σ_z crece pero mantiene una forma similar que se esparce a radios más grandes, mientras que a radios internos σ_z parece casi plano. La evolución de la altura del disco Figura 3, que es incialmente plana para todos los discos por construcción. Se puede ver que todos los discos tienen un comportamiento similar, caracterizado por el desarrollo de una figura triangular que crece en las partes internas del disco, y una pendiente positiva en las partes externas. Este triángulo refleja la evolución de un pseudo-bulbo con forma de X/cacahuate, dado que esta forma no está presente antes de que la inestabilidad de pandeo o *buckling* suceda.

Los perfiles para las galaxias con orientación paralela a $A_{\rm halo}$, presentan características similares a las de orientación menor, pero existe una diferencia visible en $z_{1/2}$ en las partes externas de los discos, que presentan un aumento tremendo en $z_{1/2}$ con respecto a los de orientación menor, esto está relacionado con el desacoplamiento de las estructuras de anillo que ocurren para todas las simulaciones con ángulo $\theta_{\rm ori}$ alto.

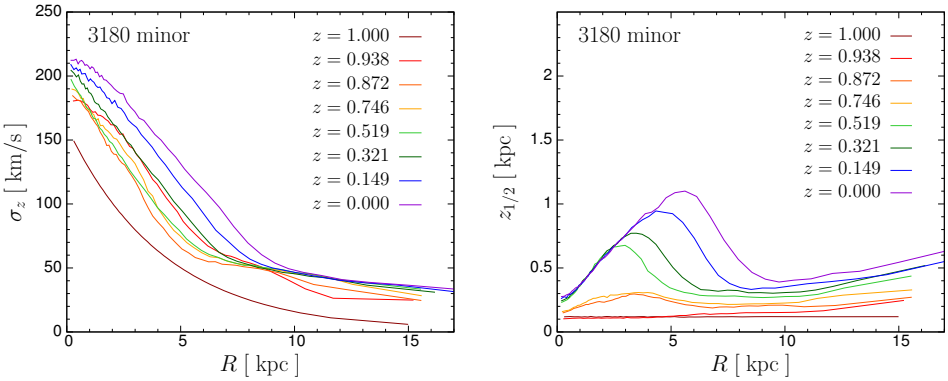

Figura 3: Dispersion de velocidades en la dirección z, σ_z (panel izquierdo), y la mediana de la coordenada z (panel derecho) del disco `3180` con $L_{\rm disk}$ orientado paralelo a $C_{\rm halo}$.

Calentamiento del Disco y Evolución de la Barra

En esta sección se muestra la evolución del calentamiento del disco ζ, fortaleza de la barra A_2 y su conexión con la evolución del patrón de velocidad de la barra $\Omega_{\rm bar}$. Los análisis presentados aquí son vitales para entender la evolución morfológica de las galaxias, así como las propiedades estructurales y cinemáticas presentadas arriba.

Calentamiento Vertical ζ

Para medir cuánto se calienta el disco a lo largo de la simulación, se calcula el parámetro del calentamiento vertical ζ. Esta cantidad se define como $\zeta = \sigma_z/\sigma_{z,0}$, donde σ_z es la dispersión total de velocidades a lo largo de la dirección z a un tiempo dado, y $\sigma_{z,0}$ es la dispersión inicial del disco a $z = 1$. La evolución del disco para los discos con $L_{\rm disk}$ orientado paralelo a $C_{\rm halo}$y $A_{\rm halo}$se muestra en la Figura 4.

Se ve que la evolución de ζ para todas las galaxias es similar. Todos ellos presentan uno o dos brincos pronunciados que son transiciones de un estado estable a otro. Las transiciones surgen porque durante su evolución los discos giran en estados "metaestables", que cuando se vuelven inestables se dispara cierto mecanismo que incrementa el calentamiento del disco para alcanzar un nuevo estado estable. Como se menciona anteriormente, este efecto parece aparecer por lo menos una vez en todos los discos estudiados en este trabajo. Como se verá después este mecanismo es la llamada inestabilidad de buckling de la barra, como también lo señalaron DeBuhr et al. (2012) y Yurin & Springel (2015).

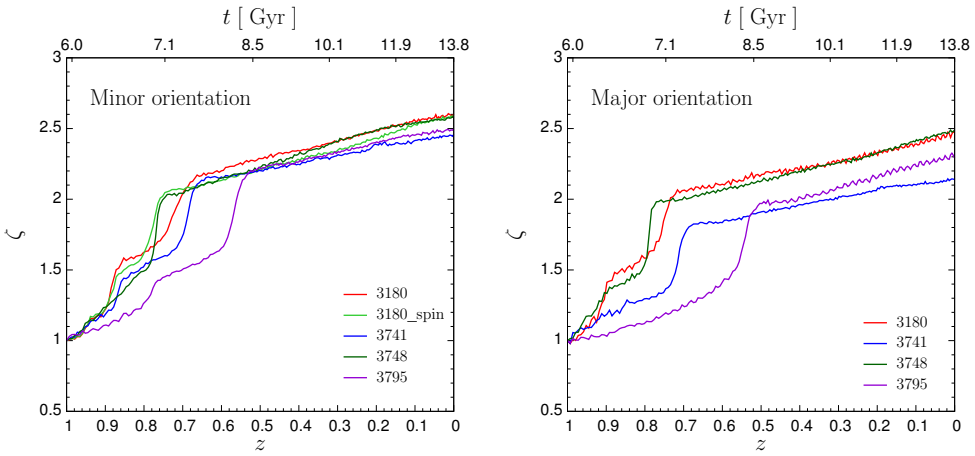

Figura 4: Evolución del calentamiento vertical ζ desde $z = 1$ a $z = 0$ para los discos con $L_{\rm disk}$ orientados paralelos a $C_{\rm halo}$(panel izquierdo) y $A_{\rm halo}$(panel derecho).

Fortaleza de la Barra A_2

La fortaleza de la barra se midió utilizando la amplitud del modo $m = 2$ de Fourier A_2. Un método similar al descrito por Yurin & Springel (2015) se utilizó en este trabajo. Se calculó la fortaleza de la barra utilizando 30 bins cilíndricos con número igual de partículas dentro de un radio de $2R_{\rm d}$, para calcular los coeficientes

$$a_2^{(b)} = \sum_{i \in b} m_i \cos(2\phi_i) \qquad b_2^{(b)} = \sum_{i \in b} m_i \sin(2\phi_i) \qquad c_2^{(b)} = \sqrt{a_2^2 + b_2^2} \tag{5}$$

donde m_i es la masa y ϕ es el ángulo azimutal de cada partícula, y la suma se lleva a cabo para todas las partículas dentro del bin b. La amplitud del modo $m = 2$ de Fourier es entonces calculada como

$$A_2 = \frac{\sum_b R_b c_2^{(b)}}{\sum_b' R_b' M_b'} \tag{6}$$

donde R_b es el radio de la partícula más externa del bin, M_b es la masa total del bin. Los resultados de las simulaciones con $L_{\rm disk}$ orientado paralelo a $C_{\rm halo}$ y $A_{\rm halo}$ se muestran en la Figura 5.

Se observa que todos los discos presentan una evolución similar de A_2, que se divide en dos fases principales: la primera caracterizada por oscilaciones rápidas de la amplitud A_2 y la segunda por un crecimiento oscilatorio con un crecimiento continuo hasta $z = 0$. Al final del tiempo de simulación todas las barras tienen amplitudes A_2 similares, que van de 0.4 a 0.5.

Grandes decrementos en A_2 están acoplados a los brincos en ζ, esto parece indicar que el desencadenamiento de los mecanismos de calentamiento están relacionados estrechamente a la fortaleza de la barra. Esto es evidente para el gran brinco en ζ que empata con el momento en que se desarrolla la inestabilidad de buckling y el decremento en A_2. Esto ha sido reportado previamente en la literatura (e.g. DeBuhr et al. 2012; Dubinski et al. 2009), además es observado también que el brinco pequeño en ζ, que es visible para algunos discos, está también asociada a la primer caída significante de A_2.

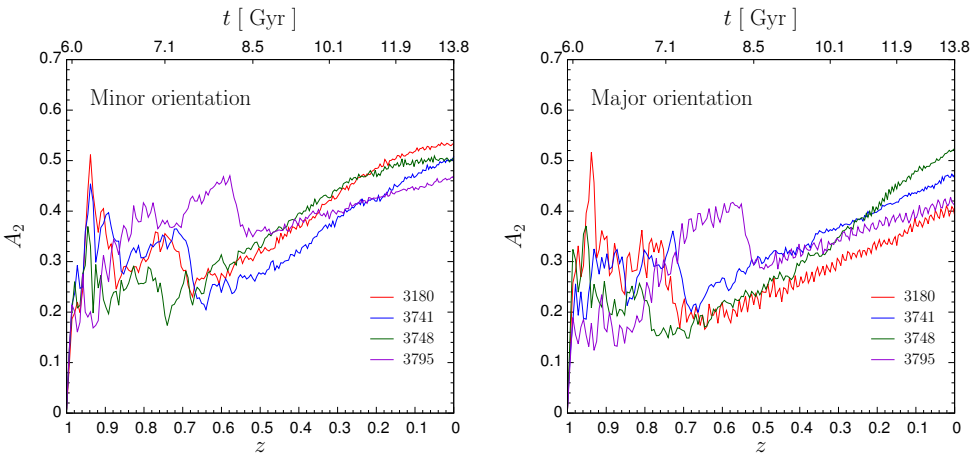

Figura 5: Evolución de la fortaleza de la barra, A_2, desde $z = 1$ a $z = 0$ de los discos con $L_{\rm disk}$ orientados paralelos a $C_{\rm halo}$ (panel izquierdo) y $A_{\rm halo}$ (panel derecho).

Resonancias y la inestabilidad de la Barra

Las órbitas estelares se dicen resonantes con una perturbación asimétrica cuando

$$\Omega_p = \Omega_\phi + \frac{l}{m}\Omega_R \tag{7}$$

donde l es un entero con signo, m un entero sin signo, Ω_p el patrón de velocidad de la perturbación, Ω_ϕ la frecuencia orbital, y Ω_R es la frecuencia radial alrededor del radio guía. donde $\Omega_{\rm R} = \kappa$ para la approximaciónfor the epicycle approximation (e.g. Binney & Tremaine 2008; Sellwood 2014).

En este trabajo estamos interesados en las regiones definidas por la Ecuación (7) cuando $l = -1$, conocida como la resonancia interna de Lindblad (ILR, por sus siglas en inglés). Estas regiones que están localizadas dentro de co-rotación, surgen debido a la frecuencia corrida por efecto Doppler a la cual un objeto encuentra la onda $m(\Omega_\phi - \Omega_{\rm p}) = \Omega_R$. Las resonancias con $2m$, también llamadas resonancias ultraharmónicas (UHR, por sus siglas en inglés), juegan un papel importante en la evolución de la barra y el calentamiento del disco.

Es importante hacer referencia al parámetro adimensional $\mathcal{R}$ definido por Elmegreen (1996) $\mathcal{R} = R_{\rm corot}/R_{\rm bar}$ donde $R_{\rm bar}$ es la longitud de la barra y $R_{\rm corot}$ corresponde al radio de co-rotación. Contopoulos (1980) demostró que las barras no pueden exceder el radio de co-rotación, por lo tanto la condición de $\mathcal{R} \geq 1$ se debe satisfacer para todas las barras. Este parámetro es útil ya que nos permite distinguir de una forma sencilla entre barras 'lentas' $\mathcal{R} > 1.4$ y barras 'rápidas' $1 \lesssim \mathcal{R} \lesssim 1.4$ (Rautiainen et al., 2005).

Las Figuras 6 a 8 muestran la evolución del disco y barra del modelo `3180_minor`. El panel superior de la Figura 6 muestra la evolución de ζ, A_2 y $\mathcal{R}$. Las seis regiones indicadas por las líneas verticales punteadas delimitan el antes, durante y después de los brincos en ζ. La primer región se caracteriza por un crecimiento leve en ζ, uno pronunciado en A_2 y un decremento en $\mathcal{R}$ por lo que indica una rápida evolución de una barra lenta a una rápida. Esto es consecuencia de la rápida respuesta del disco al momento en que este se vuelve vivo. Como se puede ver en $R \simeq 1$ la barra prácticamente toca co-rotación, esto sucede porque la barra rápida se encuentra por encima de la ILR por lo que no hay nada que prevenga que la barra alcance co-rotación.

La segunda fase se caracteriza por pequeño brinco en ζ, un decremento en A_2 y un incremento en $\mathcal{R}$, lo que significa que la barra se encoje y debilita al tiempo que la estructura vertical del disco cambia de un estado a otro. El patrón de la barra $\Omega_{\rm bar}$ toca el máximo de la ILR y termina alrededor de la resonancia ultraharmónica $\Omega - \kappa/8$ (UHR8). Se ve claramente cómo el brinco en ζ se observa en la estructura vertical del disco como una ligera corrugación visto de canto. La posición y velocidad promedio vertical, $\langle z \rangle$ y $\langle v_z \rangle$ respectivamente, revelan que el brinco en ζ y la asimetría morfológica son causados por lo que parecen ser modos de oscilación verticales en la región que corresponde a la barra. Estos modos presentan una alternancia entre los máximos y mínimos de $\langle v_z \rangle$ y $\langle z \rangle$, indicando la posibilidad de que las estrellas viajen de arriba a abajo en esta región a medida que orbitan el centro de la galaxia. Este comportamiento es similar al de un oscilador harmónico en el sentido que yendo del máximo al mínimo de $\langle z \rangle$, corresponde a velocidad máxima negativa $\langle v_z \rangle$, y que moviéndose del mínimo al máximo de $\langle z \rangle$, corresponde a un máximo en velocidad postivia. Es importante notar también que estos modos están delimitados dentro de la región entre la terminación de la barra y la ILR, sugiriendo que estos modos de oscilación surgen como un fenómeno del tipo cavidad resonante en el que las regiones de resonancias orbitales (ILR y UHR8 en este caso), actúan como puntos nodales, imponiendo la condición de frontera requerida para la amplificación de estas "ondas estacionarias".

Los seis modos se mantienen casi-estacionarios hasta que ζ empieza a asentarse en la tercer fase, durante la cual los modos empiezan a enrollarse en la dirección de rotación, pero siempre manteniendo la alternancia. A medida que el disco se estabiliza estos modos se mezclan y

desaparecen en una región de ζ prácticamente plano. Similar a la segunda fase, los modos están bien delimitados por la ILR y la terminación de la barra, fase durante la cual ésta tiende a coincidir con la región UHR8, como se ve en 6. Esto último se observa como un valor casi constante de $\mathcal{R}$.

La cuarta región corresponde al segundo salto en ζ, que como se menciona arriba corresponde a la llamada inestabilidad buckling. Se puede observar que durante este tiempo la fortaleza de la barra A_2 se reduce a medida que $\mathcal{R}$ crece, indicando un rápido encogimiento de la barra, que se observa en el cuarto panel inferior de la Figura 6 por el estado inicial y final de la barra (líneas punteadas y sólidas respectivamente). Este encogimiento es acompañado por un cruce de la región UHR4, similar al cruce de UHR8 observado durante el primer brinco en ζ. La Figura 8 muestra que la vista de canto de la galaxia presenta características que no son solamente asimétricas verticalmente vistas a través del eje intermedio del tensor del momento de inercia de la barra (vista xz, panel superior derecho de la Figura 8), pero también es asimétrico si se observa a través del eje mayor de la barra (vista yz, panel superior derecho de la Figura 8). Los picos verticales (estructura tipo cuerno) en la parte superior de la galaxia y las terminaciones de la región casi plana en la parte inferior del disco están bien trazadas por las regiones $\langle z \rangle$ diferentes de cero, que se ven como regiones azules y rojas en los paneles medio e inferior de la Figura 8, el color azul indica posición vertical $z > 0$ con respecto al plano del disco, mientras que el color rojo indica $z < 0$. De la misma forma que la Figura 7 las regiones diferentes de cero de $\langle z \rangle$ y $\langle v_z \rangle$ corresponden a modos de oscilación vertical dentro de la región delimitada por la ILR y la terminación de la barra cerca de UHR4. Estos modos se mantienen casi estacionarios durante el brinco y comienzan a enrendarse a medida que el disco busca un nuevo estado estable durante la quienta fase de la Figura 6.

Existen varias caracteristicas importantes durante la quinta fase, la cual empieza después del segundo brinco en ζ cuando la barra cruza abruptamente UHR4 y de forman los cuatro modos de oscilación. Después de la formación de estos modos los discos se asientan en una configuración estable en la que la barra termina en la UHR4. Similar a la tercer fase, ésta está caracterizada por un crecimiento moderado en ζ y A_2, y un $\mathcal{R}$ constante, mientras la barra sigue la UHR4 (Figura 6). En este tiempo los modos de oscilación desarrollados durante el brinco en ζ se reacomodan en una nueva configuración que se mantiene estable hasta el final de esta fase. De nuebo los modos de $\langle z \rangle$ y $\langle v_z \rangle$ se mantienen alternados y delimitados por la ILR y la terminación de la barra en UHR4. Estos modos no son tan pronunciados como los anteriores pero son los que duran más, desapareciendo solamente haste que la barra se separa de UHR4.

El panorama general de la evolución de los discos parece ser la siguiente: al momento en que el disco se vuelve vivo y responde a la presencia del halo de materia oscura que interactúa

con él, la componente del disco experimenta varios camnios en su morfología que incluyen el desarrollo de brazos espirales fuertes y una barra rápida, que puede llegar a co-rotación dado que el patrón de velocidad de la barra $\Omega_{\rm bar}$ se encuentra por encima de la ILR. A medida que el disco evoluciona, la ILR se levanta y trata de estabilizar la barra. Una vez que la barra es estable ésta experimenta una desaceleración gradual, ya sea por transferencia de momento angular o fricción dinámica con el halo (e.g. Athanassoula 2003; Dubinski et al. 2009; O'Neill & Dubinski 2003), haciendo que $\Omega_{\rm bar}$ disminuya constantemente durante su evolución. Esto juega un papel importante ya que es el único mecanismo que causa que la barra se mueva en el diagrama de frecuencias, por lo tanto es responsable de la interacción de la barra con las regiones resonantes.

Cuando $\Omega_{\rm bar}$ ha disminuido lo suficiente y la barra cruza la ILR, la terminación de la barra determina cómo evoluciona la región interna del disco. Después de rebotar en co-rotación, la terminación de la barra está localizada en una región donde las UHRs se acumulan, y a medida que $\Omega_{\rm bar}$ disminuye, la terminación de la barra empieza a acercarse a la region de UHR8 hasta que el cruce ocurre al mismo tiempo que la barra se contrae. Esto corresponde al primer brinco en ζ y el crecimiento de los seis modos verticales. Estos modos empiezan a enrollarse en la dirección de rotación y se borran a medida que el disco alcanza una nueva configuración estable con la barra terminando en UHR8. Durante este tiempo, la barra continúa desacelerando al mismo tiempo que su terminación se mantiene fija en UHR8, hasta que la desaceleración es suficiente para separar la barra de esta región.

Tan pronto la barra se acerca a UHR4, ésta se contrae a medida que cruza la región UHR4, lo que resulta en el crecimiento de cuatro modos de oscilación. Al igual que los seis modos, estos son capaces de crecer de forma estacionaria mientras que el disco alcanza su nueva configuración. Cuando esto sucede, estos modos se giran y, a diferencia de los seis modos, se redistribuyen en un nuevo arreglo que se mantiene mientras la barra termina en UHR4. La barra se establece en esta resonancia hasta el punto que no puede continuar siguiendo UHR4 debido a la desaceleración experimentada. Después de esto, se separa de esta región los cuatro modos se borran, al tiempo que la simulación llega a $z = 0$.

Refernte a los modos verticales, fenómenos oscilatorios similares a los mostrados en las Figuras 6 to 8 está presente en todos los discos estudiados en este trabajo. Esto indica que las características ocurren independientemente de la orientación inicial de $L_{\rm disk}$. Sin embargo, se requiere una mejor resolución espacial para explicar completamente la presencia de este fenómeno. Aunque estas oscilaciones verticales son el mecanismo responsable del calentamiento del disco, no es claro si este fenómeno actúa como un mecanismo estabilizador, que requiere un re-acomodo rápido las familias orbitales, o si ésta es la causa de la inestabilidad debido a las

condiciones impuestas.

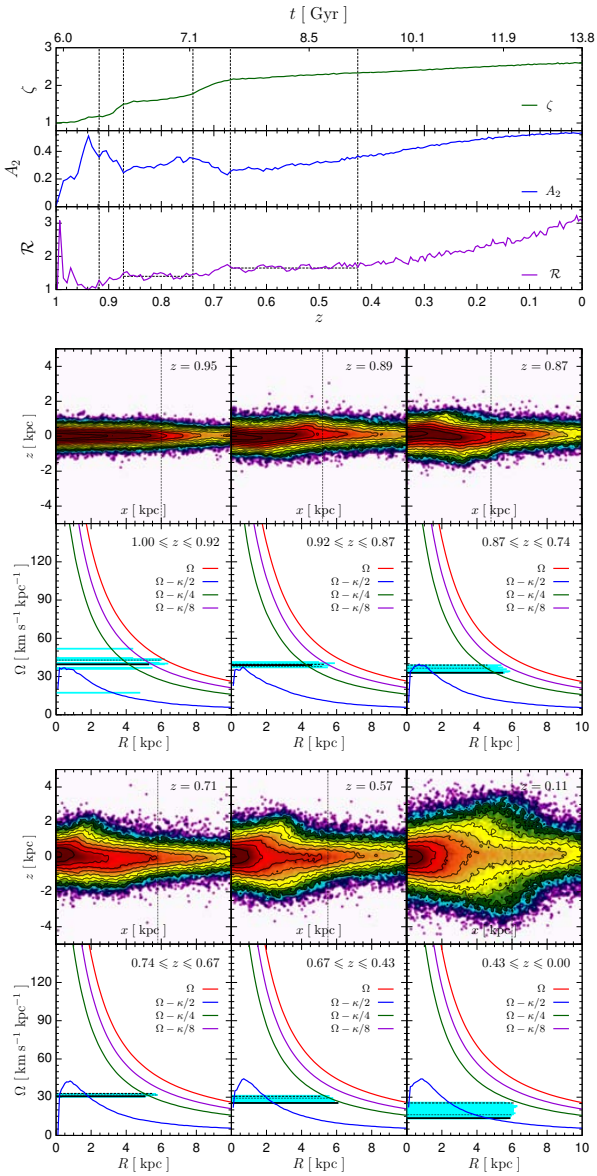

Figura 6: *Arriba.* Evolución del calentamiento vertical ζ, la fortaleza de la barra A_2, y el parámetro $\mathcal{R}$ del disco `3180_minor`. Las líneas verticales punteadas dividen las seis etapas evolutivas identificadas, mientras que las horizontales denotan un valor constante de $\mathcal{R}$. *Abajo* Comportamiento de CR, ILR, UHR4 y UHR8 junto con la evolución de la barra durante cada una de las fases definidas arriba. Las líneas horizontales corresponden a $R_{\rm bar}$ con $\Omega_{\rm bar}$; las líneas de guiones negras representan la barra al comienzo de la fase, las líneas azules durante, y las línea negra sólida al final de ésta. Cada gráfica está acompañada de una vista de canto del logaritmo de la densidad proyectada en un tiempo entre las divisiones, las gráficas tienen la misma escala horizontal y vertical. Las líneas punteadas horizontales y verticales muestran el tamaño de la barra identificado al mismo tiempo del disco mostrado.

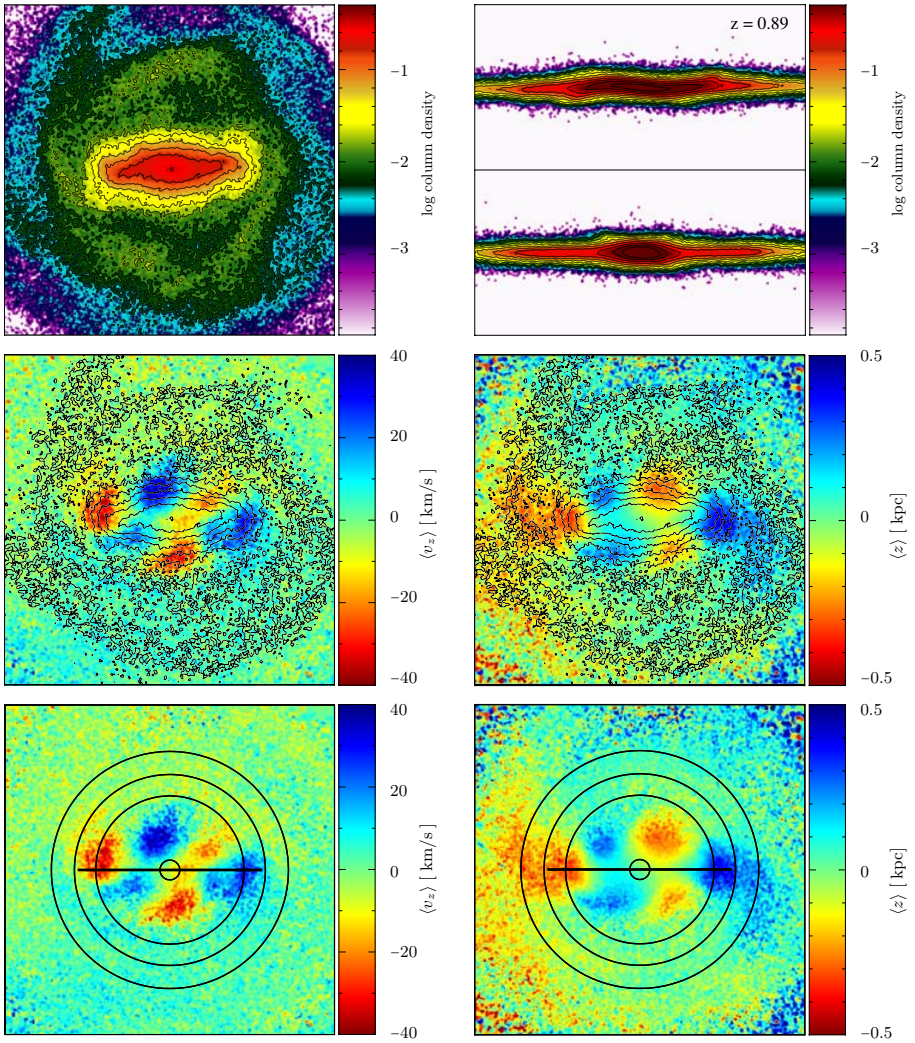

Figura 7: Disco `3180_minor` durante el primer brinco en ζ (segunda fase de la Figura 5.14). *Paneles superiores.* Gráficas de densidad del disco, panel superior izquierdo muestra la proyección xy y el panel superior derecho muestra la proyección xz (arriba) y yz (abajo); los colores muestran el logaritmo de la densidad columnar en unidades arbitarias. *Medio.* Velocidad vertical promedio (izquierda) y posición vertical promedio (derecha) del disco visto de cara, las lineas de contorno son las mismas que las mostradas en el panel superior izquierdo. *Paneles inferiores.* Igual que los páneles intermedios sin las líneas de contorno. Los círculos marcan las regiones de ILR (central), UHR4 (segundo), UHR8 (tercero) y CR (cuarto), la línea horizontal indica la longitud de la barra. Todas las proyecciones xy tienen 20 kpc en cada lado, las proyecciones xz y yz tuenen 10 kpc en la dirección z. Este snapshot corresponde al primer brinco en ζ, que coincide con el cruce de la barra de la UHR8. Se puede ver que el doblez/corrugación del disco se relaciona con el calentamiento vertical inducido por el crecimiento de los modos de oscilación (regiones azul-rojo de los paneles medios e inferiores), estos están delimitados entre la ILR y la UHR8 donde la barra termina. Las regiones con valor diferente de cero de $\langle v_z \rangle$ están alternadas con las regiones con $\langle z \rangle$ diferentes de cero, indicando una oscilación vertical en conjunto entre estos modos.

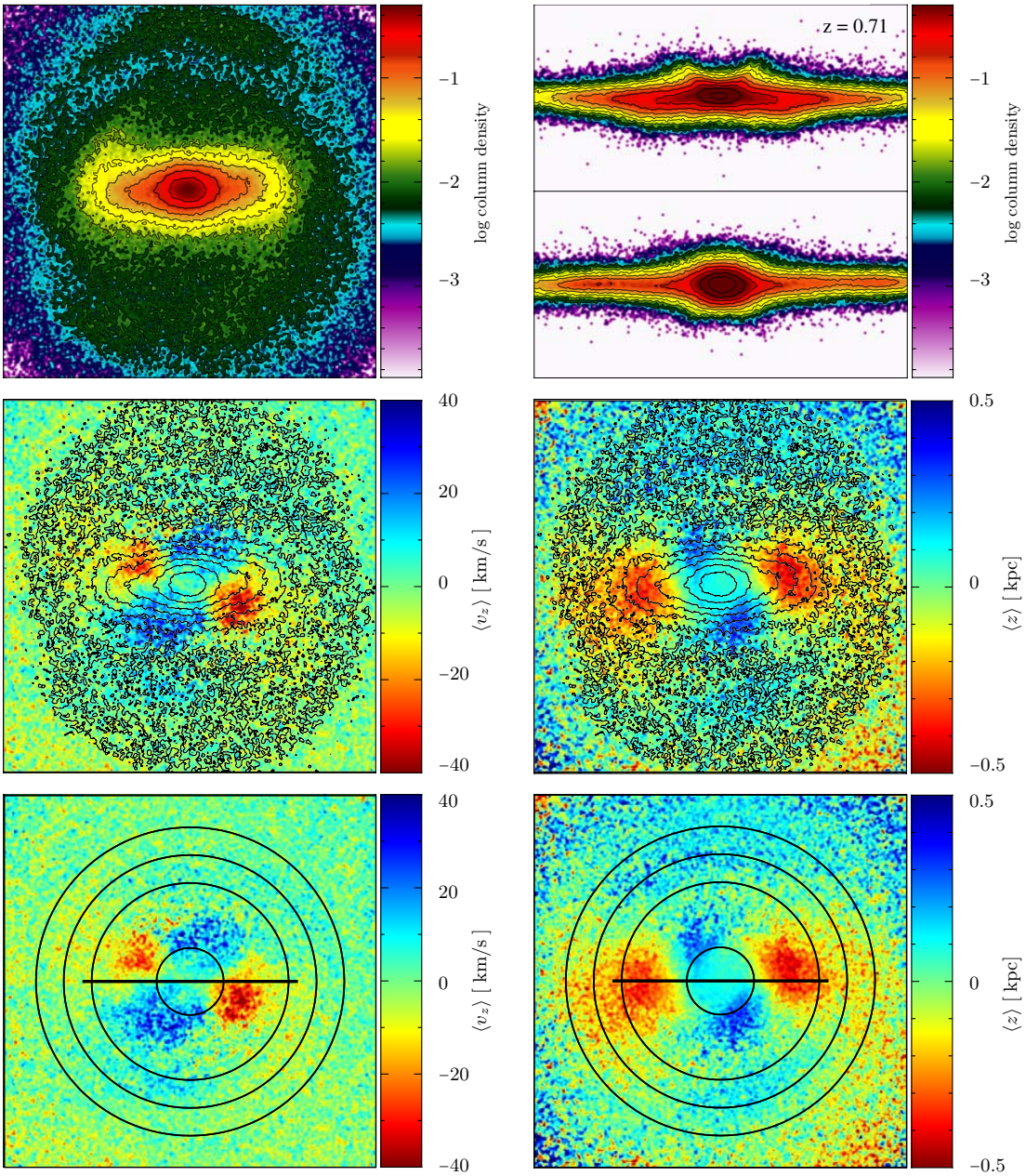

Figura 8: Igual que la Figura 7 pero durante el segundo brinco en ζ, i.e. durante la fase de la Figura 6. Esta fase corresponde a la barra cruzando la region UHR4. La vista de canto muestra en la parte superior del disco dos desplazamiento verticales prominentes, estructuras tipo "cuerno" (siempre formada en la misma dirección que $L_{\rm disk}$ para todos los discos), y dos picos débiles en la parte baja de los discos, estas características aparecen como regiones con valores distintos de cero en los páneles medios e inferiores. Como en la Figura 7, las regiones con $\langle v_z \rangle$ y $\langle z \rangle$ diferente de cero están alternadas. En este caso solamente cuatro modos se presentan y están ligados por la ILR y la barra terminada cerca de UHR4.

Inclinación del Disco y Estructuras tipo Anillo

En esta sección se presenta la evolución de la orientación de $L_{\rm disk}$ con respecto a la orientación original de los discos. Se ve que independientemente de su orientación inicial todos los discos experimentan cierto grado de inclinación, de forma tal que a mayor $\theta_{\rm ori}$ mayor es la inclinación esperada para el disco. Se muestra también como estructuras de anillo que no son coplanares con el disco son características exclusivas de los discos con ángulo $\theta_{\rm ori}$ grandes, que se puede explicar por la respuesta del halo durante el crecimiento del disco.

Reorientación de $L_{\rm disk}$

Al tiempo que el disco se vuelve vivo, su movimiento no está restringido a un plano dado, por lo que son libres de moverse en cualquier dirección durante su evolución, experimentando una inclinación debido a la interacción con su halo de materia oscura. Este fenómeno ha sido estudiado también por DeBuhr et al. (2012) and Yurin & Springel (2015), sin embargo, a pesar de usar los mismos halos de materia oscura en amnbos trabajos, los resultados presentados ahí no concuerdan.

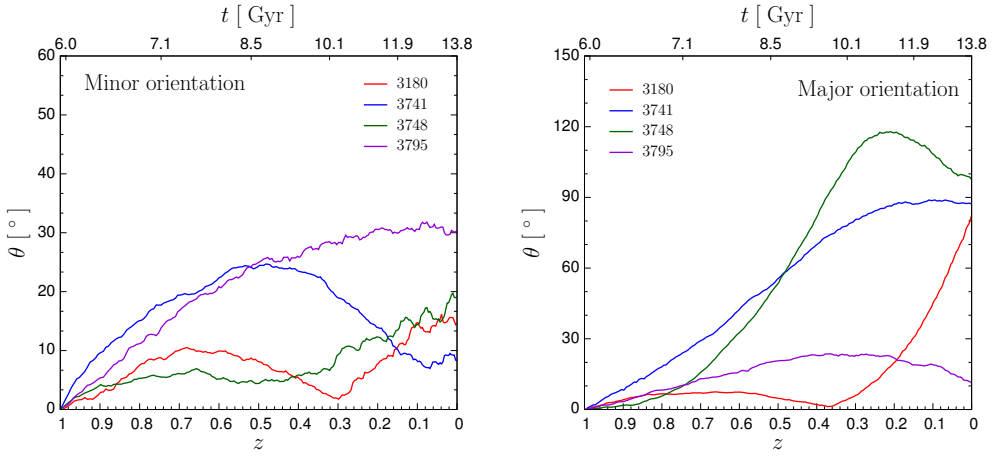

Figura 9: Evolution the angular momentum orientation of the inner 7 kpc with respect to the initial orientation from $z = 1$ to $z = 0$ of minor-oriented (top-left), major-oriented (top-right), 3180 (bottom-left) and 3795 (bottom-right) disks.

La inclinación del disco se calcula midiendo el ángulo θ entre el momento angular de las partículas dentro de una esfera de 7 kpc y la orientación inicial de $L_{\rm disk}$. La evolución de θ para todos los discos se presenta en la Figura 9. Los discos orientados a lo largo del eje menor presentan un menor grado de inclinación, con valores de θ entre 8° y 30° a $z = 0$. Los discos orientados inicialmente paralelos al eje mayor presentan los ángulos θ más grandes de

todas las simulaciones, con valores de θ entre 82° y 95° a excepción de 3795 que se desvía del comportamiento del grupo y solamente termina con un ángulo de 11°.

A pesar de las tendencias mostradas por todos los discos, su reorientación no se explica fácilmente pues no depende solamente de los discos, sino también del halo anfitrión que juega un papel crucial. Varios estudios dan una idea en la alineación entre el disco y el halo. Bailin & Steinmetz (2005) y Hayashi et al. (2007) mostraron que el spin del halo de materia oscura tiende a alinearse con su eje menor del momento de inercia en las regiones internas, y Zhang et al. (2015) afirma que el material del disco sigue al momento angular del halo en estas regiones. Estos resultados indican que los discos tienden a alinearse con el eje menor de los halos, que es la razón que se observe una mejor estabilidad que en otras orientaciones. Es importante tener en mente que el halo no responde como un todo a la presencia del disco, y que solamente las regiones internas son afectadas por la galaxia, como mostró Bailin et al. (2005).

Estructuras Anulares en Orientaciones con $\theta_{\rm ori}$ grande

Para todos los discos con un ángulo $\theta_{\rm ori}$ grande, se forman estructuras anulares del material de los radios más externos, indicando que estas estructuras pueden surgir debido que éstas están menos ligadas gravitacionalmente que el resto del disco.

Para entender el origen y evolución de estas estructuras junto con la inclinación del disco, se necesita también un análisis detallado del halo, el cual está más allá del alcance de este trabajo. No obstante, se realiza una descripción cuantiativa de la evolución de estas estructuras para el disco 3748 con $L_{\rm disk}$ orientado paralelo a $A_{\rm halo}$. Se mencionó arriba que DeBuhr et al. (2012) caracterizó estas estructuras con el ángulo θ_{warp} solamente a tres tiempos distintos de su simulación, pero este enfoque puede no dar un panorama claro de la evolución debido al alto grado de reorientación independiente experimentada por el disco y los anillos. En este trabajo estos objetos se caracterizan con tres ángulos distintos, que son calculados utilizando el momento angular del material del disco utilizando bins esféricos.

El ángulo α, que es equivalente a θ_{warp}, se mide como el ángulo entre el momento angular contenido en un bin, y el momento angular L del bin más interno a un tiempo dado; β es el ángulo entre L de un bin a un redshift z dado, y el L del mismo bin pero a $z = 1.0$, que es el equivalente a θ (Figura 9) pero medido para cada bin radial; y γ es el ángulo de L de un bin a un redshift z, y el eje menor del tensor del momento de inercia de una esfera (no caparazón) con el mismo radio que el bin. Los resultados para el disco 3748 se muestran en la Figura 10.

De los ángulos α y β de la Figura 10, se puede ver que la reorientación en conjunto es la misma para los ∼12 kpc más internos del disco. El ángulo α muestra esta característica es un ángulo prácticamente constante cerca de cero. Es claro que la estructura anular surge

de las partes externas del disco, α muesta que los radios más externos son los que se separan primero y los que alcanzan la desviación más grande del resto del disco, que se explica debido al hecho que éstos son los menos ligados. Después de alcanzar un valor máximo de a $z \sim 0.2$, α muestra un decremento que indicaría que el ángulo entre el momento angular del disco y el anillo disminuye, sin embargo esto no es del todo cierto, debido a la presencia del segundo disco. Es visto claramente que el anillo principal está rotando prácticamente en la dirección opuesta del disco, y también a la rotación del segundo disco, entonces un decremento en α surge debido a la naturaleza vectorial de L, y no solamente de la reorientación del disco. Esto demuestra que la descripción utilizando solamente un ángulo, como hecho por DeBuhr et al. (2012), es una aproximación útil pero no es completamente correcto, más bien se necesita un análisis más elaborado (e.g. analizar los dos anillos por separado).

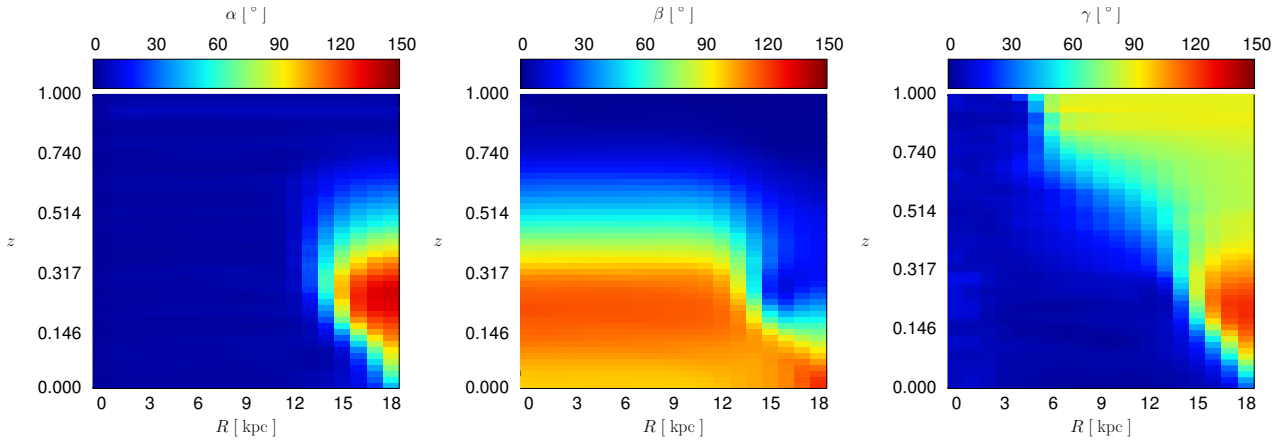

Figura 10: Gráficas de superficie de color de la evolución de los ángulos α, β, y γ del disco `3748_major` como función del radio R y redshift z.

El ángulo γ muestra que los radios más internos $R \leq 4$ está alineada con el eje menor del halo, después una transición marcada a $\gamma \simeq 90°$ en la que el disco se alinea con el eje intermedio del halo. Como se menciona arriba, esto puede ser la causa de la separación entre las regiones internas y externas. La evolución de γ entonces muestra que las regiones del disco están inicialmente no alineada con el eje menor del halo (i.e. $R \gtrsim 4$ kpc) experimenta un decremento en γ durante la evolución del disco, a medida que se reorienta, pero mantiene las partes más internas alineadas con su respectivo eje menor. Esto indica que el disco y el halo interno están acoplados y se mueven (reorientan) como un todo tratando de alinear el disco con los ejes menores de los radios externos. Ese panorama es consistente con el alto número de vueltas que el halo interno experimenta, como encontró Bett & Frenk (2012). Con respecto a los radios externos, el mismo comportamiento de α se ven en γ de $z \sim 0.4$ to $z = 0$, sugiriendo que el anillo o anillos parecen no seguir el eje menor del halo.

Discusión

Implicaciones del Método

Enfoque N-cuerpos para la Formación de Galaxias

La formación y evolución de galaxias de disco se debe estudiar en principio utilizando simulaciones hidrodinámicas que incluyan física de bariones (e.g. Kim et al. 2014a; Marinacci et al. 2014; Scannapieco et al. 2012; Vogelsberger et al. 2014b). No obstante, aún existe desacuerdo entre simulaciones de estado del arte (e.g. Scannapieco et al. 2012) con respecto al modelaje hidrodinámico, i.e. retroalimentación, formación estelar, etc., por lo tanto la capacidad de cada código y su implementación de la física *subgrid* para producir galaxias cuyas propiedades concuerden con las observadas. Sin embargo, se han realizado varias mejoras recientemente tanto en simulaciones tipo *zoom-in* (Marinacci et al., 2014), y simulaciones cosmológicas hidrodinámicas de caja completa (Vogelsberger et al., 2014b).

El método implementado en este trabajo provee un enfoque complementario a la formación de galaxias utilizando solamente la técnica de N-cuerpos, por lo tanto los resultados obtenidos aquó pueden ser comparados hasta cierto punto a las simulaciones de formación de galaxias y observaciones. A pesar de que un entendimiento completo de la formación y evolución de galaxias, y los procesos involucrados en ellas requieren simulaciones como las mencionadas arriba, aún existen preguntas abiertas que pueden ser abordadas utilizando simulaciones de N-cuerpos. Adicionalmente el espacio de parámetros den simulaciones de formación de galaxias es enorme, y diferentes tratamientos de retroalimentación y formación estelar afectan mucho los restultados de las simulaciones, incluso si se utiliza el mismso tratamiento pero diferente código (Scannapieco et al., 2012), he ahí la dificultad de separar los efectos de dichos parámetros. Por otro lado, el enfoque de N-cuerpos permite estudiar los efectos generados puramente por la interacción gravitacional, por lo tanto si un efecto similar se observa en ambos tipos de simulaciones, éste se puede atribuit a la interacción gravitacional y no a ningún modelo de física *subgrid*. Sin embargo, se debe tener cuidado para evitar efectos no deseados, como lo pueden ser relajación de dos cuerpos (Sellwood, 2013).

Implicaciones Astronónicas

Modelo ΛCDM y Ambiente Cosmológico

Como se describe arriba, este estudio adopta el modelo cosmológico ΛCDM con parámetros en concordancia con las restricciones de Wmap-9. A pesar de que el modelo ΛCDM se ha considero en años recientes como el modelo cosmológico estándar, y las restricciones impuestas

por *Planck* (Planck Collaboration et al., 2014) y WMAP-9 (Hinshaw et al., 2013) a partir de mediciones de la CMB indican una marcada preferencia para este modelo, aún existen problemas abiertos que incluso incluyendo la física de la componente bariónica no pueden ser contestados aún (ver e.g. Weinberg et al. (2013)), como lo son el problema de núcleo-cúspide de los halos de materia oscura, donde simulaciones tipo *zoom-in* de algunos grupos no muestran evidencia de núcleos (Marinacci et al., 2014) mientras que otras sí (Mollitor et al., 2015). Una vez dicho esto, un estudio de la evolución de discos estelares en un contexto cosmológico distinto como lo es WDM (e.g. Colín et al. 2000), SIDM (e.g. Fry et al. 2015), o γCDM y νCDM (e.g. Schewtschenko et al. 2015) podrían, en principio, proveer un diferente ambiente para los halos seleccionados y por lo tanto los discos simulados.

Modos Verticales y la Inestabilidad Buckling

El hecho que la terminación de la barra trate de mantenerse fija alrededor de las regiones UHR, sugiere que las UHRs actúan como atractores de estados estables de la barra. Esto se soporta por el hecho de que durante estas fases el calentamiento vertical ζ es casi constante, y que la contracción súbita de la barra, durante el brinco en ζ, parece indicar que la barra trata de alcanzar estas configuraciones en un proceso de "relajación violenta". Esto sugiere que el patrón de velocidad de la barra $\Omega_{\rm bar}$ disminuye, independientemente del mecanismo responsable, y la termiación de la barra se acerca a regiones de resonancia, las UHRs jalan la barra hacia ellas (causando la contracción, el brinco en ζ y los modos), de tal forma que la terminación de la barra se mantiene fija en estas regiones. Esto último puede ser la razón de las fases estables, que llegan después de los brincos en ζ, parecen presentar una oscilación amortiguada en $\mathcal{R}$ al rededor de un valor constante durante este tiempo. Las fases posteriores surgen entonces como consecuencia del aparente forzejeo entre la inevitable desaceleración de la barra y su tendencia a terminar en regiones resonantes.

Este panorama general es soportado por estudios previos como el de Elmegreen (1996), quien usando evidencia observacional, sugiere que las resonancias orbitas en la región cerca de corrotación, donde orbitas $2m$ se juntan, son responsables de la locación de la terminación de la barra. Resultados similares son encontrados numéricamente por Patsis et al. (1997), cuyo análisis orbital de NGC 4314 predice que las órbitas periódicas estables más largas se encuentran en la resonancia 4:1, que también es reportada en simulaciones de formación de galaxias por Okamoto et al. (2015). Esto indica, coomo lo sugirió Elmegreen (1996), que las barras tienden a terminar en resonancias ultraharmónicas $2m$.

Yurin & Springel (2015) y DeBuhr et al. (2012) atribuyen el brinco en ζ al fenómeno de la inestabilidad de buckling y no presentan mayor análisis. El acortamiento de la barra durante

el segundo brinco en ζ, corresponde a dicha inestabilidad, que es consistente con resultados presentados por Martinez-Valpuesta & Shlosman (2004) y Martinez-Valpuesta et al. (2006). Se muestra que la inestabilidad de buckling surge debido a la presencia de modos de oscilación en patrones tipo onda estacionaria, que se ven como regiones con valores diferentes de cero en $\langle z \rangle$ y $\langle v_z \rangle$en el disco. Comportamiento similar en $\langle z \rangle$ durante la inestabilidad ha sido también mostrado por Debattista et al. (2006) en simulaciones con halos rígidos. Aunque estas regiones en $\langle z \rangle$ coinciden más o menos con la locación de los cuatro modos vistos en este trabajo, no se discuten fenómenos tipo oscilaciones en dicho trabajo.

Galaxias de Anillo Polar

Es razonable asociar las estructuras exteriores de los discos orientados a lo largo del eje mayor y con $\theta_{\rm ori}$= 60, con las mostradas por las Galaxias de Anillo Polar (PRG, por sus siglas en inglés) debido a la semejanza mostrada por los anillos en las simulaciones, como se muestra en la Figura 11. A pesar de que el propósito de este trabajo no se enfoca en reproducir las PRGs, existen algunas características en común entre nuestras galaxias simuladas y las PRGs observadas que nos sugieren pensar en una posible conexión entre estas dos.

El caso de NGC 660 es de interés debido a varios aspectos: (1) el disco que rota lentamente mencionado arriba; (2) los estudios observacionales de van Driel et al. (1995) de NGC 660 determinaron que el anillo sigue un perfil de luminosidad exponencial, que por construcción es esperado en nuestras simulaciones; y (3) que el disco tiene un pseudo-bulbo con forma de X/cacahuate. Otras similitudes surgen de observaciones de Moiseev (2014), quien identificó un alabeo en la parte externa del disco correspondiente a la distribución de HI, y una superposición del material de la galaxia central y el anillo, que es interpretada como la intersección de órbitas de los componentes con diferentes espines que se pueden observar en el campo de velocidad de la galaxia. Estas características pueden ser asociadas al material difuso causado por la precesión del anillo con el material dejado cuando en el anillo se separa del resto de la galaxia.

Sin embargo, también hay diferencias importantes entre NGC 660 y los discos simulados. Por ejemplo, van Driel et al. (1995) estiman un diámetro de $\sim$ 11 kpc para el disco y 31 kpc para el anillo, mientras que en nuestras simulaciones la diferencia en los diámetros es mucho menos debido al mecanismo de formación. Adicionalmente ellos calculan que la masa del anillo es como el 75% de la masa del disco, proporción que es mucho mayor que la nuestra ($< 10\%$). La diferencia en masas y diámetros puede surgir debido a varios factores, como lo son la aproximación utilizada aquí, la ausencia de gas y su física en nuestras simulaciones, o que de hecho NGC 660 no se formó por un proceso similar al descrito aquí.

La conexión observada entre las PRGs y las estructuras encontradas en este trabajo no pu-

den ir más allá de una simple comparación debido a las características de este estudio y muchos aspectos se deben de tomar en cuenta. Primero que nada, este estudio analiza simulaciones de N-cuerpos sin gas ni su física, lo que es extremadamente importante para poder comparar la formación estelar con la observada en las PRGs. Segundo, no es claro qué tan viable es el escenario donde el gas acretado por el halo se da una configuración similar a la de nuestros discos orientados paralelos al eje mayor en un contexto cosmológico, y si la descripción puede considerar la fracción de las PRGs observadas. Finalmente, se necesita una mejor resolución espacial y en masa tanto del halo como del disco para resolver adecuadamente todos los componentes de la galaxia para poder comparar con las PRGs observadas. Sin embargo, existe la posibilidad de un escenario de formación de PRGs sea similar al observado en las simulaciones pueda representar un model viable, pero se necesitan estudios más detallados. Es importante mencionar que la muestra disponible de PRGs es baja, escencialmente el Catálogo de Galaxias de Anillo Polar por Whitmore et al. (1990), y recientemente, se ha renovado el esfuerzo para tener un catálogo aún más grande de estos sistemas galácticos utilizando el SDSS (ver Moiseev et al. 2011).

Figura 11: Comparación morfológica entre el disco 3795 mayor y NGC 660. Crédito de imagen: Immo Gerber and Dietnar Hager, Observatorio TAO.

Comentarios Finales

Se presentó un estudio de la dinámica y evolución de discos estelares en un contexto cosmológico. Utilizando una versión modificada de la versión pública del código GADGET-2, se simuló el crecimiento de una galaxia de disco a través de un aumento gradual de un disco exponencial dentro de un halo de materia oscura cosmológico de alta resolución. Estos halos se seleccionaron imponiendo restricciones en su masa, historia de acreción y un ambiente aisaldo. Se corrieron un total de trece simulaciones siguiendo la evolución de cuatro discos, uno para

cada halo seleccionado, para los cuales se consideraron varias orientaciones de su momento angular. Los modelos estudiados incluyen el disco con su momento angular $L_{\rm disk}$ orientado paralelo tanto al eje menor y mayor del tensor de momento de inercia del halo, con $L_{\rm disk}$ describiendo un ángulo $\theta_{\rm ori}$ con respecto al eje menor, y discos con estas orientaciones pero rotando en dirección opuesta, los modelos `spin`.

A tiempos tempranos, todos los discos desarrollan brazos espirales, con una considerable preferencia de las orientaciones menor y mayor de desarrolar brazos espirales de gran diseño. Orientaciones intermedias de $\theta_{\rm ori}$ muestran una transición de gran diseño hacia espirales floculantes a medida que $\theta_{\rm ori}$ incrementa. Al final del tiempo de simulación, la morfología de cara de los discos muestra una barra prominente, un anillo alrededor de la barra, y estructuras débiles en las partes externas del disco.

La estructura de canto de todos los discos exhibe características comunes, como lo son una corrugación del disco y un pseudo-bulbo con forma de X/cacahuate. La diferencia más notable se observa en discos con un $\theta_{\rm ori}$ grande, que muestran una estructura de anillo que se separa del resto del disco. No se encontraron diferencias notables entre los discos `spin` y `no-spin`.

La densidad superficial ,Σ, y vertical ,ρ, es también similar para todos los discos. La evolución de la densidad superficial Σ muestra una ligera desviación del perfil exponencial inicial. La densidad vertical ρ muestra un ensanchamiento del perfil debido al calentamiento del disco; convergencia en las radios más internas como resultado de la formación de un núcleo tipo caja en el centro del disco; y un ensanchamiento fuerte en los radios medios debido al crecimiento del pseudo-bulbo con forma de X/cacahuate.

El perfil de la dispersión de velocidades en dirección z, σ_z, muestra un incremento gradual para todos los discos a todos radios, caracterizado por una pendiente pronunciada en la región interna $r \lesssim 2R_{\rm d}$, y una más plana en radios externos $r \gtrsim 2R_{\rm d}$. Un incremento notable en σ_z se observa debido a la presencia y crecimiento de la barra. La evolución de el pseudo-bulbo con forma de X/cacahuate se apreceia como una forma triangular en el perfil de la altura del disco, $z_{1/2}$. Se muestra que en las partes externas $z_{1/2}$ aumenta a medida que el ángulo $\theta_{\rm ori}$ incrementa debido a la presencia de alabeos que se vuelven más evidentes en orientaciones con $\theta_{\rm ori}$ más grandes. Un incremento aún más grande en $z_{1/2}$ se observa en orientaciones mayores y $\theta_{\rm ori}$= 60, resultado de la estructura de anillo que se desprende del disco en estos modelos.

Se muestra que las fases exhibidas por el calentamiento del disco, ζ, la fortaleza de la barra, A_2, y el parámetro $\mathcal{R}$, se explica por la interacción entre la barra y regiones de resonancia. Un brinco simultáneo en ζ, una caída en A_2, y un aumento en $\mathcal{R}$ es visto durante estas interacciones acompañadas por el crecimiento de modos verticales estacionarios. Se observa que estos modos se desarrollan cuando la terminación de la barra cruza regiones de resonancia, específicamente $\Omega -$

$\kappa/8$ (UHR8) y $\Omega - \kappa/4$ (UHR4). Estos modos son responsables de producir corrugaciones en el disco durante el cruce de UHR8, y la inestabilidad de buckling cuando el cruce de UHR4 ocurre. Los modelos también muestran una tendencia por que la barra termine en estas resonancias, así como exhibir una configuración aparentemente estable vista como un ligero incremento en ζ y un casi constante $\mathcal{R}$.

Todos los modelos experimentan re-orientación de su momento angular $L_{\rm disk}$ durante su evolución. Se esperan ángulos mayores para modelos con un ángulo $\theta_{\rm ori}$ grande, sin embargo, excepciones a la regla pueden existir. Independientemente de la evolución del ángulo θ, los discos paralelos al eje mayor y con $\theta_{\rm ori}$= 60 presentan estructuras de anillo que se separan del resto del disco. Como estas estructuras presentan larga duración, $\sim$ 6 Gyrs, y son similares a la morfología de las Galaxias de Anillo Polar (PRGs), es razonable considerar este mecanismo como posible escenario de formación de PRGs.

Para los modelos con orientación mayor, se observa una gran redistribución de la masa en las partes internas del halo como consecuencia del crecimiento del disco. A $z_{\rm live}$, $L_{\rm disk}$ de estos modelos se alinea paralelo al eje menor a radios internos, mientras que los radios externos sorprendentemente se alinean con el eje intermedio, siendo una posible explicación de la gran inclinación que se observa en estos discos. La evolución del ángulo entre el vector de momento angular de un bin cilíndrico y el vector de momento angular más interno, α, y el ángulo entre el momento angular del bin y el eje menor del halo medido a ese mismo radio, γ, muestran que $L_{\rm disk}$ trata de alinearse con el eje menor del halo a radios cada vez más grandes, manteniendo las regiones ya ajustadas alineadas. Esto sugiere que existe un acoplamiento fuerte entre la distribución de masa del halo interno y el momento angular del disco, en el que el eje menor se encuentra como orientación preferida.

No obstante, existen varias preguntas que quedan por ser abordadas. Un análisis más extenso de los resultados presentados aquí incluyen: una investigación de posibles mecanismos responsables de la envolvente triangular en $z_{1/2}$; un estudio profundo de las diferencias entre los modelos `spin` y `no-spin`, específicamente para examinar los efectos producidos por los subhalos que describen órbitas prógradas para un modelo y retrógadas para el otro; y una descripción más amplia de los modos de oscilación estacionarios a través de estudios del rol de las resonancias verticales $\Omega - \nu/m$. Trabajo futuro incluirá un análisis más profundo de la transferencia de momento angular entre el disco, la barra y el halo, análisis orbital, y análisis muy detallado en la evolución del momento angular y la redistribución de materia en los halos.

En conclusión,

- Las simulaciones de N-cuerpos son aún una herramienta útil para estudiar la dinámica de sistemas no colisionales, como lo son discos estelares dentro de halos cosmológicos. Sin em-

bargo, se necesitan simulaciones que incluyan gas y su física para obtener una descripción completa de la evolución de estos sistemas, lo que también daría mejor entendimiento de la posible conexión entre los resultados obtenidos aquó y las PRGs observadas, por ejemplo, NGC 660.

- La metodología implementada en este trabajo provee un endoque complementario a la formación de de galaxias y permite seguir la evolución de galaxias de disco. Este método puede extendido fácilmente para incluir componentes adicionales de la galaxia, e.g. un bulbo, para estudiar la evolución de discos en diferentes cosmologías, ambientes, etc.
- La inestabilidad de buckling de la barra, asó como corrugaciones en el disco, son producto de fenómenos tipo ondas estacionarias producidos por la interacción de la terminación de la barra con regiones de resonancia de la galaxia.
- Se confirma que el momento angular del disco se alinea preferentemente paralelo al eje mejor del halo. Se observa que los modelos orientados paralelos al eje mayor tienden a alinearse paralelos al eje menor a radios cada vez más grandes a medida que se inclina durante su evolución, lo que sugiere que existe un acoplamiento fuerte entre la distribución de masa entre la distribución de masa del halo interno y el momento angular del disco..
- Las estructuras de anillo mostradas por modelos paralelos al eje mayor y $\theta_{\rm ori}$= 60 se espera que sean producto de la desalineación entre el momento angular de radios externos del disco y el eje menor del momento de inercia del halo. Como estas estructuras se encuentran consistentemente en dichas orientaciones, y se observa que mantienen su estructura durante varios Gyrs, estas configuraciones se encuentran dentro de uno de los posibles escenarios de formación de PRGs.

Chapter 1

Introduction

The formation and evolution of galaxies is a topic that astronomers have been trying to understand for many years. Since the observations performed by William and Caroline Herschel, that placed our sun at the center of the Milky Way (Herschel, 1785), passing by the studies made by Shapley, that located the sun at two-thirds the size of the galaxy from its center, to the first 'simulation' of the interaction of galaxies by Holmberg (1941), these objects have been target of study among scientific community, and in general an endless source of fascination for mankind.

Galaxies are collections of (billions of) stars that are gravitationally bounded and supported by rotation in the case of disk galaxies, or by the 'pressure' of random motion of stars in the case of the elliptical or spheroidal galaxies. These objects present a wide range in mass and size, from dwarf galaxies with mass of $\sim 10^8 M_\odot$ and diameter of a few kpc (e.g Small and Large Magellanic Clouds), to masses of $\sim 10^{13}$ $M_\odot$ and diameters of tens of kpc of cD galaxies at the center of galaxy clusters (e.g. ESO 146-IG 005 within Abell 3827 cluster, Carrasco et al. 2010).

These objects display several forms that arise either by the secular evolution of the galaxy or by the interaction and/or merger with another one (see Fig. 1.1). The predominant shapes are spheroids and disks, which are commonly also known as early and late type galaxies respectively in the Hubble sequence. Disk galaxies show important features that have been target of interest and study for many years, the spiral arm structure (see e.g. M 51 in Fig. 1.1), that generally spans over the entire galaxy, and the bar structure that dominates the central part of it (e.g. Fig. 1.2). Bars are of particular importance because roughly 67% of all spiral galaxies present either strong or weak bars (Barazza et al., 2008; Eskridge et al., 2000), and given the fact that there is observational evidence that suggests the presence of a bar in the Milky Way (Weinberg, 1992).

Additionally, some disk galaxies display features and configurations that are not commonly

found in the whole population of galaxies, such as warps (see Fig. 1.3) and an off-plane components shown by Polar Ring Galaxies (hereafter PRGs, see Fig. 1.4). Studies of both of these features have generally tried to attribute these structures to the interaction of the main galaxy with an orbiting galaxy or subhalo (e.g. Kim et al. 2014b for warps and Bournaud & Combes 2003 for PRGs); however, it is of interest to explore the possibility that these configurations are a product solely of the secular evolution of the galaxy, which has been done in isolated simulation by Jeon et al. (2009), but has not been addressed in a cosmological context.

Despite that galaxies can be found in isolation, or as part of groups or clusters, they are typically separated from each other by distances of the order of Megaparsecs (Mpc), which is two to three orders of magnitude greater than their typical size. In addition, galaxies are not just randomnly distributed throughout the space, in fact, they are organized in a configuration that is known as the cosmic web (see Fig. 1.5), also known as large-scale sturcutre of the universe.

Although the distribution of galaxies and matter of the universe presents structure, it is in general uniformly distributed in space, in accordance to the cosmological principle, which states that the universe is in fact homogeneous and isotropic, i.e. rougly speaking, matter is distributed equally in all directions. It is important to note that the cosmological principle does not apply to all scales, specifically discrepancies are found at small scales, but as we study larger and larger volume elements of the universe, the cosmological principle becomes more exact. Nonetheless, structures have been found in the universe that may present a challenge to it, such as the Sloan Wall (SW, Geller & Huchra 1989), whose proper size at present epoch extends about ~ 240Mpc or the Sloan Great Wall (SGW) that extends over ~ 450Mpc (Gott et al., 2005); both structures are shown in Fig. 1.5. However, studies by Yadav et al. (2010) have set an upper limit of $\sim 260\,h^{-1}$Mpc $\simeq 370$ Mpc for inhomogeneities to exist, that in addition to the results presented by Park et al. (2012), using data from SDSS and the Horizon Run 2 (Kim et al., 2011), have concluded that the SGW is consistent with the cosmological principle.

The ΛCDM paradigm has been considered in recent years as the 'standard' cosmological model (see Section 2.1.4 for further details). This model has its basis on the cosmological principle and Einstein's theory of general relativity, in which the evolution of the universe is determined by the interaction of its different energy contributions, composed of $\sim 72\%$ of dark energy, that expands space pulling things apart, and $\sim 28\%$ of matter (Hinshaw et al., 2013), that tries to group them.

The expanding nature of the universe has been known since 1920's when Edwin Hubble (1929), using Cepheid period-luminosity relation discovered by Henrietta Leavitt (Leavitt &

Pickering, 1912), showed that the great majority of the galaxies were moving away from us. In fact, it is now well known that the universe is not in fact expanding away from us, but it does so in all directions. Moreover recent studies have showed that the universe is not only expanding, but it is doing so in an accelerated manner (Perlmutter et al., 1999; Riess et al., 1998).

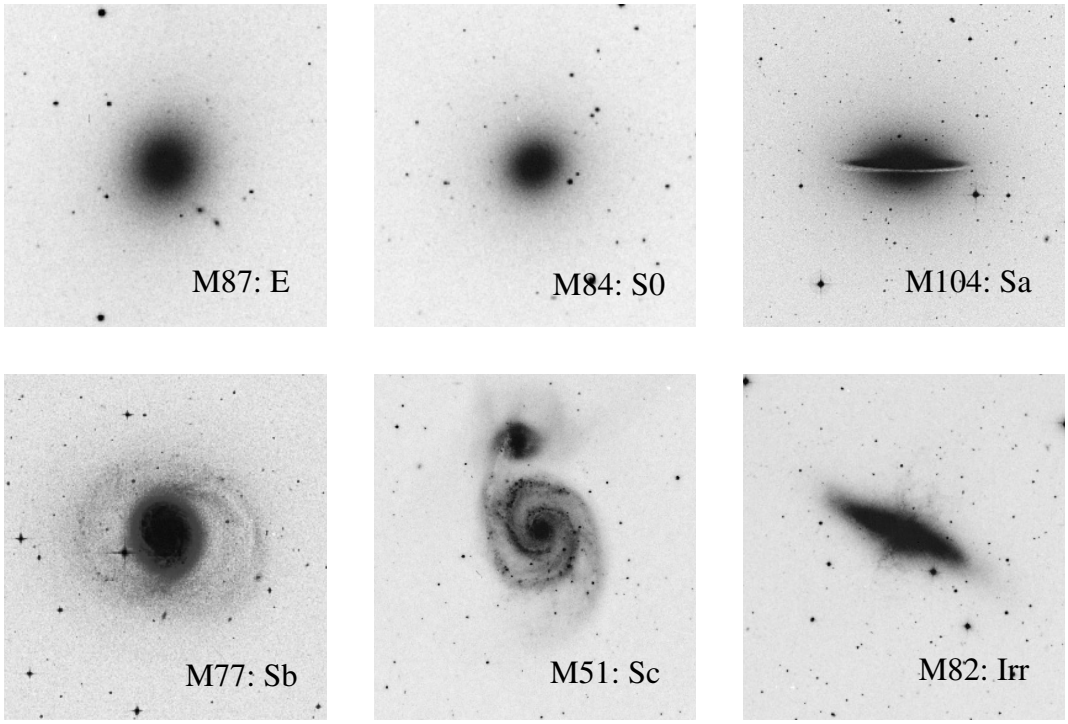

Figure 1.1: Snapshots of galaxies with different morphologies, ordered and labeled according the Hubble sequence. Image Credit Peacock (1999, p. 388)

Figure 1.2: Galaxy NGC 1300. A disk galaxy with a bar. Image credit NGC 1300: Hubble Heritage Team, ESA, NASA.

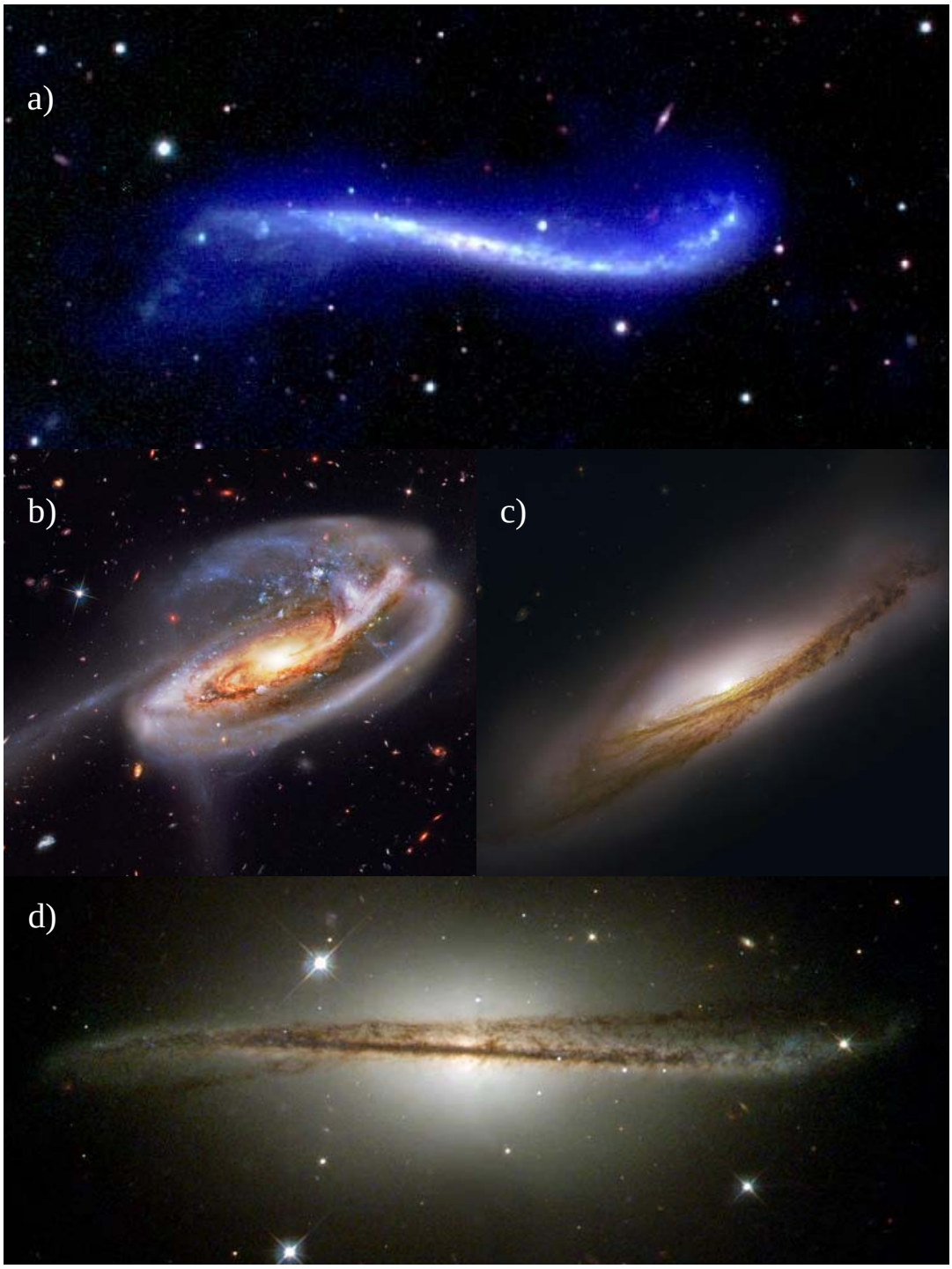

Figure 1.3: Examples of warped galaxies. a)UGC 3697, b) "Tadpole Galaxy" UGC 10214 c) NGC 3190 and d) ESO 510-13. Image credit UGC 3697: L. D. Matthews (CfA), J. M. Uson (NRAO). Image credit UGC 10214: NASA, H. Ford (JHU), G. Illingworth (UCSC/LO), M.Clampin (STScI), G. Hartig (STScI), the ACS Science Team, and ESA. Image credit NGC 3190: Data - Hubble Legacy Archive, ESA, NASA Processing - Robert Gendler. Image credit ESO 510-13: Hubble Heritage Team (STScI/AURA), C. Conselice (U. Wisconsin/STScI), NASA.

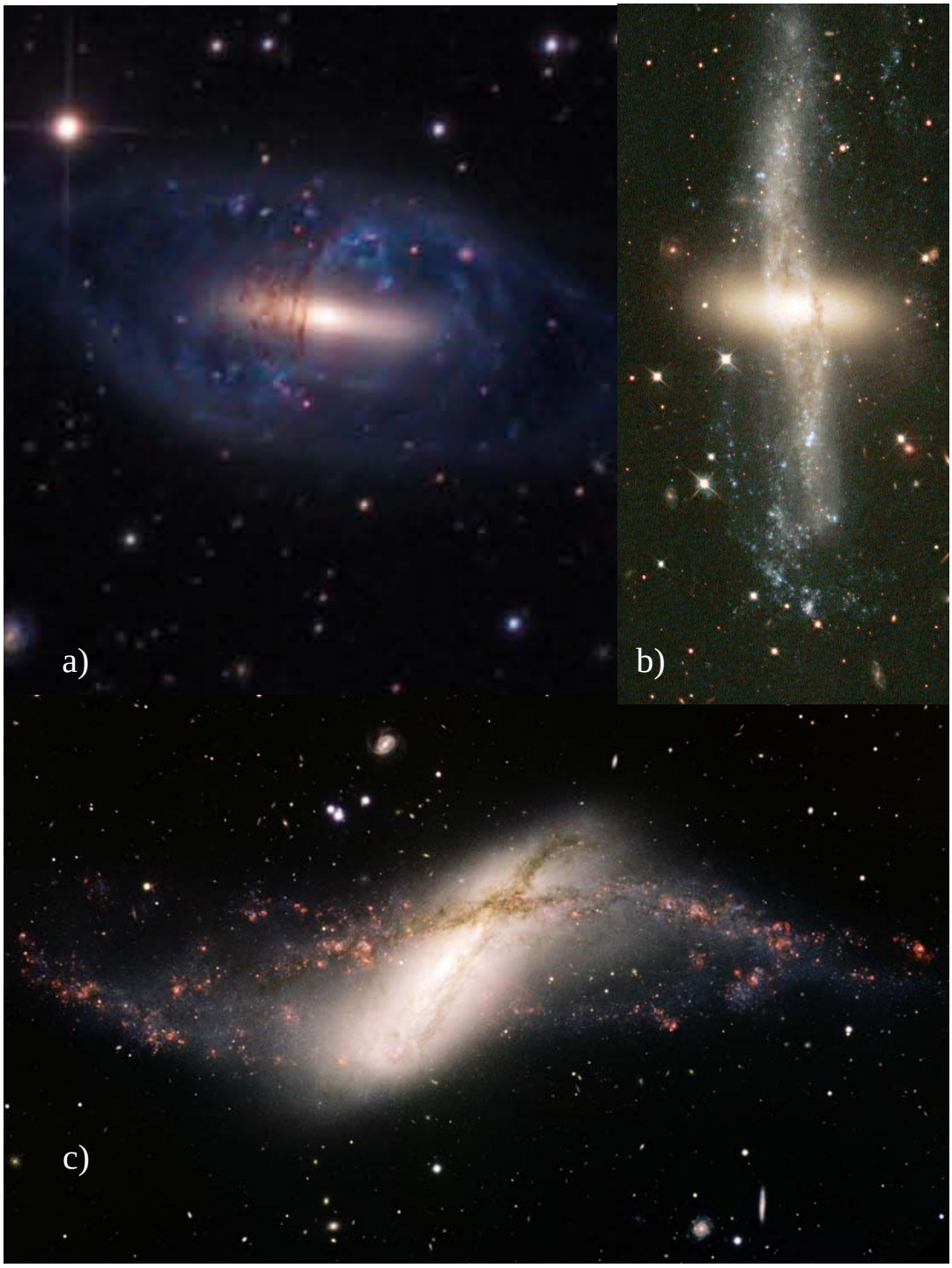

Figure 1.4: Examples of polar ring galaxies. a) NGC 2685 . b) NGC 4650 and c) NGC 660. Image credit & copyright NGC 2685: Ken Crawford. Image credit NGC 4650: J. Gallagher (UW-M) & the Hubble Heritage Team (AURA/ STScI/ NASA). Image credit NGC 660: Data - Gemini Observatory/AURA. Color composite - Travis Rector, University of Alaska Anchorage.

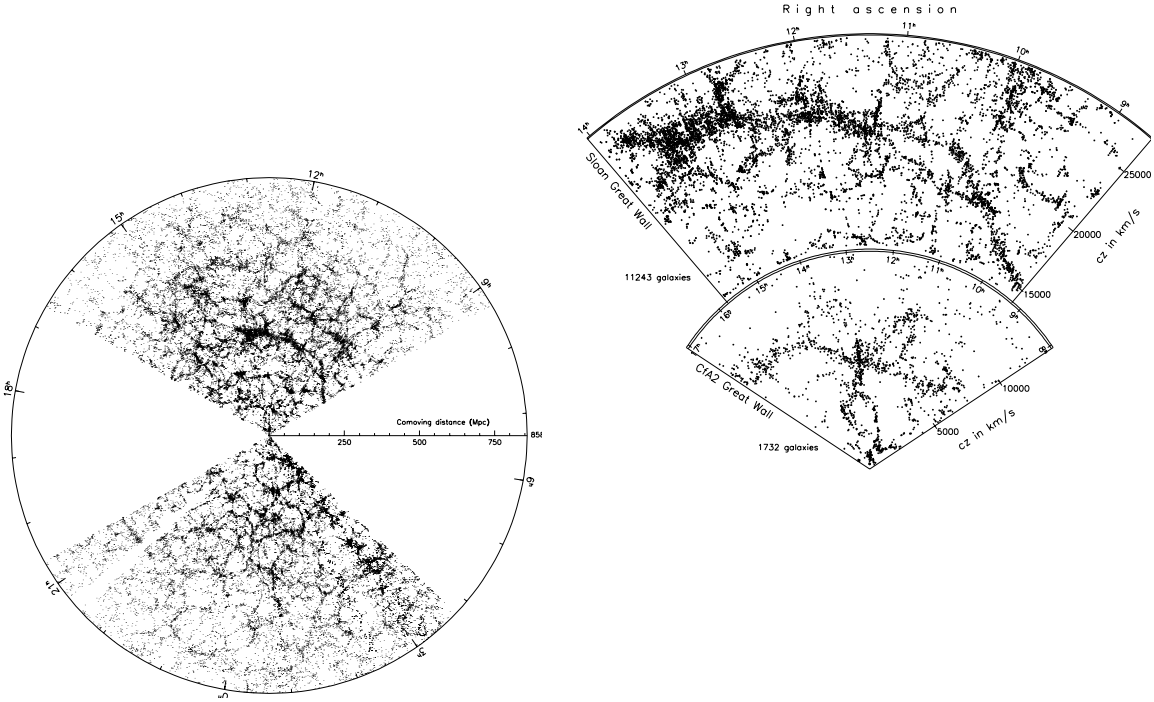

Figure 1.5: Galaxy map from the SDSS, showing the observable LSS of the universe. The points shown are individual galaxies from the main and bright red galaxy samples of the SDSS. Left panel shows the SW and the SGW. Imge taken from Gott et al. (2005)

Numerical simulations are one of the most important tools that helps us to understand the universe and the phenomena that occur in it. Problems like the hierarchical formation of large-scale structure of the universe and the formation and evolution of galaxies are treated mainly with N-body and hydrodynamic simulations (e.g. Boylan-Kolchin et al. 2009; Klypin et al. 2011; Vogelsberger et al. 2014a) due to the complexity and non-linear nature of these problems.

The dynamics of galaxies have been studied in isolated conditions over many years, in both secular evolution (e.g. Dubinski et al. 2009), and mergers of galaxies and satellites (e.g. Velazquez & White 1999). Recent zoom-in and high-resolution hydrodynamical cosmological simulations, which study the formation of galaxies (e.g. Marinacci et al. 2014; Scannapieco et al. 2012; Vogelsberger et al. 2014b), have also permitted us to study the evolution of galaxies in a cosmological context. The main difference between the isolated and cosmological approaches is how the galactic components are treated, as a rather idealized isolated system, or as a product of cosmic evolution.

Constraints imposed by *Planck* (Planck Collaboration et al., 2014) and WMAP-9 (Hinshaw et al., 2013) measurements of the Comic Microwave Background (CMB) indicate a remarkable preference for the ΛCDM cosmological model as standard model, although, there are still open

problems that even simulation that include baryon physics cannot answer yet (see e.g. Weinberg et al. 2013). Such problems include the cusp-core inner profile of dark matter halos, where zoom-in simulations of some groups do not show evidence of cores in halos (Marinacci et al., 2014) while others do (Mollitor et al., 2015).

Hydrodynamic simulations with its corresponding baryon physics should be the main tool to study the formation and evolution of galaxies. However, the parameter space in such simulations of galaxy formation is enormous, making that different treatments of feedback and star formation highly affect the outcome of simulations as has been recently shown in code-comparison studies such as the Aquila project (Scannapieco et al., 2012). This makes more difficult to separate the effects produced by each one of those parameters; on the other hand, the N-body approach permits us to study the effects arisen purely by gravitational interaction, hence still being a very useful tool.

This Work

This work presents a study of the evolution of galactic stellar disks embedded in Milky Way-mass like dark matter halos obtained from cosmological simulations. These halos were selected to had had a 'quiet' accretion history since $z = 1$ and fulfill an isolation criterion. Zoom-in simulations of these halos were performed, and a stellar disk is introduced to study the dynamics and non-axisymmetric properties of these disks.

Similar work has previously been done by DeBuhr et al. (2012), Athanassoula et al. (2013) and Yurin & Springel (2015). However, these works either do not use cosmological dark matter halos and/or Milky Way-like galaxies (Athanassoula et al., 2013), or the treatment they use is unclear and might introduce undesired effects that may affect the dynamics of the system (DeBuhr et al., 2012).

This work is organized as follows. In Chapter 2 are presented fundamental concepts of Cosmology. In Chapter 3 a brief review of the codes used in this work is presented. In Chapter 4 it is presented the methodology implemented to set the initial conditions for the simulations of stellar disks. The results of the evolution of these disks are presented in Chapter 5. Finally, a discussion of the method and results is given in Chapter 6, and conclusions and future work are presented in 7.

Chapter 2

Fundamental Concepts

In this chapter, fundamental concepts of Cosmology, that are relevant to the problem considered in this work are explained. A brief summary of concepts and equations that describe the behavior and dynamics of ΛCDM cosmology are presented.

2.1 Cosmology

In order to understand the cosmological context in which disk galaxies are studied here, in this Section are explained fundamental concepts, equations and approximations that describe the ΛCDM model. First the Friedmann equations are introduced to describe ΛCDM in a simple form. Then theories of structure formation and dynamics of linear perturbations are addressed. Finally, a summary of the density fields that characterize the large scale and how simple power spectrum and transfer functions define the properties of cosmological evolution.

2.1.1 The Robertson-Walker Metric

The standard cosmological models are based on the assumption that the universe is homogeneous and isotropic at large scales. Homogeneity guarantees that the same properties can be measured independently of the location where an observer is placed, and isotropy means the properties are the same in every direction an observer looks. This Cosmological Principle is not exact at small scales, but as we study larger and larger volumes of the observable universe, the more precise this cosmological principle appears to be. Although some features of the universe like the Sloan Wall (SW) (Geller & Huchra, 1989) and Sloan Great Wall (SGW) (Gott et al., 2005) challenge the validity of the cosmological principle, studies from N-body simulations by Kim et al. (2011) suggest that SW-like and SGW-like structures are consistent with ΛCDM

cosmology, therefore it is still a good approximation for modeling the universe.

In order for the isotropy of the cosmological principle to be correct, there should not be any preferred direction in the universe of any physical attribute. This means that if there exists any variations in a physical quantity for an observer that perceives its surroundings as isotropic, it has to be a function of radius only. For the velocity field this implies that the only allowed behaviors are radial contraction or expansion, so it can be written

$$\delta\mathbf{v} = H\delta\mathbf{x} \tag{2.1}$$

where H is a constant and $\delta\mathbf{x}$ and $\delta\mathbf{v}$ are the relative position and velocity to the observer. Equation (2.1) is also known as Hubble's law, since it has the same form as the relation found by Hubble (1929), who using the period-luminosity relation of Cepheid variables determined that galaxies appear to recede from the Milky-Way (MW) with a velocity linearly proportional to the distance, which is expected from a universe in accordance with the cosmological principle.

A useful tool to describe the properties of a given system is through its metric, which can be understood as the equation that measures space-time distance between two locations/events. For the universe described above the metric at a given time t can be written as

$$\mathrm{d}l^2 = a^2(t)\left[\frac{\mathrm{d}r^2}{1-Kr^2} + r^2(\mathrm{d}\vartheta^2 + \sin^2\vartheta\mathrm{d}\varphi)\right] \tag{2.2}$$

where $a(t)$ is a time-dependent scale factor which relates the coordinates (r, ϑ, φ) of the observer to true physical distances, and K is a constant with values +1, 0, and -1. For an expanding (or contracting) three-sphere its radius can be written as $R(t) = a(t)R_0$, where the scale factor $a(t)$ relates its radius at time t to a comoving radius R_0 that does not change despite the expansion (contraction). Following Mo et al. (2010), polar coordinates (r, ϑ, φ) can be transform to cartesian coordinates (x, y, z, w) by

$$\begin{aligned} x^2{+}y^2 + z^2 + w^2 &= a^2(t)R_0^2 \\ x &= a(t)r\sin\vartheta\cos\varphi \\ y &= a(t)r\sin\vartheta\sin\varphi \\ z &= a(t)r\cos\vartheta \\ w &= a(t)(R_0^2 - r^2)^{1/2} \end{aligned} \tag{2.3}$$

thus a line element is

$$\mathrm{d}l^2 = \mathrm{d}x^2 + \mathrm{d}y^2 + \mathrm{d}z^2 + \mathrm{d}w^2 = a^2(t)\left[\frac{\mathrm{d}r^2}{1-r^2/R_0^2} + r^2(\mathrm{d}\vartheta^2 + \sin^2\vartheta\mathrm{d}\varphi)\right] \tag{2.4}$$

From Eqs. (2.2) and (2.4) K and R_0 are related so that $K = +1$ is the metric of a three-sphere with $R_0 = 1$ and finite volume; $K = 0$ yields $R_0 \to \infty$, meaning that the three-sphere is then an Euclidean flat space with infinite volume; and $K = -1$ is obtained when $R_0 \to i$, thus line element becomes $\mathrm{d}l^2 = \mathrm{d}w^2 - \mathrm{d}x^2 - \mathrm{d}y^2 - \mathrm{d}z^2$ describing a hyperbolic three-surface with no boundaries and infinite volume. Thus, K can be interpreted as the space-time curvature as $K = +1$ means positive curvature, $K = 0$ no curvature (flat space-time), and $K = -1$ negative curvature. The four-metric of space-time is then written as

$$\mathrm{d}s^2 = c^2\mathrm{d}t^2 - \mathrm{d}l^2 = c^2\mathrm{d}t^2 - a^2(t)\left[\frac{\mathrm{d}r^2}{1 - Kr^2} + r^2(\mathrm{d}\vartheta^2 + \sin^2\vartheta\mathrm{d}\varphi^2)\right] \tag{2.5}$$

where c is the speed of light. Equation (2.5) is known as the Robertson-Walker metric, which is the basis of many cosmological models. From an observer at $r = 0$ the proper distance is

$$l = a(t)\int_0^r \frac{\mathrm{d}r'}{\sqrt{1 - Kr'^2}} = a(t)\chi(r) \tag{2.6}$$

where $\chi(r)$ is the comoving distance given by

$$\chi(r) = \begin{cases} \sin^{-1}(r) & (\mathrm{K} = +1) \\ r & (\mathrm{K} = 0) \\ \sinh^{-1}(r) & (\mathrm{K} = \text{-}1) \end{cases} \tag{2.7}$$

The Hubble paramter $H(t)$ at a given time t is defined as the rate of change of the proper distance l between any two observers at t, that is $\mathrm{d}l/\mathrm{d}t \equiv H(t)$, using Eq. (2.6) gives

$$H(t) = \frac{\dot{a}(t)}{a(t)} \tag{2.8}$$

where the over-dot is the time derivative. The behavior of $a(t)$ thus determines the rate of expansion or contraction, and, as will be seen later, depends on the specific matter content of a given universe. The Hubble parameter at present epoch is called the Hubble constant H_0, and is commonly expressed as

$$h \equiv \frac{H_0}{100\ \mathrm{km\ s^{-1}Mpc^{-1}}} \tag{2.9}$$

Recent measurements of the Cosmic Microwave Background (CMB) by the 9-year Wilkinson Microwave Anisotropy Probe (WMAP-9) (Hinshaw et al., 2013) have constrained the value of h to 0.697, and *Planck* probe (Planck Collaboration et al., 2014) to 0.671.

2.1.2 Light Redshift in an Expanding Universe

Observational Astronomy is in its majority based of the measurement of light from distant objects. Light is also known to present wave- and particle-like behavior, and it is due to its wave-like nature that Doppler shift phenomena affects how we measure it. In the expanding universe described above lets imagine a light ray traveling radially as seen from an observer at origin $r = 0$, Eq. (2.5) can be written

$$\frac{c\mathrm{d}t}{a(t)} = \frac{\mathrm{d}r}{\sqrt{1 - Kr^2}} \tag{2.10}$$

due to the fact that light propagation implies $\mathrm{d}s = 0$. Since the time of its emission t_e to time of its observation t_o, a light wave will travel a distance

$$\int_{t_e}^{t_o} \frac{c\,\mathrm{d}t}{a(t)} = \int_0^{r_e} \frac{\mathrm{d}r}{\sqrt{1 - Kr^2}} \tag{2.11}$$

where r_e is the position from where the photon was emitted. Additionally, it has to be taken into account that the emission of a photon is not instantaneous but has a finite time. From one crest to the next one, a time δt_e must pass, which will also implicate an interval δt_o when observed, thus

$$\int_{t_e+\delta t_e}^{t_o+\delta t_o} \frac{c\,\mathrm{d}t}{a(t)} = \int_0^{r_e} \frac{\mathrm{d}r}{\sqrt{1 - Kr^2}} \tag{2.12}$$

which can be decomposed in intervals such that

$$\int_{t_e+\delta t_e}^{t_o+\delta t_o} \frac{c\,\mathrm{d}t}{a(t)} = \int_{t_e}^{t_o} \frac{c\,\mathrm{d}t}{a(t)} + \int_{t_o}^{t_o+\delta t_o} \frac{c\,\mathrm{d}t}{a(t)} - \int_{t_e}^{t_e+\delta t_e} \frac{c\,\mathrm{d}t}{a(t)} \tag{2.13}$$

Thus from Eqs. (2.11) and (2.12)

$$\int_{t_o}^{t_o+\delta t_o} \frac{c\,\mathrm{d}t}{a(t)} = \int_{t_e}^{t_e+\delta t_e} \frac{c\,\mathrm{d}t}{a(t)} \tag{2.14}$$

as $\delta t_e \ll t_e$ and $\delta t_o \ll t_o$,

$$\frac{\delta t_e}{a(t_e)} = \frac{\delta t_o}{a(t_o)} \tag{2.15}$$

which yields to

$$\frac{\delta t_o}{\delta t_e} = \frac{a(t_o)}{a(t_e)} = \frac{\lambda_o}{\lambda_e} = \frac{\nu_e}{\nu_o} \tag{2.16}$$

For an expanding universe $a(t_0) > a(t_e)$, thus the period and wavelength of the photon increase, while its frequency decreases. Defining the redshift parameter $z \equiv (\lambda_o - \lambda_e)/\lambda_e$, from Eq. (2.16) the ratio of the scale factors is

$$1 + z = \frac{a(t_o)}{a(t_e)} = \frac{\lambda_o}{\lambda_e} \tag{2.17}$$

where a_0 is normalized to 1 at present epoch, so Eq. (2.17) translates in the commonly used relation

$$a = \frac{1}{1+z} \tag{2.18}$$

From Eqs. (2.17) and (2.16) it can be understood that expansion of the space between the observer and the emitter, causes the photon wavelength to stretch as it travels through space. Thus, different observers along the same line would measure different wavelengths for the same emitted photon. Thus, redshift z does not only allows us to measure the expansion of the space, but is also a tool to measure both distance and time between an observer and an emitting object.

2.1.3 Friedmann Equations

The dynamics of the expansion of the Universe are described by the different solutions to the Friedmann equation

$$\left(\frac{\dot{a}}{a}\right)^2 = \frac{8\pi G}{3}\rho - \frac{Kc^2}{a^2} + \frac{\Lambda c^2}{3} \tag{2.19}$$

where ρ is the total density content in the universe, i.e. matter, radiation and vacuum, and is independent of the equation of state; K is the same curvature as above, and Λ is known as the cosmological constant, i.e. the contribution from the expanding universe; and from Eq. (2.8) it can be seen that $\dot{a}/a$ is the Hubble parameter $H(t)$. Models that obey the Friedmann equation are called Friedmann-Robertson-Walker (FRW) cosmologies.

The Friedmann equation is derived from energy conservation of the kinetic and gravitational potential energy of a system. Formally it is derived from the general relativity Einstein field equations and the Robertson-Walker metric, but it can also be derived from Newtonian gravity under certain assumptions. A full derivation of this equation is beyond the scope of this work, but it is suggested for interested readers to consult Liddle (2003) for the Newtonian derivation, while the general relativity derivation is presented in a simple form in Mo et al. (2010), and more detailed in Weinberg (2008).

Nonetheless, as the universe expands ρ is also a function of time, so in order to solve Eq. (2.19) it is necessary to describe how ρ evolves. The equation that describes ρ evolution is sometimes referred as the fluid equation and is derived from the first law of thermodynamics assuming that the expansion of the universe is adiabatic at all times. The fluid equation is expressed as

$$\dot{\rho} + 3\frac{\dot{a}}{a}\left(\rho + \frac{P}{c^2}\right) = 0 \tag{2.20}$$

where P is the pressure of the material. Adding a new variable P requieres another equation so that solutions can be found for the set of equations, thus for a given equation of state $P(\rho)$, the evolution of ρ and P can be calculated from the fluid equation.

In order to completely describe the dynamics of the expansion it is also necessary to know the second time derivative of the scale factor, which indicates that the expanding universe is accelerating ($\ddot{a} > 0$), decelerating ($\ddot{a} < 0$), or is expanding at a constant rate ($\ddot{a} = 0$). The equation that describes $\ddot{a}$ evolution is derived by differentiating Eq. (2.19) with respect to time and substituting terms of Eq. (2.20). The acceleration equation is then

$$\frac{\ddot{a}}{a} = -\frac{4\pi G}{3}\left(\rho + 3\frac{P}{c^2}\right) + \frac{\Lambda c^2}{3} \tag{2.21}$$

where both density and pressure acts as sources of gravity.

From Eq. (2.19) the cosmological constant Λ can be considered as an energy component with equivalent mass density $\rho_\Lambda = \Lambda c^2/8\pi G$, thus Friedmann equation can be written in a simpler form considering density ρ as the sum of all different contributions $\rho = \rho_{\rm m} + \rho_{\rm rad} + \rho_\Lambda$. With the later in mind, if it is considered a universe with no curvature (i.e. $K = 0$) and it can be expressed

$$\rho_c = \frac{3}{8\pi G}H^2(t) \tag{2.22}$$

as the critical density required for a universe to be flat. Universes with $\rho > \rho_c$ are said to be spatially closed, whereas universes with $\rho < \rho_c$ be spatially open. Using the concept of critical density it is convenient to define the density parameter

$$\Omega(t) \equiv \frac{\rho(t)}{\rho_c(t)} \tag{2.23}$$

where ρ accounts either for the total density, or one of its multiple constituents. Thus, in cosmology the content of the different components is expressed in terms of its respective density parameter

$$\Omega_{\rm m} = \frac{\rho_{\rm m}}{\rho_c}, \qquad \Omega_\Lambda = \frac{\rho_\Lambda}{\rho_c}, \qquad \Omega_{\rm r} = \frac{\rho_{\rm r}}{\rho_c}, \qquad \Omega_K \equiv -\frac{Kc^2}{H^2a^2} = 1 - \Omega \tag{2.24}$$

where Ω_K arises from rearranging terms of the Friedmann equation and diving by ρ_c in order to get $1 = \Omega - Kc^2/a^2H^2$. It is important to notice that as ρ and H vary with time, the density parameter is also a time-dependent quantity. A flat universe ($K = 0$) requires the sum of all contribution to Ω equal 1 at all times, thus whichever is the form of these contributions, they must adjust to keep in balance.

From the density dependence on the scale factor, $H(a)$ and hence $\Omega(a)$ can be computed from

$$H^2(a) = H_0^2 \left[\Omega_{\Lambda,0} + \Omega_{{\rm m},0}a^{-3} + \Omega_{{\rm r},0}a^{-4} + \Omega_{K,0}a^{-2}\right] \tag{2.25}$$

where the subscript '0' stands for present day value, so at present time $a = 1$ the Hubble parameter $H = H_0$.

Solutions to simple cases of the Friedmann equation can be obtained by taking into account only the dominant component of Ω, which from Eq. (2.25) can be understood as different epochs were the universe is either dominated by matter, radiation or cosmological constant. These solutions can be consulted in several textbooks (e.g. Liddle 2003; Mo et al. 2010; Peacock 1999) although their derivation is not presented here, the most important results are shown in Table 2.1.

Although these models are very useful to understand the behavior of a universe under certain assumptions, it is necessary to compare the observations with the results predicted by these models. This task that is not easy because observable objects like galaxies or clusters of galaxies

are product of nonlinear gravitational evolution that is not easy to study analytically, it is there where N-body and hydrodynamic simulations are useful tools to confront models with observations.

Table 2.1: Solutions to simple cases of Friedmann equation.

Dominated by	$H^2 =$	$\rho \propto$	$a \propto$
matter	$8\pi G\rho_{\rm m}/3$	a^{-3}	$t^{2/3}$
radiation	$8\pi G\rho_{\rm r}/3$	a^{-4}	$t^{1/2}$
Λ	$\Lambda c^2/3$	-	$\exp(t)$

2.1.4 The ΛCDM Cosmological Model

There exists several cosmological models that are studied by different research groups around the world. Nonetheless there is one that has been accepted by most of the scientific community as 'standard' due to the concordance of model predictions with several observations, the ΛCDM cosmology. This model is based on the cosmological principle and Einstein's theory of general relativity, and is characterized by three main components that are Dark Energy (DE), Dark Matter (DM), and an early inflationary phase.

As in the equations described above, Λ stands for the cosmological constant, and is also known as vacuum energy or (the above mentioned) dark energy due to its unknown nature. The existence of DE arises from the necessity to add a repulsive effect that explained the faster expansion of the Universe than would be expected from the sole gravitational interaction on large scales, which is done by a negative pressure field that fills uniformly the Universe. The nature of this DE is still unknown and is beyond the objectives of the ΛCDM model, which does not intend to describe the origin of this component (so as for DM), but to assume its existence to explain the observed properties of the Universe.

The CDM part of the model stands for Cold Dark Matter. The DM is said to be all matter component that cannot be seen, i.e. does not interact with light, but its presence can be inferred and measured form its gravitational interaction with baryonic (common) matter. There are several phenomena that has led to the belief of the existence of DM, for example the flat nature of galaxies rotation curves rather than decaying ones, expected from the amount of observable matter (e.g. Begeman 1989); or the lack of mass in galaxy clusters where all the visible matter cannot account for the total mass estimated to produce strong gravitational lensing (e.g. Limousin et al. 2008). In general, results tend to suggest that the amount of luminous matter is just $\sim 10\%$ of the total mass, thus as this 'missing' mass, that only interact

through gravity, cannot be seen in any wavelength of the electromagnetic spectrum, it is said to be dark. Consequently, the matter content is decomposed in two components

$$\Omega_{\rm m} = \Omega_{\rm b} + \Omega_{\rm dm} \tag{2.26}$$

where 'b' stands for baryonic, and 'dm' for dark matter, sometimes also noted with the subscript *c*. Despite this differentiation in the nature of matter, all equations presented above are left the same since it is the mass and the gravitational interaction the one that has an effect on the dynamics of the universe and space-time curvature, and not the nature of the matter. Nevertheless, the evolution of each component is different due to the fact that DM only interacts gravitationally, while the different baryon components (stars, gas and dust) are affected by several processes besides gravity, such as radiative cooling, stellar winds, star formation, supernovae feedback, etcetera. Results from WMAP-9 measurements of CMB Hinshaw et al. (2013) have determined that contributions of the main components to be $\Omega_{\rm b} = 0.235$, $\Omega_{\rm dm} = 0.0464$ and $\Omega_\Lambda = 0.7185$, where $\sim 95\%$ of the total energy density of the Universe corresponds to the 'double-dark' components.

Dark Matter is said to be hot, warm or cold in an analogous manner to the behavior of a system of gas particles, where their internal movement rises with increasing temperature, and vice versa. The difference between 'types' DM is essentially the kinetic energy of its constituent particles that will affect DM aggregation at the smallest scales. So CDM "consists of a weakly interacting particles whose velocity dispersion in the early universe was too small to erase structure on galactic or sub-galactic scales" (Weinberg et al., 2013). Although there is very good agreement with large-scale observations, the disagreement with small-scale ones has led to alternative models (e.g. Warm Dark Matter or Self-Interacting Dark Matter) to gain popularity during the past years, for the purposes of this work those models are not discussed here.

The last ingredient of the standard ΛCDM cosmology is the existence of an inflationary phase at early epochs, during which the Universe experienced a rapid exponential expansion, more or less 10^{-36} seconds after the Big Bang driven by a negative-pressure vacuum energy density. The inflationary initial conditions were originally proposed by Guth (1981), and emerge as a solution to the negligible probability that the Universe has been flat since its beginning (flatness problem), and to the homogeneity observed in the Cosmic Microwave Background (CMB) in regions that were causally disconnected at the time of last scattering surface (horizon problem). Thus cosmic inflation is the mechanism that can explain the flatness, homogeneity and isotropy of the universe, on which ΛCDM is based on.

2.1.5 Dynamics of Structure Formation and Linear Perturbations

The observed properties of the Universe at all scales and different light wavelengths give us some insight on the initial state of the Universe and the processes responsible for the growth of small-scale inhomogeneities in a large-scale homongeneity. Here are presented in a simple form the equations used that describe the evolution of cosmological perturbations of a pressureless non-relativistic fluid under a Newtonian linear regime. This approximation is valid for structures where causality can be considered instantaneous, when density contrast against background is much smaller than unity, and when the interparticle separation is much smaller than the scales of interest.

This treatment requieres that DM to be considered as a fluid, so its time evolution is described by the same equations of a common fluid. The general fluid description is expressed as the evolution of density ρ and velocity $\mathbf{u}$ fields that interact throgh gravity given by the potential ϕ

$$\frac{D\rho}{Dt} + \rho\nabla\cdot\mathbf{u} = 0 \qquad \text{Continuity Equation} \tag{2.27}$$

$$\frac{D\mathbf{u}}{Dt} = -\frac{\nabla P}{\rho} - \nabla\phi \qquad \text{Euler Equation} \tag{2.28}$$

$$\nabla^2\phi = 4\pi G\rho \qquad \text{Poisson Equation} \tag{2.29}$$

where

$$\frac{D}{Dt} = \frac{\partial}{\partial t} + \mathbf{v}\cdot\nabla \tag{2.30}$$

is called the convective or Lagrangian derivative, and describes the time derivative as a quantity that moves with the fluid. i.e. respect to the moving coordinate system of the fluid. The continuity equation (Eq. 2.27) expresses the conservation of mass through time; the Euler equation (Eq. 2.28) defines the equations motion, and the Poisson equation (Eq. 2.29) characterizes the gravitational field. From Euler equation (Eq.2.28) it can be seen that the pressure gradient term is valid for describing baryons (which needs an equation of state $P = P(\rho)$ to close the set equations), but it is dropped when describing DM, which can be considered as a pressureless fluid.

For an expanding Friedmann-Robsertson-Walker universe, it is convenient to use coordinates that move with the expansion, known as comoving coordinates, which are defined as

$$\mathbf{r} = a(t)\mathbf{x} \tag{2.31}$$

where $\mathbf{x}$ is the comoving coordinate and is fixed independently of the expansion, and $\mathbf{r}$ is the physical spatial coordinate which is the result of scaling the comoving coordinate, in terms of the scale factor $a(t)$ that describes the expansion of the Universe. Differentiating with respect to time

$$\begin{aligned} \mathbf{u} &= \dot{a}(t)\mathbf{x} + a\dot{\mathbf{x}} \\ &= \dot{a}(t)\mathbf{x} + \mathbf{v} \\ &= H(t)\mathbf{r} + \mathbf{v} \end{aligned} \tag{2.32}$$

where $\mathbf{v} \equiv a\dot{\mathbf{x}}$ is the peculiar velocity. Eq. (2.32) describes total the motion of a fluid element relative to an observer in a coordinate system that does not moves with the expansion, and is expressed as the sum of the Hubble flow plus a peculiar velocity with respect to the background. An analogy for observed galaxies would be that the first term of the *right hand side* (rhs) of Eq. (2.32) is the motion driven by the expansion of the universe, while $\mathbf{v}$ would be the motion due to is gravitational interaction with other galaxies, e.g. in a galaxy cluster. Another way to interpret $\mathbf{v}$ in Eq.(2.32) is as a perturbation in the velocity of volume elements that constitute the fluid.

In order to see how perturbations evolve it is useful to express the density field $\rho(\mathbf{x}, t)$ as

$$\rho(\mathbf{x}, t) = \bar{\rho}(t)[1 + \delta(\mathbf{x}, t)] \tag{2.33}$$

where $\bar{\rho}$ is the mean or background density and $\delta(\mathbf{x}, t)$ is a perturbation with amplitude much smaller than unity. Then substituting Eqs. (2.32) and (2.33) in Eqs. (2.27)-(2.29), considering the transformation to comoving coordinates

$$\begin{aligned} (\mathbf{r}, t) \quad &\rightarrow \quad (\mathbf{x}, t) \\ \nabla \quad &\rightarrow \quad \frac{1}{a}\nabla_{\mathbf{x}} \\ \frac{\partial}{\partial t} \quad &\rightarrow \quad \frac{\partial}{\partial t} - \frac{\dot{a}}{a}\mathbf{x} \cdot \nabla_{\mathbf{x}} \end{aligned}$$

thus, the linearized equations that describe the perturbation against an homogeneous background of a pressureless non-relativistic fluid become

$$\frac{\partial \delta}{\partial t} + \frac{1}{a}\nabla_{\mathbf{x}} \cdot [(1+\delta(\mathbf{x},t)\mathbf{v}] = 0 \qquad \text{Continuity Equation} \tag{2.34}$$

$$\frac{\partial \mathbf{v}}{\partial t} + \frac{\dot{a}}{a}\mathbf{v} + \frac{1}{a}(\mathbf{v}\cdot\nabla_{\mathbf{x}})\mathbf{v} = -\frac{\nabla_{\mathbf{x}}\Phi}{a} \qquad \text{Euler Equation} \tag{2.35}$$

$$\nabla^2_{\mathbf{x}}\Phi = 4\pi G\bar{\rho}a^2\delta \qquad \text{Poisson Equation} \tag{2.36}$$

where $\Phi \equiv \phi + a\ddot{a}x^2/2$. Although Eqs. (2.34)- (2.36) were derived under the assumption of a non-relativistic fluid and the only source of Eq. (2.29) was the dark matter density, these equation can be extended to cases where the universe contains a smooth background (i.e. densities can be taken to be uniform) of relativistic particles or vacuum energy. Thus mass density equivalent of the relativistic $\tilde{\rho}_{\rm r}$, and vacuum energy $\tilde{\rho}_\Lambda$ components, should be included as sources of gravitational potential in Eq. (2.29). Thus Poisson equation is then written as

$$\nabla^2\phi = 4\pi G(\rho + \tilde{\rho}_{\rm r} + \tilde{\rho}_\Lambda) \tag{2.37}$$

where

$$\tilde{\rho}_{\rm r} = \rho_{\rm r} + 3\frac{P_{\rm r}}{c^2} \quad ; \qquad P_{\rm r} = \frac{\rho_{\rm r}c^2}{3} \qquad \rightarrow \qquad \tilde{\rho}_{\rm r} = 2\rho_{\rm r} \tag{2.38}$$

$$\tilde{\rho}_\Lambda = \rho_\Lambda + 3\frac{P_\Lambda}{c^2} \quad ; \qquad P_\Lambda = -\rho_\Lambda c^2 \quad \rightarrow \qquad \tilde{\rho}_\Lambda = -2\rho_\Lambda \tag{2.39}$$

Nonetheless, introducing $\bar{\rho}_\Lambda$ and $\bar{\rho}_{\rm r}$ does not change Eqs. (2.34)-(2.36), since it was considered that these contributions are homogeneous δ remains unchanged, hence the source of Φ would still be the density perturbation δ against the mean density of the non-relativistic dark matter.

Expanding Eqs. (2.34)-(2.36) for cases where δ and $\mathbf{v}$ are small such that nonlinear terms vanish, the linearized equations are

$$\frac{\partial \delta}{\partial t} + \frac{1}{a}\nabla_{\mathbf{x}} \cdot \mathbf{v} = 0 \tag{2.40}$$

$$\frac{\partial \mathbf{v}}{\partial t} + \frac{\dot{a}}{a}\mathbf{v} = -\frac{\nabla_{\mathbf{x}}\Phi}{a} \tag{2.41}$$

Differentiating Eq. (2.40) with respect to time, taking the divergence of Eq. (2.41) and using Eq. (2.36), it can be written

$$\frac{\partial^2 \delta}{\partial t^2} + 2\frac{\dot{a}}{a}\frac{\partial \delta}{\partial t} = 4\pi G\bar{\rho}\delta \tag{2.42}$$

that describes the evolution of the density perturbation in the linear regime. It can be seen that gravity will cause that deviation form homogeneous distribution grow, while the second term of left-hand-side of Eq. (2.42) (Hubble drag) will tend to suppress them.

It is useful to express the evolution of perturbation δ as a plane wave with its corresponding wavevector $\mathbf{k}$, because generic perturbations can be represented as a superposition of such plane waves that evolve linearly and independent of each other. δ is then expressed as $\delta_{\mathbf{k}}$ by its Fourier transforms

$$\delta(\mathbf{x}, t) = \sum_{\mathbf{k}} \delta_{\mathbf{k}} \exp(i\mathbf{k}\cdot\mathbf{x}) \tag{2.43}$$

$$\delta_{\mathbf{k}}(t) = \frac{1}{V_u}\int \delta(\mathbf{x}, t)\exp(-i\mathbf{k}\cdot\mathbf{x})\mathrm{d}^3\mathbf{x} \tag{2.44}$$

where V_u is the volume of the box on which the perturbations are assumed to be periodic, and wavevectors $\mathbf{k}$ are in comoving units. Exploiting the fact that

$$\begin{aligned} \nabla \quad &\rightarrow \quad i\mathbf{k} \\ \nabla^2 \quad &\rightarrow \quad -k^2 \end{aligned}$$

the Fourier Transform of Eqs. (2.40), (2.41), and (2.36) are expressed as

$$\mathbf{v}_{\mathbf{k}} = \frac{ia\mathbf{k}}{k^2}\frac{\mathrm{d}\delta_{\mathbf{k}}}{\mathrm{d}t} \tag{2.45}$$

$$\frac{\mathrm{d}^2\delta_{\mathbf{k}}}{\mathrm{d}t^2} + 2\frac{\dot{a}}{a}\frac{\mathrm{d}\delta_{\mathbf{k}}}{\mathrm{d}t} = 4\pi G\bar{\rho}\delta_{\mathbf{k}} \tag{2.46}$$

$$-k^2\Phi_{\mathbf{k}} = 4\pi G\bar{\rho}a^2\delta_{\mathbf{k}} \tag{2.47}$$

2.1.6 Zel'dovich Approximation

Zel'dovich (1970) proposed an approximate solution for the growth of linear perturbations of a non-relativistic pressureless fluid in an expanding universe. Under a Newtonian approximation this kinematical approach is based on a first-order Lagrangian description of gravitational collapse due to initial perturbations.

The solution is based on a simple expression of the position $\mathbf{r}$ as a function of its Lagragian coordinate $\mathbf{q}$ and time t, and a perturbation factor $\mathbf{p}(\mathbf{q})$, in order that a single equation contains the whole picture of motion. Thus, the position $\mathbf{r}$ of constituent particles is expressed as

$$\mathbf{r}(t) = a(t)\mathbf{q} + b(t)\mathbf{p}(\mathbf{q}) \tag{2.48}$$

where $a(t)\mathbf{q}$ describes the cosmological expansion, and $b(t)\mathbf{p}(\mathbf{q})$ the perturbations. In this picture $\mathbf{q}$ and $\mathbf{p}(\mathbf{q})$ are time-independent, thus they are the initial position and displacement, $a(t)$ and $b(t)$ are known and are the same for all particles, and $b(t)$ grows more rapidly than $a(t)$ due to gravitational instability. It is important to notice that Eq. (2.48) has a similar form as Eq. (2.31), so it can be thought of as the Hubble expansion plus some perturbation that becomes negligible as $t \to 0$ $\mathbf{q}$; when $t = 0$ Eqs. (2.31) and (2.48) are the same. Some autors often refer to Eq. (2.48) as $\mathbf{r}(t) \equiv a(t)\mathbf{x} = a(t)[\mathbf{q} + b(t)\mathbf{p}(\mathbf{q})]$ to differentiate from physical, comoving and Lagrangian coordinates, though the original (Zel'dovich, 1970) definition will be used here. The first and second time derivatives of Eq. (2.48)

$$\mathbf{u} = \dot{a}\mathbf{q} + \dot{b}\mathbf{p}(\mathbf{q}) \tag{2.49}$$

$$\frac{\mathrm{d}\mathbf{u}}{\mathrm{d}t} = \ddot{a}\mathbf{q} + \ddot{b}\mathbf{p}(\mathbf{q}) \tag{2.50}$$

It can be seen that vector quantities $\mathbf{q}$ and $\mathbf{p}(\mathbf{q})$ are kept unchanged, hence Zel'dovich approximation describes particles (or volume elements) that move in the same straight given by the initial perturbation $\mathbf{p}(\mathbf{q})$.

The effects of the evolution particles described by Eq. (2.48) are directly appreciated as changes in the shape of matter distribution. This changes can be measured with the deformation tensor (also known as deformation gradient) defined as

$$F_{ij} = \frac{\partial r_i}{\partial q_j} \tag{2.51}$$

that substituting Eq. (2.48) gives

$$\begin{aligned} F_{ij} &= \frac{\partial}{\partial q_j}\left[a(t)q_i + b(t)p(q_i)\right] \\ &= a(t)\delta_{ij} + b(t)\frac{\partial p(q_i)}{\partial q_j} \end{aligned} \tag{2.52}$$

where δ_{ij} is the Kronecker delta. The Jacobian of Eq. (2.51)

$$J = \det(F) = \det\left(a(t)\delta_{ij} + b(t)\frac{\partial p(q_i)}{\partial q_j}\right) \tag{2.53}$$

gives the change in the volume due to the deformation experienced.

For an initially unperturbed cubic parcel of matter of mass M, volume $V = r^3$, and density $\rho(\mathbf{r}) = M/r^3 = M/(ax)^3 = \rho(\mathbf{x})/a^3$, that experiences compression due to gravity, following mass conservation $\rho(\mathbf{r}, t)d^3\mathbf{r} = \bar{\rho}d^3\mathbf{q}$, density can be expressed as

$$\begin{aligned} \rho(\mathbf{x}, t) &= a^3\bar{\rho}\,\det\left(\frac{\partial q_i}{\partial r_i}\right) \\ &= a^3\frac{\bar{\rho}}{\det(\partial r_i/\partial q_i)} \\ &= a^3\frac{\bar{\rho}}{\det[a(t)\delta_{ij} + b(t)(\partial p(q_i)/\partial q_j)]} \end{aligned} \tag{2.54}$$

Additionally, the second term of Eq. (2.52) becomes symmetric for growing mode of perturbations (Zel'dovich, 1970), thus the deformation tensor can be diagonalized. The eigenvalues $\alpha = \lambda_1$, $\beta = \lambda_2$, and $\gamma = \lambda_3$, of tensor $\partial p_i/\partial q_j$ using the definition $|(\partial p_i/\partial q_j) + \lambda\delta_{ij}| = 0$ are all functions of $\mathbf{q}$, so the deformation tensor can be diagonalized and in terms of the eigenvalues λ of $\partial p_i/\partial q_j$, it can be expressed as

$$F = \begin{bmatrix} a(t) - \alpha b(t) & 0 & 0 \\ 0 & a(t) - \beta b(t) & 0 \\ 0 & 0 & a(t) - \gamma b(t) \end{bmatrix} \tag{2.55}$$

thus Eq. (2.54) is re-written as

$$\rho(\mathbf{x}, t) = \frac{a^3\bar{\rho}}{(a - \alpha b)(a - \beta b)(a - \gamma b)} = \frac{\bar{\rho}}{(1 - \alpha(b/a))(1 - \beta(b/a))(1 - \gamma(b/a))} \tag{2.56}$$

Additionally, at early times when $b(t)$ is assumed to be small, it can be shown by expanding Eq. (2.56) to first-order (i.e. dropping all high-order terms of b/a) that Eq. (2.54) takes the form

$$\rho(\mathbf{x},t) = \bar{\rho}\left(1 + (\alpha+\beta+\gamma)\frac{b(t)}{a(t)}\right) = \bar{\rho}\,(1 + S(\mathbf{q})f(t)) \tag{2.57}$$

which is the same as Eq. (2.33). Hence, the initial perturbation is uniquely defined by the initial displacement $S(\mathbf{q})$. Also, as pointed out by (Zel'dovich, 1970), α, β, and γ individually provide useful information about compression, that in addition to the spatial distribution of velocity, $\mathbf{p}(\mathbf{q})$, determine the non-linear evolution of density perturbations.

As constituent particles of the initially the cube evolve according to Eq. (2.48), the volume is transformed into a parallelepiped. As gravity starts to act the volume will begin to collapse along the shortest axis, defined by the largest eigenvalue of the deformation tensor, which results in the direction of α axis. The collapse continues until inifite density is reached, at the time when $a(t) - \alpha b(t) = 0$. At this moment the parallelepiped has transformed into a 2D sheet-like structure, often called 'Zel'dovich pancakes'.

It can be seen that Eq. (2.33) arises as a special case in the Zel'dovich approximation (ZA) and not as initial condition like the perturbation description mentioned above, where the evolution of density perturbations is described under the approximation that δ and $\mathbf{v}$ are small. Additionally, the velocity and acceleration (Eqs. [2.49] and [2.50]) are always finite until $\rho = \infty$ when the pancakes form, thus Zel'dovich approximation can in principle can be extended to cases where $\delta \simeq 1$.

This scheme of linearly extrapolating velocities is exact for one-dimensional problem (see Padmanabhan 1996 for demonstration), and basically describes the collapse of parallel sheets of matter, where acceleration of each sheet is independent of $\mathbf{x}$ and the full equation of motion can be extrapolated from its initial displacement $S(q)$, until crossing occurs. Lastly, the importance of ZA is because in the three dimensional problem, the structures predicted at the final stages of the collapse, i.e. the pancakes, resemble to the 1D problem where ZA is exact; additionally, these pancakes are also typical at the initial stages of evolution of cosmological density fields, reason why this method is commonly used to set up quasi-linear initial conditions for N-body simulations (e.g. Efstathiou et al. 1985; Klypin & Shandarin 1983; Springel et al. 2005).

2.1.7 Statistical Description of Density Field

In previous sections the equations that describe the linear evolution of perturbations in the density field $\rho(\mathbf{x}, t)$ were presented, whose properties are more conveniently described by the adimensional density contrast $\delta(\mathbf{x}, t)$, which from Eq. (2.33), can be written as

$$\delta(\mathbf{x}, t) \equiv \frac{\rho(\mathbf{x}, t) - \bar{\rho}(t)}{\bar{\rho}(t)} \tag{2.58}$$

Nonetheless, instead of describing a specific configuration of field δ, it is more useful to focus on the statistical properties that δ has to have in order to match the ones observed in the matter distribution of the Universe. Thus δ is considered as a realization of a random process described by a probability distribution function $\mathcal{P}_x$.

For a number n of volume elements of the Universe, centered at $\mathbf{x}_1, \mathbf{x}_2, \cdots, \mathbf{x}_n$, it can be written

$$\mathcal{P}_x(\delta_1\delta_2\cdots\delta_n)\mathrm{d}\delta_1\mathrm{d}\delta_2\cdots\mathrm{d}\delta_n \tag{2.59}$$

as the probability that field δ has values in the range δ_i to $\delta_i + \mathrm{d}\delta_i$ at positions $\mathbf{x}_i$ ($i = 0, 1, 2, \cdots, n$). In the same manner as a phase-space distribution f, the shape of P_x is determined by its moments

$$\langle \delta_1^{\ell_1}\delta_2^{\ell_2}\cdots\delta_N^{\ell_N}\rangle \equiv \int \delta_1^{\ell_1}\delta_2^{\ell_2}\cdots\delta_N^{\ell_N} P_x(\delta_1\delta_2\cdots\delta_N)\mathrm{d}\delta_1\mathrm{d}\delta_2\cdots\mathrm{d}\delta_N \tag{2.60}$$

where ℓ_i are non-negative integers. The first moment, or mean, $\langle\delta\rangle$ is zero since the cosmological principle requires all positions and directions in the Universe to be equivalent, thus δ must be statistically homogeneous and isotropic. The second moment, or variance, is

$$\sigma^2 \equiv \langle\delta^2\rangle = \sum_{\mathbf{k}}\langle|\delta_{\mathbf{k}}|^2\rangle = \frac{1}{V_u}\sum_{\mathbf{k}}\delta_k^2 \tag{2.61}$$

where δ has been expressed as a superposition of plane waves as Eq. (2.43). And the quantity

$$P(k) \equiv \langle|\delta_k|^2\rangle \tag{2.62}$$

is the power spectrum of density fluctuations, which tell us about the amplitude of perturbations in Fourier space. In the limit that $V_u \to \infty$, the variance is then expressed as

$$\sigma^2 = 4\pi \int_0^\infty P(k) \frac{k^2 \mathrm{d}k}{(2\pi)^3} = \frac{1}{2\pi^2} \int_0^\infty P(k) k^2 \mathrm{d}k \tag{2.63}$$

Additionally to the statistical homogeneity and isotropy of δ, it can be assumed that the phases of the different Fourier modes δ_k are uncorrelated besides being random, hence from the central limit theorem, it is expected that the sum of a large number of independent random variables will tend to be normally distributed. If the process is indeed Gaussian, i.e. presents a normal distribution, only the mean and the variance are needed to fully describe the system, since odd moments of $\mathcal{P}_x$ are zero by symmetric nature of the distribution, while even moments are powers of σ (see e.g. Kendall et al. (1987)). Thus, as the mean is zero, the distribution is then entirely characterized by its power spectrum.

These normally distributed random fields are predicted by inflationary models, in which density perturbations are generated by Gaussian quantum fluctuations during the inflationary epoch (Guth, 1981; Guth & Pi, 1982). In addition, as the power spectrum is the variance of the amplitudes at a given value of k, the shape of initial fluctuation spectrum is expected to be imprinted on the universe at some arbitrarily early time. It is known from inflationary models that the primordial power spectrum $P_0(k)$ is well approximated by a power-law

$$P_0(k) = A k^{n_s} \tag{2.64}$$

where A is the initial amplitude and n_s the spectral index. The index n_s governs the balance between large- and small-scale power, hence n_s does not need to be constant over the entire range of wave numbers. Although Eq. (2.64) specifies the shape of the fluctuation spectrum the amlpitude A needs to be determined by observations.

In order to correctly describe the perturbation spectrum, there are several important features that have not been considered, and whose effects cannot be neglected for the evolution of perturbations. This means that the initial fluctuations would be influenced by interactions between different species of particles in the early universe, by interaction of matter and radiation, etc., and consequently would affect the shape of the original perturbation spectrum. The power spectrum would be then described by a function of wavenumber, that describes the wavelength dependent part of the evolution of Fourier modes. The power spectrum is then expressed as

$$P(k) = P_0(k) T^2(k) \tag{2.65}$$

where $T(k)$ is the transfer function, which relates the processed power spectrum $P(k)$ to its initial $P_0(k)$. As long as the amplitude of each Fourier mode remains small $\delta_{\mathbf{k}} \ll 1$, linear theory applies, hence each Fourier mode evolves independently and the power spectrum evolution can be scaled as

$$P(k,t) = \left(\frac{D(t)^2}{D(t_i)}\right)^2 P(k,t_i) = \left(\frac{D(t)}{D(t_i)}\right)^2 P_0(k)T^2(k) \tag{2.66}$$

where D_+ is the growth factor, which is a solution to Eq. (2.42). In a similar manner the evolution of $\delta_{\mathbf{k}}$ can be written as

$$\delta_{\mathbf{k}}(t) = \frac{D(t)}{D(t_i)} T(k)\delta_{\mathbf{k}}(t_i) \tag{2.67}$$

The transfer function is a convenient way to describe the relation between the initial conditions and the density perturbations that are observed in the post-recombination Universe. It is useful since, once the perturbation spectrum is set at some time in the early Universe, the transfer function $T(k)$ allows to calculate the power spectrum at any later times.

Although the power spectrum completely describes the statistical properties of density field δ, it is convenient to have a statistical description of δ as a function of a given scale R, besides the variance σ^2 which is integrated over all wavenumbers, hence all length scales. For this purpose it is useful to calculate the mass variance

$$\sigma_M^2 = \frac{\langle (M - \langle M \rangle)^2 \rangle}{\langle M \rangle^2} \tag{2.68}$$

where $\langle M \rangle = \langle \rho \rangle V$ is the mean mass, and the average is made over all volumes V, and σ_M is the root-mean-square mass fluctuation. Once again, expressing δ as a superposition of $\delta_{\mathbf{k}}$, the σ_M can be written as

$$\sigma_M^2 = \sum_{\mathbf{k}} \langle |\delta_{\mathbf{k}}|^2 \rangle \left[\frac{1}{V}\int_V \exp(i\mathbf{k}\cdot\mathbf{y})\mathrm{d}\mathbf{y}\right]^2 = \frac{1}{V_u}\sum_{\mathbf{k}} \delta_k^2 W^2(kR) \tag{2.69}$$

(see Coles & Lucchin (2002) for detailed derivation), where $W(kR)$ is known as window function. The integral of the left hand side of Eq. (2.69) can be expanded in spherical harmonics to be expressed as

$$W(kR) = \frac{3(\sin kR - kR\cos kR)}{(kR)^3} \tag{2.70}$$

Thus, in the limit that $V_u \to \infty$, the rms fluctuation can be written in terms of the power spectrum as

$$\sigma_M^2 = \frac{1}{2\pi^2}\int_0^\infty P(k)W^2(kR)k^2\mathrm{d}k \tag{2.71}$$

The window function $W(kR)$ has the effect to 'filter' perturbation components, in a manner that the dominant contribution to σ_M^2 will come from perturbations with wavelengths $\lambda \simeq k^{-1} > R$, since those with higher frequencies tend to be averaged out within the window volume. Another way to see this is starting from a filtration of the density field δ, which is obtained by convolution of δ with some filtering function F of characteristic length R

$$\delta(\mathbf{x}; R_F) = \int \delta(\mathbf{x}')F(|\mathbf{x} - \mathbf{x}'|; R_F)\mathrm{d}\mathbf{x}' \tag{2.72}$$

If we then express Eq. (2.72) in terms of its Fourier components, it is straightforward to see that Eq. (2.71) is the result of calculating the variance σ^2 of the density field filtered by a Heaviside-like function, known as *top-hat* filter, with non-zero value inside a sphere of radius R and zero outside of it. Equation (2.70) expresses the Fourier transform of the spherical top-hat function.

The mass variance σ_M is commonly used to normalize the amplitude of the power spectrum, as

$$\sigma_8^2 = \frac{1}{2\pi^2}\int_0^\infty W^2(k; R = 8h^{-1}\mathrm{Mpc})P(k)k^2\mathrm{d}k \tag{2.73}$$

which is the present epoch rms density fluctuations in spheres of 8 h^{-1} Mpc radius. The specific radius of 8 h^{-1} Mpc is considered to be approximately the scale where the dynamics is still linear, but this value is kept for historical reasons (Mo et al., 2010). Since perturbations on these scales may well have gone nonlinear by the present time, this value is not the same as the variance of the actual present-day mass distribution, so it has just to be taken as a normalization value, which can be constrained directly from observations, such as measurements of cluster abundance or matter power spectrum probed via weak lensing.

Chapter 3

Numerical Tools

In this chapter concepts on numerical methods and codes that were used in this work are reviewed. As will be described in detail in Chapter 4, there are several steps that need to be implemented in order to run the simulations studied in this work. The methodology implemented in this work requires a different code for each step. In Section 3.1 it is described the MUSIC code (Hahn & Abel, 2011), which was used to generate the initial conditions for the uniform and zoom-in cosmological simulations. To integrate the equations of motion, it was used the GADGET-2 code (Springel, 2005; Springel et al., 2001), described in Section 3.2. To simulate the evolution a galactic disk, it was necessary to select dark matter halos with specific characteristics, which were identified using the AHF code (Gill et al., 2004; Knollmann & Knebe, 2009), reviewed in Section 3.3. Lastly, in Section 3.4 it is presented the iterative method described by Rodionov et al. (2009), which was used to set up the initial velocities of the stellar disks.

Throughout the chapter basic knowledge of numerical simulations is assumed. Although most of the concepts are explained here, the reader is kindly referred to Moscardini & Dolag (2011) for an introductory review on numerical methods applied to cosmological and galaxy simulations.

3.1 Zoom-in Cosmological Initial Conditions: MUSIC code

MUSIC (MUlti-Scale Initial Conditions), is a code developed by Hahn & Abel (2011), that is capable of generating the initial conditions of a multiple resolution cosmological simulation. In this Section the general aspects of how the code works are briefly reviewed, while further details, e.g. numerical solution to Poisson equation, accuracy of the code, among others, can be consulted in the original paper (Hahn & Abel, 2011).

Generating the initial conditions of any N-body simulation consists of determining the start-

ing positions and velocities of the constituent particles of the simulation. In this case this is achieved my means of Lagrangian Perturbation Theory (LPT), which expresses the evolution of density perturbations in the rest frame of volume elements of the fluid. In LPT the time evolution of the position and velocity of these fluid elements is expressed as

$$\mathbf{x}(t) = \mathbf{q} + \mathbf{L}(\mathbf{q}, t) \qquad \dot{\mathbf{x}}(t) = \frac{\mathrm{d}}{\mathrm{d}t}\mathbf{L}(\mathbf{q}, t) \tag{3.1}$$

where $\mathbf{L}(\mathbf{q})$ is the displacement field, which is obtain by solving Poisson equation, and depends on the order of the perturbation.

The displacement field $\mathbf{L}(\mathbf{q})$ for first-order LPT (ZA Zel'dovich 1970, see Section 2.1.6), can can be written as the gradient of a potential Φ which is proportional to the gravitational potential ϕ, as

$$\mathbf{L}(\mathbf{q}) = -\frac{2}{3H_0^2 a^2 D_+(t)}\nabla_{\mathbf{q}}\phi(\mathbf{q}, t) \;\equiv\; D_+^{-1}(t)\nabla_{\mathbf{q}}\Phi(\mathbf{q}, t) \tag{3.2}$$

where H_0, a, and D_+ are the same as in Section 2.1, and ϕ is the gravitational potential, whose corresponding Poisson equation

$$\nabla_{\mathbf{q}}^2\phi(\mathbf{q}, t) = \frac{3}{2}H_0^2 a^2 \delta(\mathbf{q}, t) \tag{3.3}$$

has to be solved numerically in order to calculate the displacements $\mathbf{S}(\mathbf{q})$. The source of the potential is then the Gaussian overdensity field δ before any displacement is performed.

Second-order LPT (2LPT) is also implemented in MUSIC, in which the displacement field $\mathbf{S}(\mathbf{q})$ contains contributions from the gravitational potential, and a second-order potential Ψ

$$\mathbf{L}(\mathbf{q}, t) = D_+(t)\nabla_{\mathbf{q}}\Phi(\mathbf{q}, t) + D_2(t)\nabla_{\mathbf{q}}\Psi(\mathbf{q}, t) \tag{3.4}$$

that is sourced by the off-trace components of the deformation tensor, and obeys the Poisson equation

$$\nabla_{\mathbf{q}}^2\Psi(\mathbf{q}, t) = \tau(\mathbf{q}, t) \tag{3.5}$$

$$\tau(\mathbf{q}, t) = -\frac{1}{2}\sum_{i,j}\left[(\partial_i\partial_j\Phi)^2 - (\partial_i\partial_i\Phi)\,(\partial_j\partial_j\Phi)\right] \tag{3.6}$$

where $\partial_i \equiv \partial/\partial q_i$, and $D_2(t) \simeq \frac{3}{7} D_+^2(t)$. For a detailed derivation and further details on LPT the reader is refered to Bouchet et al. (1995), Bernardeau et al. (2002) and Jeong (2010).

To calculate the displacement field $\mathbf{L}(\mathbf{q})$ either for 1LPT or 2LPT scheme, it is necessary to solve the Poisson equation(s) numerically (see section 3.2 and 3.3 of Hahn & Abel 2011 for further details), for which it is necessary to specify the Gaussian overdensity field δ which is completely described by its power spectrum $P(k)$. The amplitude of density fluctuations is usually expressed in terms of the transfer function $\mathcal{T}(k)$, such that

$$P(k) = Ak^{n_s}\mathcal{T}^2(k)$$

same as Eqs. 2.64 and 2.65.

The next step consists in generating a sample of random values $\mu(\mathbf{r})$ (known as white noise) sampled from a Gaussian (normal) distribution with zero mean and unit variance, whose amplitudes require to follow the desired $P(k)$. This last step is achieved by multiplying the Fourier image of the white noise field $\tilde{\mu}(\mathbf{k})$ with the square root of the power spectrum

$$\tilde{\delta}(\mathbf{k}) = \sqrt{P(|\mathbf{k}|)}\tilde{\mu}(\mathbf{k}) = A|\mathbf{k}|^{n_s/2}\mathcal{T}(|\mathbf{k}|)\tilde{\mu}(\mathbf{k}) \tag{3.7}$$

which is done for all wavenumber $\mathbf{k}$ representable on the grid of a given resolution, and the real space $\delta(\mathbf{x})$ is obtained by inverse Fourier transformation.

As a product in Fourier space corresponds to a convolution in real space, $\delta(\mathbf{x})$ can also be expressed as

$$\delta(\mathbf{r}) = T(|\mathbf{r}|) * \mu(\mathbf{r}) \tag{3.8}$$

where '$*$' denotes convolution, and $T(r)$ is the real-space image of $\tilde{T}(k) = Ak^{n_s/2}\mathcal{T}(k)$. In order to obtain $\delta(\mathbf{x})$ a real-space transfer function $\mathcal{T}_{\mathcal{R}}(r)$ has to be calculated, and applied as a convolution kernel to the Gaussian white noise field, whose convolution is perfomed in Fourier space. This convolution has to be computed numerically by employing a discretization of the transfer function over the entire simulation volume of length $L = hN$; the white noise random field $\mu(\mathbf{x}_{ijk})$ is created on the same discretization. Then both $T(\mathbf{x}_{ijk})$ and $\mu(\mathbf{x}_{ijk})$ are Fourier transformed, multiplied element-by-element with one another and then inverse transformed to get $\delta(\mathbf{x}_{ijk})$. This is the exact process to generate the overdensity field δ in the case of uniform grid simulations, while for additional refinements additional steps have to be done.

Refining a desired region consists basically on improving its spatial and mass resolution to be able to distinguish phenomena at scales smaller than the original grid. For this purpose both

the random field and the transfer function have to be 'mapped' correctly so that the properties of the fine region be consistent with those of the coarse one. An example of the subdivision of space is shown in a refined cell is shown in the left pannel of Fig. 3.1, where the bottom-right cell of the top level ℓ is subdivided in two equal parts along each dimension to get the first refined level $\ell + 1$, which is also subdivided to get the second refined level $\ell + 2$.

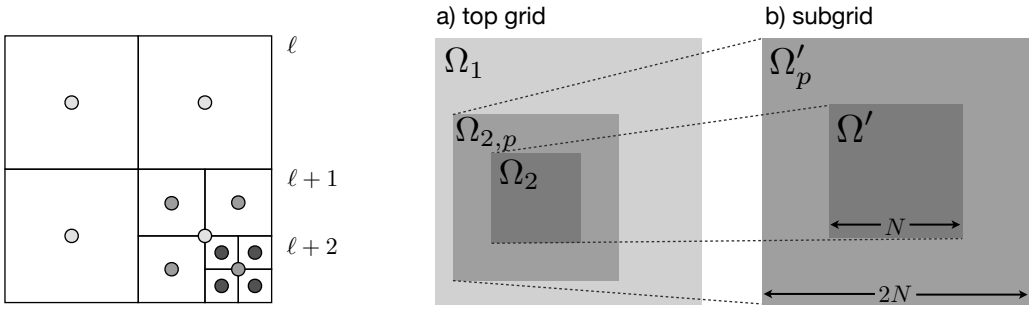

Figure 3.1: MUSIC scheme of grid refinement. *Left*: Volume subdivision of the top level ℓ into a first $\ell+1$ and a second $\ell+2$ refined level. *Right*: Schematic view of coarse region Ω_1, padding region $\Omega_{2,\mathrm{p}}$ (Ω'_{p}), and selected region for refinement Ω_2 (Ω') for top (refinement) grid. Figure taken from Hahn & Abel (2011).

The white noise consistency between levels is achieved as follows: For the first refinement an unconstrained white noise field is generated for levels ℓ and $\ell + 1$, with the variance of $\ell + 1$ being eight times that of ℓ. In order for white noise between the two levels to be consistent, first to preserve the Fourier modes of ℓ in $\ell + 1$, a Fourier transform is performed on ℓ and $\ell + 1$ in the region to be refined. All $\ell + 1$ modes $\mathbf{k}^{\ell+1}$ that are smaller than the Nyquist wavenumber of ℓ, i.e. $\mathbf{k}^{\ell+1} \leqslant \mathbf{k}^{\ell}_{Ny}$, are replaced with the respective Fourier coefficients from ℓ, and inverse Fourier transformed. Secondly, to ensure mass conservation white noise values of ℓ cells are replaced by the average over the eight children of the parent cell inside the region of interest. Further refinements can be computed by repeating the same steps at increasing resolution, in addition to parent cell correction at all levels starting at the finest one.

The convolution kernels $T(r)$ need to be generated for the top and refined levels. For this purpose different regions are delimited in each level, as shown in the right panel of Fig. 3.1. For the top grid domain Ω, three regions are identified, the refinement Ω_2, the padding $\Omega_{2,\mathrm{p}}$ and non-refined region $\Omega \setminus \Omega_2$; while the refined subgrid is divided into the refinemnt region Ω', and its corresponding resolution padding Ω'_{p}, which has twice the length in each dimension needed for the isolated Fourier convolutions. Starting from the finest level ℓ, the kernel is generated by evaluating the real-space transfer function $\mathcal{T}_{\mathcal{R}}(r)$ on the whole refined grid. The convolution kernel for ℓ is restricted to $\ell - 1$ by averaging the contributions due to the eight children cells when convolved with the kernel by means of for Ω_2 and $\Omega_{2,\mathrm{p}}$, while the rest of the domain is

sampled from $\mathcal{T}_{\mathcal{R}}(r)$.

The noise convolution for the top level ℓ is determined by computing $\delta^{\ell} = T^{\ell} * \mu^{\ell}$ on Ω with periodic boundary conditions automatically. For the first refinement $\ell + 1$ the density is the sum of three components

$$\delta^{\ell+1} = \delta^{\ell+1}_{\rm self} + \delta^{\ell+1}_{\rm coarse} + \delta^{\ell+1}_{\rm bnd}$$

The coarse grid contribution $\delta^{\ell+1}_{\rm coarse}$ is computed by zeroing μ^{ℓ} on Ω_2 to obtain $\mu^{\ell}_{\Omega\setminus\Omega_2}$, computing the convolution $\delta^{\ell}_{l} = T^{\ell} * \mu^{\ell}_{\Omega\setminus\Omega_2}$ and interpolating δ^{ℓ}_{l} between the levels. The self contribution $\delta^{\ell+1}_{\rm self}$ due to the subgrid alone $\mu^{\ell+1}$, is calculated by zeroing $\Omega'_{\rm p}$ to get $\mu^{\ell+1}_{\Omega'}$, and then calculate the convolution $\delta^{\ell+1}_{\rm self} = T^{\ell+1} * \mu^{\ell+1}_{\Omega'}$ using isolated boundary conditions. The correction term $\delta^{\ell+1}_{\rm bnd}$ is added to account for the fluctuations just outside Ω' in order to reduce error at the boundary, purpose for which the white noise field is subtracted from the eight children cells, and set to zero on Ω', so that it is non-zero only on $\Omega'_{\rm p}$ and obtain $\hat{\mu}^{\ell+1}_{\Omega'_{\rm p}}$, the convolution $\delta^{\ell+1}_{\rm bnd} = T^{\ell+1} * \hat{\mu}^{\ell+1}_{\Omega'_{\rm p}}$. The contribution of $\delta^{\ell+1}_{\rm bnd}$ is restricted also to the coarse grid in order to include information about fluctuations on smaller scales. Further refinements are obtained by the same steps, repeated at each refined level, with the difference that the coarse grid contribution is now computed using isolated boundary conditions on, and needs to be summed to all coarse contributions interpolated down to the desired level.

3.2 Integration of the Equations of Motion: GADGET-2

GAlaxies with Dark matter and Gas intEracT, GADGET, is a multipupose parallel TreeSPH (e.g. Hernquist & Katz 1989) code written by Volker Springel (Springel, 2005; Springel et al., 2001), capable of performing simulations of isolated self-gravitating systems that might include gas, such as the evolution and interaction of galaxies, and cosmological simulations, in order to study the evolution of the LSS of the universe. The evolution of self-gavitating collisinless fluid is performed with N-body approach, while collisional gas is computed by means of Smoothed Particle Hydrodynamics (SPH) (e.g. Gingold & Monaghan 1977; Lucy 1977); both gas and dark matter are represented by particles in this scheme. Computation of gravitational forces is achieved by a hybrid method in which long-range contributions are calculated using Fourier techniques with a Particle-Mesh approach, while short-range ones are computed using a hierarchical multipole expansion via Tree algorithm. In this chapter it is presented a general description of GADGET-2, focused on the evolution of N-body systems that interact solely by gravity. Other important aspects of the code, such as hydrodynamics and parallelization, are not described here, but it is kindly referred to the interested reader to Springel et al. (2001) for the first version of the code and to Springel (2005) for the version used in this work.

3.2.1 Fundamental Equations

Both stars and dark matter are modeled as self-gravitating fluids that are described by the collisionless Boltzmann equation coupled to Poisson equation

$$\frac{\partial f}{\partial t} + \mathbf{v}\frac{\partial f}{\partial \mathbf{x}} - \frac{\partial \Phi}{\partial \mathbf{r}}\frac{\partial f}{\partial \mathbf{v}} = 0 \tag{3.9}$$

$$\nabla^2 \Phi(\mathbf{r}, t) = 4\pi G \int f(\mathbf{r}, \mathbf{v}, t) \mathrm{d}\mathbf{v} \tag{3.10}$$

where Φ is the gravitational potential, and $f(\mathbf{r}, \mathbf{v}, t)$ is the mass density in phase-space, which in this approximation is sampled with a finite number of N tracer particles. The accuracy of this Monte Carlo approach is highly dependent on the number of particles used to populate the phase space, where a higher number of particles would essentially mean a better representation of f and a more accurate description of its evolution. The dynamics of the particles is described by the Hamiltonian

$$H = \sum_i \frac{\mathbf{p}_i^2}{2m_i a(t)^2} + \frac{1}{2}\sum_{ij} \frac{m_i m_j \varphi(\mathbf{x}_i - \mathbf{x}_j)}{a(t)} \tag{3.11}$$

where $\mathbf{x}_i$ are comoving coordinate vectors, the corresponding canonical momenta are given by $\mathbf{p}_i = a(t)^2 m_i \dot{\mathbf{x}}_i$, and a is the scale factor.

In order to suppress large-angle scattering by two-body collision, it is necessary to soften the gravitational potential at small separations. This is achieved by 'spreading' the mass of point particles using a softening kernel

$$W(r,h) = \frac{8\pi}{\pi h^3} \begin{cases} 1 - 6\left(\frac{r}{h}\right)^2 + 6\left(\frac{r}{h}\right)^3, & 0 \leqslant \frac{r}{h} \leqslant \frac{1}{2} \\ 2\left(1 - \frac{r}{h}\right)^3, & \frac{1}{2} < \frac{r}{h} \leqslant 1 \\ 0, & \frac{r}{h} > 1 \end{cases} \tag{3.12}$$

where r is the distance between two particles and h is the softening length scale. It is important to remember that for a given h, a sufficiently large number of particles is needed in order to effectively suppress the relaxation produced by two-body encounters. The softening length h for this spline kernel is equivalent to a Plummer softening length of 2.8 ϵ, this means that the minimum of the gravitational potential has the same depth for both softening lengths if

$h = 3.8\ \epsilon$. The spline kernel has the advantage that the force becomes exactly Newtonian for $r > h$ (see appendix A of Springel et al. 2001).

3.2.2 Force Computation

Tree Algorithm

Tree algorithm is a method in which gravitational force is approximated by means of a hierarchical multipole expansion. In this approach particles are grouped in such a hierarchy that the gravitational force exerted by all the members of a group on a single particle, can be approximated by the multipole moments, instead of the computed force that every single member of the group exerts on the desired particle. This approach permits to compute the force between N particles in $\mathcal{O}(N \log N)$ computations, instead of N^2 if direct summation is used.

The hierarchical grouping, which is the basis of the multipole expansion, is obtained by Barnes & Hut (1986) algorithm. The procedure starts by enclosing the whole mass distribution into a cube, known as root node. The root node is then divided by two on each direction, creating eight daughter cells, or nodes, for which the ones containing particles are iteratively subdivided into eight more sibilings, until the nodes contain a single particle, known as 'leaf' nodes. The tree is constructed such that each node contains either exactly one particle, or is progenitor to further nodes, as it is schematically illustrated in Fig. 3.2.

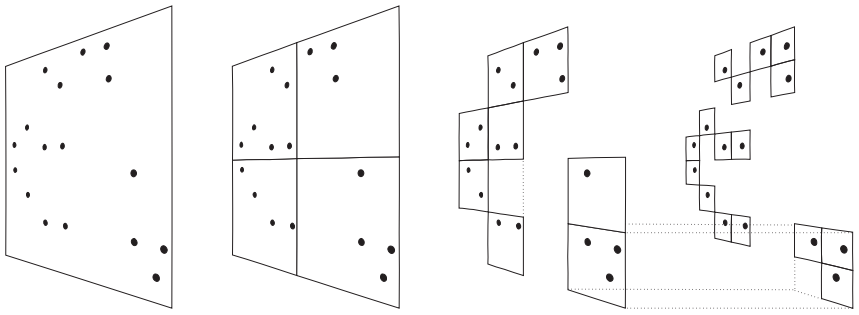

Figure 3.2: Barnes & Hut (1986) tree subdivision in two dimensions. Particles are enclosed into cubes that are iteratively subdivided by half, into eight daughter cells (nodes), until a single particle resides in each cell (leaves). Figure taken from Springel et al. (2001)

To compute the gravitational forces a 'walk' along the tree is performed. For each node, it has to be considered whether the force derived from its multipole expansion would be accurate enough or not. If true, the walk is halted and the multipole expansion is performed using the present node; if the condition is not fulfilled, the node is said to be 'opened' and the daughter

nodes are considered in turn. The accuracy of this approximation will depend highly on the opening criterion for the nodes, and will be more accurate if the tree is walked to lower levels.

There are several opening criteria that can be used while walking the tree. Two options that can be implemented in the public version of GADGET-2, the first one is a purely geometrical criterion proposed by Barnes & Hut (1986), where the force contribution of a node is considered if the particle of interest p is 'sufficiently far' from the node, such that the force from the multipole expansion results in good approximation of the true force. For a node of size l this criterion is written as

$$\theta > \frac{l}{r} \tag{3.13}$$

where θ is an accuracy parameter, and r is the distance from the center-of-mass of the node to p. For the second opening criterion, a node is considered for force computation if the amplitude of the error expected from the truncation of the multipole expansion is a small fraction of the total expected force on p. As GADGET-2 uses only monopole terms, the first non-vanishing term of the multipole expansion to be truncated is the quadrupole moment (see McMillan & Aarseth 1993). Hence the condition to be fulfilled by a node can be expressed as

$$\frac{GM}{r^2}\left(\frac{l}{r}\right)^2 \leqslant \alpha|\mathbf{a}| \tag{3.14}$$

where $(l/r)^2$ is the estimated size of quadrupole moment, α is a tolerance parameter, and $|\mathbf{a}|$ is the total acceleration of the previous timestep, which is used as an estimate of the expected force on p.

TreePM Method

TreePM is a hybrid method that results from mixing the tree algorithm and particle-mesh (PM) approach (e.g. Klypin & Shandarin 1983), in which the long-range gravitational interactions are computed via PM by Fourier methods, and the short-range is calculated by the hierarchical multipole expansion approximation via the tree method.

In this approach the gravitational potential is explicitly split in Fourier space into a long-range and short-range contributions (cf. Klessen 1997)

$$\phi_{\mathbf{k}} = \phi_{\mathbf{k}}^{\text{long}} + \phi_{\mathbf{k}}^{\text{short}} \tag{3.15}$$

with the long-range contribution

$$\phi_{\mathbf{k}}^{\text{long}} = \phi_{\mathbf{k}} \exp(-\mathbf{k}^2 r_s^2) \tag{3.16}$$

where r_s is the length scale of the force split. The short-range contribution of the potential for $r_s \ll L$ in real space is given by

$$\phi^{\text{short}}(\mathbf{x}) = -G \sum_i \frac{m_i}{r_i} \text{erfc}\left(\frac{r_i}{2r_s}\right) \tag{3.17}$$

where r_i is the smallest distance of any of the images of particle i to the point $\mathbf{x}$. As the complementary error function *erfc* suppresses rapidly the force for distances large compared to r_s, only the nearest image has any chance to contribute to the short-range force. This contribution to the force is computed by tree algorithm with the force law being modified by the short-range cut-off factor.

For the PM approach the mass assignment is done using CIC interpolation (Hockney & Eastwood, 1981) on the mesh to get the real-space density field. The discretized density field is then Fourier transformed and multiplied with the Green function in periodic boundaries $-4\pi G/k^2$ (see e.g. Efstathiou et al. 1985) modified by the exponential truncation to get $\phi_{\mathbf{k}}^{\text{long}}$. The result is then deconvolved twice for the CIC kernel $\text{sinc}^2(k_x L/2N_{\text{grid}})\text{sinc}^2(k_y L/2N_{\text{grid}})\text{sinc}^2(k_z L/2N_{\text{grid}})$ (see e.g. Hockney & Eastwood 1981), one time to correct for the smoothing effect of the CIC in the mass assignment, and a second one for the force interpolation. Lastly, the result is inverse Fourier transformed to obtain the gravitational potential on the mesh.

The force is calculated then by means of finite difference approximation (FDA), using the four-point differentiation rule

$$\left.\frac{\partial \phi}{\partial x}\right|_{ijk} = \frac{1}{\Delta x}\left[\frac{2}{3}(\phi_{i+1,j,k} - \phi_{i-1,j,k}) - \frac{1}{12}(\phi_{i+2,j,k} - \phi_{i-2,j,k})\right] \tag{3.18}$$

where $\Delta x = L/N_{\text{grid}}$ is the mesh spacing. Then, the particle positions are interpolated using CIC for consistency.

Zoom-in simulations with TreePM

The TreePM implementation can be extended to increase resolution in a desired region, i.e. for Zoom-in simulations. In order to calculate the gravitational interaction it has to be taken into account that the simulation volume is divided in two regions, a low- and a high-resolution

one, with the last one being defined as the region occupied by the selected high-resolution particles.

The low-resolution interactions are computed the same as the standard TreePM method (see above), where gravitational potential is splitted in a characteristic scale length r_s, while for the high-resolution region forces are splitted in three: the long-, mid- and short-range contributions. The cut-off scale between long- and mid-range contributions being the same r_s as for low-resolution region, and for mid- and short-range interactions a different scale length r'_s is used, which is determined by the scale of the region where high-resolution particles reside. Mid-range forces are computed by incorporating a second mesh in which PM algorithm is implemented for non-periodic boundary conditions with its proper Green function.

3.2.3 Time integration

The symplectic nature of the leap-frog integrator can be understood by noticing that the position update is equivalent to evolving the system under the Hamiltonian $H_D = 1/2\ v^2$, and the velocity update under the Hamiltonian $H_K = \Phi(r)$ (Quinn et al., 1997). The operator that evolve the system under H_D is called drift operator D, while the one that does under H_K is the kick operator K (Quinn et al., 1997)

$$D_t(\Delta t): \begin{cases} \mathbf{p}_i & \rightarrow & \mathbf{p}_i \\ \mathbf{x}_i & \rightarrow & \mathbf{x}_i + \dfrac{\mathbf{p}_i}{m_i} \displaystyle\int_t^{t+\Delta t} \frac{\mathrm{d}t}{a^2} \end{cases} \tag{3.19}$$

$$K_t(\Delta t): \begin{cases} \mathbf{x}_i & \rightarrow & \mathbf{x}_i \\ \mathbf{p}_i & \rightarrow & \mathbf{p}_i + \dfrac{\mathbf{f}_i}{m_i} \displaystyle\int_t^{t+\Delta t} \frac{\mathrm{d}t}{a} \end{cases} \tag{3.20}$$

where $\mathbf{f}_i$ is the force experienced by particle i. A time integration scheme can be derived by alternating these operators to update the position and velocity of a particle. The time integration scheme that GADGET-2 adopts is given by the time evolution operator $\tilde{U}(\Delta t)$ for an interval Δt by

$$\tilde{U}(\Delta t) = K\left(\frac{\Delta t}{2}\right) D(\Delta t) K\left(\frac{\Delta t}{2}\right) \tag{3.21}$$

known Kick-Drift-Kick (KDK) integration scheme. Although a Drift-Kick-Drift (DKD) scheme is also valid, Springel (2005) has shown that energy error in DKD grows four times the energy error produced by KDK due to time asymmetry of the leap-frog integration.

Individual and adaptive time-steps are also implemented in GADGET-2. These are required due to the large dynamic range present in simulations. Forces are then computed only for a certain group of particles in a given kick operation, while the other particles being evolved on larger time-steps and being "kicked" more rarely (Springel, 2005). Taking into account that the long-range force contribution changes more slowly than the short-range one, the time evolution operator $\tilde{U}(\Delta t)$ becomes

$$\tilde{U}(\Delta t) = K_{\rm lr}\left(\frac{\Delta t}{2}\right) \times \left[K_{\rm sr}\left(\frac{\Delta t}{2m}\right) D\left(\frac{\Delta t}{m}\right) K_{\rm sr}\left(\frac{\Delta t}{2m}\right)\right]^m K_{\rm lr}\left(\frac{\Delta t}{2}\right) \tag{3.22}$$

where m is a positive integer, $K_{\rm lr}$ and $K_{\rm sr}$ are the long- and short-range kick operators respectively. In this scheme the short-range evolution is performed explicitly by cycling a series of KDK operations, where forces are computed by Tree algorithm, between $K_{\rm lr}$ operations, where forces are calculated using PM method, this scheme exploits the fact that PM forces are updated on all the grid at the same time.

The time-step criterion implemented in GADGET-2 for collisionless particles has the form

$$\Delta t_{\rm grav} = \min\left[\Delta t_{\rm max}, \left(\frac{2\eta\epsilon}{|\mathbf{a}|}\right)^{1/2}\right] \tag{3.23}$$

where η is an accuracy parameter, ϵ is the gravitational softening, and $|\mathbf{a}|$ is the acceleration of the particle. Both η and $\Delta t_{\rm max}$ are input parameters at the beginning of a simulation. When TreePM method is used, this time-step criterion only applies to the short-range dynamics, while the size of the PM step is determined by $\Delta t_{\rm max}$.

3.3 Halo identification tool: AHF

AMIGA HALO FINDER (AHF) is a numerical tool developed by Knollmann & Knebe (2009) from a previous version MHF by Gill et al. (2004), that identifies and analyzes dark matter halos in cosmological simulations. AHF's identification algorithm follows an Adaptive Mesh Refinement (AMR) scheme (e.g. Klypin et al. (2001); Kravtsov et al. (1997)), capable of distinguishing up to several levels of substructure inside the identified dark matter halos. In this section it is briefly presented the algorithm that AHF follows to identify dark matter halos and their corresponding substructure on a cosmological simulation. For further details, such as parallelization and comparison with other halo identification tools, the interested reader is referred to Knollmann & Knebe (2009) and AHF's user manual.

To find bound structures in a simulation AHF starts by covering the whole simulation box with a uniform grid, the domain grid. In each cell of the domain grid the particle density, not mass density, is calculated by means of a Triangular-Shaped-Cloud (TSC) (Hockney & Eastwood, 1981) weighing scheme. If the particle density in a cell exceeds the refinement criterion for the domain grid, the cell is then covered with a finer grid of half the side length. Then on each cell of the refined grid, the particle density is recalculated, and an additional cell is constructed if the particle density exceed the refinement criterion for a fine grid. This procedure is repeated until all the cells from the finest grid do not exceed the refinement criterion and no additional grids need to be constructed. This procedure is visualized in the left panel of Fig. 3.3 where three different level of refinement grids are shown in magenta, superimposed to a density render in green.

Halos and their respective substructure are easy to find due to the hierarchy of the constructed grids. From the finest grid, isolated regions are identified and marked as possible halos. On the next level, the same procedure is repeated, but now the identified regions from the finer grid are linked to their corresponding volume in the coarser grid. A tree of nested grids is constructed, where halos are followed from the finest level, leaves, to the coarser levels, branches, until background density is reached. If two marked regions are isolated in a fine level, but are linked on the next coarser grid, the two branches of the grid tree join. This is schematically shown in the top row of the right panel of Fig. 3.3, where nested rectangles represent the leaves and branches of the tree.

The classification of substructure is done by processing each tree starting from the coarsest level downward to the finer ones. If a level, or branch, splits into two or more, it has to be decided where the main branch continues, hence which one of the refinements represents the host halo. This decision is made by counting the particles contained within each of the refinements, and the one containing the most particles is considered as the main branch, whereas the others are marked as substructures. As this procedure is recursive, sub-substructures can also be identified. This is shown in the colored rows of the right panel of Fig. 3.3; the yellow branch is first refined only once (third row), and then refined into two (fourth row), where the finest yellow branch marks the host halo, and the orange a subhalo.

The list of all halos (host and substructure) is constructed in the following way. First, all particles inside a leaf are assigned to the center of the grid where they lie. When two halos 'meet' on a coarse level, all particles within a sphere with radius of half the distance to the host halo are assigned as possible members of the subhalo. The edge of the subhalo is determined first by determining the position where its density profile encounters a minimum before it starts to rise due to the presence of the host halo (see AHF's user manual); then unbound particles

are removed (see appendix of Knollmann & Knebe 2009) and the size of the halo is re-adjusted one more time. The host halos are initially determined by all particles that reside up to the radius where the isodensity contour $\rho_{\rm iso}$ exceeds virial oversendity $\Delta_{\rm vir}$ times the background density ρ_b, i.e. $\rho_{\rm iso} < \Delta_{\rm vir}(z)\rho_b$. Then, as done with subhalos, the halo is considered in isolation and unbound particles are iteratively removed.

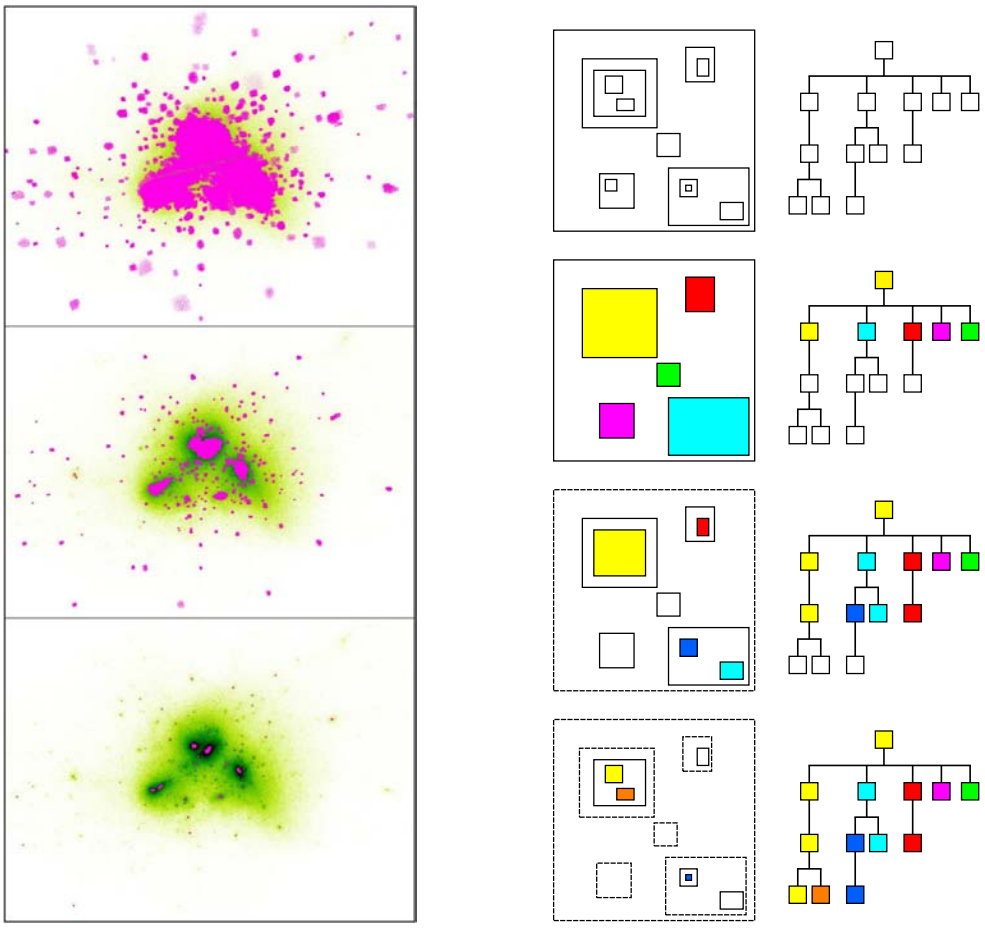

Figure 3.3: AHF identification algorithm. *Left panel.* Three consecutive refinement levels of grid structure (magenta) superimposed to a projected density render (yellow-green) of a particle distribution. *Right panel.* Classification of grid refinements in a tree structure. The top row shows an arbitrary grid structure on the left with its corresponding tree structure on the right. The host halo and subhalos are identified first by considering the whole coarsest grid as part of the host halo, subsequently, the main branch continues in the isolated region that has the largest number of particles; 'sub-branches' are also split in the same way. In the second row it is shown that the yellow region is selected as host halo while the others are automatically marked as substructure. The third row shows how sub-substructure can be identified when repeating the same procedure for subhalos: the host subhalo is the one with the largest number of particles (light blue) and other regions are marked as sub-subhalos (dark blue). *Note.* Colors between left and right panels are not related. Figures taken from Gill et al. (2004) and Knollmann & Knebe (2009) respectively.

Properties of halos and subhalos, such as mass, spin, triaxiality, among others, are computed using the list of bound particles obtained from the procedure described above. These properties are the ones that were considered to select the dark matter halos used in this study. Further details are presented in Chapter 4.

3.4 Construction of Stellar Systems in Equilibrium: The Iterative Method

The iterative method described by Rodionov et al. (2009), is an algorithm for constructing phase models in equilibrium. This method was originally proposed by Rodionov & Sotnikova (2006), updated in Rodionov & Orlov (2008), with its final version for constructing stellar and dark matter systems in Rodionov et al. (2009), an extension of this method for a baryonic component is presented in Rodionov & Athanassoula (2011), but that implementation is beyond the purposes of this work.

The algorithm implemented in this method permits to construct systems with an arbitrary desired mass distribution and kinematic properties. The algorithm of this method is based on constrained, or guided evolution, in order that the solution presents a number of desired kinematic parameters or constraints, and the fact that any non-equilibrium system will tend more or less fast to a stable equilibrium (Rodionov et al., 2009). The iterative method is useful for the construction of initial conditions for N-body simulations of stellar systems, and as will be explained in Chapter 4 it is used in this work to initialize the velocities of stellar disks in cosmological dark matter halos.

The procedure starts by constructing an N-body system with a desired mass distribution. The system is then evolved for a small period of time, small enough to prevent instabilities to develop. After this 'infinitesimal' evolution, the system will not have the initial mass distribution nor the desired kinematic properties, and here is where adjustments are made. The mass distribution is easily corrected by preserving a copy of the initial distribution of the system, and to retain memory of the evolution the velocities then need to be transfered from the evolved system to the original one. Additionally, if kinematic constrains are needed, adjustments to the velocities of each particle need to be made, without modifying other parameters. These steps are iteratively repeated until the system is sufficiently closed to an equilibrium state and has the desired mass distribution and kinematic properties.

For example, if a specific radial velocity dispersion profile $\sigma_R(R)$ is desired for a galaxy, after each evolutionary step, the radial velocity of the particles need to be changed in order to fix the radial profile. The model is divided into $n_{\rm div}$ concentric cylindrical annuli, and for each annulus

j, the target value of $\sigma_R^j = \sigma_R(R_j)$ is computed, where R_j is the mean value of the R coordinate of all particles in the jth ring. The new velocity of the ith particles in the j region is modified as

$$v_{R,i} = v'_{R,i}\frac{\sigma_R^j}{\sigma_R'^j} \tag{3.24}$$

where $v'_{R,i}$ is the current value of the radial velocity of the ith particle, $v_{R,i}$ is the corrected ith particle radial velocity, and $\sigma_R'^j$ is the current value of radial velocity dispersion in part j (Rodionov et al., 2009). Using this scheme permits that the $\sigma_R(R)$ profile of them model converges to the desired profile.

For further examples and details on the iterative method, such as the velocity transfer from the evolved model to the original system, the interested reader is referred to Rodionov et al. (2009), Rodionov & Sotnikova (2006) and Rodionov & Orlov (2008).

Chapter 4

Methodology

In this chapter the methodology followed to simulate the dynamics of stellar disks in cosmological dark matter halos is presented. This chapter has been organized as follows: In section 4.1 is described how the host halos of the galaxies were selected from low-resolution cosmological simulations, and then re-simulated using the zoom-in technique to achieve a higher space and mass resolution. In Section 4.2 the method used to approximate the growth of a galactic disk at the center of the selected halos is presented. In this study instead of studying a unique disk model for all halos (e.g. DeBuhr et al. 2012; Yurin & Springel 2015), a semi-analytic model (Mo et al., 1998) was used to determine the properties of the simulated disks based on those of their host halos, thus a disk with unique properties is obtained for each one of the selected halos. Each disk is then oriented with its angular momentum $L_{\rm disk}$ making an angle $\theta_{\rm ori}$ with respect to its host halo principal axes of the inertia tensor. Finally, disks are taken to dynamical equilibrium by iteratively evolving their initial state so that the halo-disk system starts its evolution in a relaxed state. The parameters of all simulations are also given throughout this chapter.

4.1 High Resolution Cosmological MW-like Halos

Cosmological simulations and simulations on the dynamics and evolution of galaxies differ typically several orders of magnitude in size and mass (e.g. Boylan-Kolchin et al. 2009; Dubinski et al. 2009; Klypin et al. 2011), this is why it is sometimes difficult or even impossible to study the dynamics of galaxies in a cosmological context without a huge amount of computational resources (e.g Vogelsberger et al. 2014a).

There are several approximations that can be used to tackle this problem. One of them is to simulate smaller cosmological periodic boxes with a constant overdensity (or underdensity)

in order to account for large-scale perturbations (the DC mode, Pen 1997; Sirko 2005, e.g. simulations by Zemp et al. 2012). Other method, the so-called zoom-in technique, consists on identifying a region of interest in a low-resolution cosmological simulation, and add a greater number of particles at the initial condition in that region to obtain a higher space and mass resolution (e.g. Avila-Reese et al. 2011; Colín et al. 2010; Springel et al. 2008). The later approach is adopted in this study.

The whole set of simulations were run in accordance to the ΛCDM cosmological model characterized by the density parameters of $\Omega_{\rm m} = 0.288$ and $\Omega_\Lambda = 0.712$, the mass fluctuation in a sphere of 8 h^{-1} Mpc of $\sigma_8 = 0.830$, spectral index $n_s = 0.971$, and a Hubble constant of $H_0 = 69.33$ km s^{-1}Mpc^{-1} at the present time. These values are consistent with the cosmological constraints from WMAP-9 (Hinshaw et al., 2013).

To set up the disk simulations, the first step was to run an N-body cosmological simulation of 512^3 particles on a box of 100 h^{-1}Mpc per side, in order to identify dark matter halos whose properties resemble the ones of the Milky Way's dark matter halo, this was achieved with Amiga Halo Finder AHF (see Section 3.3), a publicly available halo identification tool (Gill et al., 2004; Knollmann & Knebe, 2009). Halos were selected by setting restrictions on the host halo mass ($9 \times 10^{11} \leqslant M_{\rm halo}/h^{-1}\, M_\odot \leqslant 1.25 \times 10^{12}$), a 'quiet' accretion history (maximum mass accreted in a merger of $M_{\rm sub} < 1.2 \times 10^{10} M\odot$) since $z = 1$, and an isolation criterion, so that there's not a neighbor with mass $M_{\rm neighbor} > 0.5 M_{\rm halo}$ inside a sphere of radius of 2 h^{-1} Mpc at $z = 0$, in order to study the secular evolution of MW-like galaxies in a cosmological context.

Since the 512^3 uniform cosmological simulation requires a lot of computational resources (e.g. RAM memory) in regions that might be not of interest, a lower mass resolution simulation was carried out using 256^3 particles on the same box, so that the selected halos in the high-resolution simulation were identified in this new lower-resolution one and were re-simulated later with the zoom-in technique. In this way, most of the computational effort is focused in the region of interest. Figure 4.1 compares the large-scale structure (LSS) of the universe in both simulations at different redshifts. The same process for selecting dark matter halos was repeated for the 256^3 simulation, with the intention of finding halos that resemble the ones found in the 512^3 simulation. If a halo was found with the same properties in both runs, it was marked as a possible candidate. Several halos met the requirements in both simulations, but only four of them were chosen for the purpose of this work.

MUSIC (Hahn & Abel, 2011) (see Section 3.1) was used to increase by a factor of 4096 times better mass resolution for the regions of interest of the 256^3 simulation. The particles in the region with the highest resolution reached an effective mass equivalent to a uniform simulation of 4096^3 particles in a box of the same size, but without the huge computational cost that such

simulation would imply. Table 4.1 lists the parameters of all dark matter-only simulations, including the two uniform (CAMB-256, CAMB-512) and the four zoom-in simulations of the selected halos. A visual example of a selected halo and its enclosing region for all resolutions is illustrated in Figure 4.2, and a detailed comparison of all halos at $z = 0$ is given in Table 4.2.

Table 4.1: Parameters of all dark matter-only simulations. $N_{\rm p}$ indicates the number of particles in the simulation with mass $M_{\rm p}$. For the zoom-in simulations $N_{\rm p}$ with asterisk indicates the total number of particles in the whole simulations, while $N_{\rm p}$ without asterisk indicates the number of particles in each of the refinement levels.

Name	Type	$L_{\rm box}$ [h^{-1} Mpc]	N_p	$M_{\rm p}$ [h^{-1} $M_\odot$]
CAMB-256	uniform	100	16,777,216	4.764×10^9
CAMB-512	uniform	100	134,217,728	5.955×10^8
3180-cosmo	zoom-in	100	*18,997,714	-
			16,765,624	4.764×10^9
			70,986	5.955×10^8
			115,920	7.443×10^7
			23,8848	9.304×10^6
			1,806,336	1.163×10^6
3741-cosmo	zoom-in	100	*18,889,298	-
			16,765,666	4.764×10^9
			71,600	5.955×10^8
			109,376	7.443×10^7
			243,840	9.304×10^6
			1,698,816	1.163×10^6
3748-cosmo	zoom-in	100	*19,085,424	-
			16,765,204	4.764×10^9
			73,996	5.955×10^8
			115,024	7.443×10^7
			260,352	9.304×10^6
			1,870,848	1.163×10^6
3795-cosmo	zoom-in	100	*18,827,124	-
			16,765,696	4.764×10^9
			71,460	5.955×10^8
			109,456	7.443×10^7
			244,672	9.304×10^6
			1,635,840	1.163×10^6

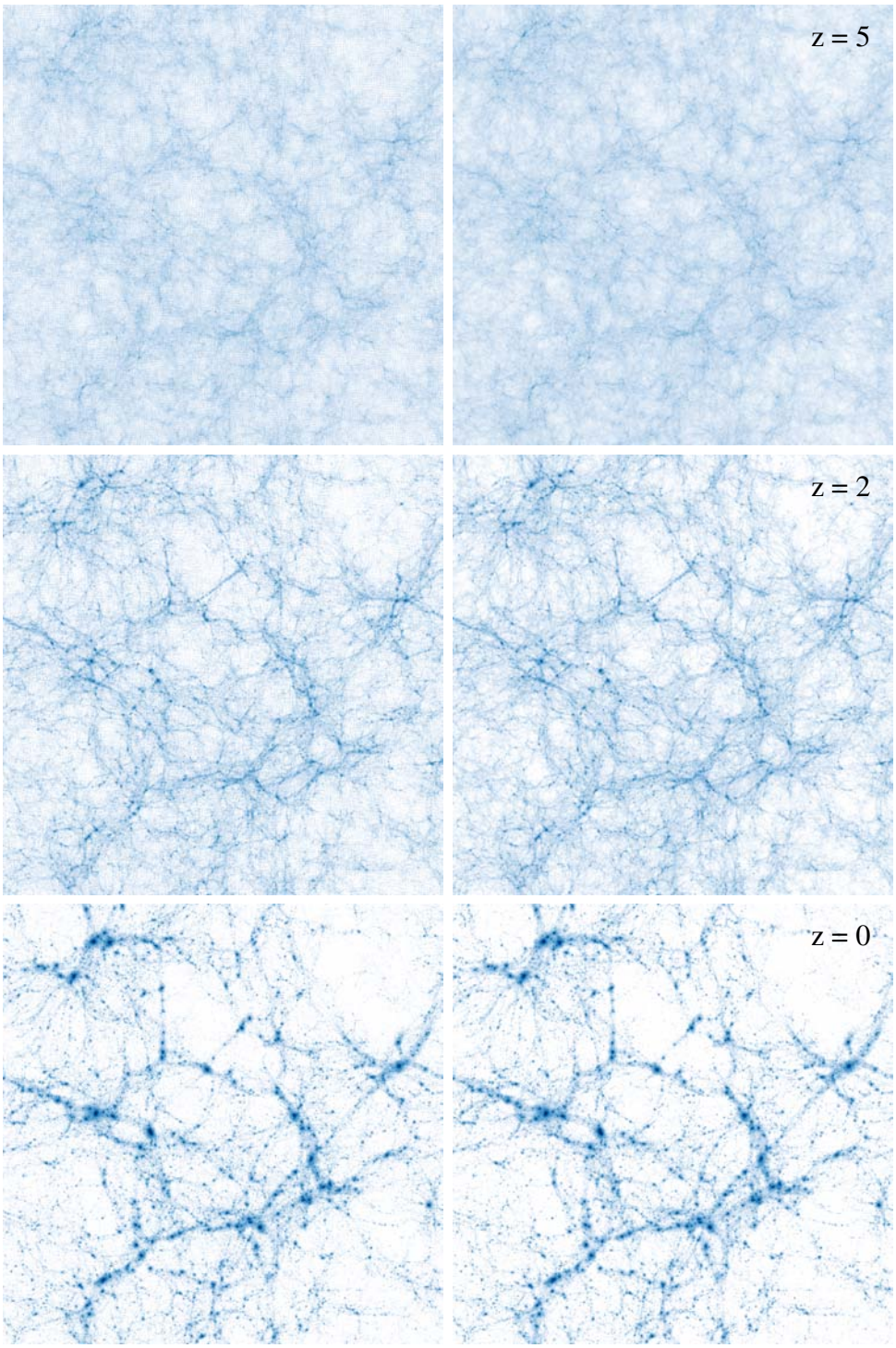

Figure 4.1: Slices of the evolution of the cosmological simulations CAMB-256 (256^3 particles, left column) and CAMB-512 (512^3 particles, right column), the redshift is indicated at each row. The LSS is well represented by the lower resolution simulation, in comparison to the high-resolution one. The slices shown have 100 h^{-1} Mpc on each side and 40 h^{-1} Mpc depth.

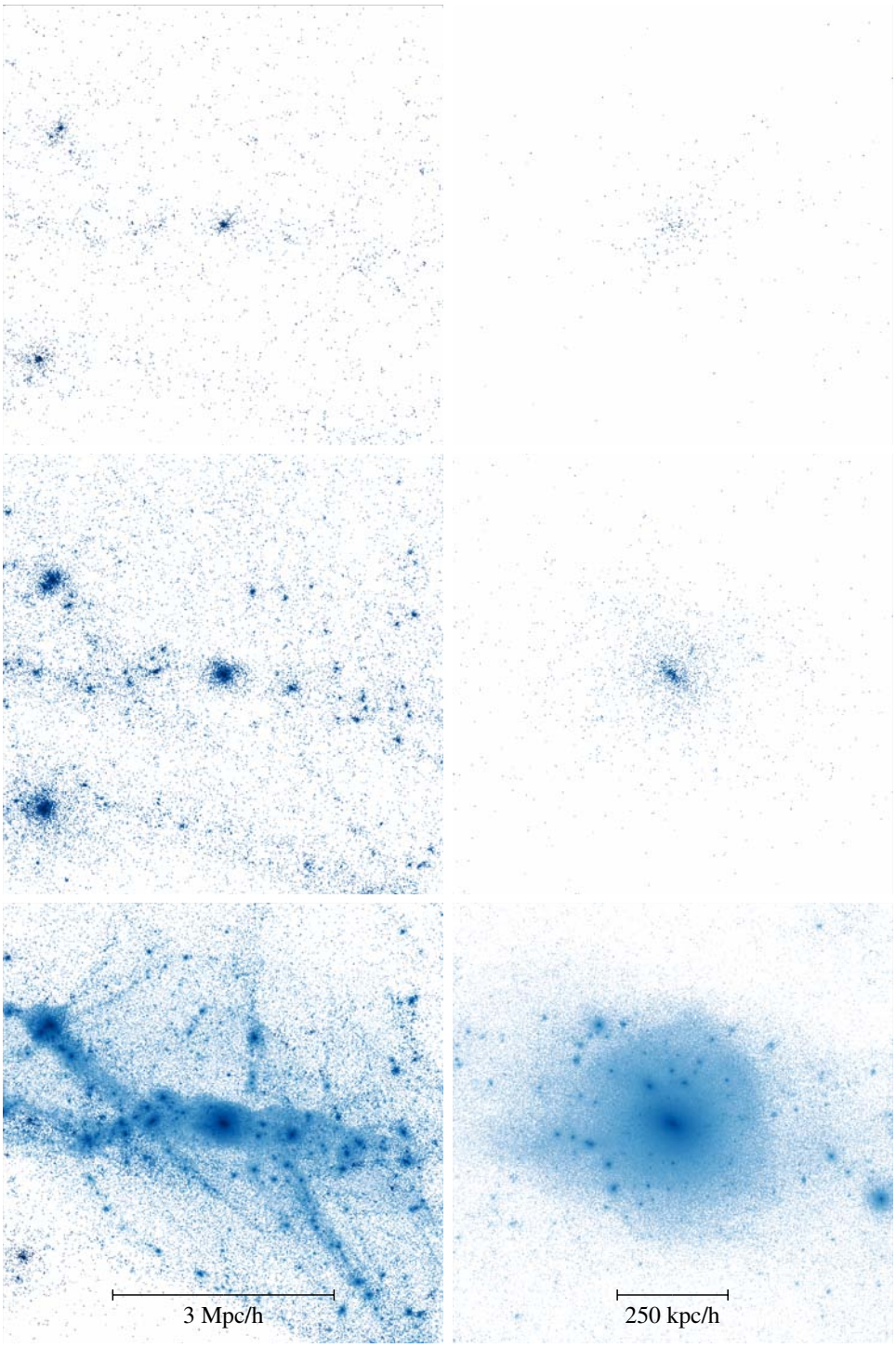

Figure 4.2: Halo `3180` (right column) and its surrounding region (left column) at $z = 0$ in simulations CAMB-256 (top row), CAMB-512 (middle row), and 3180-cosmo (bottom row). Zoomed-in region has 512 (4096) times better mass resolution than 512^3 (256^3) particle simulation, see Table 4.1 for comparison of particle masses.

Table 4.2: Characteristics of the four selected dark matter halos in cosmological simulations of 256^3, 512^3 particles and the zoom-in ones. $N_{\rm p}$ refers to the number of particles that constitute the halo, $R_{\rm vir}$ virial radius, $V_{\rm c}$ is the maximum of the circular velocity, b/a is the ratio of the intermediate to major axis of inertia tensor, c/a is the ratio of minor to major axis, and concentration c. These characteristics are given by AHF, and are computed using all particles inside $r_{\rm vir}$.

Halo	Simulation	$M_{\rm vir}$ [10^{12} h^{-1} $M_\odot$]	N_p	$R_{\rm vir}$ [h^{-1} kpc]	$V_{\rm c}$ [km/s]	b/a	c/a	c
3180	CAMB-256	1.353	231	272.76	199.56	0.775	0.726	16.664
	CAMB-512	1.376	1,781	274.13	198.93	0.962	0.857	16.091
	3180-cosmo	1.368	1,065,511	273.37	196.99	0.961	0.794	15.612
3741	CAMB-256	1.162	194	262.36	193.27	0.892	0.824	18.227
	CAMB-512	1.267	1,595	267.13	193.78	0.926	0.899	16.217
	3741-cosmo	1.229	985,195	263.81	198.36	0.923	0.838	18.271
3748	CAMB-256	1.291	194	274.61	198.93	0.866	0.753	18.173
	CAMB-512	1.190	1,548	261.07	191.08	0.853	0.751	16.582
	3748-cosmo	1.188	910,586	260.84	196.43	0.864	0.751	18.377
3795	CAMB-256	1.233	192	264.32	196.26	0.912	0.837	17.526
	CAMB-512	1.298	1,685	168.88	197.49	0.887	0.833	16.842
	3795-cosmo	1.355	991,510	272.51	197.11	0.814	0.686	15.837

4.2 Including the Stellar Disks in the Cosmological Halos

Galaxy formation cannot be completely understood without including baryons and its physics, hence they have to be simulated to some extent at least. The approach followed in this study assumes an adiabatic growth of a rigid exponential disk potential using a fixed distribution of particles. In this way the shape and dynamics of the host dark matter halos respond to the presence of a slowly growing disk, instead of suddenly inserting several $10^{10} M_\odot$ at the center of the dark matter halo, which would generate undesired artificial effects.

For simplicity a linear growth of the mass of the disk $m_{\rm d}$ was assumed between an initial redshift $z_{\rm insert}$, when the disk is inserted, and a final redshift $z_{\rm live}$, when the disk stops growing and reaches the assumed total mass for this component. This work adopts $z_{\rm insert} = 1.3$ and $z_{\rm live} = 1.0$, same as DeBuhr et al. (2012) and Yurin & Springel (2015). The mass density distribution of the disk is simply a time dependent function of the total mass, more specifically

$$\rho(R, z, a) = \frac{m_{\rm d}(a)}{4\pi R_{\rm d}^2 z_{\rm d}} \, e^{-R/R_{\rm d}} \, \mathrm{sech}^2\left(\frac{z}{z_{\rm d}}\right) \tag{4.1}$$

with R and z being the cylindrical coordinates, $R_{\rm d}$ and $z_{\rm d}$ are the radial and vertical scales of the disk respectively, a is the cosmological scale factor, and $m_{\rm d}$ is the total mass of the disk at a given time, with $m_{\rm d}(z_{\rm live}) = M_{\rm d}$. The $M_{\rm d}$, $R_{\rm d}$ and $z_{\rm d}$ of all disks were estimated with the method described by Mo et al. (1998), in which the radial scale length of the disks depends on the host halo properties, so the size of the disks will change from one halo to another.

In this method all the disks start to grow with an initial mass of $m_{\rm d} = 1\ M_\odot \times N_{\rm p}$ at $z_{\rm insert}$, this is done to avoid computational errors when calculating the gravitational interaction between massive and massless particles with GADGET-2 (Springel, 2005; Springel et al., 2001). For the parameters used in this work this would mean an initial disk mass of $5 \times 10^5 M_\odot$ distributed among 500,000 particles, which is less than the mass of a single particle of the highest resolution, as shown in Table 4.1. This approach is somewhat similar to the one implemented by DeBuhr et al. (2012) and Yurin & Springel (2015), nevertheless some procedures in DeBuhr et al. (2012) methodology are not explained throughly, in addition that both DeBuhr et al. (2012) and Yurin & Springel (2015) approaches use a unique disk model for all their studied halos, in contrast with our procedure, as indicated above.

In order to achieve our objective two modifications to the public version of GADGET-2 were performed. The first modification increases the DISK-type particle masses according to Eq. (4.1), between $z_{\rm insert}$ and $z_{\rm live}$. The second modification arises from the necessity that the positions of the disk particles remain fixed during the disk's growth to maintain the desired potential, and that the distribution stays always centered at the minimum of the halo potential well, to approximate correctly the growth of a galaxy. The 'best' approach, using only N-body computation, would be to calculate the center of mass or center of the potential each time-step, and place all the disk particles at that position at all times. This would imply a considerable amount of computational cost, because (a) the identification of new host halo particles due to accretion, and (b) due to the computation of its gravitational potential and finding its minimum. Instead an alternative approach is implemented in this work, this consists in inserting a test live particle at the center of the halo, moving with halo instantaneous velocity at $z_{\rm insert}$, and track it as it moves along with the halo center, disks particles would simply copy the displacements of the tracking particle.

Despite the simplicity of this method, its precision is highly dependent on the number of particles in the vicinity of the desired location, and the mass of the test particle. As it is a live particle, it interacts gravitationally with the rest of the halo making it orbit around the halo center. To test the accuracy of this method five simulations were run, changing the mass of the tracking particle and adding the initial nearly massless disk. The masses adopted for the test particle were 1 $M_\odot$, 1, 8 and 64 times the *highest resolution dark matter particle* (hrdmp, see

Table 4.1). Results are shown in Figure 4.3.

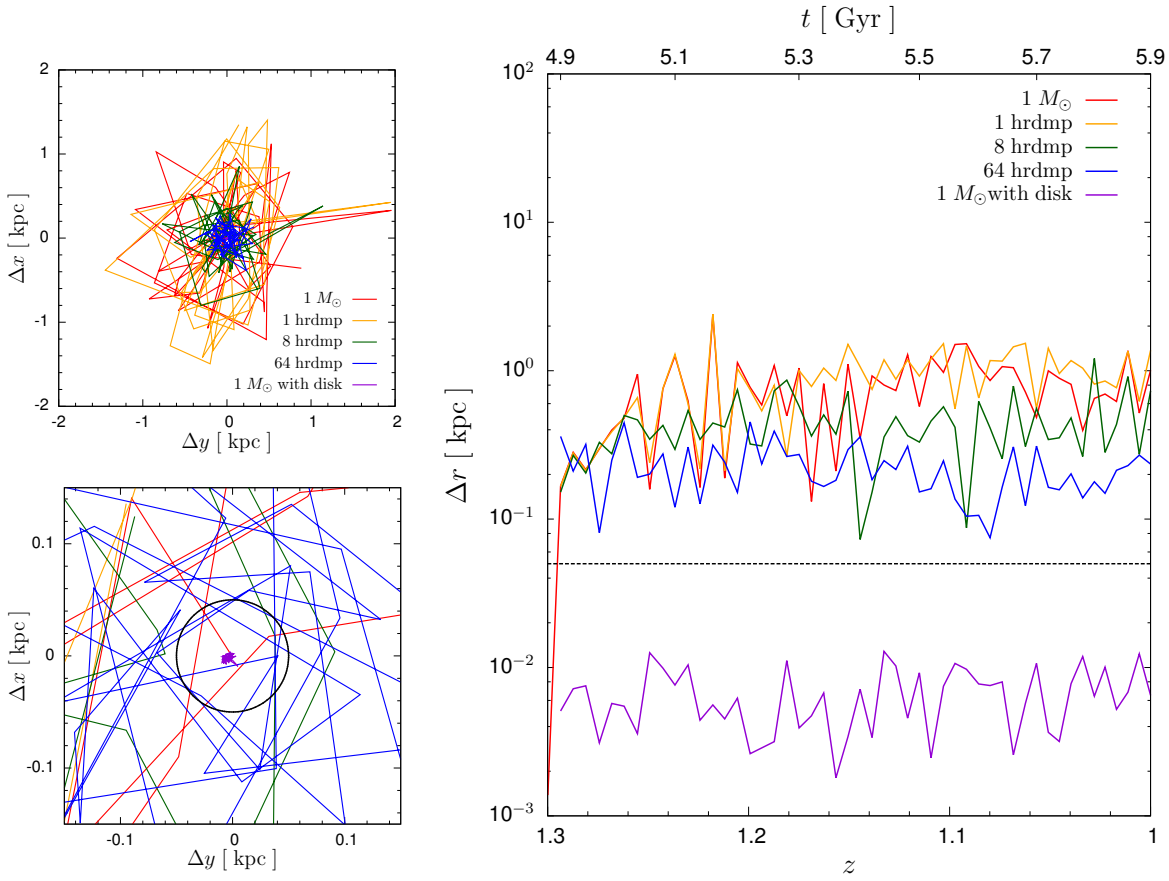

Figure 4.3: Distance between halo center and the tracking particle from $z = 1.3$ to $z = 1.0$ for different tracking particle masses. Left panels show xy distance, a black circle indicates softening length $h_{\rm soft}$ used for disk particles. Right panel shows $\Delta r = \sqrt{\Delta x^2 + \Delta y^2 + \Delta z^2}$, the dotted line indicates $h_{\rm soft}$. The method implemented including the disk remains well centered with deviations below $h_{\rm soft}$.

As expected the higher the mass of the tracking particle, the less movement it has with respect to the center of the halo, but the more it would affect the local particle distribution at the center of the dark matter halo. The top-left panel of Figure 4.3 shows that despite the center of the halo is followed by the tracking particle, high deviations are presented for the scales of interest, since the distance between the center and the particle is several times the typical vertical scale, $z_{\rm d}$, of galactic disks. The large variation is a consequence of the small number of dark matter particles at the very center of the halo. This problem was solved by adding the disk particles that populate the region of interest, making the tracking particle movement to be restricted to a radius much smaller than $R_{\rm d}$ and $z_{\rm d}$, and, most important, below the softening

length $h_{\rm soft} = 50\ h^{-1}\,{\rm pc}$, used for disk particles in all simulations. Displacement is shown in Figure 4.3 as a magenta line, and $h_{\rm soft}$ as a black circle in the bottom-left panel, and a dotted line in the right panel.

Previous work (e.g. Hayashi et al. 2007) has shown that halo angular momentum is expected to align parallel to the minor axis of the inertia tensor of the halo. Nonetheless, principal axes of the inertia tensor and angular momentum of cosmological halos change between their inner and outer parts (e.g. Bett & Frenk 2012). Hence, a disk aligned parallel to a principal axis of halo inertia tensor, does not necessarily is aligned parallel to its angular momentum. Motivated by this fact several orientations of disk angular momentum $L_{\rm disk}$ are explored.

In order to discern the effects of the triaxility of the halo, $L_{\rm disk}$ was oriented with respect to the principal axes of the inertia tensor of the host halo. This study hence follows a similar procedure as the one adopted by DeBuhr et al. (2012) and Yurin & Springel (2015), and extends the same by investigating additional orientation that were not presented in those works.

The simulations were run by orienting the disk (a) with its angular momentum $L_{\rm disk}$ parallel to the minor $C_{\rm halo}$ and major $A_{\rm halo}$ axis of the inertia tensor, (b) with $L_{\rm disk}$ making an angle $\theta_{\rm ori}$ with respect to the $C_{\rm halo}$, oriented along the minor-major axis plane, and (c) with the disk rotating in the opposite direction of the original orientation. The principal axes of the moment of inertia tensor were calculated using particles inside a sphere containing half mass of the halo at $z_{\rm insert}$. In Fig. 4.4 these orientations are illustrated for a halo-disk system at $z_{\rm insert}$ and $z_{\rm live}$. In this figure it can also be seen that during the disk growth the particle distribution does not change in size, and the disk is growth by increasing the mass of disk particles. It is important to notice that for each halo a unique disk (particle distribution) is used for all orientations.

The characteristics of all disk simulated are enlisted in Table 4.3. Orientations indicated as 'minor' are the ones in which $L_{\rm disk}$ is oriented parallel to $C_{\rm halo}$, 'major' when $L_{\rm disk}$ is parallel to $A_{\rm halo}$, and, '30deg' and '60deg' when $L_{\rm disk}$ is making an angle $\theta_{\rm ori}$ with respect to $C_{\rm halo}$ of 30 and 60 degrees respectively; disks for which an opposite angular momentum orientation was explored are marked as 'spin'.

The mass contribution of halo and disk component to the system is shown in Fig. 4.5, where the rotation curve is displayed for all minor-oriented disks at $z_{\rm live}$. For simplicity the rotation curve is computed as the circular velocity V_c that corresponds to all the mass inside a sphere of a given radius r, i.e.

$$V_c = \sqrt{\frac{GM(<r)}{r}} \tag{4.2}$$

where, G is the gravitational constant, $M(<r)$ is the total mass within a sphere of radius R.

For all disks except 3795, the mass contribution at small radii is slightly dominated by the disk, while at outer radii V_c is dominated by the halo, where a flat rotation curve is displayed by all the systems. As the same disk was used for all orientations and the mass contribution is averaged on spherical bins, similar rotation curves are displayed by all disk orientations, hence only V_c for minor-oriented systems are shown.

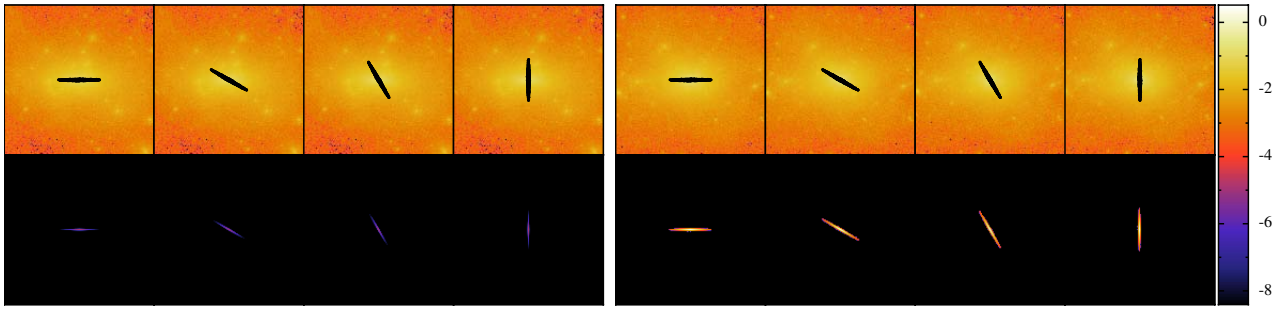

Figure 4.4: Orientations of the disk angular momentum with respect to the minor axis of the inertia tensor of halo particles inside its half-mass radius at $z_{\rm insert}$: parallel (first column), 30° (second column), 60° (third column) and parallel to the major axis (fourth column). Left panels illustrate the initial configuration with a 'massless' disk at $z = 1.3$, and the right panels show the system after the disk has grown at $z = 1.0$. Each panel has a comoving size of 150 h^{-1} Mpc on each side. First row panels display a logarithmic column density render (in arbitrary units) of the host halo, with the disk particles superimposed as black dots, while in the second row panels a logarithmic column density render of the disk is shown. The same color scale was used for all renders.

Disks are expected to be stable against bar formation if the criterion of Efstathiou et al. (1982)

$$Q_{\rm bar} \equiv \frac{v_{\rm max}}{(GM_{\rm d}/R_{\rm d})^{1/2}} > 1.1 \tag{4.3}$$

if fulfilled. Where $v_{\rm max}$ is the maximum value of the total rotation curve, while $R_{\rm d}$ is the disk radial scale-length and $M_{\rm d}$ is the disk mass. $Q_{\rm bar}$ for all disks at $z_{\rm live}$ are shown in Table 4.3, none of the disks fulfill the condition expressed in Eq. 4.3. Hence, in principle, bars are expected to form in all the simulations.

After the dark matter halo has responded to the gravitational presence of the growing disk, the only missing step in setting up the initial conditions is to assign velocities to the rigid particles of the disk. For this purpose the iterative method proposed by Rodionov et al. (2009) (described in Section 3.4) was used. The iterative method allows to construct dynamically

relaxed systems with or without dynamical restrictions. As this work studies the evolution of the disks within a cosmological environment, the initial conditions require the disk to be stable in the presence of its cosmological host halo.

Table 4.3: Parameters for all disk simulations. Run name indicates disk angular momentum orientation, $M_{\rm d}$ is the disk mass, $N_{\rm p}$ particle number, $R_{\rm d}$ and $z_{\rm d}$ are disk radial and vertical scale length respectively. $Q_{\rm bar}$ is Efstathiou et al. (1982) stability parameter calculated at $z = 1$.

Disk	Run name	$M_{\rm d}$ $[10^{10}\,h^{-1}\,M_{\odot}]$	N_p	$R_{\rm d}$ $[\,h^{-1}\,{\rm kpc}\,]$	$z_{\rm d}$ $[\,h^{-1}\,{\rm kpc}\,]$	$Q_{\rm bar}$	Notes
3180	minor	4.348	500,000	1.493	0.149	0.776	
	minor_spin	4.348	500,000	1.493	0.149	0.776	spin opposite to 3180 minor
	30deg	4.348	500,000	1.493	0.149	0.777	
	30deg_spin	4.348	500,000	1.493	0.149	0.777	spin opposite to 3180 30deg
	major	4.348	500,000	1.493	0.149	0.774	
3741	minor	3.744	500,000	1.491	0.149	0.793	
	major	3.744	500,000	1.491	0.149	0.792	
3748	minor	3.189	500,000	1.337	0.133	0.805	
	major	3.189	500,000	1.337	0.133	0.801	
3795	minor	4.711	500,000	2.031	0.203	0.840	
	30deg	4.711	500,000	2.031	0.203	0.839	
	60deg	4.711	500,000	2.031	0.203	0.838	
	major	4.711	500,000	2.031	0.203	0.835	

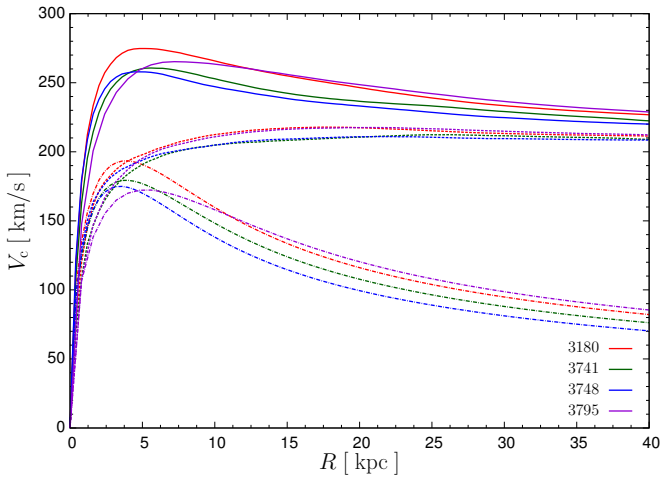

Figure 4.5: Circular velocity rotation curve at $z = 1$ of all minor-oriented disks. The solid line shows the total rotation curve, dashed line the contribution of the halo, and dot-dashed line the disk contribution.

The iterative method allows to do this by setting halo particles as boundary condition. i.e. as a rigid potential. This method is used instead of fitting potentials (e.g. DeBuhr et al. 2012) or

using symmetric particle distributions that may resemble the host halo, since those procedures might introduce spurious behavior at the time the disk goes live. In order to avoid errors arisen by the spherical cut-off of AHF's identified halo, halo particles inside a $2\,R_{\rm vir}$ sphere were used as boundary condition. In order to check the stability of the constructed disks, the stability parameter derived by Toomre (1964)

$$Q_{\rm Toomre} \equiv \frac{\sigma_R\ \kappa}{3.36\,G\,\Sigma} \tag{4.4}$$

was computed for all disks. The value of $Q_{\rm Toomre}$ as a function of radius R is shown in Fig. 4.6 for all minor-oriented disks. From Fig. 4.6 it can be seen that all disks fulfill the stability critical value of 1, and are expected to be locally stable against axisymmetric instabilities at all radii. Similarly to V_c, as all parameters in Eq. 4.4 are similar for all orientations, except for σ_R, hence only minor-oriented disks are shown.

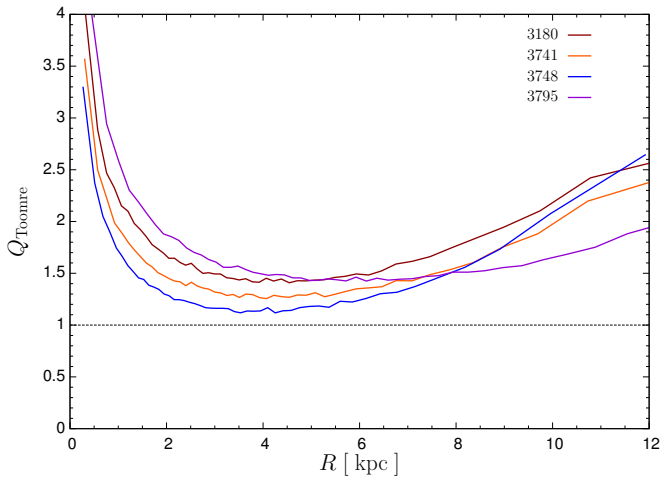

Figure 4.6: Toomre Q parameter at $z = 1$ of all minor-oriented disks. The dashed lines indicates stability limit for local stability. As seen all disks are locally stable at all radii against axisymmetric perturbations.

Chapter 5

Results

Results from all simulations described in Chapter 4 are presented here. In Section 5.1 face-on and edge-on views of all disks illustrate their morphological evolution. It is shown that despite the initial orientation of the angular momentum of the disk, $L_{\rm disk}$, the final structure of the galaxy presents similar features such as a prominent peanut or X-shaped bar, a ring, and remnants of spiral arms. In Section 5.2 are shown the disks surface, Σ, and vertical, ρ, densities, the velocity dispersion along z-direction , σ_z, and height $z_{1/2}$ evolution. Although all disks present a similar $\Sigma(r)$ through their evolution, there is a clear difference in the height, $z_{1/2}$, on the outer parts for minor- and major-oriented simulations on the outer parts of the disks due to the presence of non-disk-coplanar ring structures. Section 5.3 presents the evolution of vertical heating ζ and bar strength A_2 of the disks, and shows how the different evolutionary phases of these two quantities relate to the interaction of the bar with resonances. Finally, Section 5.4 presents the evolution of disk tilting and the development of non-disk-coplanar ring structures in disks with high angle, $\theta_{\rm ori}$, with respect to the minor axis of halo inertia tensor.

Throughout this chapter descriptions and analyses are mainly presented in three groups. The first one consists of the models with the disk angular momentum oriented parallel to the minor and major axis of the halo, and will be referred as minor-oriented and major-oriented respectively; the second group consists of `3180_spin` disks; and the third group corresponds to all orientations of the `3795` disk (see Table 4.3). For simplicity the angular momentum of the disk and the halo will be referred as $L_{\rm disk}$ and $L_{\rm halo}$ respectively. Additionally, the principal axes of the inertia tensor are always measured at half-mass radius of the halo, unless otherwise specified, and major, intermediate and minor axes will be referred to as $A_{\rm halo}$, $B_{\rm halo}$ and $C_{\rm halo}$ respectively.

5.1 Morphological Evolution

The morphological evolution of the disks is illustrated with face-on views that are shown in Figure 5.1 for minor-oriented disks, and in Figure 5.2 for major-oriented disks, edge-on views for both groups are illustrated in Figure 5.3. Minor-oriented disks present a similar evolution in two main stages, which will be analyzed in detail in Section 5.3. The first phase covers approximately the first two Gyrs of evolution (top four panels of Figure 5.1). This epoch is characterized by, firstly, developing two main tightly wounded spiral arms, that start at the edges of a long bar for all disks, except model `3795`, which seems to have a weaker and shorter bar (Fig. 5.1 second row). Then disks appear to experience a weakening of the bar and multiple arm-like structures, except for `3795` (Fig. 5.1 third row). These features start to erase at the end of this stage. During the second phase, approximately the last six Gyrs of evolution, the face-on structure of all disks present: a prominent bar, that shortens and slows down at the time its amplitude becomes stronger (see Section 5.3); a ring outside the bar; and blur structures in the outer parts of the disk, which in some cases are spiral arms (e.g. disk `3180` at $z = 0$), while for others they seem to be ring segments instead (e.g. disk `3795` at $z = 0$).

These two stages are also well distinguished in the edge-on view evolution (Fig. 5.3 top panels). The first stage shows a 'quiet' vertical evolution, in which certain disks show some kind of corrugation, (e.g. disk `3180` Fig. 5.3 third row), weak warps (e.g. `3741` Fig. 5.3 second and third rows), vertical peaks that are asymmetric with respect to z-plane (Fig. 5.3 fourth row), or a combination of all. The asymmetric peaks are a feature that is present during the transition from one stage to another, as will be explained in Section 5.3. The second phase, as seen in the face-on illustrations, presents a gradual evolution of the same general structure of all disks, which consists of a peanut or X-shaped bar (e.g. Combes & Sanders 1981), and a thick disk that keeps heating till $z = 0$. A quantitative analysis of all these face-on and edge-on features will be held in Sections 5.2 and 5.3.

Major-oriented disks present, in general, similar behavior as those with $L_{\rm disk}$ aligned with the minor axis. Face-on view of these disks (Fig. 5.2) shows also the evolutionary stages mentioned above for minor-oriented cases. Nevertheless, there are slight differences during the first stage, in which the multiple spiral arms appear to diffuse faster, except for disk `3795` for which its grand-design arms seems to persist quite longer than its minor-oriented case. During the second phase major-oriented disks show no notable differences with respect to the face-on evolution of minor cases, the prominent bar with a ring surrounding it, and the arm-like structure in the outer parts. Despite the fact that face-on views look alike regardless of the $L_{\rm disk}$ orientation, it is the edge-on view (Fig. 5.3 bottom panels) that shows clear differences with respect to minor-oriented galaxies. During the first stage of evolution, all disks present vertical features

in the outer parts of the disks that were absent, or weaker in the minor-oriented case. These accounts for the warping of the disk, which is present in all major-oriented cases, while being absent in most of the minor-oriented ones.

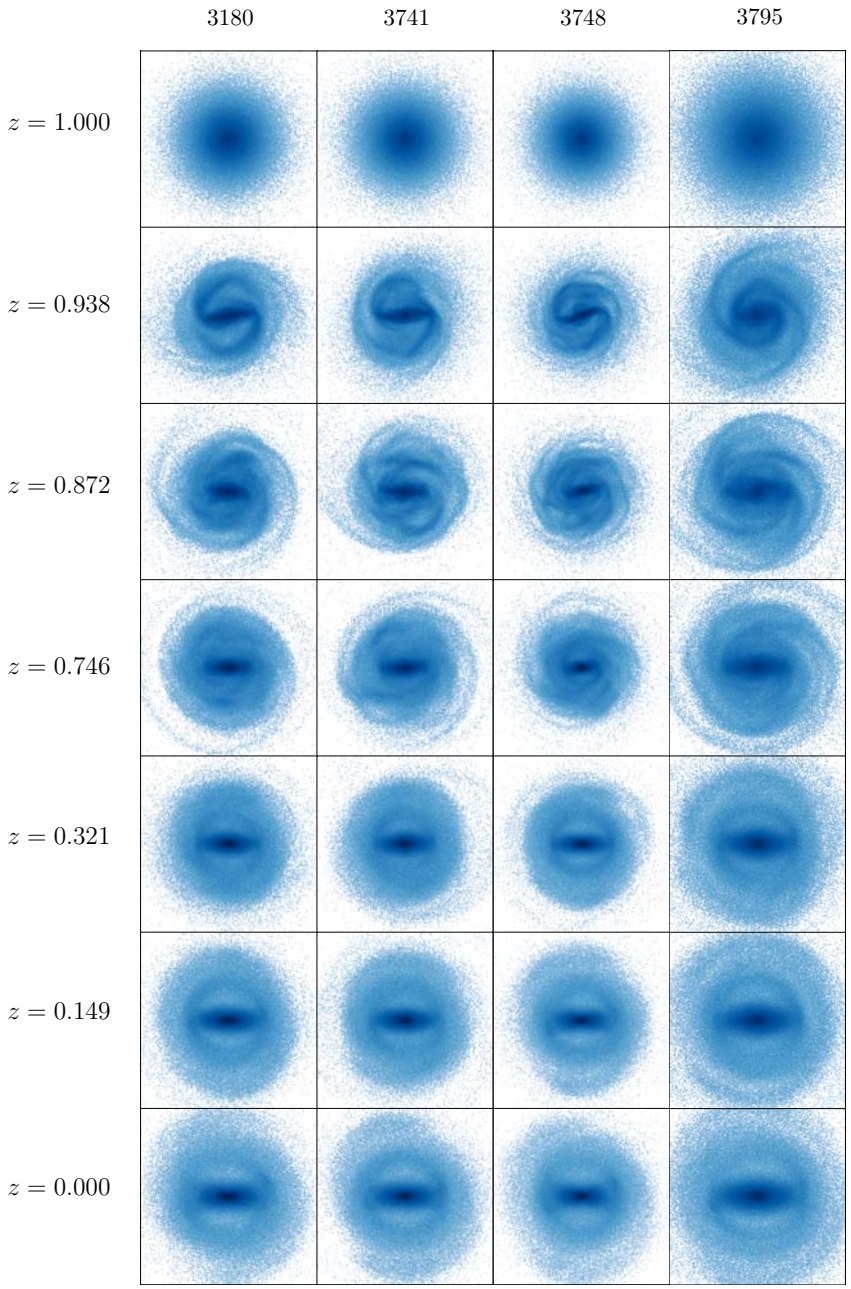

Figure 5.1: Face-on view of the evolution of all stellar disks with angular momentum initially oriented parallel to the minor axis.Each panel has a physical length of 40 kpc (physical units) on each side. Disks are oriented with disk major axis of the inner 7 kpc along x-direction, and disk minor axis and angular momentum along z-direction (pointing out of the page). Column density is rendered in arbitrary units using the same logarithmic scale for all disks.

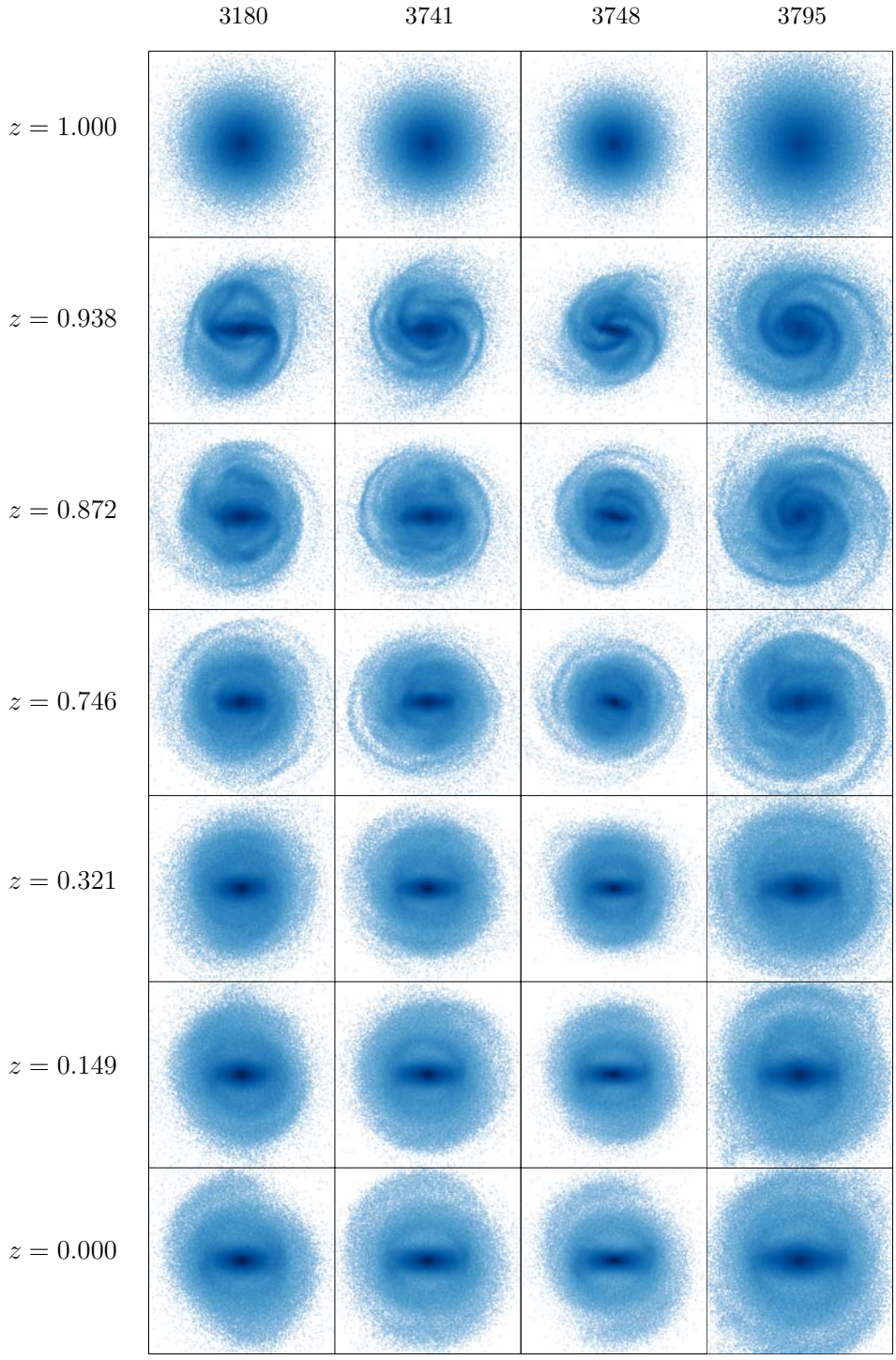

Figure 5.2: Face-on view of the evolution of all stellar disks with angular momentum initially oriented parallel to the major axis.All panels are rendered with the same characteristics as Figure 5.1.

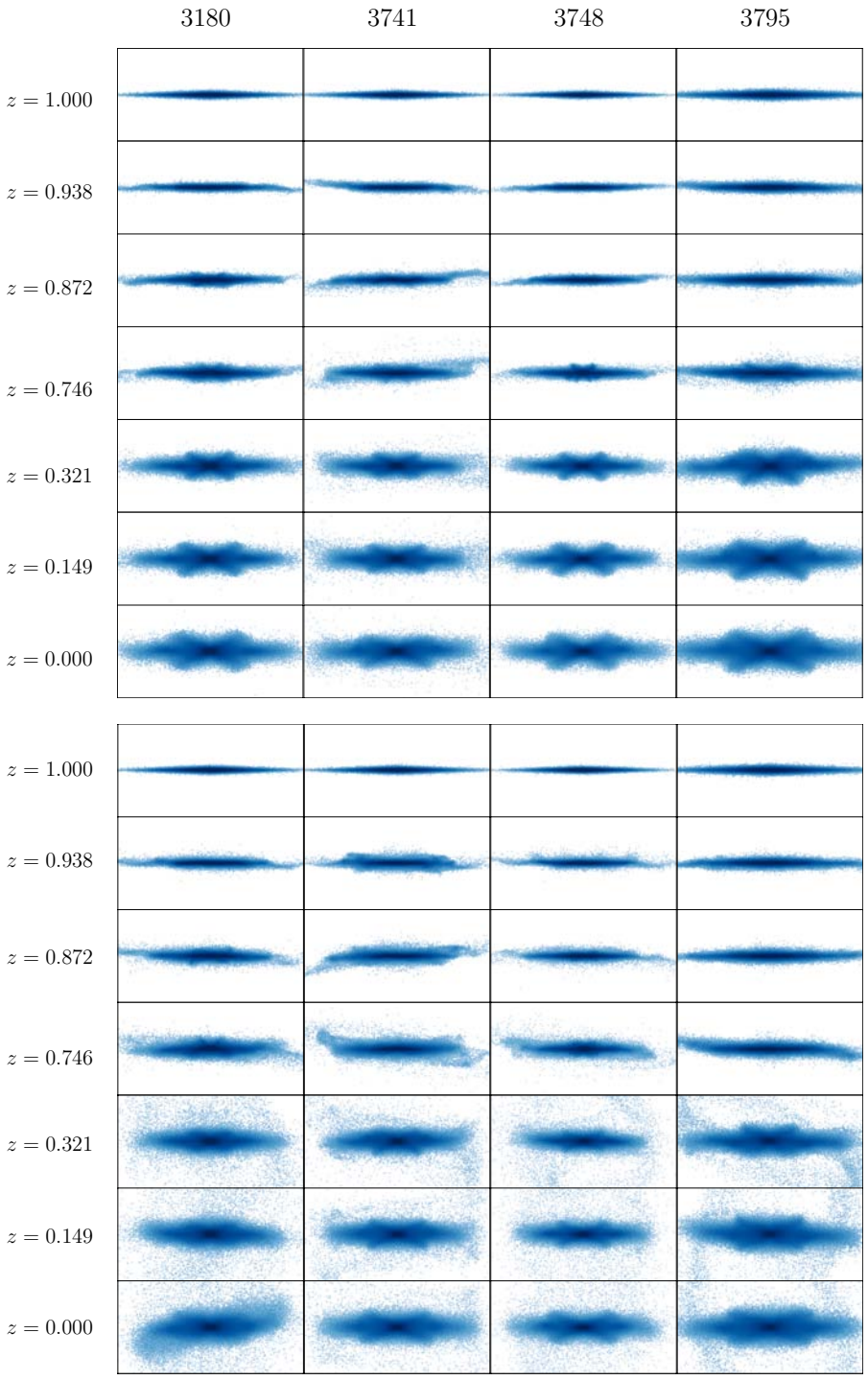

Figure 5.3: Edge-on view of the evolution of all stellar disks with angular momentum initially oriented parallel to minor (top panels) and major (bottom panels) axis of halo inertia tensor. Each panel has a physical length of 10 kpc on the vertical side and 20 kpc on the horizontal one. Disks are oriented and rendered with the same characteristics as Figure 5.1

The most striking difference between minor- and major-oriented disks is appreciated during the second phase of evolution. During this phase, ring sections of the galaxy separate completely from the plane described by the inner 7 kpc of the disk. This means that as the galaxy evolves and changes its orientation, there is a section that completely decouples from this 'bulk tilting', forming a coplanar ring that keeps rotating around the center of the galaxy, but with an angular momentum orientation $L_{\rm ring}$ different than $L_{\rm disk}$. At $z = 0$ this is evident for `3795` and `3748` disks (Fig. 5.3), while `3180` and `3741` show structures that appear to be a transition phase of the decoupling. The last row of Fig. 5.3 of disk `3180` shows that these features appear to have their origin on the above mentioned warps of the outer parts of the galaxies. These structures have also been reported by DeBuhr et al. (2012), nevertheless they observe this phenomenon in some minor- and major-oriented disks, while in this work are only seen in galaxies with high $\theta_{\rm ori}$ (i.e. all major and `3795_60deg` disks). This will be addressed in more detail in Section 5.4.

Face-on and edge-on views of the evolution of `spin` and `no-spin` disks are shown in Figs. 5.4 and top panels of Fig. 5.6. Comparing `no-spin` minor and 30deg orientations (Fig. 5.4 columns 1 and 3) the only noticeable difference in the first stage is a small weakening of the two main spiral structures, along with small spirals that seem to form from the two principal ones. While during the second phase, both orientations display the same features as those previously mentioned for all disks. Comparing both `spin` and `no-spin` models, it is also evident that `spin` disks show the same features as their `no-spin` counterparts.

These results are not surprising due to the selected origin of the coordinate system in which the inertia tensor is calculated, that is the position of maximum density of the halo, which coincides with the center of mass, and the minimum of the gravitational potential of the halo. For this choice two important facts should be noted: (1) if the halo has a plane of symmetry, the center of mass must lie in that plane, which also contains two of the principal axes, with the third one being perpendicular to that plane; and (2) if the halo has an axis of symmetry of any order, the center of mass must lie on that axis, which is also one of the principal axes of inertia (Landau & Lifshitz, 1976). Therefore, as the method implemented in this work orients $L_{\rm disk}$ with respect to the principal axes, and the mass distribution of the disk stays symmetric during its growth, a symmetry in the mass distribution of the halo with respect to disk plane is expected. This way `spin` disks 'see' a mirrored image of that seen by the `no-spin` ones, with the exception of the distribution of dark matter subhalos, in addition that prograde orbits for `no-spin` disks will be retrograde for `spin` ones, and viceversa. The differences in the morphology and angular momentum exchange that orbiting subhalos may have are not analyzed in this work but are left for future studies.

Lastly, the evolution of several orientations of disk `3795` is display in Figs. 5.5 and 5.6

(bottom panels). Similar to what has been seen throughout this section, all `3795` orientations display the same two evolutionary stages, with the second one being "universal" for every disk studied with this method, leaving the first stage as the only point of comparison. Focusing on the second and third rows of Fig. 5.5, it can be seen that as the angle $\theta_{\rm ori}$ between $L_{\rm disk}$ and $C_{\rm halo}$ increases, spiral structure changes from a grand-design to a flocculent galaxy, presenting the grand-design structure when $L_{\rm disk}$ is parallel to $A_{\rm halo}$. This seems to indicate that spiral structure is more stable when $L_{\rm disk}$ is oriented parallel to $A_{\rm halo}$ and $C_{\rm halo}$.

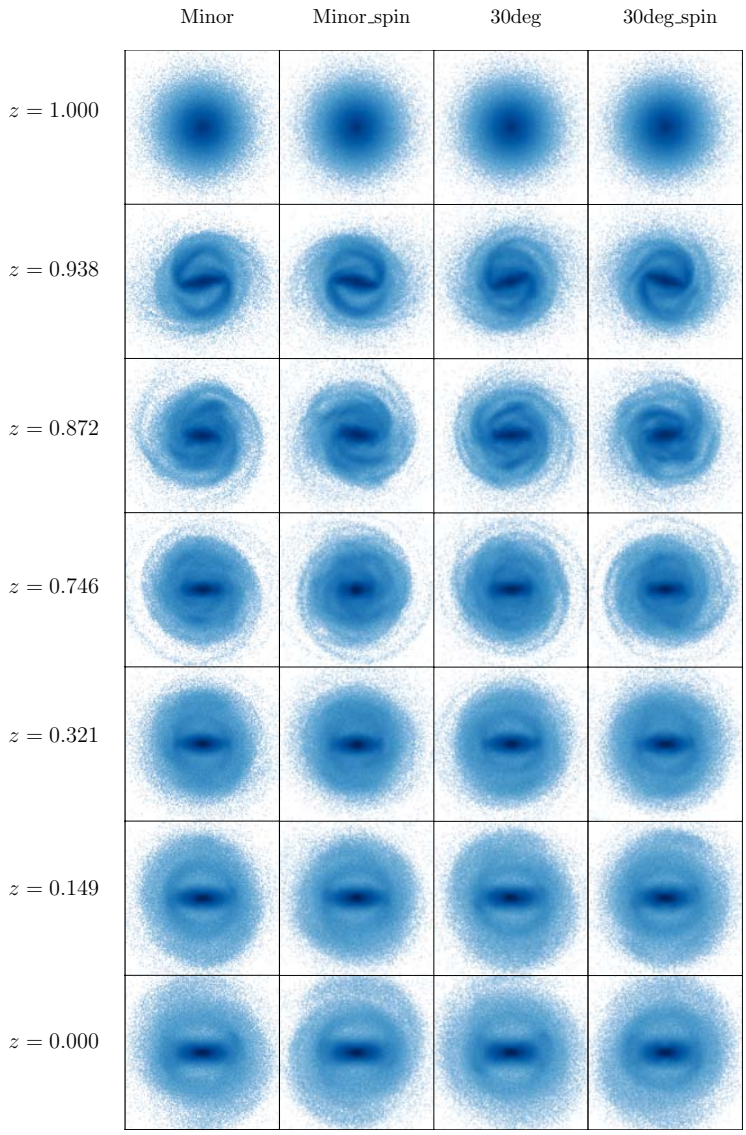

Figure 5.4: Face-on view of the evolution of inverted spin disks and the original orientation of `3180` disk. Disks are rendered with the same parameters as Figure 5.1, except for 'spin' disks whose angular momentum points towards the page.

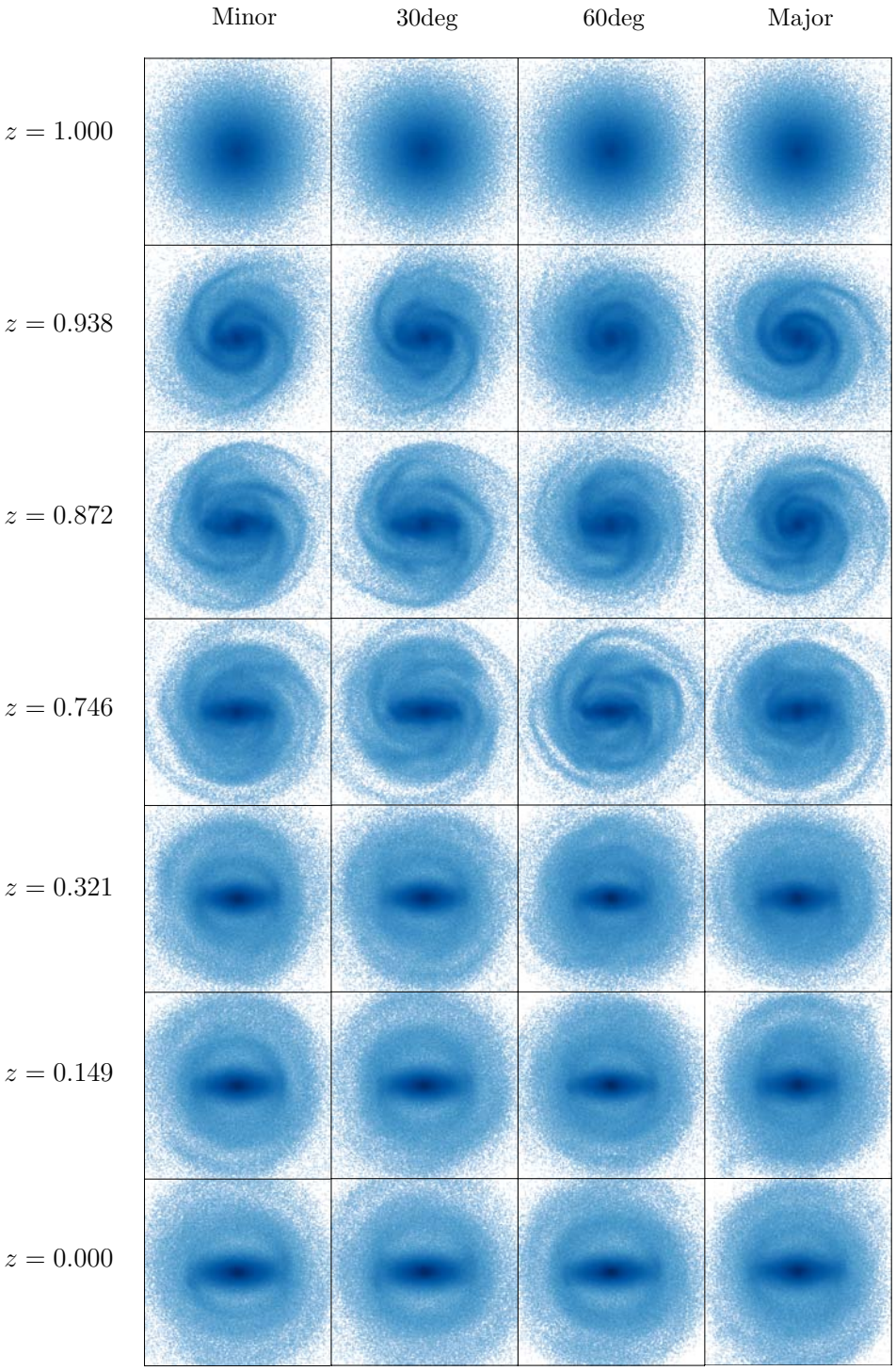

Figure 5.5: Face-on view of the evolution of all orientations studied for `3795` disk. All panels are rendered with same characteristics as Figure 5.1.

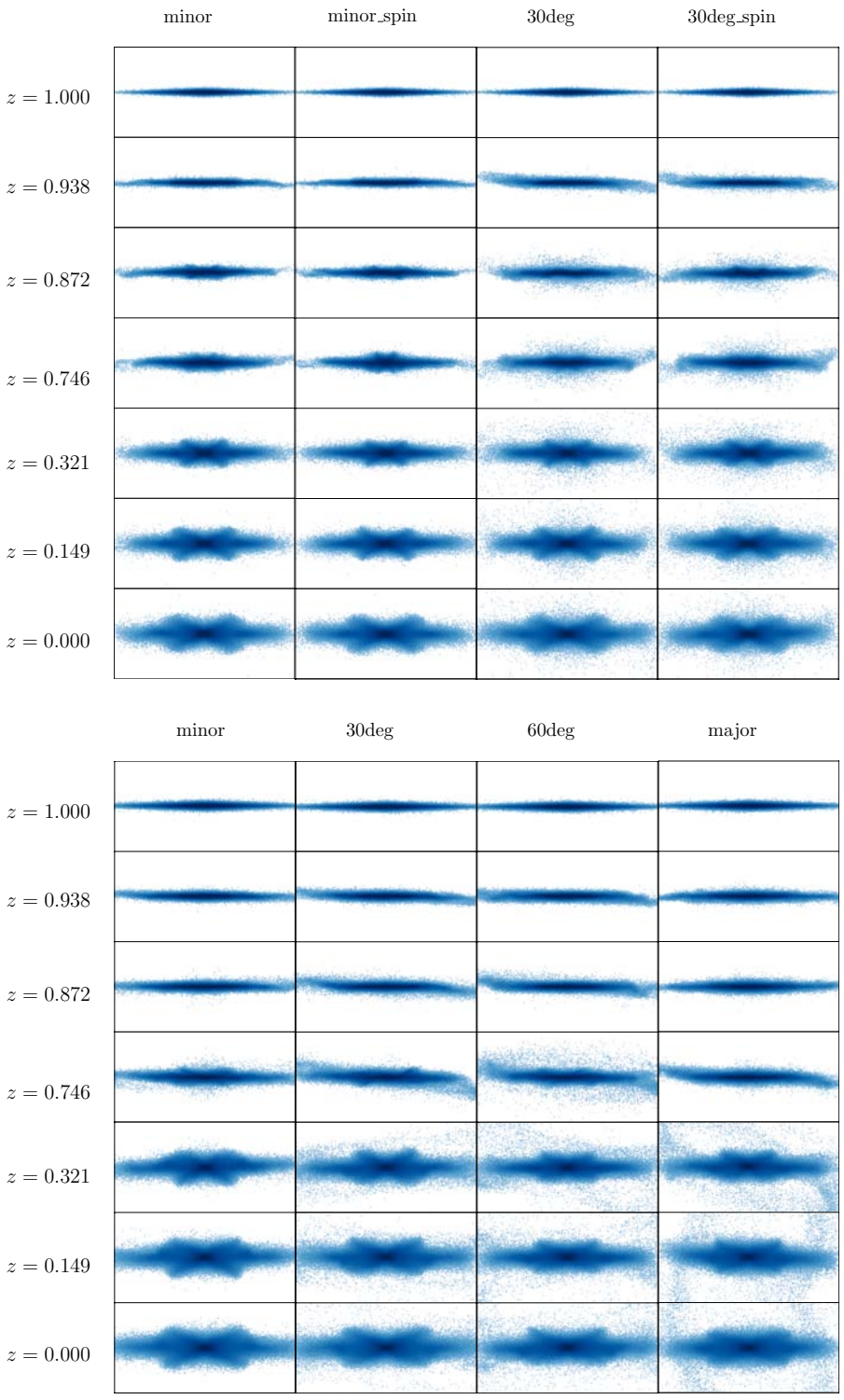

Figure 5.6: Edge-on view of the evolution of `3180` model with counterrotating disks (top panels), and all orientations of the `3795` disk (bottom panel). All panels are rendered with the same parameters as Figure 5.3

5.2 Measuring the evolution of the Disks

As shown in Section 5.1 all the disks show similar features on their structural properties, nevertheless measurements are needed to understand the structures identified visually. This section presents the evolution of disks' surface and vertical density profiles, Σ and $\langle\rho\rangle$ respectively, showing how the material of the disks rearrange radial and vertically, and how this is related to the properties seen in the morphological evolution. Vertical velocity dispersion $\sigma_z(r)$ and the median of disk particles' height $z_{1/2}$ are used to measure how different parts of the disks experience different heating throughout the simulation.

5.2.1 Disk Surface and Vertical Density

Surface density radial profile $\Sigma(R)$ is calculated using the total mass of disk particles inside cylindrical bins, while vertical density profile $\langle\rho\rangle$ is calculated in three regions encompassing cylindrical shells with radii of 4, 8, and 12 kpc. The presence of the non-disk-coplanar ring structures seen in Section 5.1 for high $\theta_{\rm ori}$ orientations, may indicate that using cylindrical bins may not be the best way to measure quantities because of the tilt they experience, which causes the outer particles to 'invade' inner cylindrical radii. Nevertheless in the case of the density profiles this does not represent an important source of noise due to the fact that the density of these ring structures is almost negligible with respect to the density of the rest of the galaxy. For other quantities such as angular momentum, cylindrical bins introduce considerable noise, making the use of spherical bins a better choice.

The evolution of the density profiles of minor-oriented disks is shown in Fig. 5.7. Surface density profiles present a similar behavior for all disks, which can be divided in three regions. The first one corresponds to the innermost part of the disks, starting at the center of the disk and ending at the radius where Σ at a given redshift z first crosses the initial Σ profile, the middle region corresponds to radii limited by the first and the second crossings of the initial Σ curve, and the third region then covers all radii after the second crossing of the initial curve. The radii at which these crossings occur are not fixed in time due to the constant evolution of the galaxies. These regions are consistent with the picture that as the simulation evolves, disk particles redistribute due to the formation of the features observed in Section 5.1. The first region presents an increment in Σ through all the simulation time, and represents the pseudo-bulge structure that forms and grows at the center of all galaxies. The presence of the pseudo-bulge partially explains the decrement in Σ with respect to the initial condition in the second region, given that material from the second region is 'added' to the first one as the pseudo-bulge grows. The third region experiences a notable increment in Σ (almost one order

of magnitude), from $z = 1$ to $z = 0$, nevertheless this is not a gradual increment, as the one observed in the inner region, as can be seen by multiple crossings during the first ~ 2 Gyrs of evolution. The multiple crossings are consequence of the multiple spiral structures that affect the outermost parts of the galaxy during the first evolutionary phase observed in Section 5.1. As mentioned in Section 5.1, the second evolutionary phase is characterized by the gradual development of a bar, a ring, and spirals or ring segments in the outermost radii of the disk. These ring segments or spirals are responsible for accumulating material at large radii, hence increasing Σ, which is evident after $z = 0.519$ for all disks as can be seen in Fig. 5.7. After this time none of the Σ curves crosses again the initial profile.

The vertical density ρ was computed in three regions defined by cylindrical shells at radii of 4, 8 and 12 kpc. For minor-oriented disks ρ is shown in the left panel of Fig. 5.7. As can be seen for all disks, the evolution of ρ in the inner part the galaxy presents a decrement of the peak and a broadening of the profile. Nevertheless at some point the peak converges to a value, while the broadening remains increasing; the convergence is present in all disks. In the middle regions the peak also decreases but does not converges, and here is where the profile broadens the most in all of the disk. The third regions, as the other two, shows a decrement of the peak that does not converge and a broadening similar to the one observed for the inner region.

These results are consistent with the general edge-on morphology of the disks shown in Section 5.1; the convergence observed at the innermost bins accounts for the 'boxy' structure observed at the very center of all galaxies, which expands in radius but remains almost fixed in height; the high broadening of the second region accounts for the evolution of the 'arms' of the peanut/X-shaped pseudo-bulge, which once formed, keeps growing in height; the third region shows the heating of the region outside of the bar. In general all disks display the same behavior for all regions except for the third region of disk `3795` that shows, during the second phase of evolution, a similar broadening as the intermediate region. This is only due to the higher length scale of this particular disk, for which the bar has reached this region by that evolution time.

The Σ and ρ profiles for major-oriented disks are shown in Fig. 5.8. It can be seen a similar behavior with respect to the minor-oriented disks. For Σ the same three regions are present for all disks, with the exception of disk `3748` for which the evolution of the outer parts remains below the initial Σ value. The later is consistent with what is shown in the fourth and fifth row of Fig. 5.2: during this epoch the disk seems to shrink a little before the outer arm-like structures develop and expand to greater radii causing Σ to rise above the initial profile. This decrement in Σ of disk `3748` can also be explained by the ring structure that starts to decouple from the disk approximately at $z \sim 0.6$ (see Section 5.4.2). This may be the result of the interaction with a specific subhalo, and that due to disk's orientation is not present in the minor one.

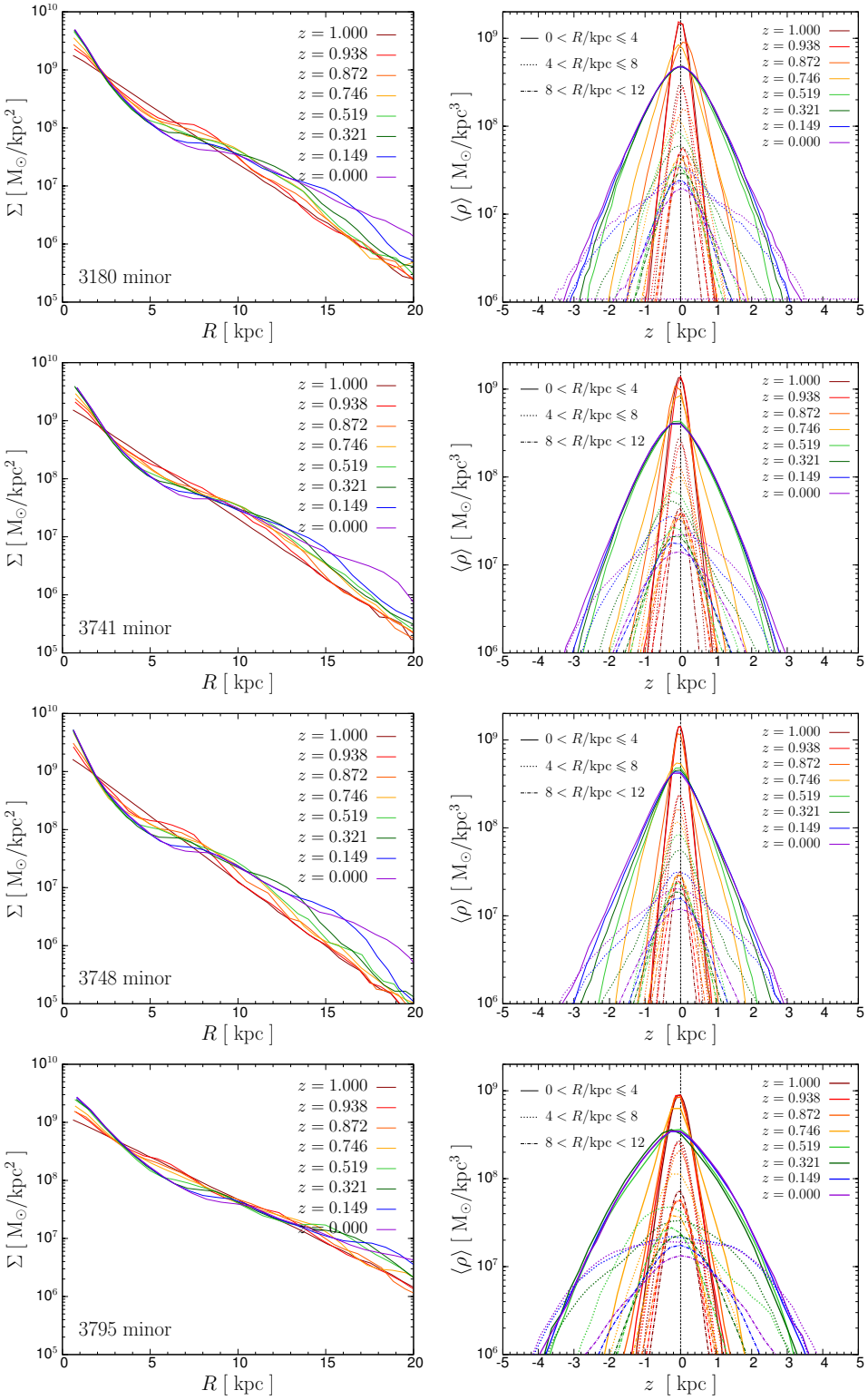

Figure 5.7: Surface density Σ (left panels) and vertical density $\langle\rho\rangle$ (right panels) of all disks with angular momentum L_{disk} oriented parallel to the minor axis C_{halo} of the host halo inertia tensor.

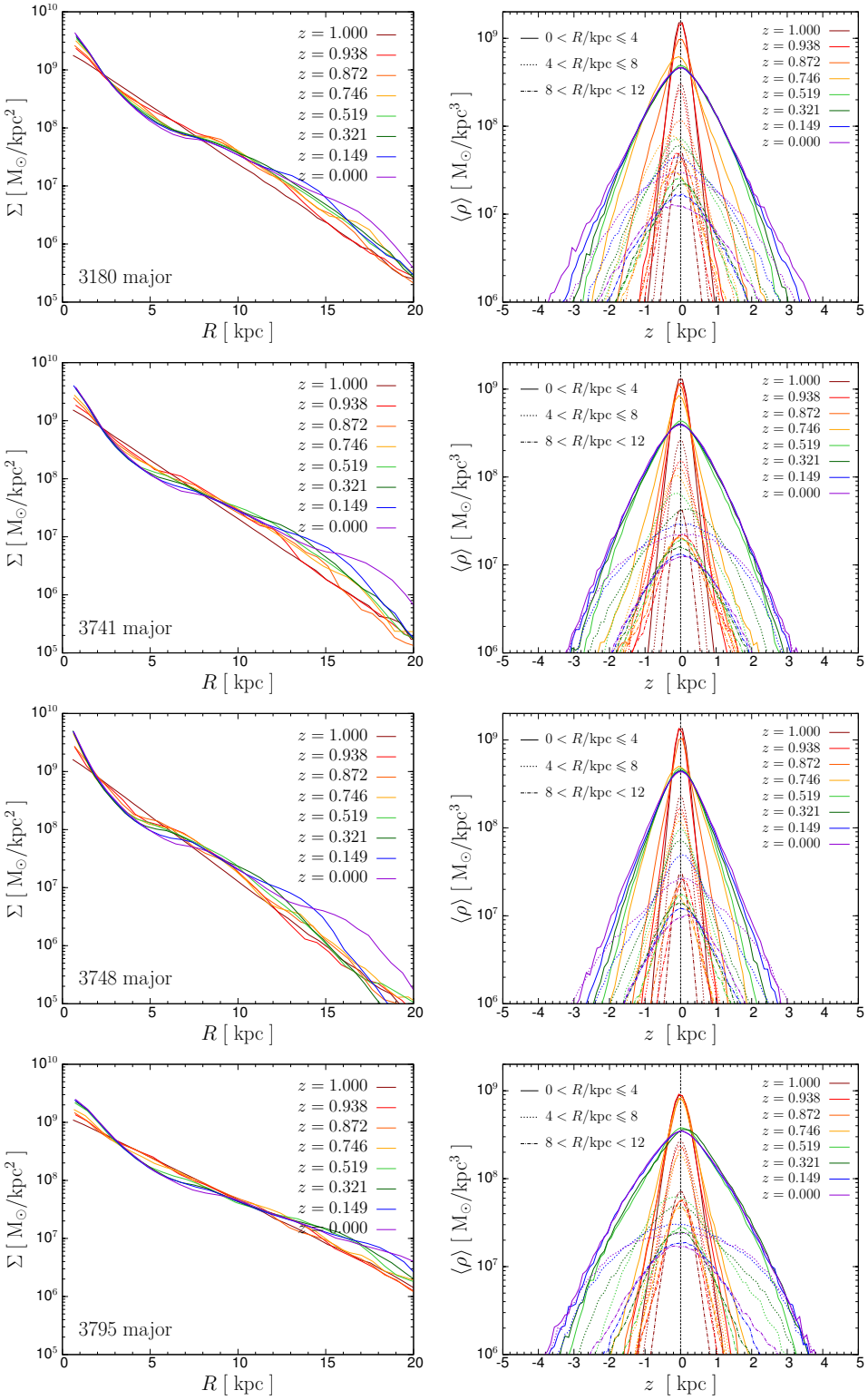

Figure 5.8: Surface density Σ (left panels) and vertical density $\langle\rho\rangle$ (right panels) of all disks with angular momentum L_{disk} oriented parallel to the major axis A_{halo} of the host halo inertia tensor.

The density profiles of the rest of disks `3180` and `3795`, are similar to the rest of the disks, hence are not shown. This indicates that the general density distribution of isolated (without experiencing mergers) stellar disks in cosmological context does not depend highly on the initial $L_{\rm disk}$ orientation, with the exception of the ring structures found in high $\theta_{\rm ori}$ orientations, that spread out material of the outermost radii from the plane of the disk. These results are consistent with the density profiles reported by DeBuhr et al. (2012) and Yurin & Springel (2015) who also carried out similar simulations, with differences in the specific cosmological environment of each halo, the disks $Q_{\rm Toomre}$ and the methodology used to set up the initial conditions.

5.2.2 Velocity Dispersion σ_z and Disk Height $z_{1/2}$

In order to study the kinematics of the vertical structure of the disks, the evolution of the vertical velocity dispersion, σ_z, and the profile of the median of the absolute value of z-coordinate, $z_{1/2}$, profiles are analyzed in this section. For the computation of both quantities cylindrical bins of equal number of particles. Velocity dispersion is calculated as the standard deviation of the velocity in each radial bin as

$$\sigma_z^2 = \langle v_z^2 \rangle - \langle v_z \rangle^2 \tag{5.1}$$

where v_z is the velocity parallel to z-direction; $z_{1/2}$ is the median of $|z|$, being an indicator of the vertical extension of the particles at a given radius.

The evolution of these quantities is shown in Fig. 5.9 for minor-oriented disks. It is clear that σ_z grows at all radii for all simulations. There is also an evident difference in the evolution of the inner and the outer region in σ_z profile. At inner radii, σ_z profile grows but keeps a similar shape that spreads to larger radii, while at the outermost radii σ_z seems to nearly flatten. Disks height $z_{1/2}$ evolution is presented in the right panels of Fig. 5.9, which is initially flat for all disks by construction. It can be seen that all disks have similar behavior, characterized by the development of a growing 'triangular' shape in the inner parts of the disks, and a positive slope for the outer parts. This triangle reflects the evolution of the peanut-shaped pseudo-bulge, since this shape is absent before the buckling instability happens. It is important to notice that the slope of the triangle remains almost constant for each disk, while its lower right displaces with time. This displacement seems to be related with the crossing of both regions of σ_z profile mentioned above, indicating that both regions are related with the evolution of the peanut-shaped pseudo-bulge.

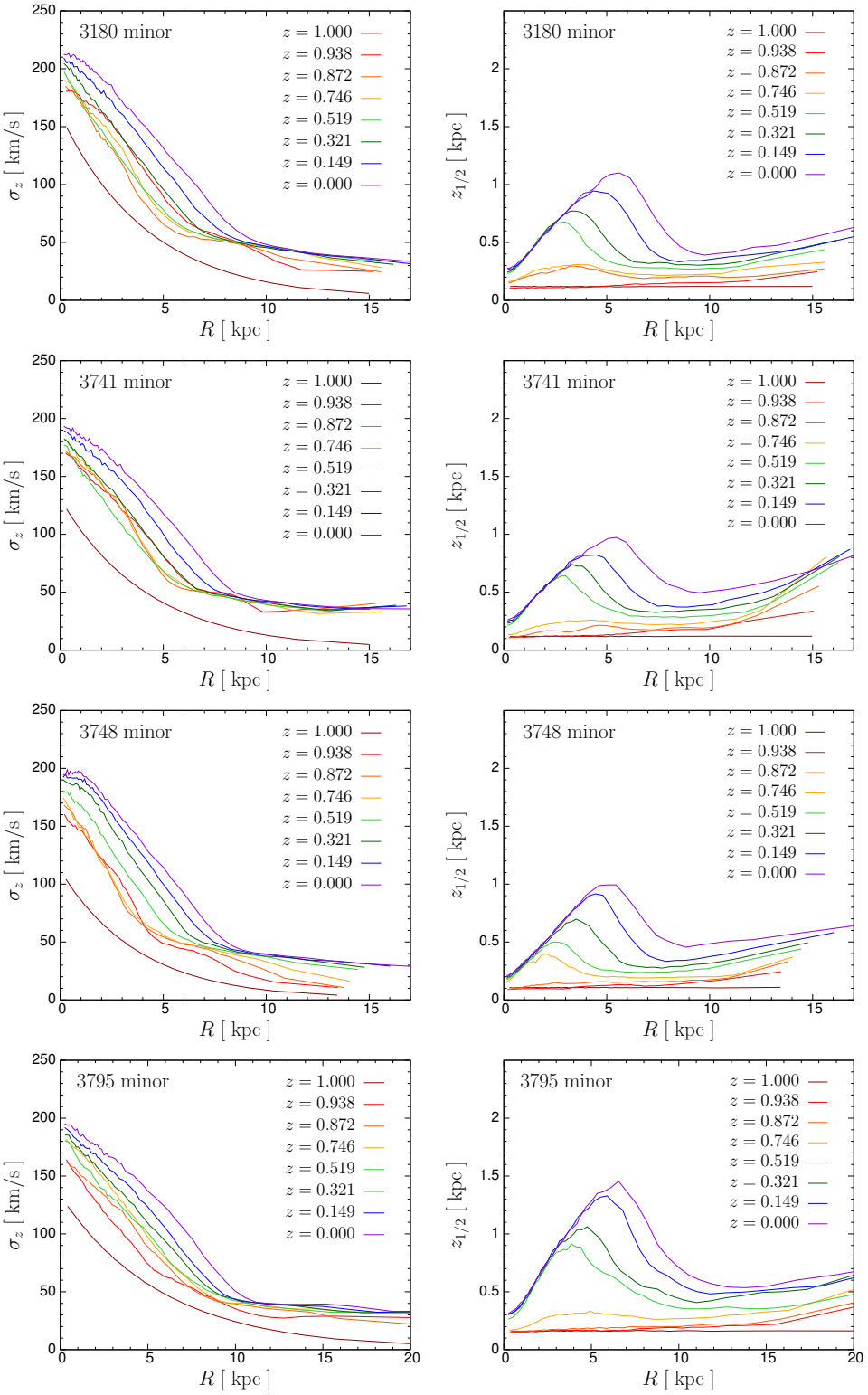

Figure 5.9: Velocity dispersion σ_z along z-direction (left panels) and median of z-coordinate $z_{1/2}$ (right panels) of all disks with L_{disk} oriented parallel to minor axis C_{halo} of host halo inertia tensor.

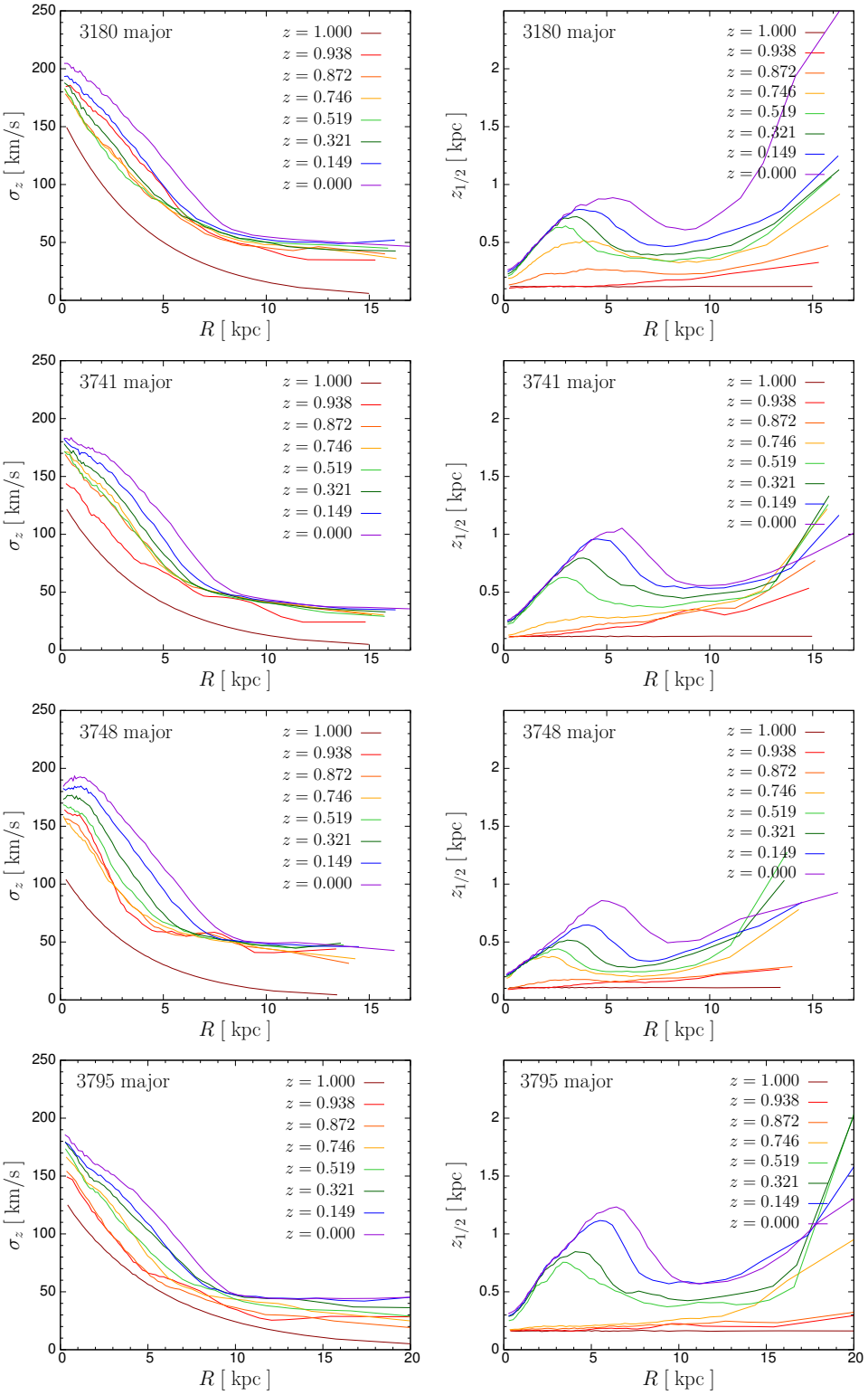

Figure 5.10: Velocity dispersion σ_z along z-direction (left panels) and median of z-coordinate $z_{1/2}$ (right panels) of all disks with L_{disk} oriented parallel to major axis A_{halo} of host halo inertia tensor.

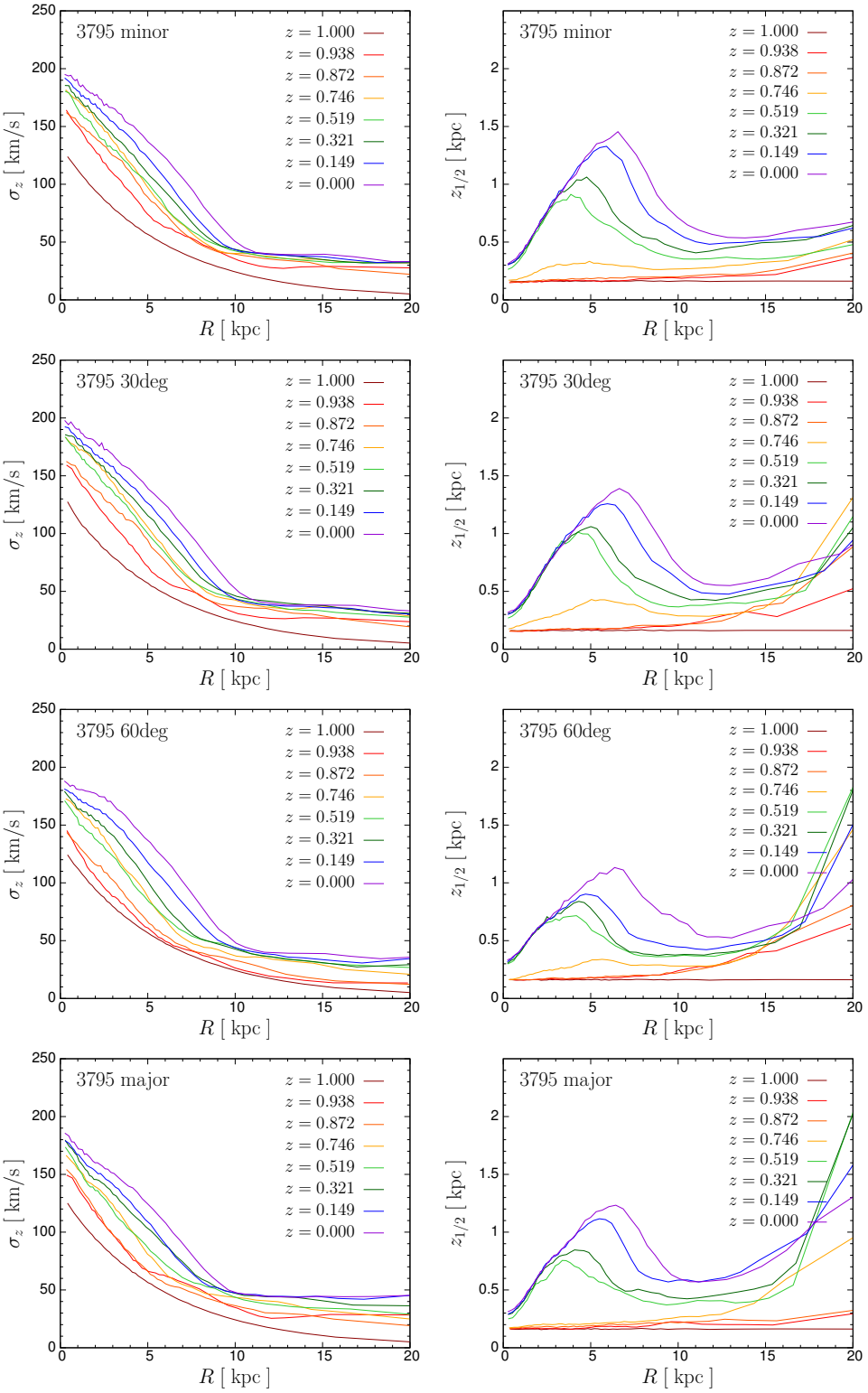

Figure 5.11: Velocity dispersion σ_z along z-direction (left panels) and median of z-coordinate $z_{1/2}$ (right panels) of all orientations of disk `3795`.

Profiles of major-oriented galaxies are presented in Fig. 5.10. In the case of σ_z major-oriented disks present the same features as the ones for minor-oriented cases, but there exists a visible difference in $z_{1/2}$. As can be seen in the $z_{1/2}$ profiles (Fig. 5.10 right panels) the outer parts of the disks present a tremendous increment of $z_{1/2}$ with respect to the minor-oriented ones, this is clearly related with the decoupled ring structures that occur in all high-$\theta_{\rm ori}$simulations. A transition of this effect can be seen in Fig. 5.11 where profiles for `3795` disks are shown, indicating that $z_{1/2}$ in the outer parts is orientation dependent. `3180 spin` disks profiles present no noticeable differences, thus are not presented here.

5.3 Disk Heating and Bar Evolution

In this section the evolution of the disk relative vertical heating ζ, bar strength A_2 and their connection with the evolution of the bar pattern speed $\Omega_{\rm bar}$ is shown. The analyses presented here are vital to understand the morphological evolution of galaxies presented in Section 5.1, and all the structural and kinematic properties presented in Section 5.2.

Firstly, it is analyzed how vertical heating ζ (Section 5.3.1) of all disks presents different evolutionary stages, separated by quick and violent jumps that makes ζ to behave like a step function, it is shown that some disks, independently of their initial orientation, present one or two of this pronounced jumps during their evolution. Bar strength is measured using $m = 2$ Fourier mode (Section 5.3.2). In general, its evolution shows at least two different evolutionary stages, the first one associated with the rapid formation of the bar when the disk goes live, and the second characterized by a regular growth of the amplitude, A_2, which corresponds to the time when the bar has reached a stable configuration. Last part of this section addresses the evolution of bar size and the pattern speed, $\Omega_{\rm bar}$, and the different phases experienced throughout all the simulation (Section 5.3.3). It is also explained how the evolution phases of the bar relate to the ones observed in the morphology, A_2 and ζ of the disk, which are associated with vertical bulk motion in inner parts of the disk due to the presence of standing waves which are product of the interaction of the bar with resonant regions of the disk.

5.3.1 Vertical Heating ζ

In order to measure how much the disk heats through the simulation, the relative vertical heating parameter ζ is computed. This quantity is defined as

$$\zeta = \frac{\sigma_z}{\sigma_{z,0}} \tag{5.2}$$

where σ_z is the total velocity dispersion along z-direction at a given time, and $\sigma_{z,0}$ is the initial velocity dispersion of the disk at $z = 1$. The evolution of vertical heating ζ for all disks is shown in Fig. 5.12.

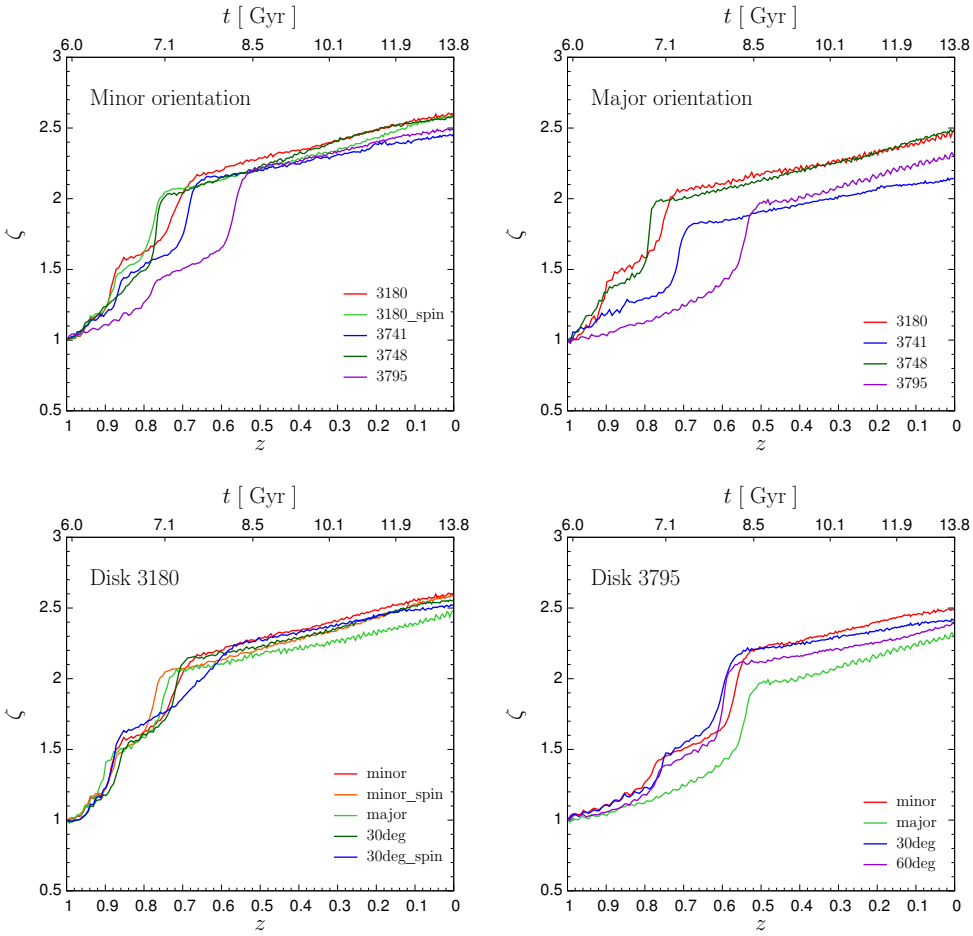

Figure 5.12: Evolution of vertical heating ζ from $z = 1$ to $z = 0$ of minor-oriented (top-left), major-oriented (top-right), 3180 (bottom-left) and 3795 (bottom-right) disks.

It can be seen that ζ evolution of all galaxies is quite similar. All of them present one or two pronounced jumps which are transitions from a state of stability to another. In addition to that, almost all of them reach ζ values of ~ 2.5 at $z = 0$. The transitions arise because during their evolution disks rotate in metastable configurations, that when becomes unstable triggers some mechanism that increases disk heating in order to reach a new stable state. As mentioned before this effect seems to appear at least one for all disks studied in this work. For the disks that present two jumps, the first one is always the smaller of the two, and the second one has a similar amplitude $\Delta\zeta \simeq 0.6$ as the unique jump of the rest of the simulations, indicating

that the same mechanism is responsible for the big jump in all simulations. As will be seen below this mechanism is the so called buckling instability of the bar, as was also pointed out by DeBuhr et al. (2012) and Yurin & Springel (2015). It is interesting to understand why some disks present the first jump while the others do not; this will become clearer when analyzing the evolution of $\Omega_{\rm bar}$in Section 5.3.3.

5.3.2 Bar Strength A_2

Bar strength was measured using the amplitude of the $m = 2$ Fourier mode A_2. A similar method as the one described by Yurin & Springel (2015) was used in this work. Bar strength is computed using 30 cylindrical bins with equal number of particles within a radius of $2R_{\rm d}$, to calculate the coefficients

$$a_2^{(b)} = \sum_{i \in b} m_i \cos(2\phi_i) \tag{5.3}$$

$$b_2^{(b)} = \sum_{i \in b} m_i \sin(2\phi_i) \tag{5.4}$$

$$c_2^{(b)} = \sqrt{a_2^2 + b_2^2} \tag{5.5}$$

where m_i is the mass and ϕ_i the azimuthal angle of each particle, and the sum is perfomed for all particles inside bin b. The amplitude of $m = 2$ Fourier mode is then calculated as

$$A_2 = \frac{\sum_b R_b c_2^{(b)}}{\sum_b' R_b' M_b'} \tag{5.6}$$

where R_b is the radius of the outermost particle of the bin, M_b is the total mass of the bin. Results for all simulations are shown in Fig. 5.13.

It is observed that all disks present a similar evolution of A_2, which, as can be seen, is divided in two main phases, with the first one being characterized by rapid oscillations in A_2 amplitude and the second one by an oscillating steady growth of the bar till $z = 0$. At the end of the simulation time all bars have similar A_2 amplitudes, ranging from 0.4 to 0.5. This results coincide with the evolutionary phases and similar bar morphology observed in Section 5.1.

As can be noticed with results of Section 5.3.1, huge decrements in A_2 are coupled to the jumps seen in ζ, this seems to indicate that the trigger of the heating mechanisms is closely related to bar strength. This is evident from the big jump in ζ that matches with the time of the buckling instability in the bar and the decrement in A_2. This has also been previously

reported in the literature (e.g. DeBuhr et al. 2012; Dubinski et al. 2009), furthermore it is also observed that the small jump in ζ, that is visible for some disks, is also associated with the first significant drop of A_2, which is evident for all `3180` disks, except `3180_30deg_spin` (Fig. 5.13). As will be seen in Section 5.3.3, the drops in A_2 and jumps in ζ are caused by the interaction of the bar with the resonant regions of the galaxy.

It is important to notice that the general evolution of bar amplitude A_2 appears to be not dependent on the orientation of L_{disk} as can be seen in `3180` and `3795` plots (Fig. 5.13 bottom panels). However, it has been showed that the exchange of angular momentum of the bar with the central dark parts of the dark matter halo plays an important role in the dynamics of the system (e.g. Athanassoula 2014; Villa-Vargas et al. 2009); thus further analyses on the interaction of the bar with dark matter halo is needed, though, as this project focuses only on the disk properties, those studies are left for future work.

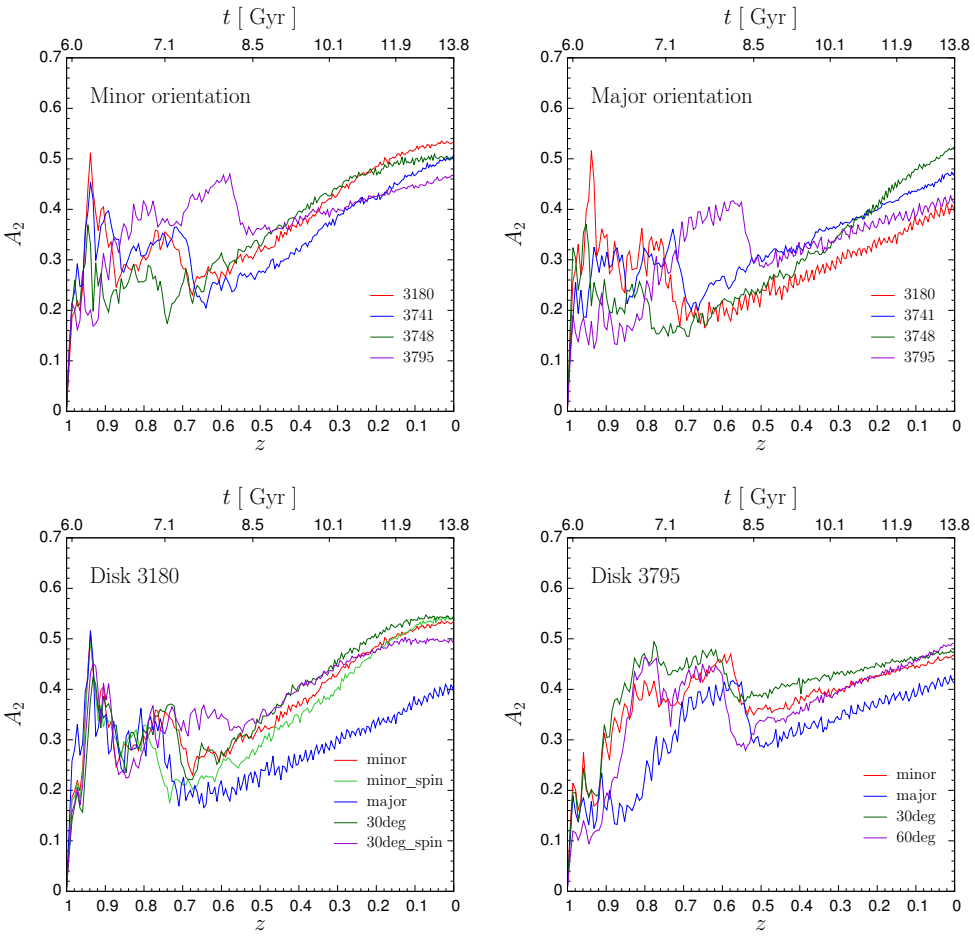

Figure 5.13: Evolution of bar strength A_2 from $z = 1$ to $z = 0$ of minor-oriented (top-left), major-oriented (top-right), 3180 (bottom-left) and 3795 (bottom-right) disks.

5.3.3 Resonances and Bar instabilities

As has been seen throughout this chapter all disks studied present similar structural and kinematic properties. In most of them it has been identified the existence of two distinguishable phases that are divided by the development of what is known as the buckling instability of the bar (e.g. Sellwood 2014). In some quantities such as ζ and A_2 of certain disks, there is observed another phase that does not lasts too long before changing to the common second evolutionary stage. Here, it is presented an analysis on the bar evolution and an attempt to further explain the cause of these evolutionary phases is done.

Stellar orbits are said to be in resonance with an axisymmetric disturbance when

$$\Omega_p = \Omega_\phi + \frac{l}{m}\Omega_R \tag{5.7}$$

where l is a signed integer, m an unsigned integer, Ω_p the pattern speed, Ω_ϕ the orbital frequency, and Ω_R is the radial frequency around the guiding radius, where $\Omega_\mathrm{R} = \kappa$ for the epicycle approximation (e.g. Binney & Tremaine 2008; Sellwood 2014).

In this work we are interested in the regions defined by Eq. (5.7) when $l = -1$, known as Inner Lindblad Resonance (ILR). These regions, that are located inside corotation, arise due to the Doppler shifted frequency at which an object encounters the wave $m(\Omega_\phi - \Omega_\mathrm{p}) = \Omega_R$. As will be seen later in this section, resonances with $2m$, also called ultraharmonics resonances (UHR), play an important role in the evolution of the bar and disk heating.

It is important to recall the adimensional parameter $\mathcal{R}$ defined by Elmegreen (1996)

$$\mathcal{R} = \frac{R_\mathrm{corot}}{R_\mathrm{bar}} \tag{5.8}$$

where R_bar is the bar length and R_corot is its corresponding corotation radius. Contopoulos (1980) demonstrated that bars cannot exceed corotation radius, thus the condition of $\mathcal{R} \geq 1$ must be satisfied for all bars. This parameter is useful as it allows us to distinguish between 'slow' $\mathcal{R} > 1.4$ versus 'fast' $1 \lesssim \mathcal{R} \lesssim 1.4$ bars (Rautiainen et al., 2005) in a simple form.

In order to study correctly the evolution of the bar it is necessary to determine R_bar as accurate as possible. In literature there exist several methods to calculate bar length, some of them presented by Athanassoula & Misiriotis (2002), and compared by Scannapieco & Athanassoula (2012), who found good agreement between the three methods. In this study it is followed the third method presented by Scannapieco & Athanassoula (2012). This method is based on the surface stellar density Σ measured along the directions of major and intermediate axis of inertia

tensor of the bar (Σ_A and Σ_B). It is based on the fact that the difference $\Sigma_A - \Sigma_B$ presents a maximum between $r = 0$ and r_{bar}, the bar length is determined by the radius where $\Sigma_A - \Sigma_B$ has dropped to a fraction of the maximum. Scannapieco & Athanassoula (2012) use a fraction value of 5%, yet R_{bar} appears to be longer than the ones observed on face-on views due to the presence of rings in the outer parts of the bar; better agreement is found when using a fraction value of 10%, therefore used in this work.

All disks show similar evolution, and the results presented here are consistent for all disks. In order to avoid repetitiveness, only the results for two simulations will be shown. The fiducial models for this analysis will be `3180_minor` and `3795_minor` due to differences in length scales and evolution times between these models.

Figures 5.14 to 5.18 show the evolution of `3180_minor` disk and bar. Top panel of Fig. 5.14 shows the evolution of ζ, A_2 and $\mathcal{R}$; ζ and A_2 evolution are the same as the ones shown in Section 5.3.1 and 5.3.2. The six regions indicated by vertical dotted lines are the ones before, during, and after the jumps in ζ. The first region is characterized by a mild grow in ζ, a pronounced growth in A_2 and a decrement in $\mathcal{R}$ thus indicating a rapid evolution from a slow to a fast bar. This is a consequence of the quick response of the disk at the moment it goes live. As can be seen when $R \simeq 1$ the bar practically touches corotation; this happens because the fast bar lies above ILRs, so there is nothing that prevents the bar from reaching corotation; no apparent vertical structure or asymmetry is appreciated in this phase.

The second phase is characterized by a small jump in ζ, a decrement in A_2 and an increment in $\mathcal{R}$, meaning that the bar shrinks and weakens while the vertical structure of the disk changes from one state to another. Bar pattern speed Ω_{bar} is now touching the maximum of ILR and terminates around the $\Omega - \kappa/8$ ultraharmonic resonance (UHR8). A snapshot of the disk during this jump is shown Fig. 5.15. It is clearly seen how the jump in ζ is observed in the vertical structure of the disk as a slight corrugation seeing edge-on. Mean vertical position $\langle z \rangle$ and mean vertical velocity $\langle v_z \rangle$ reveal that the ζ jump and the morphological asymmetry are caused by what appear to be vertical oscillation modes in the region corresponding to the bar (Fig. 5.15 middle panels). These modes present an alternation between $\langle v_z \rangle$ and $\langle z \rangle$ maximums and minimums, indicating the possibility of stars traveling up and down in this region as they orbit the center of the galaxy. This behavior mimics that of a harmonic oscillator in the sense that going from $\langle z \rangle$ maximum to minimum corresponds to maximum negative velocity $\langle v_z \rangle$, and moving from $\langle z \rangle$ minimum to maximum corresponds to maximum positive velocity. It is also important to notice that these modes are well bounded within the region between the end of the bar and the ILR, suggesting that these oscillation modes arise as a resonant cavity-like phenomenon in which regions of orbital resonance (ILR and UHR8 in this case) act as nodal

points, imposing the required boundary condition for the amplification of these 'standing' waves.

The six modes stay quasi-stationary until the ζ starts to settle at the third phase, during which the modes start to twist in the direction of rotation (Fig. 5.16), but always keeping the alternation. They intend to mix and fade, as the disk stabilizes in an almost flat ζ region. Similar to the second phase, the modes are well bounded by the ILR and the termination of the bar, which during this phase tends to coincide with UHR8 region, as seen in 5.14. The latter can be seen as a nearly constant value of $\mathcal{R}$.

The fourth region corresponds to the second (big) ζ jump, that as stated above corresponds to the so-called buckling instability. It can be seen that during this time bar strength A_2 reduces as $\mathcal{R}$ grows, indicating a rapid shrink of the bar, that is clearly observed in the fourth bottom panel of Fig. 5.14 by the initial and final state of the bar (dashed and solid black lines respectively). This shrinkage is accompanied by a crossing of the UHR4 region, similar to the crossing of UHR8 observed during the first ζ jump. Fig. 5.17 shows that edge-on view of the galaxy disk displays features that are not only vertically asymmetric viewed through the bar intermediate axis (xz view, top-right upper panel of Fig. 5.17) but also asymmetric when observed through the major axis of the bar (yz view, top-right lower panel of Fig. 5.17). The vertical peaks (horn-like structure) in the upper part of the galaxy and the ends of the almost flat region in the lower part of the disk are well traced by the $\langle z \rangle$ offsets (blue-red regions of middle and bottom right panels of Fig. 5.17; blue color indicates $z > 0$ position with respect to disk plane, while red color indicates $z < 0$). Similar to Fig. 5.15, $\langle z \rangle$ and $\langle v_z \rangle$ offsets correspond to vertical oscillation modes inside the region delimited by the ILR and the bar terminating near UHR4. These modes stay quasi-stationary during the ζ jump and start to twist as the disk reaches a new stable state during the fifth phase of Fig. 5.14.

There are several important features present during the fifth phase, which begins after the second ζ jump when the bar abruptly crossed UHR4 and four vertical oscillation modes were developed. After the formation of these modes the disks settles in a stable configuration in which the bar terminates at UHR4 region, lasting ~ 2 Gyrs in this state. As seen in the third phase, this one is also characterized by a moderate grow in ζ and A_2, and an almost constant $\mathcal{R}$ as the bar follows UHR4 (Fig. 5.14). During this time the oscillation modes developed at the jump rearrange in a new configuration that maintains stable until the end of this phase (Fig. 5.18). Again, $\langle v_z \rangle$ and $\langle z \rangle$ modes stay alternated and well bounded between ILR and bar termination at UHR4 during the ~ 2 Gyrs of the phase. Unlike the modes mentioned above, these are not as pronounced as all of the above mentioned, but are the ones that last the most. At the end of the phase when the bar separates from UHR4 these modes disappear.

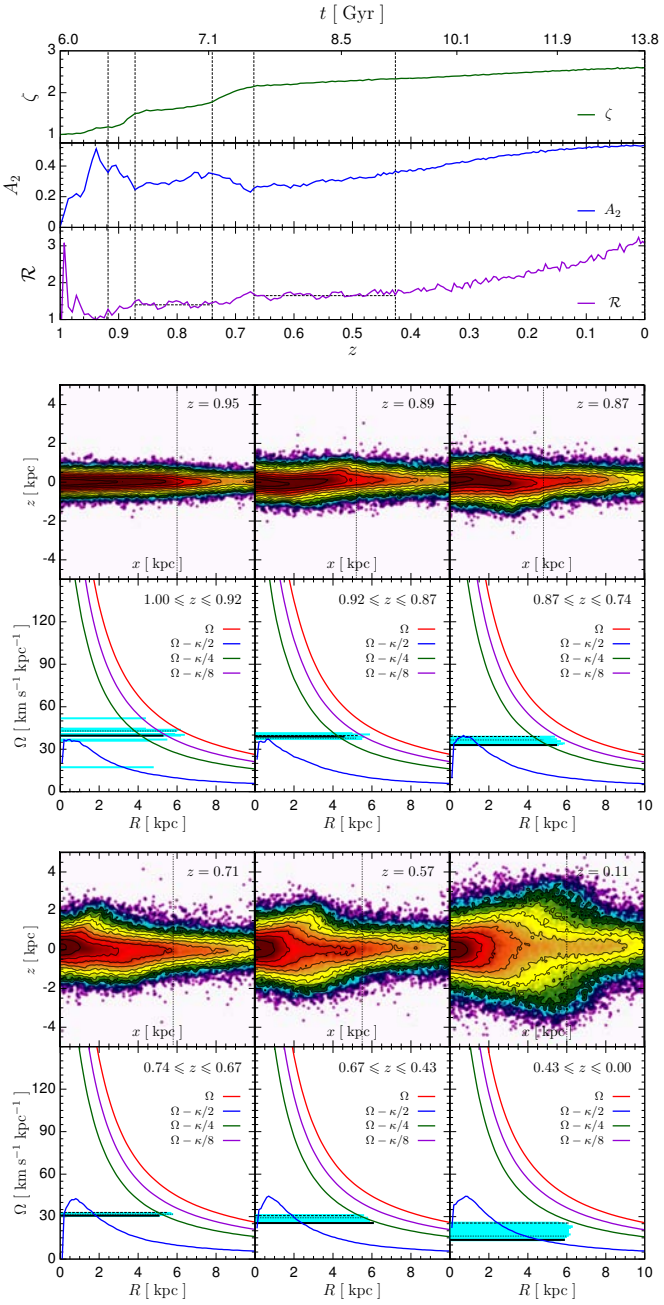

Figure 5.14: Evolution of disk `3180_minor`. *Top.* Evolution of the vertical heating ζ, bar strength A_2, and $\mathcal{R}$ parameter. Vertical dotted lines divide six evolutionary phases identified, while horizontal dotted lines highlight constancy of $\mathcal{R}$. *Bottom* Behaviour of CR, ILR, UHR4 and UHR8 along with bar evolution during each of the phases defined above. Horizontal lines correspond to $R_{\rm bar}$ with $\Omega_{\rm bar}$; black dashed lines are the bar at the start of the phase, blue solid lines in between, and black solid line at the end of it. Each plot is accompanied by a log-projected density edge-on view of the disk in a time between the divisions; plots have the same horizontal length scale. Horizontal and vertical dotted lines show the bar size identified at the same time of the disk showed.

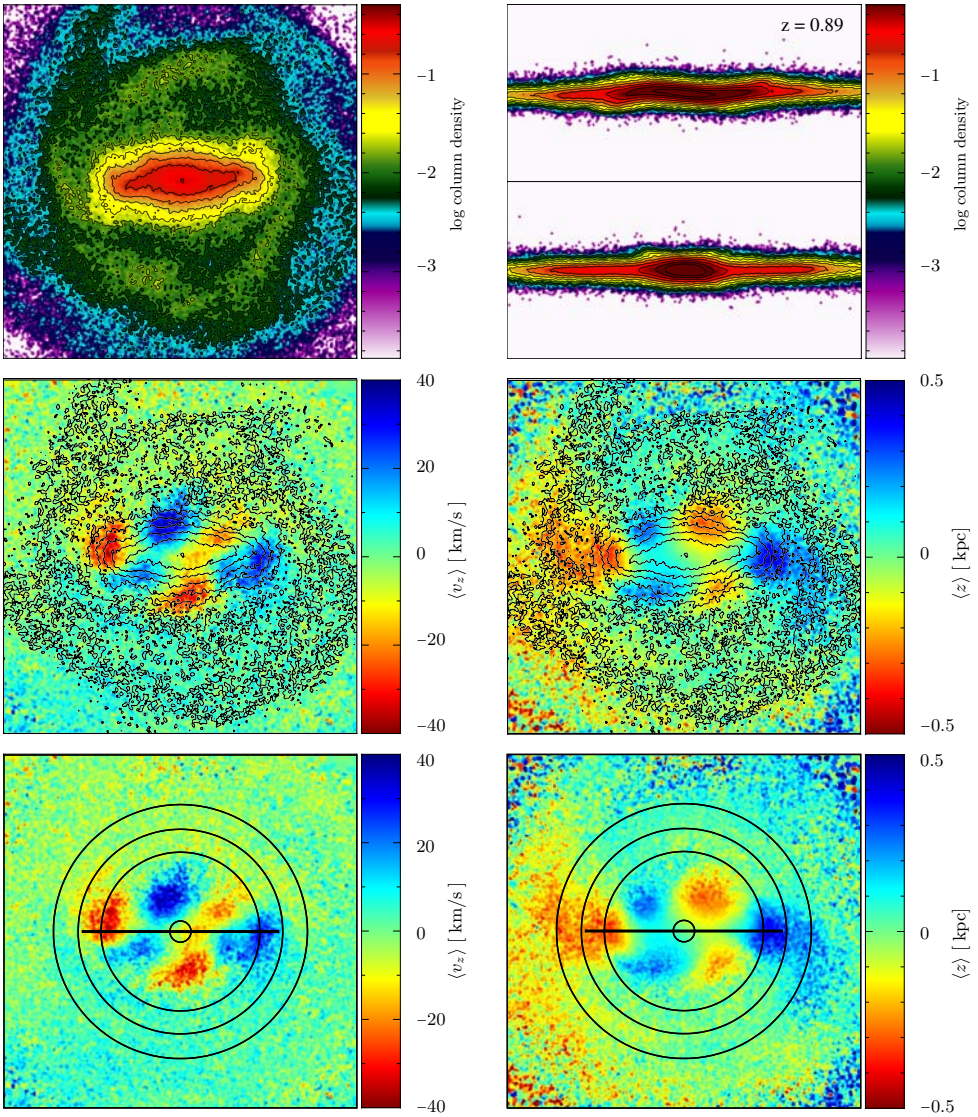

Figure 5.15: Disk `3180_minor` during the first ζ jump (second phase of Fig. 5.14). *Top panels.* Density plots of the disk, top left panel shows xy projection and top left panels shows xz (up) and yz (down) projections; colors render column density in logarithmic arbitrary units. *Middle.* Mean vertical velocity (left) and mean vertical position (right) of the disk viewed face-on, countour lines are the same as those shown in top left panel.*Bottom.* Same as middle panels without countour lines. Circles mark regions of ILR (innermost), UHR4 (second), UHR8 (third) and CR (fourth); horizontal line indicates bar length. All xy projections have 20 kpc on each side, xz and yz projection have 10 kpc on z direction. This snapshot correspond to the first jump in ζ, which coincides with the bar crossing the UHR8. It can be seen that the bending/corrugation of the disk is related to the vertical heating induced by the growth of the oscillation modes (blue-red regions of middle-bottom panels), these are well bounded between the ILR and the UHR8 where the bar terminates. $\langle v_z \rangle$ offset regions (blue-red color in middle-bottom left panels) are alternated with $\langle z \rangle$ offsets (blue-red color in middle bottoms right panels), indicating bulk vertical oscillations between these modes.

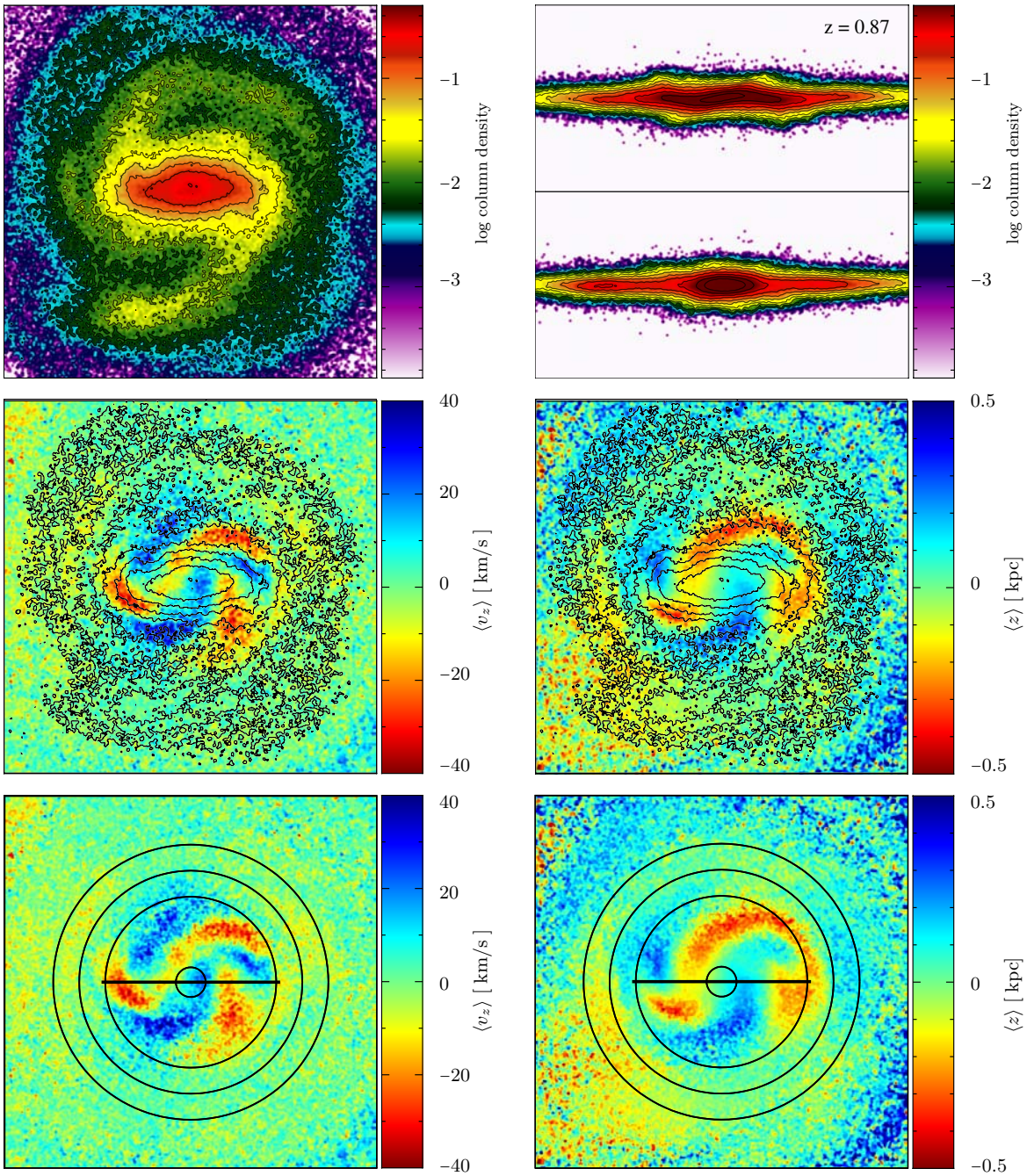

Figure 5.16: Same as Fig. 5.15 but for disk `3180_minor` after the first ζ jump, i.e. during the third phase of Fig. 5.14. This corresponds to the bar terminating at the UHR8. The edge-on profile of the galaxy shows a pronounced corrugation, peaks match the regions of vertical offset (red and blue regions of middle and bottom left panels). During this time the six modes from Fig. 5.15 twist in the same direction as galaxy rotation. As seen in Fig. 5.15 alternation between $\langle v_z \rangle$ and $\langle z \rangle$ offsets are still present. During the rest of the phase these modes eventually blur as the disk stabilizes.

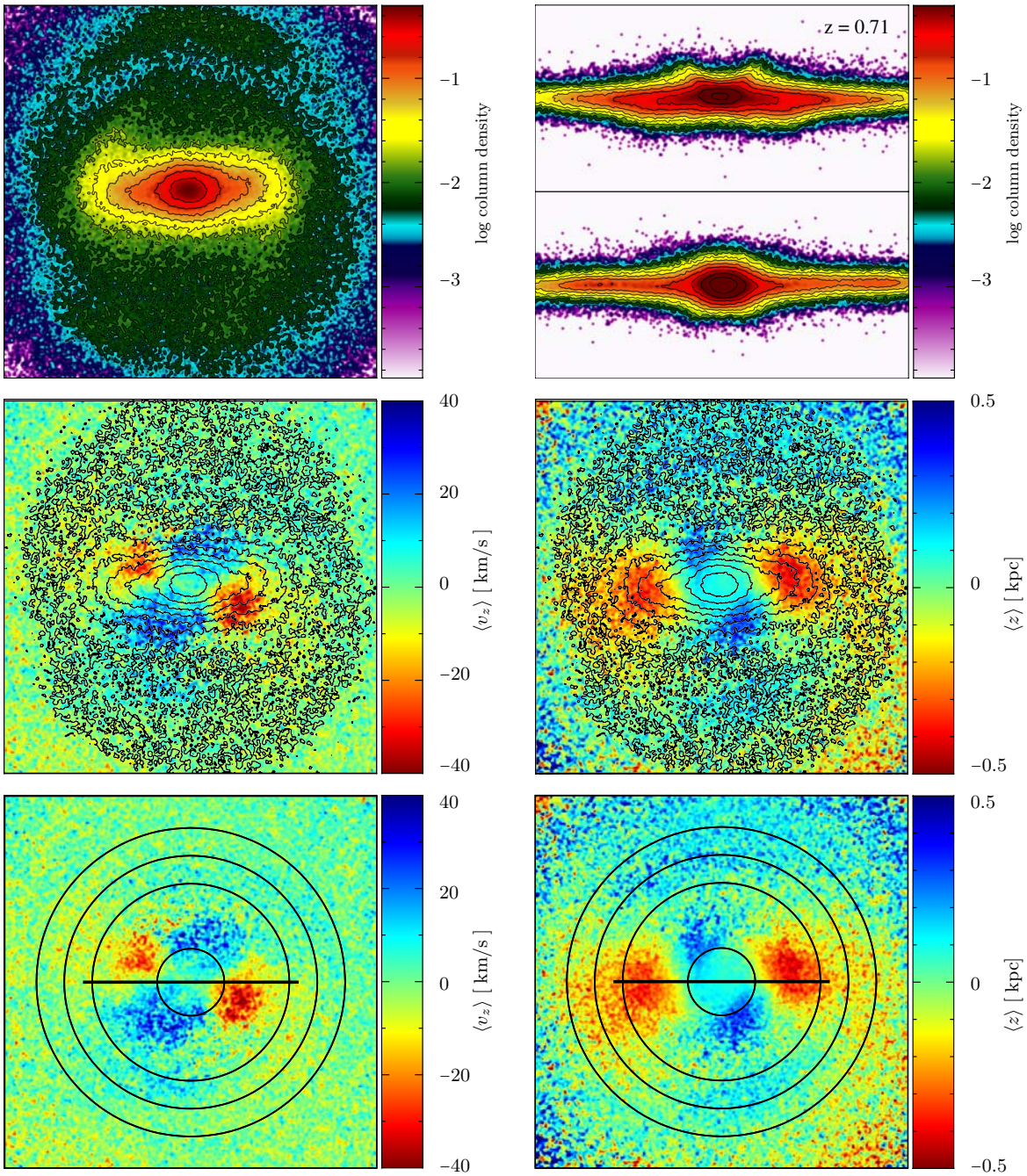

Figure 5.17: Same as Fig. 5.15 but for disk `3180_minor` at the second ζ jump, i.e. during the fourth phase of Fig. 5.14. This phase corresponds to the bar crossing the UHR4 region. The edge-on view shows on the upper part of the disk two prominent vertical displacements, 'horn'-like structure (always formed in the same direction as $L_{\rm disk}$ for all disks), and two weak peaks in the lower part of the disk; these features appear as vertical offsets in the middle and bottom left panels. As seen in Fig. 5.15, $\langle v_z \rangle$ and $\langle z \rangle$ offset regions are alternated. In this case only four modes are present and are bounded by the ILR and the bar terminating near the UHR4.

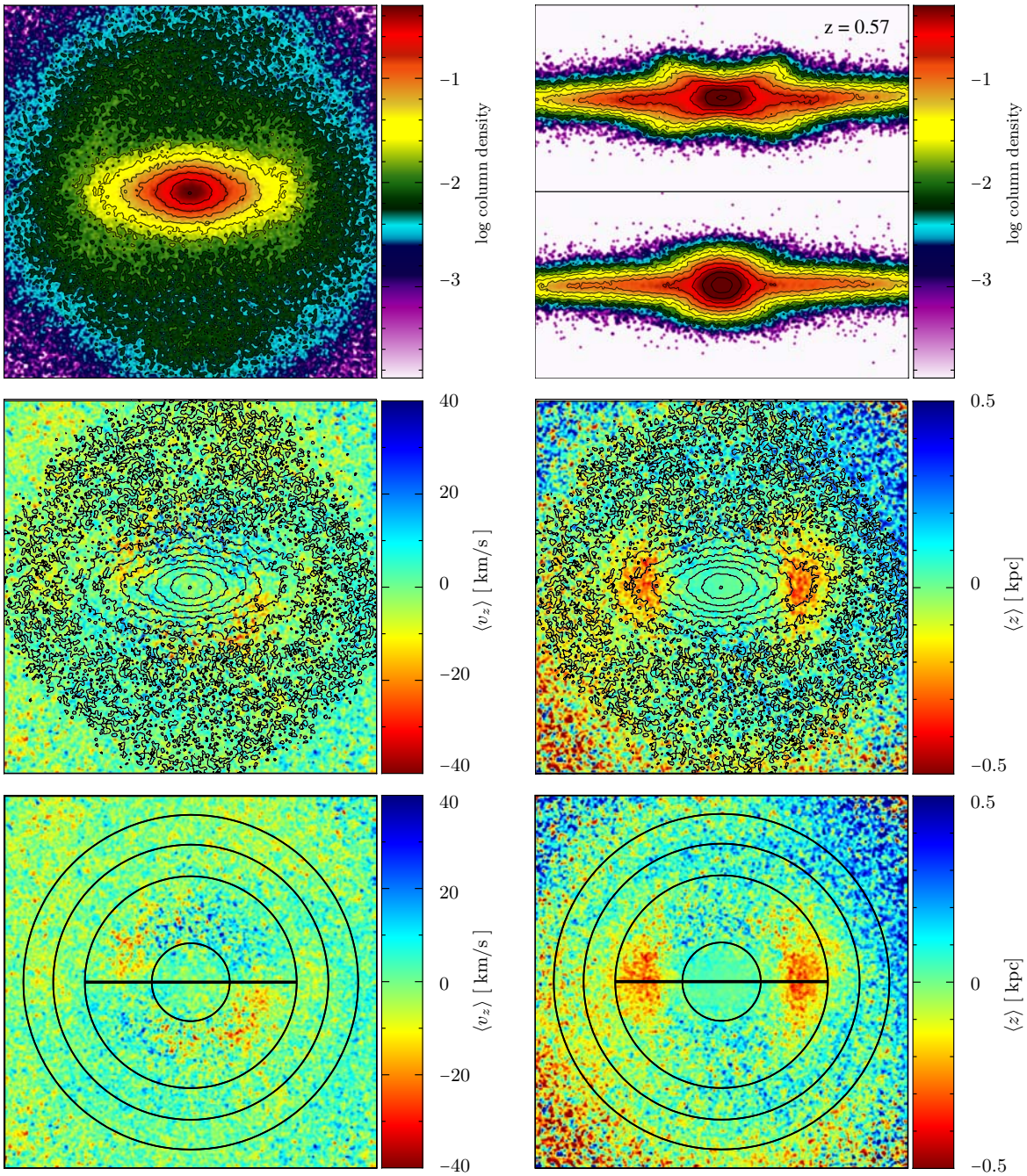

Figure 5.18: Same as Fig. 5.15 but for disk `3180_minor` after the second ζ jump, i.e. during the fifth phase of Fig. 5.14. This phase corresponds to the epoch when the bar terminates at the UHR4 in an stable state. The four (now weak) modes shown in the middle-bottom panels are 'realignments' of the modes generated during the second ζ jump (Fig. 5.17), and are also well delimited by the ILR and bar termination at the UHR4. Alternation between $\langle v_z \rangle$ and $\langle z \rangle$ offsets is still present. Unlike Fig. 5.17 $\langle z \rangle$ offsets are not distinguishable in any projected density view. These modes persist as long as the bar terminates at the UHR4.

The last phase of evolution covers the times between the separation of the bar from the UHR4 and the end of the simulation ($z = 0$). During this phase the bar strengthens and shrinks (rise in A_2 and $\mathcal{R}$) as its termination moves away from the UHR4 and appears to try reaching the ILR region (Fig. 5.14). By this time the disk has heated considerably by the two mechanisms described above and seems to stay vertically stable in this configuration (mild ζ evolution) during the ~ 4 Gyrs that this phase lasts.

The evolution of ζ, A_2 and $\mathcal{R}$ along with resonances and bar evolution of our other fiducial model, i.e. disk `3795_minor`, are shown in Fig. 5.19. The phases identified for disk `3180_minor` are the same as the ones identified for disk `3795_minor`. The first phase, present a rapid evolution of the bar due to the response of the live disk to the presence of the halo. As can be seen, bar structure ($R_{\rm bar}$ and $\Omega_{\rm bar}$) changes rapidly during this phase as the disk and bar try to stabilize (blue lines in middle-right panels of Fig. 5.19). The evolution of $\mathcal{R}$ that the bar shrinks and elongates constantly even reaching corotation. [1] The second phase is where the first ζ jump and UHR8 cross occur. Similar to disk `3180_minor` this model presents a slight corrugation of the disk appreciated in the edge-on view (Fig. 5.20), associated to the six oscillation modes. It is of remarkable importance to notice that despite the differences in size, mass, halo, etc., between the disks, these modes are presented not at the same time after $z = 1$ but at the moment that the bar crosses the UHR8 region. These modes remain quasi-stationary until the disk finds a new stable configuration in the third phase, when these modes twist (Fig. 5.19) and fade. The six modes, $\langle z \rangle$ and $\langle v_z \rangle$, of the disk `3795_minor` are alternated and delimited by the ILR and bar terminating near the UHR8 (see Figs. 5.15 and 5.16).

The fourth and fifth region of Fig. 5.19 present the same four modes as those seen for disk `3180_minor`. The same growing configuration (Fig. 5.22) and rearrangement (Fig. 5.23) is experienced by the disk during the second ζ jump (bar shrinkage and the UHR4 crossing) and the stable configuration with the bar terminating near the UHR4. The peaks of the horn-like structure are also located at ILR, and the modes are alternated and bounded by the ILR and bar terminating at the UHR4 (Figs. 5.22 and 5.23) as seen for `3180_minor` case.

From the analyses, the general picture of the evolution of the disks seems to be the following: at the time the disk turns live and responds to the presence of an interacting dark matter halo, the disk component experiences a lot of changes in its morphology that include the development of strong spiral arms and a fast long bar, which is able to reach corotation given that the bar pattern speed $\Omega_{\rm bar}$ is above the ILR. As the disk continues to evolve, the ILR rises and tries to stabilize the bar. Once the bar is stable it experiences a gradual deceleration, either by angular

[1] The blue line that exceeds corotation arises due to the presence of spiral arms that align with the bar in a configuration that the algorithm used considers part of the bar.

momentum transfer or dynamical friction with the halo (e.g. Athanassoula 2003; Dubinski et al. 2009; O'Neill & Dubinski 2003), making $\Omega_{\rm bar}$ to decrease constantly during its evolution. This plays an important role because it is one of the mechanisms that cause the bar to move in the frequency diagram, hence responsible for the interplay of the bar with its corresponding resonant zones.

When $\Omega_{\rm bar}$ has decreased enough so that the bar crosses the ILR, the bar termination determines how the inner part of the disk evolves. After bouncing at co-rotation, the end of the bar is located in a region where UHRs pile up, and as $\Omega_{\rm bar}$ decreases the bar termination starts to approach to the UHR8 region until the crossing occurs at the same time the bar experiences a subtle contraction. This corresponds to the first ζ jump and the growth of the six vertical oscillation modes. These modes start to twist in the direction of rotation and disappear as the disk reaches a new stable configuration with the bar terminating at the UHR8. During this time the bar continues slowing down as it keeps its termination fixed at the UHR8, until the deceleration is enough to separate the bar from this region.

As soon as the bar approaches to the UHR4, it contracts as it crosses the UHR4 region, which results in the growth of four oscillation modes. Similar to the six modes, these are able to grow stationary while the disk arrives to its new stable configuration. When this happens these modes twist and, unlike the six modes, redistribute in an arrangement that lasts as long the bar terminates near the UHR4. The bar settles at this resonance until it cannot continue to follow the UHR4 due to the slowdown experienced. After it separates from this region the four modes disappear, by this time all simulations have reached $z = 0$.

Regarding the vertical resonant modes, same oscillatory phenomena as the ones shown in Figs. 5.14 to 5.23 are present in all the disks studied in this work. This indicates that these features occur independently of the initial orientation of $L_{\rm disk}$. Though, better spatial and time resolution are needed in order to explain completely the presence of this phenomena, specifically for those disks that only show one jump in ζ (e.g. disk `3795_major`) and present only the six oscillation modes during very short period of time (if present at all). Even though these disks show that bar termination at UHRs argument is plausible, there is no sufficient evidence to explain the absence of the six modes at the UHR8 crossing. The resonances analysis and the morphological evolution of disk `3795` suggest that even if $\Omega_{\rm bar}$ crosses the ILR and the bar terminates at the UHR8, it is not until the bar stabilizes and the spiral arms start to fade, that these resonant modes are able to grow inside this region. Despite these vertical oscillations are the mechanisms responsible for the sudden heating of the disk, it is not clear whether this phenomenon acts as a stabilizing mechanism, which requires a fast rearrangement of the orbital families, or if it is the cause of the instability due to the conditions imposed.

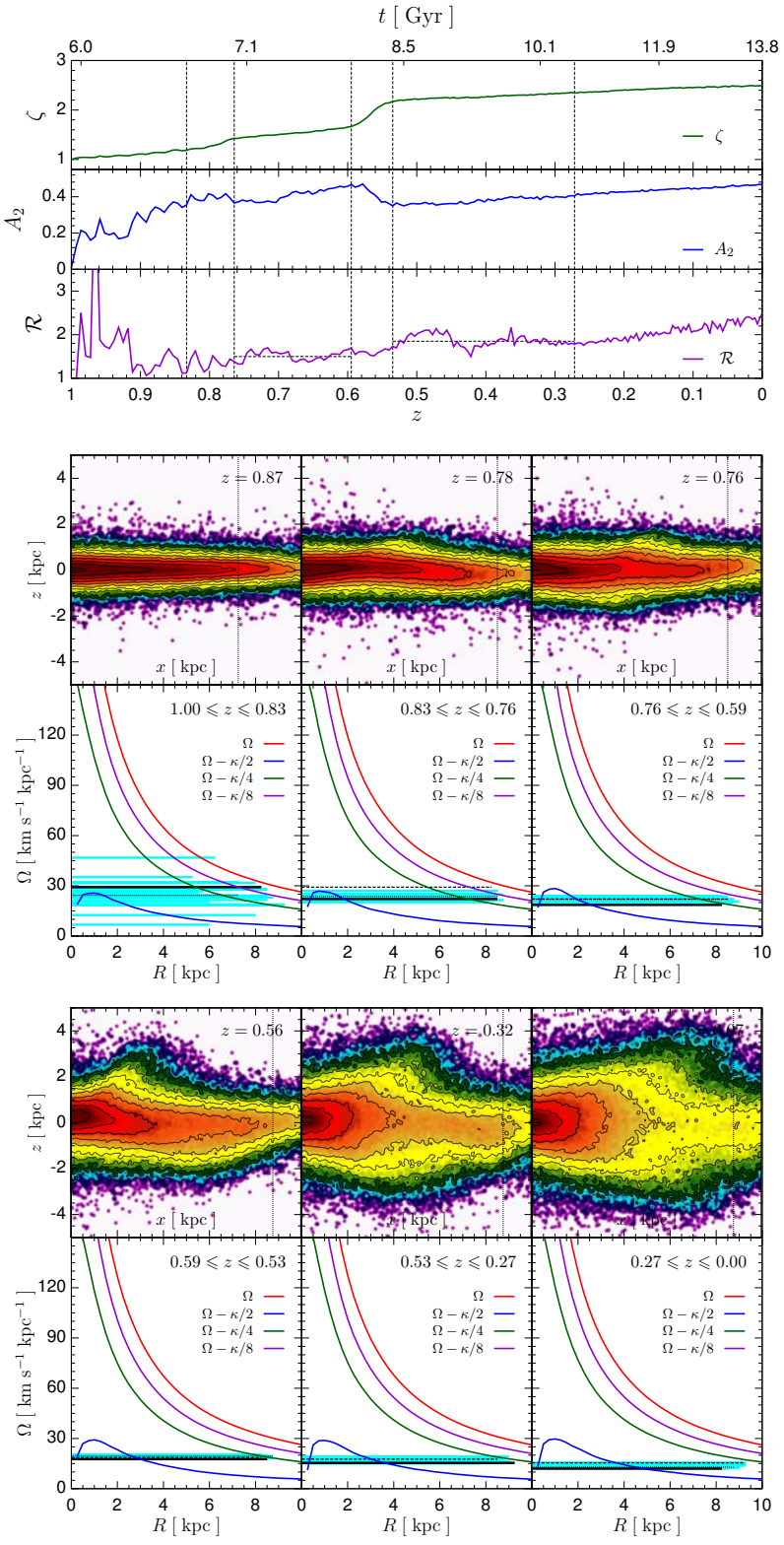

Figure 5.19: Same as Fig. 5.14 but showing the evolution of ζ, A_2, $\mathcal{R}$, and bar of disk `3795_minor`.

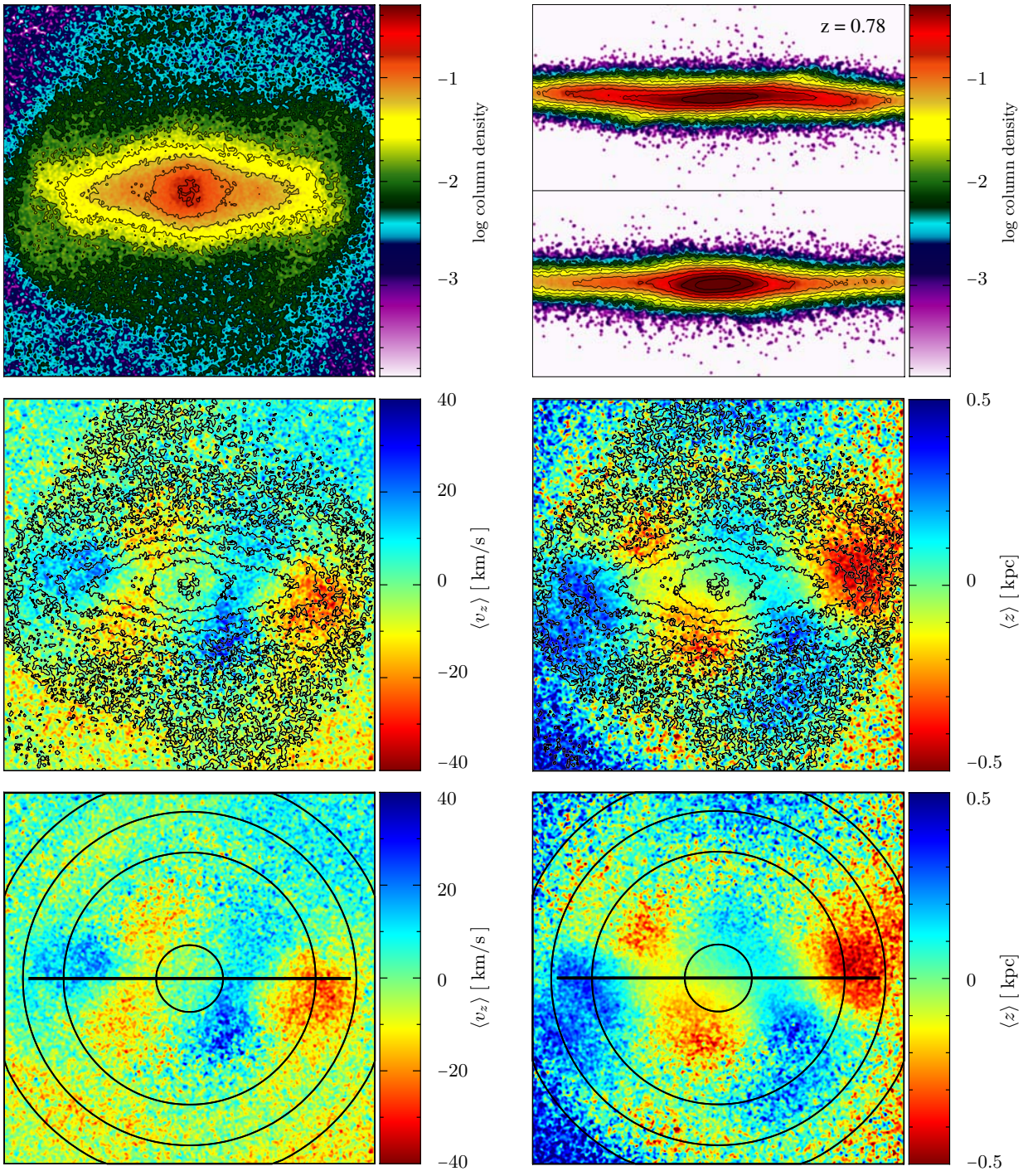

Figure 5.20: Same as Fig. 5.15 but for disk `3795_minor` at the first jump of ζ, i.e. during the second phase of Fig. 5.19. This stage corresponds to the bar crossing the UHR8 region. Edge-on view shows a slight corrugation of the disk that coincides with $\langle z \rangle$ offset regions. $\langle z \rangle$ and $\langle v_z \rangle$ offsets are alternated indicating vertical oscillations in this regions. These six modes are well bounded between the ILR and the bar terminating near the UHR8, and stay quasi-stationary during the jump.

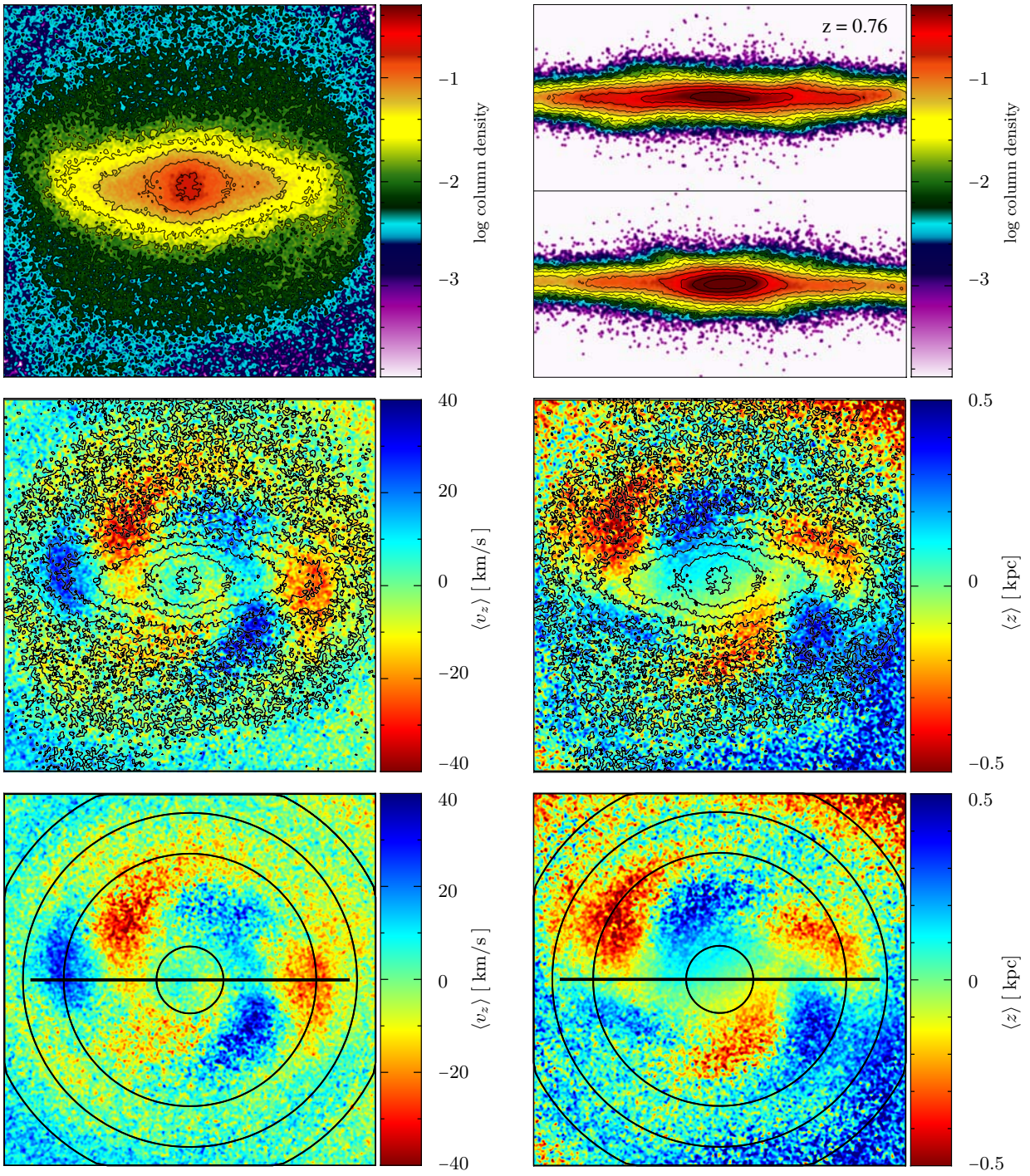

Figure 5.21: Same as Fig. 5.15 but for disk `3795_minor` after the first jump of ζ, i.e. during the third phase of Fig. 5.19. This stage corresponds to the bar terminating at the UHR8 in a stable state. The six quasi-stationary modes of Fig. 5.20 are twisted (same as in Fig. 5.16) in the same direction of $L_{\rm disk}$. The $\langle v_z \rangle$ and $\langle z \rangle$ modes keep their alternation and are still bounded by the ILR and where the bar ends at the UHR8. During this phase these modes eventually erase.

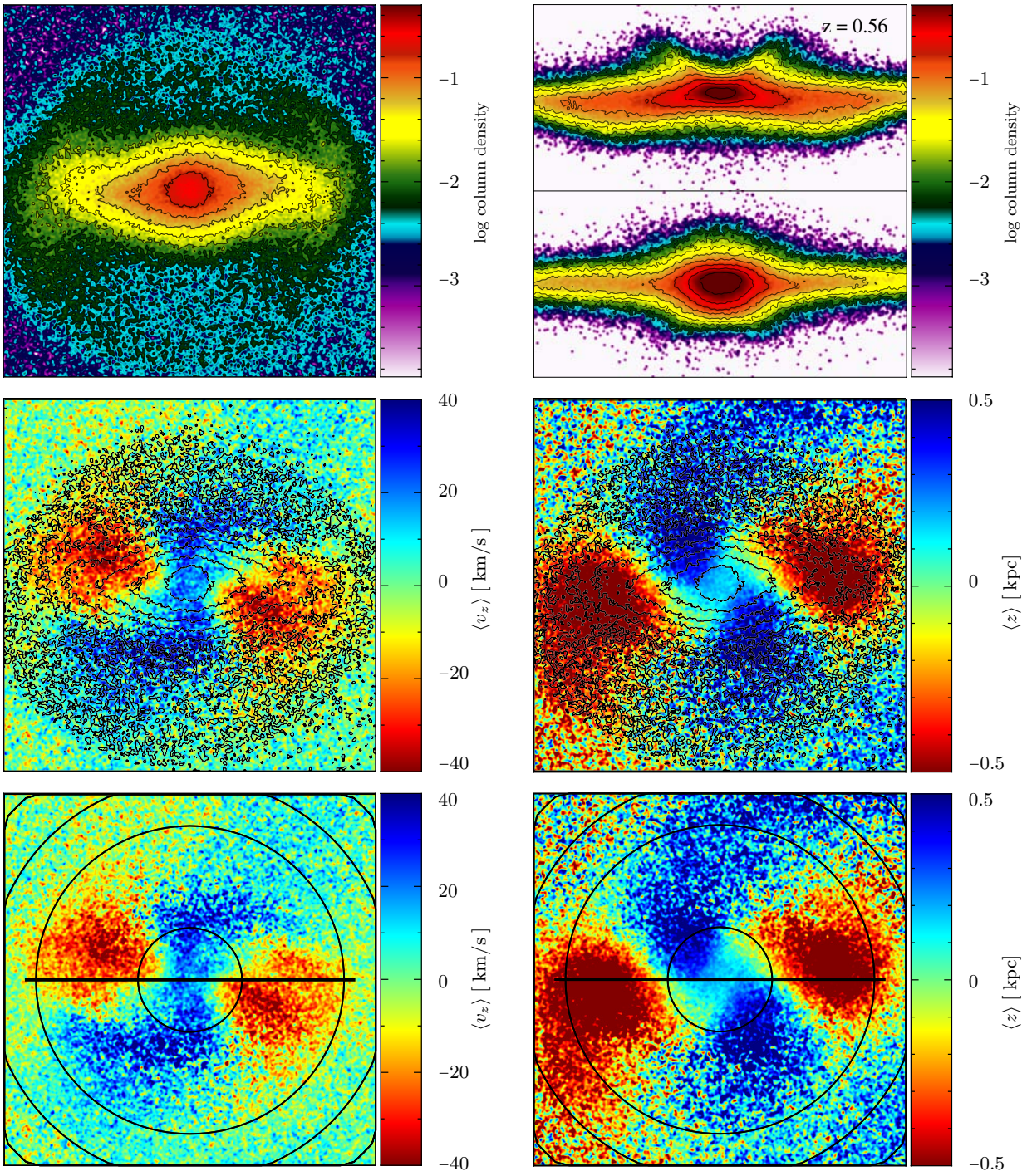

Figure 5.22: Same as Fig. 5.15 but for disk `3795_minor` at the second jump of ζ, i.e. during the fourth phase of Fig. 5.19. This stage corresponds to the bar crossing the UHR4 region. Unlike the first jump (Fig. 5.20) only four quasi-stationary modes are developed. The horn-like structure is also shown by the disk, it can be seen that the peaks of this structure are located at the ILR. $\langle v_z \rangle$ and $\langle z \rangle$ modes are alternated and bounded between the ILR and where the bar terminates near the UHR4 region.

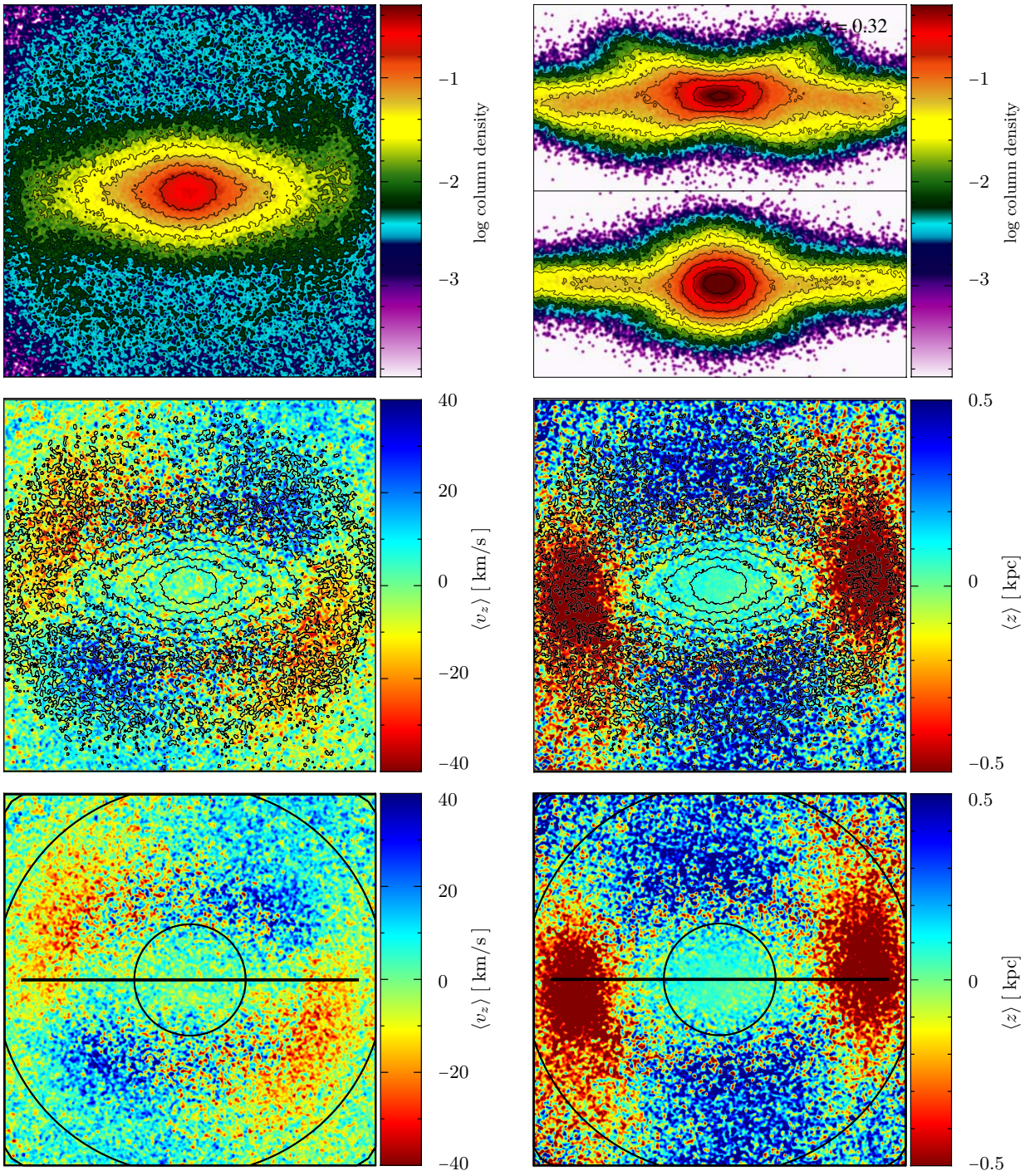

Figure 5.23: Same as Fig. 5.15 but for disk `3795_minor` after the second jump of ζ, i.e. during the fifth phase of Fig. 5.19. This stage corresponds to the bar in a stable state terminating near the UHR4. $\langle z \rangle$ offsets are slightly seen in edge-on views; negative (positive) $\langle z \rangle$ offsets are located at the end of major (intermediate) axis of the bar. These modes keep their alternation and presence until the bar separates from the UHR4, thereafter these modes vanish.

5.4 Disk Tilting and Ring-like structures

Throughout the whole chapter, face-on and edge-on views of the disks have been shown with the major axis of the bar oriented along the x-direction and $L_{\rm disk}$ along the z-direction. This does not imply that the disks always keeps the same initial orientation. In this section is presented the evolution of $L_{\rm disk}$ orientation with respect to the original orientation of the disks (Section 5.4.1), it is seen that all disks independently of their initial orientation experience some degree of tilt, in such a way that the greater $\theta_{\rm ori}$ is, the bigger the tilt expected for the disk. It is also shown how ring structures that are not coplanar with the disk are features exclusive of major-oriented cases (Section 5.4.2), which might be explained by the response of the halo during disk growth.

5.4.1 Reorientation of $L_{\rm disk}$

At the time when stellar disks go live, their motion is not restricted to a given plane, thus they are free to move in any direction during their evolution, experiencing a tilt due to their interaction with their dark matter halo. Disk tilting has been also reported in similar N-body simulation by DeBuhr et al. (2012) and Yurin & Springel (2015). Although, the same dark matter halos were used in both simulations, the results presented in those studies do not concur.

Disk tilting was calculated by measuring the angle θ between the angular momentum of particles in a sphere of 7 kpc and the initial orientation of $L_{\rm disk}$. The evolution of θ for all disks is presented in Fig. 5.24. Minor-oriented disks are the group that presents the less amount of tilting, with θ ranging from 8° to 30° at $z = 0$. Disks initially oriented along the major axis of dark matter halo present the largest θ of all simulations, at $z = 0$ ranges from 82° to 95° except for `3795` which deviates from the group behavior and only ends with a tilting angle of 11°. The distinction made for disk `3795_major` arises because it is the exception for the general behavior of all disks, for which θ increases when $\theta_{\rm ori}$ is bigger, thus `3795_major` is the only case that θ is lower at $z = 0$ than the ones for its smaller $\theta_{\rm ori}$ counterparts. Additionally all major disks, except `3795`, appear to converge at $z = 0$ to a $\theta \simeq 90°$, which would indicate that these disks try to orient along minor axis.

Regarding to the intermediate $\theta_{\rm ori}$ orientations (bottom panels of Fig. 5.24), θ is alway larger when $\theta_{\rm ori}$ is bigger, except `3795_major`. It can be seen from disks `3180` that major orientation appear to be in a metastable state until something triggers a rapid change in its orientation. Similar 'bounces' are displayed by both `3180_minor` and `3180_30deg` which may indicate a common mechanisms that affects disk's orientation (e.g. orbiting subhalos).

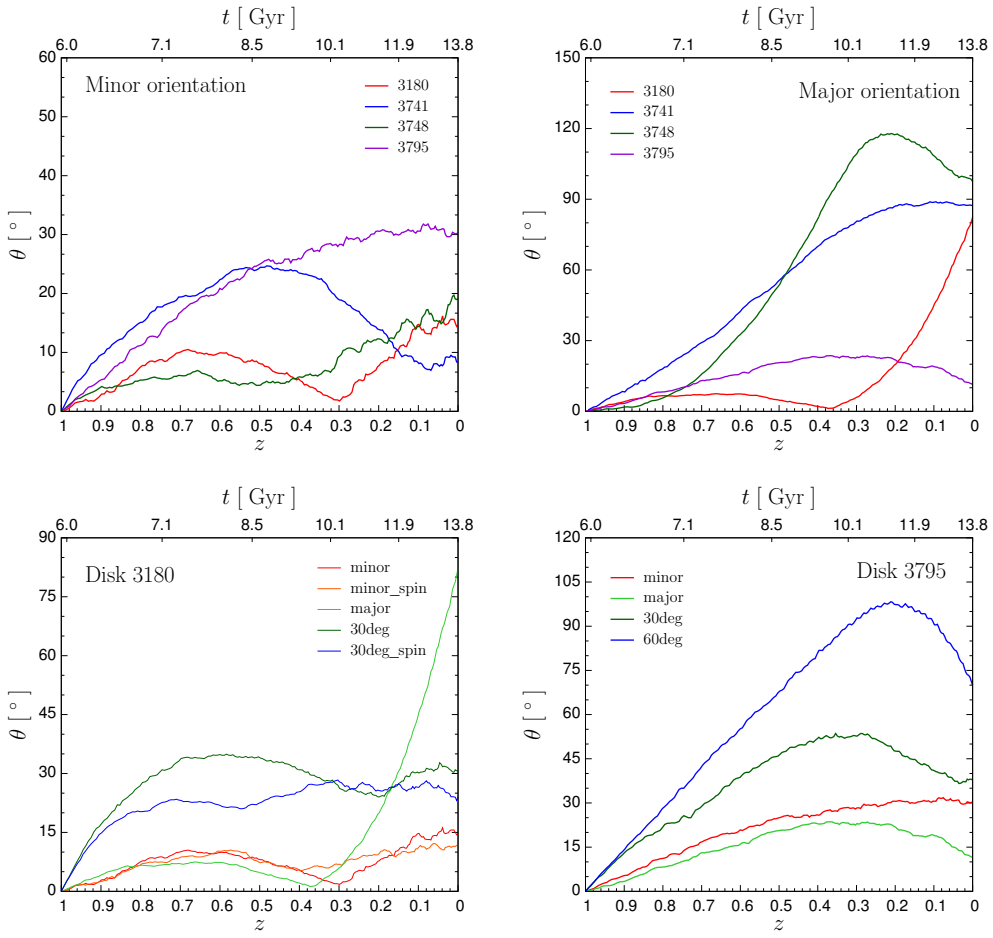

Figure 5.24: Evolution the angular momentum orientation of the inner 7 kpc with respect to the initial orientation from $z = 1$ to $z = 0$ of minor-oriented (top-left), major-oriented (top-right), 3180 (bottom-left) and 3795 (bottom-right) disks.

In their studies Yurin & Springel (2015) reported an average value of 35° for disks oriented along minor axis, ranging from $\sim$ 5° to $\sim$ 65°, and an average of 60° major-oriented disks ranging from 30° to $\sim$ 95°; DeBuhr et al. (2012) reported a minimum of 30° and maximum of 60° minor-oriented disks, and an angle ranging from $\sim$50° to 150° for major-oriented ones. The three studies agree that minor-orientated disks tend to present smaller θ that the major-oriented cases, nonetheless there are some exceptions found in this work and in Yurin & Springel (2015), for which some cases with major orientations present smaller angles than the minor ones, which as mentioned by Yurin & Springel (2015), shows that halo minor axis offers better stability to tilting than the major on, which is true for almost all disks. The differences between our results and the ones of those works, is that angles for minor orientations are larger than ours, while the angles obtained here for major orientations lie above of those presented by Yurin & Springel (2015) and below of DeBuhr et al. (2012).

Differences in the results of the three studies might arise due to several factors: the specific methodology used to grow the stellar disk and the velocity assignment to disks particles; the constraints used to select the host dark matter halos from cosmological simulation (i.e. halo environment) and the code used to integrate the equations of motion.

Despite of the tendencies shown by all disks, their reorientation is not easily explained as it does not depend solely on the disks but also on the host halo which plays a crucial role. Several studies provide some insight on the disk and halo alignment. Bailin & Steinmetz (2005) and Hayashi et al. (2007) showed that dark matter halo spin tends to align with its minor axis, and Zhang et al. (2015) affirms that disk material traces the angular momentum of dark matter halos in the inner regions. These results indicate that the disks will tend to align with halos minor axis, which is why it is observed a better stability than other orientations, nonetheless Bailin & Steinmetz (2005) affirm that the slight misalignment between halo minor axis and angular momentum causes the disks to be generally misaligned with their host halo. It is also important to take into account that halo does not respond as a whole to the presence of the disk, and are only the inner parts affected by the galaxy as shown by Bailin et al. (2005), who also support the picture of the alignment of the disk with the inner halo, which in addition to the difference in reorientation experienced by the inner halo Bett & Frenk (2012) will affect the amount of tilt experienced by the disk.

All the circumstances mentioned above are evident when we take into account the growth of the disk. As mentioned in Chapter 4, rigid disks were inserted in the live halos, in order to the halos respond to the presence of a growing disk. As the orientation of the disk remains fixed during this epoch, the response of the halo will be different for each orientation. In the case of minor-oriented disks, the principal axes of inertia of the inner parts of the halo do not change drastically because $C_{\rm halo}$ is essentially aligned with disk minor axis. For non-minor models the axes of the inertia tensor do change due to the misalignment of the minor axis of the disk and the $C_{\rm halo}$, i.e. the flat mass distribution of the disk will tend to flatten the mass distribution of the halo. Therefore, despite the distribution is kept fixed, the angle with respect to $C_{\rm halo}$ will not be the same as the original $\theta_{\rm ori}$. As the external parts of the halo are not affected by the disk (Bailin et al., 2005) a transition between minor to major axis along the same direction is possible. As will be shown below, this causes that the disk inside $\sim$ 2 $R_{\rm d}$ to be aligned parallel to minor axis of the central region of the host halo, even if it was originally the major one, while the outer parts of the disk will not be aligned neither to the minor nor major axis. This disagrees with DeBuhr et al. (2012) who affirmed that "the halo axes show very little twist over the inner 50 kpc", when the inner halo shows a noticeable transition from one principal axis to the others.

5.4.2 Ring Structures in high $\theta_{\rm ori}$ orientations

In Section 5.1 it was mentioned that the most striking difference between low and high $\theta_{\rm ori}$ galaxies is the presence of ring structures that are not coplanar with the rest of the stellar disk. These ring structures can be clearly seen at $z = 0$ in all edge-on views of all major-oriented disks (Fig. 5.3) and `3795_60deg` (Fig. 5.6). The presence of these structures was noted by DeBuhr et al. (2012), who measure these features with the warp angle θ_{warp} at $z = 1.0$, $z = 0.5$ and $z = 0$, but they do not provide a detailed picture of its evolution. Additionally it is not clear how θ_{warp} was calculated; Yurin & Springel (2015) who used a larger sample of the Aquarius dark matter halos did not report this phenomena in their simulations, pointing out that minor- and major-oriented disks yield qualitatively very similar results.

Independently of the evolution of the angle θ, all of high $\theta_{\rm ori}$ models present ring structures. Th evolution of these structures for all disks oriented along major axis is shown in Fig. 5.25. For each disk two different sequences are shown, the top row is a log projected density of the disk and ring, while the bottom row corresponds to 2D velocity maps. They provide a clear picture of what happens with each disk, since the structural evolution is seen with density map, and the kinematic behavior of each component is obtained with the velocity map, making it easier to perform comparison with data acquired from observations.

For all disks, ring structures form from the material of the outermost radii, indicating that these structures may arise due to the low gravitational binding of these regions in comparison with the rest of the disk. Although all disks with ring structures present different evolution, the unique properties of each disk give a broader idea of the phenomena observed. For example, disks presenting these features can be classified by the amount of material spread between the ring and the galaxy, with the limits being a ring completely separated from the disk with no material between them, and a disk without a separated ring. Examples of these cases would be `3795` for the former and `3180` for the latter. Disk `3795` shows an almost non-reorienting disk with a ring tilting clockwise as seen from Fig. 5.25 perspective, the density plot shows that ring material is almost localized exclusively in the ring surroundings, while the velocity map reveals material spread but without connecting with their initial region. Moreover, disk `3180` shows a more noticeable amount of diffuse material between the ring and the disk, which is seen as a strong warping of the galaxy at $z = 0$ in both density and velocity map.

However, all disks cannot be separated with such a simple classification, which is case for disks `3741` and `3748`. Disk `3741` shows a quite interesting behavior, displaying an outer structure that follows the disk despite of being separated, however this outer material is not in the form of a 'pure' ring but rather presents a helical structure, which is appreciated in the density and velocity maps at redshifts 0.32 and 0.15. On the other hand, disk `3748` displays two separate

ring structures that are not distinguishable from the density plot, but are evident from the velocity map. Though these two structures contain different amount of material, one being denser than the other, the former show similar behavior as the rings of other disks, while the latter, the weaker, seems to be remnant of the original configuration of the galaxy, conserving disk's original angular momentum orientation.

To fully understand the origin and evolution of these structures along with disk tilting, a detailed analysis of the halo is also needed, which is beyond the scope of this work. Nonetheless, a quantitative description of the evolution of this structures is done for the cases of major orientations of disks `3748` and `3795`. These disks are of interest due to the double-ring feature displayed by `3748` and the distinct ring on a no so strong tilting `3795` disk. It was mentioned above that DeBuhr et al. (2012) characterized this structures with the angle θ_{warp} only at three given snapshot of their simulation, but as seen in Fig. 5.25 this approach may not give a clear picture of the evolution due to the high amount of independent reorientation experienced by the disk and the rings. In this work these features are characterized with three different angles, which are calculated using angular momentum of disk material using spherical bins. These bins are used instead of cylindrical ones in order to correctly account for the ring particles that might occupy inner cylindrical radii due to the tilting of both components.

The angle α, which is equivalent to θ_{warp}, is measured as the angle between the angular momentum contained in a bin, and the innermost bin L at a given time; β is the angle between the L within the bin at a given redshift z, and the L of that same bin but at $z = 1.0$, which is the equivalent of θ (Fig. 5.24) but at each radii; and γ is the angle between the L of that bin at redshift z, and the halo minor axis of the inertia tensor of a sphere (not shell) with the same radius of the bin. The results are displayed using color surface plots as a function of radius R, and redshift z. Color codes are used for the angle α, β or γ, in this way a detailed description of the evolution at all radii and during the whole simulation can be visualized with ease. Results for disks `3748` and `3795` are shown in Figs. 5.26 and 5.27, respectively.

From angles α and β of disk `3748` of Fig. 5.26, it can be seen that the bulk reorientation of the disk is the same for the inner $\sim$12 kpc of the disk. The angle α shows this feature as an almost constant near zero angle of this radii through all the evolution, and β as the same color gradients for all these radii, hence a vertical cut to β within $R \leq 12$ kpc would reproduce θ shown in Fig. 5.24. It is clear that the ring features arise from the outer parts of the disk, α shows that the outermost radii are the ones to separate first and the ones that reach the highest deviation from the rest of the disk, which are explained due to the fact that the outermost radii are the less bound and thus the first expected to separate from the disk. After reaching a peak value at $z \sim 0.2$, α shows a decrement which would indicate that the angle between the angular

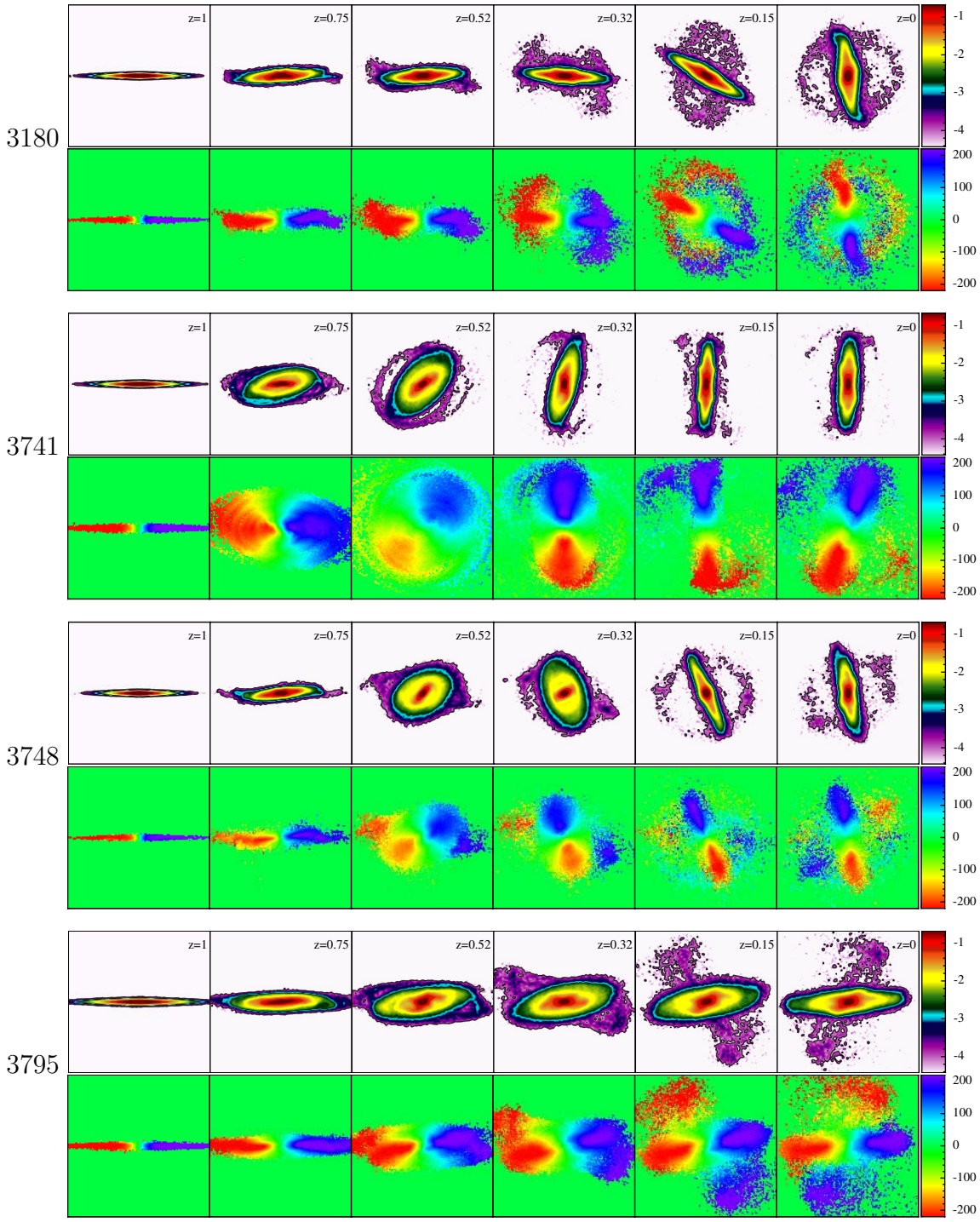

Figure 5.25: Density render and velocity map of all major-oriented disks. Each panel shown has 40 kpc on each side, top row of each disk pair shows column density in logarithmic arbitrary units, while color of the bottom panels renders mean line-of-sight velocity $\langle v_{\rm los} \rangle$ in km/s. All disks ring-like structures separate from the disk in different directions than of disk's bulk tilting, and independently of the amount of reorientation experienced by the disk. All disks are plotted with the same orientation as the disk at $z = 1$.

momentum of the disk and ring is decreasing. However that is not true, because of the presence of the second ring. From Fig. 5.25 it is clearly seen that the primary ring is almost rotating in the opposite direction of the disk, and also opposite to the rotation of the second ring, thus this decrement in α arises due to the vectorial nature of L, and not only from a reorienting ring. This demonstrates that a description using a single angle, as done by DeBuhr et al. (2012), is a useful approximation but is not completely correct, rather a more elaborated analysis is needed (e.g. analyzing the two streams separately).

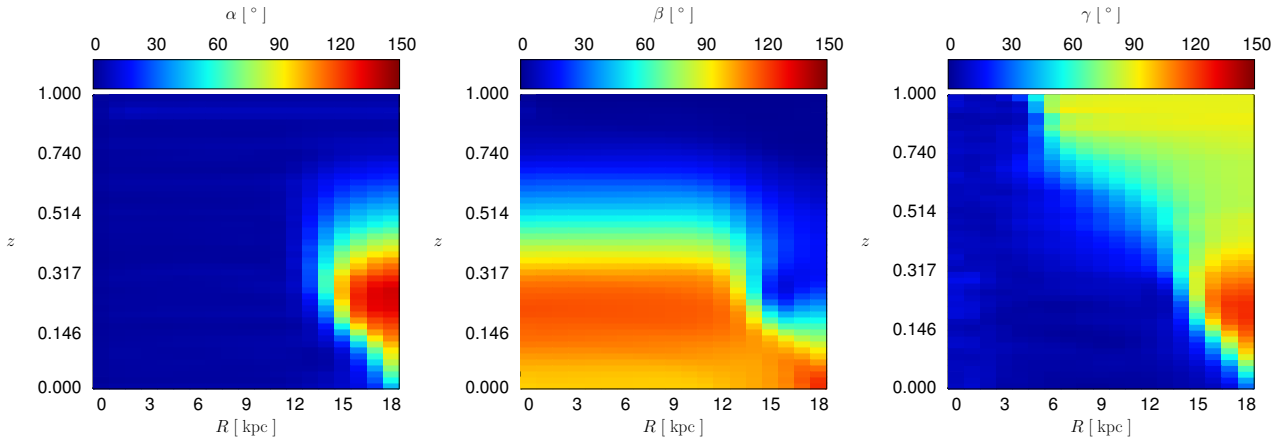

Figure 5.26: Surface color plots of the evolution of angles α, β, and γ of disk `3748_major` as a function of radius R and redshift z.

Besides the bulk tilting for $R \leq 12$ kpc β shows that the outer part does not tilt until $z \sim 0.2$ when the rest of the disk has tilted above 100°. It thus can be said that the disk is the one that separates from the initial orientation while the ring is left behind. The angle γ shows that the innermost radii $R \leq 4$ are aligned with halo's minor axis, then a steep transition to $\gamma \simeq 90°$ for the disk to be aligned with halo intermediate axis. As mentioned before this might be the cause of the separation between the inner and the outer parts. The evolution of γ then shows that the regions of the disk that are initially not aligned with halo minor axis (i.e. $R \gtrsim 4$ kpc) experience a decrement in γ during the evolution of the disk, as it reorients, but keeping the innermost parts well aligned with their respective minor-axis. This indicates that the disk and the inner halo are coupled and move (or reorient) as a whole trying to align the disk with the minor-axes of outer radii. This picture is consistent with the higher amount of 'flips' that the inner halo experiences, as found by Bett & Frenk (2012). Regarding the outer radii, the same behavior of α is seen as in γ from $z \sim 0.4$ to $z = 0$, implying that the ring or rings appear not to follow halo minor axis, a separated study is under way.

The angles of disk 3795 (Fig. 5.27) show somewhat different behavior as the ones for disk 3748. The angle α shows what is to be expected from a unique ring, a region that experiences bulk tilting inside $R < 19$ kpc, and an outer part that gradually increases as it separates from the rest of the disk. The bulk reorientation in β shows a mild increase and decrease for radii $R < 19$ kpc, again a vertical cut to the color map reproduces θ of Fig. 5.24. The similarity between α and β is explained because of the small tilt shown by the disk.

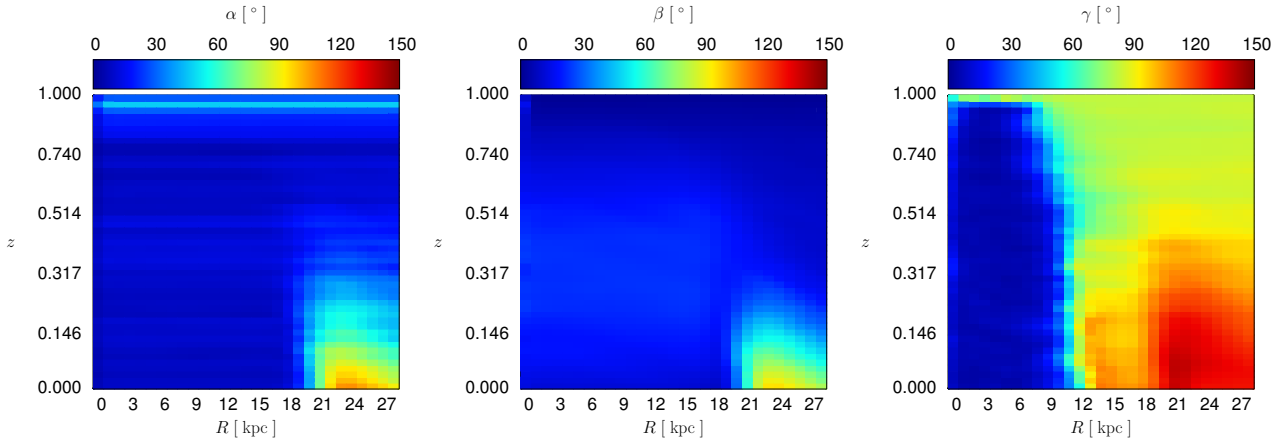

Figure 5.27: Surface color plots of the evolution of angles α, β, and γ of disk 3795_major as a function of radius R and redshift z.

The evolution of γ shows very interesting features. The first one is mostly an alignment of the inner region with halo minor axes at these radii $R < 10$ kpc, similar to what was seen for disk 3748. The radii that were originally not aligned with halo major axis, i.e. $9 < R/\text{kpc} < 19$, presents an increasing γ, which would mean that the halo at this radii does not follow the disk but seems to tilt in the opposite direction. Nonetheless, it should be remembered that the principal axes of inertia are indeed axes and not vectors, i.e. the 'positive' and 'negative' directions of these axes should in principle be equivalent. Taking this into account $\gamma > 90$ would mean that the halo minor axis appears to be orienting with L_{disk}, but we are measuring γ with respect to the other 'side' of the axis. However, these results do not provide enough information to affirm this reorientation of the halo. For $R > 19$ kpc, γ indicates that the ring drifts from its initial angle with respect to the minor axis; however, it is not clear if the ring just drifts or tries to align with the minor axis.

Chapter 6

Discussion

In this chapter is presented a discussion of the methodology described in Chapter 4 and the results shown in Chapter 5. In Section 6.1, it is discussed the limitations of the simulations and the N-body approach to galaxy formation implemented in this work, as well as the cosmological context in which disks were simulated, while in Section 6.2, a discussion of the astronomical implications of the method and the results, specifically regarding the peanut/X-shaped pseudobulge, the buckling instability and the ring structures, is presented.

6.1 Implications of the Method

N-body approach for Galaxy Formation

The formation and evolution of disk galaxies should in principle be studied by means of hydrodynamical simulations including the corresponding baryon physics (e.g. Kim et al. 2014a; Marinacci et al. 2014; Scannapieco et al. 2012; Vogelsberger et al. 2014b). Nonetheless, there still exists disagreement between state-of-the-art simulations (e.g. Scannapieco et al. 2012) regarding hydrodynamical modeling, i.e. feedback, star formation, cooling, etcetera. Therefore the capability to produce galaxies whose properties are in concordance to the observed ones will highly depend each code and its sub-grid physics implementation. Nevertheless, several improvements have been made recently both in hydrodynamical zoom-in simulations (Marinacci et al., 2014), and full-box cosmological hydrodynamical simulations (Vogelsberger et al., 2014b). Producing galaxies with properties similar to those of the Milky Way have been for the former, and a set of them consistent with the observed stellar and baryonic Tully-Fisher relation for the later.

The method implemented in this work provides a complementary approach to galaxy formation using only the N-body technique, hence the results obtained here can only be compared

to certain degree to simulations of galaxy formation and, of course, observations. Although, a complete understanding of the formation and evolution of galaxies, and the processes involved in them require simulations as the ones mentioned above, there are still unanswered questions that can be tackled using N-body simulations. In addition, the parameter space in simulations of galaxy formation is enormous, and different treatments of feedback and star formation (even the same sub-grid physics but different code) highly affect the outcome of simulations (Scannapieco et al., 2012), therefore the difficulty to separate the effects produced by such parameters. On the other hand, the N-body approach permits us to study the effects arisen purely by gravitational interaction, hence if a similar effect is observed in N-body and hydrodynamical simulations, it can be attributed to the gravitational interaction and not to any sub-grid model. However, care has to be taken to avoid undesired/spurious effects, such as relaxation due to two-body interaction (Sellwood, 2013).

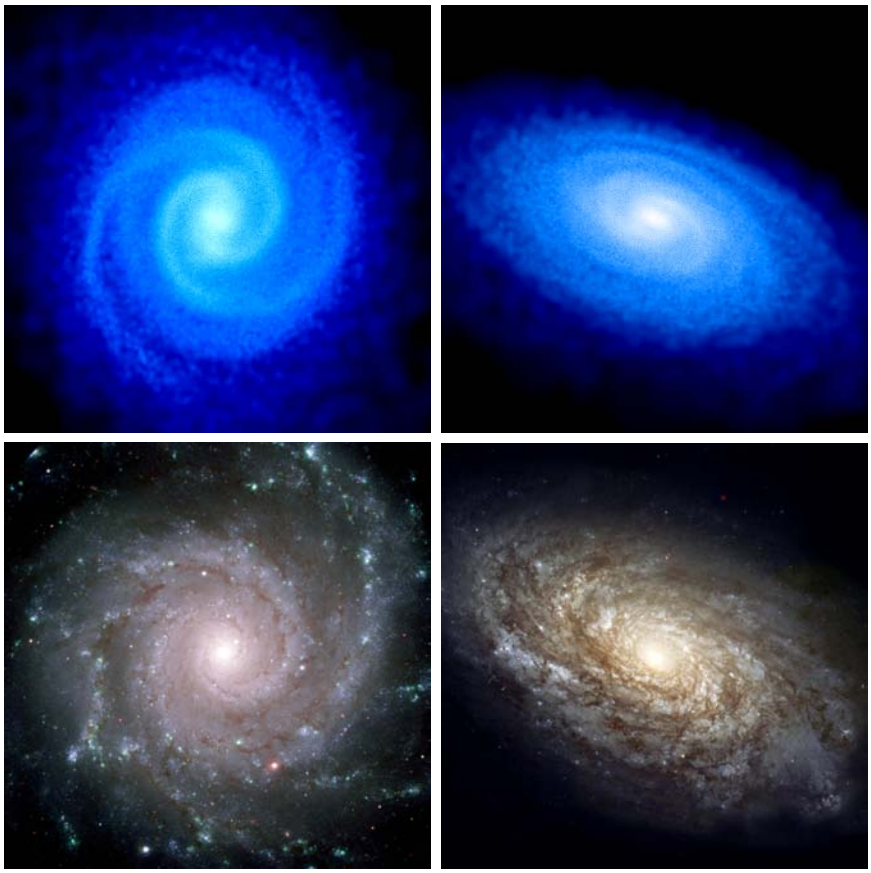

Figure 6.1: Comparison of grand design spiral structure displayed by model `3795_major` (top left) and M74 (bottom left), and flocculent spirals shown by model `3795_60deg` (top right), and NGC 4414 (bottom right).
Image Credit M74: Gemini Observatory, GMOS Team.
Image Credit NGC 4414: The Hubble Heritage Team (AURA/STScI/NASA).

A clear advantage of the method implemented here over hydrodynamical simulation, is the ability to 'control' variables to explore different scenarios. The most obvious example of this is the capability to chose different orientations and spin of the disk for a single halo. In principle the method can be easily extended to explore several disk masses, scale length, additional disk components such as a bulge, as well as different formation times in a similar fashion as has been done by DeBuhr et al. (2012) and Yurin & Springel (2015).

Although the purpose of this work does not intend to reproduce any observed morphology or configuration of an observed galaxy, it is important to notice that the method implemented here is able to 'mimic', at least visually, the morphology displayed by some real galaxies. Examples of this are the grand design spirals of M 74 that are similar to those displayed by `3795_major`, or the focculent spiral morphology of NGC 4414 by `3795_60deg`, as is shown in Fig. 6.1, in addition to the similar configuration to Polar Ring Galaxies displayed by all major- and $\theta_{\rm ori}$= 60 disks, as will be discussed below.

6.2 Astronomical Implications

ΛCDM Cosmology and Cosmological Environment

As described above, this study adopted the ΛCDM cosmological model with parameters in accordance to WMAP-9 cosmological constraints (see Chapter 4 for details). Although ΛCDM model has been considered in recent years as the 'standard' cosmological model, and constraints imposed by *Planck* (Planck Collaboration et al., 2014) and WMAP-9 (Hinshaw et al., 2013) measurements of CMB, indicate a remarkable preference for this model, there are still open problems that even including baryon physics cannot be answered yet (see e.g. Weinberg et al. (2013)), such as the cusp-core problem of dark matter halos, where zoom-in simulations of some groups do not show evidence of cores in halos (Marinacci et al., 2014) while others do (Mollitor et al., 2015). Having said this, a study of the evolution of stellar disks in different cosmologies such as WDM (e.g. Colín et al. 2000), SIDM (e.g. Fry et al. 2015), or γCDM and νCDM (e.g. Schewtschenko et al. 2015) would, in principle, provide a different environment for the selected halos and hence for the simulated disks. Nonetheless such studies will remain pending until a resolution convergence analysis of the simulations presented here is done.

Vertical Modes and the Buckling Instability

The fact that the bar termination tries to keep fixed around the UHR regions suggests that the UHRs act as attractors of stable states of the bar. This is supported by the fact

that during these phases a nearly constant vertical heating ζ is observed, and that the sudden contractions of the bar, during the jumps in ζ, seem to indicate that the bar tries to reach this configurations in a 'violent relaxation' process. This suggests that as the bar pattern speed $\Omega_{\rm bar}$ decreases, whichever mechanism is responsible for, and the bar termination approaches to resonant regions, the UHRs pull the bar towards them (thus causing the contraction of the bar, the ζ jump and the modes), so that the bar ending remains fixed at these locations. The latter may be the reason that stable phases, that come after the jumps in ζ, seem to present a damped oscillation in $\mathcal{R}$ around a constant value during this time. Later phases of evolution then arise as a consequence of the apparent struggle between the inevitable slowdown of the bar and its tendency to terminate at a resonant region.

This general picture is supported by previous studies such as Elmegreen (1996), who using observational evidence, suggested that orbit resonances in the region near corotation radius, where $2m$ orbits pile up, are responsible for the location of the bar ending. Similar results were found numerically by Patsis et al. (1997), whose orbital analysis of NGC 4314 predicted that the longest stable periodic orbits are found at 4:1 resonance; also reported in galaxy formation simulations by Okamoto et al. (2015). This indicates that, as suggested by Elmegreen (1996), bars tend to terminate at $2m$ ultraharmonic resonances.

Yurin & Springel (2015) and DeBuhr et al. (2012) attribute the jump in ζ to the so-called buckling instability phenomenon and present no further analysis. The shortening of the bar during the second ζ jump, which corresponds to the buckling instability, is consistent with results presented by Martinez-Valpuesta & Shlosman (2004) and Martinez-Valpuesta et al. (2006). In Section 5.3.3 it was shown that the buckling or bending of the bar arises due to the presence oscillation modes in a standing wave-like patterns, seen as offsets in $\langle z \rangle$ and $\langle v_z \rangle$in specific regions of the disk component. Similar behavior in $\langle z \rangle$ during the buckling has also been shown by Debattista et al. (2006) in simulations with rigid halos. Even that these $\langle z \rangle$ offsets more less coincide with the locations of the four modes seen in this work, no oscillation-like phenomena was noticed there.

Observational studies of wavelike phenomena in the Milky-Way (e.g. the 'wobbly' galaxy) have been of recent interest in the literature. Some examples are the wavelike perturbations in the North-South asymmetry of the number density and bulk velocity found by Widrow et al. (2012) in stars of the solar neighborhood; the sound wave-like behavior on the vertical velocity component of the solar neighborhood found by Williams et al. (2013) studying red-clump giants of RAVE survey; and the vertical oscillation of the galaxy detected with water and methanol masers by Bobylev & Bajkova (2015). Due to the nature of the observations (i.e. at Solar neighborhood) the authors of these studies attribute the wave-like phenomena to the presence of

spiral arms or satellite/subhalo interaction, and do not consider the bar as possible mechanism. There are numerical and analytical studies that supports the spiral arms (e.g. Faure et al. (2014)), and the interacting satellite (e.g. Gómez et al. 2013; Widrow et al. 2014) scenarios. Nonetheless there is also analytical work by Monari et al. (2015) that demonstrates, by means of perturbation theory, that vertical bulk motion in external parts of the disk can be caused by the perturbation of the bar. This can give some insight on the bulk vertical motion near the bar, because, despite the regions of interest are not the same, the results presented here show a strong resemblance to those of Monari et al. (2015).

Regarding the satellite/subhalo interaction, there is no doubt that these could be responsible for the oscillatory phenomena observed. However, the results presented here suggest that the oscillations observed in our simulation are mainly caused by the disk intrinsic evolution (in a live triaxial halo), rather that been originated only by the action of satellites. However, subhalos do might play a crucial role in the specific time at which jumps occur and evolutionary phases last, either by dynamical friction or angular momentum exchange within the disk-halo interaction, which would retard or accelerate a given event depending on the orientation and spin of the disk. The latter can be seen in the evolution of ζ of all `3180` disks (Fig. 5.12 bottom-left panel), in which all disks show similar behavior, but the moment and duration of each phase change even for disks with same $\theta_{\rm ori}$ but different spin.

It is reasonable to look for a wave-like explanation of the features presented in this section since wave nature of galactic phenomena has been studied in literature from the classic work of Lin & Shu (1964), who attributed the spiral pattern in galaxy disks to the propagation of density waves, to more recent papers such as Sellwood & Carlberg (2014), who studied the scenario in which spirals arms in simulations are explained by recurrent transient spiral modes, and Widrow & Bonner (2015) who studied the breathing- and bending- modes of the galaxy.

Sellwood & Carlberg (2014) emphasize that the word *mode* should only be used to refer to waves that remain fixed in shape and present an exponential growth, otherwise they should be called *wavepackets*. Sellwood & Carlberg (2014) also stress that modes are standing-waves that cause instabilities through positive feedback, even that they do not last indefinitely, as they eventually saturate and decay. These conditions appear to be fulfilled by the oscillatory phenomena observed here. As mentioned above it is reasonable to think of $\langle v_z \rangle$-$\langle z \rangle$ offsets as cavity modes, due to the fact that they only appear in specific configurations where the bar and resonant regions act as nodal points, imposing a boundary condition in which only the waves that can fit full oscillations in the cavity (i.e. resonant modes) will grow as standing waves, while all other frequencies will annihilate with each other.

In the results presented above it is seen that as the bar evolves and moves in the frequency

diagram, the boundaries change too and so do the wavelengths that satisfy the standing wave requirements, implying that not all the modes that were able to grow will be able to meet the new conditions. This means that modes capable to find a new configuration that fulfills the standing wave requirements will prevail (e.g. four modes after the ζ jump) while those that don't will vanish (e.g four modes after the bar-UHR4 separation). In a smaller scale this implies that these standing waves will manifest as specific orbital families that are responsible for the vertical heating and the 3D shape of the bar. These orbital families should be consistent with the ones found by Pfenniger & Friedli (1991) and Combes et al. (1990), for which stars at vertical orbital resonances ($m(\Omega_\phi - \Omega_p) = \nu$), should act as an efficient heating mechanism, in addition to be the building blocks of the peanut shape structure of the bar.

A visual inspection of these four oscillation modes, suggest a connection with the spiral structure of the disk at those times, this can be appreciated when the four modes arise. It can be observed in Figs. 5.17 and 5.22 that negative $\langle z \rangle$ regions are located at the ends of the bar where the spiral structure starts, thus the twisting experienced by these modes can also be seen as two asymmetric density streams (continuation of spiral arms) that tangle and move vertically in the same direction of $L_{\rm disk}$. The face-on view evolution of the disk structure shows strong resemblance to the manifold morphology shown in fig. 6 of Athanassoula et al. (2009a) (i.e. parameters $Q_{\rm m} = 9$ and $r_{\rm L} = 6$) corresponding to spiral arms entering through the ends of the bar and mildly interlacing at the center. This asymmetric bending of bar, seen as 'horn-like' structures when viewed edge-on, has also been observed in isolated simulations (e.g Martinez-Valpuesta & Shlosman 2005; O'Neill & Dubinski 2003), nevertheless in all of our simulations the peanut/X-shaped pseudobulge appears right after this unique buckling, and not after a second one (e.g. Martinez-Valpuesta & Shlosman 2005; Martinez-Valpuesta et al. 2006), which, as has been seen in this section, would be accompanied by another jump in ζ.

Lastly, as mentioned above some features presented by the disks in our simulations might be explained using manifold theory of galactic features such as rings and spiral arms (Athanassoula, 2012; Athanassoula et al., 2009a, 2010, 2009b; Romero-Gómez et al., 2007, 2006). This possibility also arises due to the presence of long-lived ring structures displayed by almost all galaxies after the buckling of the bar (Section 5.1), and the location of $\langle z \rangle$ offsets, which might be related to the Lagrangian points at given times of the simulation. Further analysis of this relation is beyond the scope of this work.

Polar Ring Galaxies

It is reasonable to associate these outer structures with the ones displayed by Polar Ring Galaxies (PRGs) due to the resemblance shown by the rings in the simulations, as shown in

Fig. 6.2. Although the purpose of this work does not intend to reproduce PRGs, there are some common features between our simulated galaxies and observed PRGs that lead us to think of a possible connection between these two. One example is the rotation velocity of the ring, though it is subject to debate whether the ring is slower (e.g NGC 660 Moiseev 2014; van Driel et al. 1995; NGC 4262 Khoperskov et al. 2014b), or faster than the disk (e.g. SPRC-7 Khoperskov et al. 2014b), we find that our simulations agree with former picture as seen in Fig. 5.25.

The case of NGC 660 is of interest due to several aspects: (1) the slower rotating disk mentioned above; (2) the observational studies from van Driel et al. (1995) of NGC 660 determined that the ring followed an exponential luminosity profile, which by construction is also expected for our simulations; and (3) that the disk has a boxy/X-shaped bulge, as those shown in this chapter. Other similarities arise from observations by Moiseev (2014), who identified a warp in the outer disk corresponding to the HI distribution, and an overlapping of material from central disk and the ring, which is interpreted as the intersection of orbits of components with different spin, which can be observed from the velocity field of the galaxy. These features can be associated to the diffuse material caused by the precession of the ring and the material left behind when the ring detaches from the rest of the galaxy, which is clearly seen for disk `3180_major` in Figs. 5.3 and 5.25.

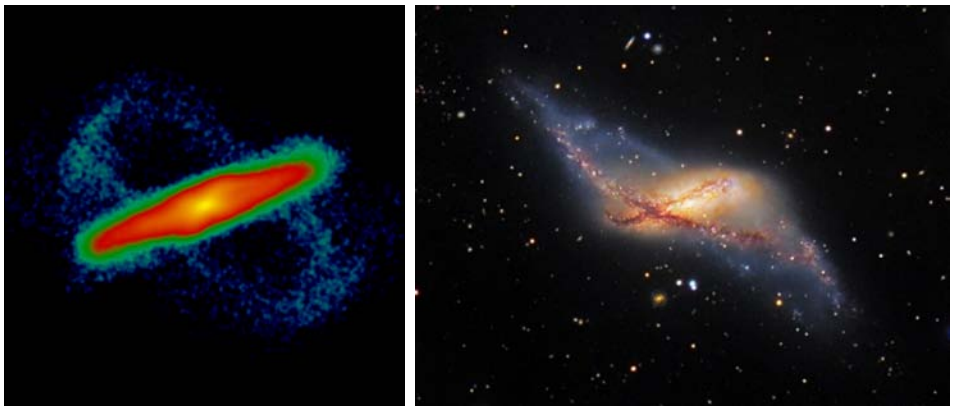

Figure 6.2: Morphological comparison between 3795 major disk and NGC 660. NGC 660 image credit: Immo Gerber and Dietnar Hager, TAO Observatory

However, the are also important differences between NGC 660 and our simulated disks. For example, van Driel et al. (1995) estimate a diameter of ~ 11 kpc for the disk and 31 kpc for the ring, while in our simulations the difference in diameters is much smaller due to the formation mechanism. Additionally they calculate a ring mass of about 75% the mass of disk, proportion, much bigger than the ones from ours ($< 10\%$). The difference in masses and diameters may arise due to numerous facts, such as the approximation used here, the absence of gas and its

physics in our simulations or that in fact NGC 660 did not formed from a similar process as the one described here.

Despite the differences mentioned, the connection between our simulations and the PRGs arises from:

- **Formation scenario.** Brook et al. (2008) used cosmological hydrodynamical simulations to study the formation of polar structures in galaxies, although their simulation results on the formation of a Polar Disk Galaxy (PDG), they argue that the formation of these features is simply the product of continuous gas accretion whose angular momentum is misaligned with the central galaxy, and the formation of PRGs may arise due to a transition from PDG to PRG. Bournaud & Combes (2003) studied the origin of PRGs from the tidal gas accretion from a companion and merger scenario. Although both approaches produce PRGs, Bournaud & Combes (2003) argue that the tidal accretion one better explains the existence of PRGs. Nevertheless, it is still an open question if all PRGs have a common formation picture or if the different configurations observed come from several formation scenarios.

- **Stability.** The stability of gaseous and stellar rings in simulations has been reported broadly in the literature (e.g. Bournaud & Combes 2003; Brook et al. 2008; Khoperskov et al. 2014a). Some of them show stability for a couple of Gyrs (Brook et al., 2008), while others assuming different formation scenarios are report a stability of $\sim$ 8-10 Gyrs (Bournaud & Combes, 2003). Although the stability of these disks arises from self-gravity, studies by Khoperskov et al. (2014a) of non-self-gravitating gaseous disks show stability for some orbital periods. In our simulations rings are stable for at least $\sim 5-6$ Gyrs.

- **Shape of dark matter halo.** Khoperskov et al. (2014b) introduced a method to determine the shape of the distribution of dark matter halo by fitting spheroids that vary with radius. Their results suggest a flattened halo towards the PR plane for SPRC-7, and a transition from prolate to oblate for NGC 4262. In a similar work using the same method Moiseev et al. (2015) argued that the differences in specific configuration of PRGs determine a specific flattening of the halo for each object, which may indicate the absence of a single universal formation scenario for all PRGs. However, the distribution shape estimated depends highly on the model assumed and in additional information from observations, thus the results obtained will only be as reliable as the precision of these two. A comparison of Moiseev et al. (2015) results with the ones of this work is shown in Fig. 6.3. It is important to take into account that the halo at $z = 1$ has not interacted with

a live disk yet, while at $z = 0$ has had enough time to interact reaching a PR-like configuration. The estimated potential for NGC 4262 does not resemble that of the density of a simulated halo, even for $z = 1$ rigid disk, while SPRC 260 shows a better resembling. Results for NGC 4262 are intriguing because the gravitational equipotential surfaces are expected to show a smoother change in comparison with then isodensity surfaces, rather than presenting abrupt changes in their shape within few kiloparsecs.

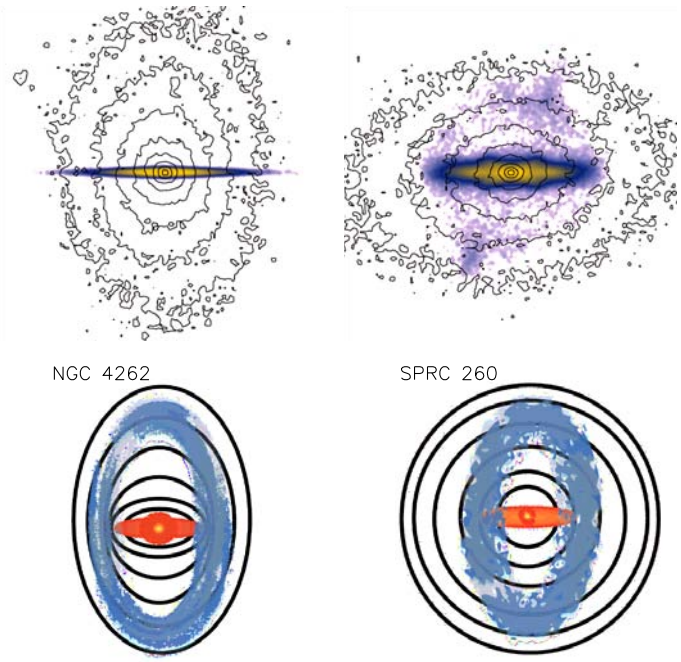

Figure 6.3: *Top.* Isodensity contours of `3748_major` dark matter halo at $z = 1$ (left) and at $z = 0$ (right).*Bottom.* Dark matter halo potential taken from Moiseev et al. (2015).

The connection between observed PRGs and the structures found in this work cannot go much further from a simple comparison due to the features of this study and several aspects have to be taken into account. First of all, this study analyzes pure N-body simulations without gas nor its related physics, which is extremely important in order to compare the star formation with the observed in PRGs. Secondly, it is not clear the viability of a scenario where the gas is accreted by the hal o in a configuration similar to that of our major-oriented disks in a cosmological context, and if that that picture can account for the fraction of observed PRGs. Finally, better mass and spatial resolution is needed for the halo and disk to resolve adequately all the components of the galaxy in order to compare with the observed PRGs. Though, the possibility of a PRG formation scenario similar to the one observed for the high $\theta_{\rm ori}$ simulations studied in this work may represent a viable model, but more detailed studies need to be performed. It

is worth to mention that the available sample of PRGs is quite low, essentially the Polar Ring Catalog by Whitmore et al. (1990), and recently, has been a renovated effort to have a larger catalog of these galactic systems using SDSS (see Moiseev et al. 2011).

Chapter 7

Concluding Remarks

An N-body study of the dynamics and evolution of stellar disks in a cosmological context was presented. Using a modified version of the publicly available code GADGET-2, the growth of a disk galaxy was done by gradually increasing the mass of an exponential disk inside high-resolution cosmological dark matter halos. These halos were selected by setting restrictions on their mass, accretion history, and to be in an isolated environment. A total of thirteen simulations were perfomed by following the evolution of four disks, one for each one of the selected halos, for which several orientations of disk angular momentum were considered. The models studied include disks with its angular momentum $L_{\rm disk}$ oriented parallel to either the minor or major axis of halo inertia tensor, with $L_{\rm disk}$ making an angle $\theta_{\rm ori}$ with respect to minor axis, and disks with these orientations but rotating in the opposite direction, the `spin` models.

At early times, all disks develop spiral arms, with a remarkable preference for the minor and major orientations to develop grand design spirals. Intermediate $\theta_{\rm ori}$ orientations show a transition from grand design towards flocculent spirals as $\theta_{\rm ori}$ increases. At the end of the the simulation time, the general face-on morphology of the disks exhibits a prominent bar, a ring around the bar, and weak structures in the outer parts of the disk.

The edge-on structure of all disks displays common features such as a corrugation of the disk and a peanut/X-shaped pseudo-bulge. The most striking difference is observed in disks with large $\theta_{\rm ori}$ orientations, which display a ring structure that separates from the rest of the disk. No notable differences in the morphology between `spin` and `no-spin` disks were found.

The surface, Σ, and vertical, ρ, density is also similar for all the disks. The evolution of the surface density Σ shows slight deviations from the initial exponential profile. The vertical density ρ display a broadening of the profile due to disk heating; a convergence at the innermost radii, as a result of the formation of a 'boxy core' at the center of the disk; and a strong broadening in the middle region due to the growth of the peanut/X-shape pseudo-bulge.

The velocity dispersion, σ_z, profile for all disks displays a gradual increment at all radii, characterized by a pronounced slope in the inner regions $r \lesssim 2R_{\rm d}$, and a flatter one in the outer radii $r \gtrsim 2R_{\rm d}$. A noticeable increment in σ_z is observed due to the presence and growth of the bar. The morphological evolution of the peanut/X-shape pseudo-bulge is appreciated as a triangular shape in the disk height, $z_{1/2}$, profiles. It is shown that in the outer parts $z_{1/2}$ rises as the angle $\theta_{\rm ori}$ increases due to the presence of warps that become more evident in orientations with larger $\theta_{\rm ori}$. An even greater increment in $z_{1/2}$ is appreciated in major-oriented and $\theta_{\rm ori}$= 60 models, which results from the ring structure that decouples from the disk in these models.

It is shown that the phases displayed by disk heating, ζ, bar strength, A_2, and parameter $\mathcal{R}$, are explained by the interaction between the bar and resonance regions. A simultaneous jump in ζ, drop in A_2, and rise in $\mathcal{R}$ is seen during these interactions accompanied by the growth of stationary vertical oscillation modes. It is observed that these modes develop when the bar termination crosses resonance regions, specifically $\Omega - \kappa/8$ (UHR8) and $\Omega - \kappa/4$ (UHR4). These modes are responsible for producing corrugations in the disk during the UHR8 crossing, and the buckling instability when the UHR4 crossing occurs. The models also display a tendency for the bar to terminate at these resonances, as well as exhibiting an apparent stable configuration observed as a steady mild increment in ζ and a nearly constant $\mathcal{R}$.

All models experience reorientation of their angular momentum $L_{\rm disk}$ during the course of their evolution. Bigger tilting angles θ are expected for models with large $\theta_{\rm ori}$, nonetheless exceptions to the rule may exist. Independently of the evolution of angle θ, major-oriented and $\theta_{\rm ori}$= 60 models present ring structures that separate from the rest of the disk. As these structures are long-lived, lasting $\sim$ 6 Gyrs, and present a similar morphology as Polar Ring Galaxies (PRGs), it is reasonable to consider this mechanism as possible PRG formation scenario.

For major-oriented models, a large redistribution of inner halo mass is observed, as a consequence of the growth of the disk. At $z_{\rm live}$, $L_{\rm disk}$ of these models is aligned parallel to minor axis at inner radii, while outer radii are surprisingly aligned with the intermediate axis, being then a possible explanation of the large tilt and the ring structure observed in these disks. The evolution of the angle between the angular momentum of a cylindrical bin and the innermost angular momentum, α, and the angle between the angular momentum of the bin and the halo minor axis measured at the same radius of the bin, γ, show that $L_{\rm disk}$ tries to align with minor axis of the halo at ever larger radii, while keeping the already adjusted regions aligned. This suggests that there exists a strong coupling between the mass distribution of the inner halo and the angular momentum of the disk, in which the minor axis is found as a favored orientation.

Nonetheless there are several questions that remain to be addressed. Extended analysis of the results presented here include: an investigation of the possible mechanisms responsible for

the fixed envelope of the triangular shape in the $z_{1/2}$; a profound study of the differences between `spin` and `no-spin` models, more specifically to examine the effects produced by the the subhalos that describe prograde orbits for one model and retrograde for the other; and a broader description of the stationary wave-modes by studying the role vertical resonances $\Omega - \nu/m$. Future work will also cover a deeper analysis of the angular momentum transfer between disk, bar and halo, orbital analysis, a very detailed analysis on the evolution of the angular momentum and matter redistribution of the halos.

In conclusion,

- N-body simulations are still a useful tool to study the dynamics of collisionless systems, such as a stellar disk embedded in cosmological dark matter halos. Nonetheless, simulations including gas and its related physics are needed to get a complete picture of the evolution of these systems, which would also provide further insight into the possible connection between the results obtained here and observed PRGs, for example, NGC 660.
- The methodology implemented in this work provides a complementary approach to galaxy formation and allows to follow up the evolution of disk galaxies. This method can be easily extended to include additional components of the galaxy, e.g. bulge, to study the evolution of disks in different cosmologies, environments, etc.
- The buckling instability of the bar, as well as corrugations in the disk, are product of standing wave-like phenomena produced by the interaction of the bar termination with resonance regions of the galaxy.
- The angular momentum of the disk is confirmed to preferably align parallel to minor axis of the halo. Major-oriented models are observed to align parallel to minor axis at ever larger radii as they tilt/tumble during their evolution, suggesting the existence a strong coupling between the mass distribution of the inner halo and the angular momentum of the disk.
- The ring structures displayed by major-oriented and $\theta_{\rm ori}= 60$ models are expected to be product of the misalignment between the angular momentum of outer radii of the disk and the minor axis of halo inertia tensor. As these features are consistently found only in such orientations, and are observed to preserve their structure for several Gyrs, these configurations are within one of the proposed possible formation scenario of PRGs.

References

Athanassoula, E. 2003, MNRAS, 341, 1179

—. 2012, MNRAS, 426, L46

—. 2014, MNRAS, 438, L81

Athanassoula, E., Machado, R. E. G., & Rodionov, S. A. 2013, MNRAS, 429, 1949

Athanassoula, E. & Misiriotis, A. 2002, MNRAS, 330, 35

Athanassoula, E., Romero-Gómez, M., Bosma, A., & Masdemont, J. J. 2009a, MNRAS, 400, 1706

—. 2010, MNRAS, 407, 1433

Athanassoula, E., Romero-Gómez, M., & Masdemont, J. J. 2009b, MNRAS, 394, 67

Avila-Reese, V., Colín, P., González-Samaniego, A., Valenzuela, O., Firmani, C., Velázquez, H., & Ceverino, D. 2011, ApJ, 736, 134

Bailin, J., Kawata, D., Gibson, B. K., Steinmetz, M., Navarro, J. F., Brook, C. B., Gill, S. P. D., Ibata, R. A., Knebe, A., Lewis, G. F., & Okamoto, T. 2005, ApJ, 627, L17

Bailin, J. & Steinmetz, M. 2005, ApJ, 627, 647

Barazza, F. D., Jogee, S., & Marinova, I. 2008, ApJ, 675, 1194

Barnes, J. & Hut, P. 1986, Nature, 324, 446

Begeman, K. G. 1989, A&A, 223, 47

Bernardeau, F., Colombi, S., Gaztañaga, E., & Scoccimarro, R. 2002, Phys. Rep., 367, 1

Bett, P. E. & Frenk, C. S. 2012, MNRAS, 420, 3324

Binney, J. & Tremaine, S. 2008, Galactic Dynamics: Second Edition (Princeton University Press)

Bobylev, V. V. & Bajkova, A. T. 2015, MNRAS, 447, L50

Bouchet, F. R., Colombi, S., Hivon, E., & Juszkiewicz, R. 1995, A&A, 296, 575

Bournaud, F. & Combes, F. 2003, A&A, 401, 817

Boylan-Kolchin, M., Springel, V., White, S. D. M., Jenkins, A., & Lemson, G. 2009, MNRAS, 398, 1150

Brook, C. B., Governato, F., Quinn, T., Wadsley, J., Brooks, A. M., Willman, B., Stilp, A., & Jonsson, P. 2008, ApJ, 689, 678

Carrasco, E. R., Gomez, P. L., Verdugo, T., Lee, H., Diaz, R., Bergmann, M., Turner, J. E. H., Miller, B. W., & West, M. J. 2010, ApJ, 715, L160

Coles, P. & Lucchin, F. 2002, Cosmology: The Origin and Evolution of Cosmic Structure, Second Edition

Colín, P., Avila-Reese, V., & Valenzuela, O. 2000, ApJ, 542, 622

Colín, P., Avila-Reese, V., Vázquez-Semadeni, E., Valenzuela, O., & Ceverino, D. 2010, ApJ, 713, 535

Combes, F., Debbasch, F., Friedli, D., & Pfenniger, D. 1990, A&A, 233, 82

Combes, F. & Sanders, R. H. 1981, A&A, 96, 164

Contopoulos, G. 1980, A&A, 81, 198

Debattista, V. P., Mayer, L., Carollo, C. M., Moore, B., Wadsley, J., & Quinn, T. 2006, ApJ, 645, 209

DeBuhr, J., Ma, C.-P., & White, S. D. M. 2012, MNRAS, 426, 983

Dubinski, J., Berentzen, I., & Shlosman, I. 2009, ApJ, 697, 293

Efstathiou, G., Davis, M., White, S. D. M., & Frenk, C. S. 1985, ApJS, 57, 241

Efstathiou, G., Lake, G., & Negroponte, J. 1982, MNRAS, 199, 1069

Elmegreen, B. Astronomical Society of the Pacific Conference Series, Vol. 91, , IAU Colloq. 157: Barred Galaxies, ed. R. ButaD. A. Crocker & B. G. Elmegreen, 197

Eskridge, P. B., Frogel, J. A., Pogge, R. W., Quillen, A. C., Davies, R. L., DePoy, D. L., Houdashelt, M. L., Kuchinski, L. E., Ramírez, S. V., Sellgren, K., Terndrup, D. M., & Tiede, G. P. 2000, AJ, 119, 536

Faure, C., Siebert, A., & Famaey, B. 2014, MNRAS, 440, 2564

Fry, A. B., Governato, F., Pontzen, A., Quinn, T., Tremmel, M., Anderson, L., Menon, H., Brooks, A. M., & Wadsley, J. 2015, MNRAS, 452, 1468

Geller, M. J. & Huchra, J. P. 1989, Science, 246, 897

Gill, S. P. D., Knebe, A., & Gibson, B. K. 2004, MNRAS, 351, 399

Gingold, R. A. & Monaghan, J. J. 1977, MNRAS, 181, 375

Gómez, F. A., Minchev, I., O'Shea, B. W., Beers, T. C., Bullock, J. S., & Purcell, C. W. 2013,

MNRAS, 429, 159

Gott, III, J. R., Jurić, M., Schlegel, D., Hoyle, F., Vogeley, M., Tegmark, M., Bahcall, N., & Brinkmann, J. 2005, ApJ, 624, 463

Guth, A. H. 1981, Phys. Rev. D, 23, 347

Guth, A. H. & Pi, S.-Y. 1982, Physical Review Letters, 49, 1110

Hahn, O. & Abel, T. 2011, MNRAS, 415, 2101

Hayashi, E., Navarro, J. F., & Springel, V. 2007, MNRAS, 377, 50

Hernquist, L. & Katz, N. 1989, ApJS, 70, 419

Herschel, W. 1785, Royal Society of London Philosophical Transactions Series I, 75, 213

Hinshaw, G., Larson, D., Komatsu, E., Spergel, D. N., Bennett, C. L., Dunkley, J., Nolta, M. R., Halpern, M., Hill, R. S., Odegard, N., Page, L., Smith, K. M., Weiland, J. L., Gold, B., Jarosik, N., Kogut, A., Limon, M., Meyer, S. S., Tucker, G. S., Wollack, E., & Wright, E. L. 2013, ApJS, 208, 19

Hockney, R. W. & Eastwood, J. W. 1981, Computer Simulation Using Particles

Holmberg, E. 1941, ApJ, 94, 385

Hubble, E. 1929, Proceedings of the National Academy of Science, 15, 168

Jeon, M., Kim, S. S., & Ann, H. B. 2009, ApJ, 696, 1899

Jeong, D. 2010, PhD thesis, University of Texas, Austin

Kendall, M., Stuart, A., & Ord, J. K. 1987, Kendall's Advanced Theory of Statistics

Khoperskov, S., Moiseev, A., Khoperskov, A., & Saburova, A. S. in , Astronomical Society of the Pacific Conference Series, Vol. 486, Multi-Spin Galaxies, ASP Conference Series, ed. E. IodiceE. M. Corsini, 221

Khoperskov, S. A., Moiseev, A. V., Khoperskov, A. V., & Saburova, A. S. 2014b, MNRAS, 441, 2650

Kim, J., Park, C., Rossi, G., Lee, S. M., & Gott, III, J. R. 2011, Journal of Korean Astronomical Society, 44, 217

Kim, J.-h., Abel, T., Agertz, O., Bryan, G. L., Ceverino, D., Christensen, C., Conroy, C., Dekel, A., Gnedin, N. Y., Goldbaum, N. J., Guedes, J., Hahn, O., Hobbs, A., Hopkins, P. F., Hummels, C. B., Iannuzzi, F., Keres, D., Klypin, A., Kravtsov, A. V., Krumholz, M. R., Kuhlen, M., Leitner, S. N., Madau, P., Mayer, L., Moody, C. E., Nagamine, K., Norman, M. L., Onorbe, J., O'Shea, B. W., Pillepich, A., Primack, J. R., Quinn, T., Read, J. I., Robertson, B. E., Rocha, M., Rudd, D. H., Shen, S., Smith, B. D., Szalay, A. S., Teyssier,

R., Thompson, R., Todoroki, K., Turk, M. J., Wadsley, J. W., Wise, J. H., Zolotov, A., & AGORA Collaboration29, t. 2014a, ApJS, 210, 14

Kim, J. H., Peirani, S., Kim, S., Ann, H. B., An, S.-H., & Yoon, S.-J. 2014b, ApJ, 789, 90

Klessen, R. 1997, MNRAS, 292, 11

Klypin, A., Kravtsov, A. V., Bullock, J. S., & Primack, J. R. 2001, ApJ, 554, 903

Klypin, A. A. & Shandarin, S. F. 1983, MNRAS, 204, 891

Klypin, A. A., Trujillo-Gomez, S., & Primack, J. 2011, ApJ, 740, 102

Knollmann, S. R. & Knebe, A. 2009, ApJS, 182, 608

Kravtsov, A. V., Klypin, A. A., & Khokhlov, A. M. 1997, ApJS, 111, 73

Landau, L. & Lifshitz, E. 1976, Mechanics, Butterworth Heinemann (Butterworth-Heinemann)

Leavitt, H. S. & Pickering, E. C. 1912, Harvard College Observatory Circular, 173, 1

Liddle, A. 2003, An Introduction to Modern Cosmology (Wiley)

Limousin, M., Richard, J., Kneib, J.-P., Brink, H., Pelló, R., Jullo, E., Tu, H., Sommer-Larsen, J., Egami, E., Michałowski, M. J., Cabanac, R., & Stark, D. P. 2008, A&A, 489, 23

Lin, C. C. & Shu, F. H. 1964, ApJ, 140, 646

Lucy, L. B. 1977, AJ, 82, 1013

Marinacci, F., Pakmor, R., & Springel, V. 2014, MNRAS, 437, 1750

Martinez-Valpuesta, I. & Shlosman, I. 2004, ApJ, 613, L29

Martinez-Valpuesta, I. & Shlosman, I. The Evolution of Starbursts, ed. , S. HüttmeisterE. MantheyD. Bomans & K. Weis, 189–195

Martinez-Valpuesta, I., Shlosman, I., & Heller, C. 2006, ApJ, 637, 214

McMillan, S. L. W. & Aarseth, S. J. 1993, ApJ, 414, 200

Mo, H., van den Bosch, F. C., & White, S. 2010, Galaxy Formation and Evolution

Mo, H. J., Mao, S., & White, S. D. M. 1998, MNRAS, 295, 319

Moiseev, A. in , Astronomical Society of the Pacific Conference Series, Vol. 486, Multi-Spin Galaxies, ASP Conference Series, ed. E. IodiceE. M. Corsini, 61

Moiseev, A., Khoperskov, S., Khoperskov, A., Smirnova, K., Smirnova, A., Saburova, A., & Reshetnikov, V. 2015, Baltic Astronomy, 24, 76

Moiseev, A. V., Smirnova, K. I., Smirnova, A. A., & Reshetnikov, V. P. 2011, MNRAS, 418, 244

Mollitor, P., Nezri, E., & Teyssier, R. 2015, MNRAS, 447, 1353

Monari, G., Famaey, B., & Siebert, A. 2015, ArXiv e-prints

Moscardini, L. & Dolag, K. Dark Matter and Dark Energy, ed. , S. MatarreseM. ColpiV. Gorini & U. Moschella (Springer Netherlands), 217–237

Okamoto, T., Isoe, M., & Habe, A. 2015, PASJ, 67, 63

O'Neill, J. K. & Dubinski, J. 2003, MNRAS, 346, 251

Padmanabhan, T. 1996, Cosmology and Astrophysics through Problems

Park, C., Choi, Y.-Y., Kim, J., Gott, III, J. R., Kim, S. S., & Kim, K.-S. 2012, ApJ, 759, L7

Patsis, P. A., Athanassoula, E., & Quillen, A. C. 1997, ApJ, 483, 731

Peacock, J. A. 1999, Cosmological Physics

Pen, U.-L. 1997, ApJ, 490, L127

Perlmutter, S., Aldering, G., Goldhaber, G., Knop, R. A., Nugent, P., Castro, P. G., Deustua, S., Fabbro, S., Goobar, A., Groom, D. E., Hook, I. M., Kim, A. G., Kim, M. Y., Lee, J. C., Nunes, N. J., Pain, R., Pennypacker, C. R., Quimby, R., Lidman, C., Ellis, R. S., Irwin, M., McMahon, R. G., Ruiz-Lapuente, P., Walton, N., Schaefer, B., Boyle, B. J., Filippenko, A. V., Matheson, T., Fruchter, A. S., Panagia, N., Newberg, H. J. M., Couch, W. J., & Project, T. S. C. 1999, ApJ, 517, 565

Pfenniger, D. & Friedli, D. 1991, A&A, 252, 75

Planck Collaboration, Ade, P. A. R., Aghanim, N., Armitage-Caplan, C., Arnaud, M., Ashdown, M., Atrio-Barandela, F., Aumont, J., Baccigalupi, C., Banday, A. J., & et al. 2014, A&A, 571, A16

Quinn, T., Katz, N., Stadel, J., & Lake, G. 1997, ArXiv Astrophysics e-prints

Rautiainen, P., Salo, H., & Laurikainen, E. 2005, ApJ, 631, L129

Riess, A. G., Filippenko, A. V., Challis, P., Clocchiatti, A., Diercks, A., Garnavich, P. M., Gilliland, R. L., Hogan, C. J., Jha, S., Kirshner, R. P., Leibundgut, B., Phillips, M. M., Reiss, D., Schmidt, B. P., Schommer, R. A., Smith, R. C., Spyromilio, J., Stubbs, C., Suntzeff, N. B., & Tonry, J. 1998, AJ, 116, 1009

Rodionov, S. A. & Athanassoula, E. 2011, A&A, 529, A98

Rodionov, S. A., Athanassoula, E., & Sotnikova, N. Y. 2009, MNRAS, 392, 904

Rodionov, S. A. & Orlov, V. V. 2008, MNRAS, 385, 200

Rodionov, S. A. & Sotnikova, N. Y. 2006, Astronomy Reports, 50, 983

Romero-Gómez, M., Athanassoula, E., Masdemont, J. J., & García-Gómez, C. 2007, A&A, 472, 63

Romero-Gómez, M., Masdemont, J. J., Athanassoula, E., & García-Gómez, C. 2006, A&A, 453, 39

Scannapieco, C. & Athanassoula, E. 2012, MNRAS, 425, L10

Scannapieco, C., Wadepuhl, M., Parry, O. H., Navarro, J. F., Jenkins, A., Springel, V., Teyssier, R., Carlson, E., Couchman, H. M. P., Crain, R. A., Dalla Vecchia, C., Frenk, C. S., Kobayashi, C., Monaco, P., Murante, G., Okamoto, T., Quinn, T., Schaye, J., Stinson, G. S., Theuns, T., Wadsley, J., White, S. D. M., & Woods, R. 2012, MNRAS, 423, 1726

Schewtschenko, J. A., Wilkinson, R. J., Baugh, C. M., Bœhm, C., & Pascoli, S. 2015, MNRAS, 449, 3587

Sellwood, J. A. 2013, ApJ, 769, L24

—. 2014, Reviews of Modern Physics, 86, 1

Sellwood, J. A. & Carlberg, R. G. 2014, ApJ, 785, 137

Sirko, E. 2005, ApJ, 634, 728

Springel, V. 2005, MNRAS, 364, 1105

Springel, V., Wang, J., Vogelsberger, M., Ludlow, A., Jenkins, A., Helmi, A., Navarro, J. F., Frenk, C. S., & White, S. D. M. 2008, MNRAS, 391, 1685

Springel, V., White, S. D. M., Jenkins, A., Frenk, C. S., Yoshida, N., Gao, L., Navarro, J., Thacker, R., Croton, D., Helly, J., Peacock, J. A., Cole, S., Thomas, P., Couchman, H., Evrard, A., Colberg, J., & Pearce, F. 2005, Nature, 435, 629

Springel, V., Yoshida, N., & White, S. D. M. 2001, New A, 6, 79

Toomre, A. 1964, ApJ, 139, 1217

van Driel, W., Combes, F., Casoli, F., Gerin, M., Nakai, N., Miyaji, T., Hamabe, M., Sofue, Y., Ichikawa, T., Yoshida, S., Kobayashi, Y., Geng, F., Minezaki, T., Arimoto, N., Kodama, T., Goudfrooij, P., Mulder, P. S., Wakamatsu, K., & Yanagisawa, K. 1995, AJ, 109, 942

Velazquez, H. & White, S. D. M. 1999, MNRAS, 304, 254

Villa-Vargas, J., Shlosman, I., & Heller, C. 2009, ApJ, 707, 218

Vogelsberger, M., Genel, S., Springel, V., Torrey, P., Sijacki, D., Xu, D., Snyder, G., Bird, S., Nelson, D., & Hernquist, L. 2014a, Nature, 509, 177

Vogelsberger, M., Genel, S., Springel, V., Torrey, P., Sijacki, D., Xu, D., Snyder, G., Nelson, D., & Hernquist, L. 2014b, MNRAS, 444, 1518

Weinberg, D. H., Bullock, J. S., Governato, F., Kuzio de Naray, R., & Peter, A. H. G. 2013, ArXiv e-prints

Weinberg, M. D. 1992, ApJ, 384, 81

Weinberg, S. 2008, Cosmology (Oxford University Press)

Whitmore, B. C., Lucas, R. A., McElroy, D. B., Steiman-Cameron, T. Y., Sackett, P. D., & Olling, R. P. 1990, AJ, 100, 1489

Widrow, L. M., Barber, J., Chequers, M. H., & Cheng, E. 2014, MNRAS, 440, 1971

Widrow, L. M. & Bonner, G. 2015, MNRAS, 450, 266

Widrow, L. M., Gardner, S., Yanny, B., Dodelson, S., & Chen, H.-Y. 2012, ApJ, 750, L41

Williams, M. E. K., Steinmetz, M., Binney, J., Siebert, A., Enke, H., Famaey, B., Minchev, I., de Jong, R. S., Boeche, C., Freeman, K. C., Bienaymé, O., Bland-Hawthorn, J., Gibson, B. K., Gilmore, G. F., Grebel, E. K., Helmi, A., Kordopatis, G., Munari, U., Navarro, J. F., Parker, Q. A., Reid, W., Seabroke, G. M., Sharma, S., Siviero, A., Watson, F. G., Wyse, R. F. G., & Zwitter, T. 2013, MNRAS, 436, 101

Yadav, J. K., Bagla, J. S., & Khandai, N. 2010, MNRAS, 405, 2009

Yurin, D. & Springel, V. 2015, MNRAS, 452, 2343

Zel'dovich, Y. B. 1970, A&A, 5, 84

Zemp, M., Gnedin, O. Y., Gnedin, N. Y., & Kravtsov, A. V. 2012, ApJ, 748, 54

Zhang, Y., Yang, X., Wang, H., Wang, L., Luo, W., Mo, H. J., & van den Bosch, F. C. 2015, ApJ, 798, 17